Doctoral Thesis

Theoretical Reaction Mechanistic Studies on Energetic Nanomaterials and Li-CO$_2$ Battery via Multi-Scale Molecular Simulation

Woo Cheol Jeon

Department of Chemical Engineering

Graduate School of UNIST

2020

Theoretical Reaction Mechanistic Studies on Energetic Nanomaterials Li-CO$_2$ Battery via Multi-Scale Molecular Simulation

Woo Cheol Jeon

Department of Chemical Engineering

Graduate School of UNIST

ULSAN NATIONAL INSTITUTE OF
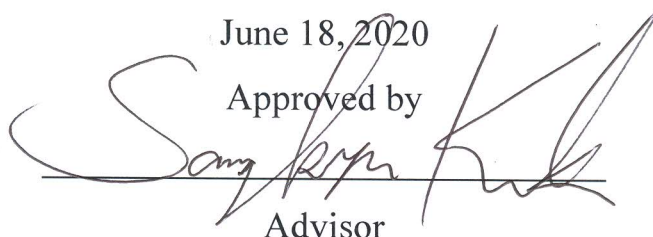SCIENCE AND TECHNOLOGY

Theoretical Reaction Mechanistic Studies on Energetic Nanomaterials and Li-CO$_2$ Battery via Multi-Scale Molecular Simulation

A thesis/dissertation

submitted to the Graduate School of UNIST

in partial fulfillment of the

requirements for the degree of

Doctor of Philosophy
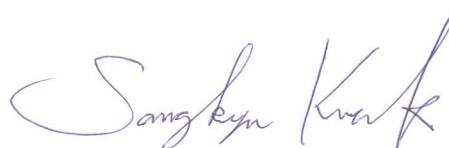
Woo Cheol Jeon

June 18, 2020

Approved by

Advisor

Sang Kyu Kwak

Theoretical Reaction Mechanistic Studies on Energetic Nanomaterials and Li-CO$_2$ Battery via Multi-Scale Molecular Simulation

Woo Cheol Jeon

This certifies that the thesis of Woo Cheol Jeon is approved.
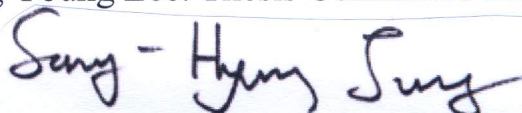
June 18, 2020

_____

Advisor: Sang Kyu Kwak

_____

Seok Ju Kang: Thesis Committee Member #1

_____

Jun Hee Lee: Thesis Committee Member #2

_____

Chang Young Lee: Thesis Committee Member #3

_____

Sang-Hyun Jung: Thesis Committee Member #4

Abstract

In recent years, the development of energy systems with improved efficiency has become an important issue in the industrial manufacturing field due to the depletion of traditional energy fuels and ever-increasing commercial demands. Amid this sweeping trend, nanomaterials, which can exert different novel properties to those in conventional macroscopic materials, can be utilized for various energy applications. Nanomaterials play a major role in energy release and energy source. For application in energy release and energy sources, nanomaterials need to release high thermal energy from a relatively low energy level of external shocks or need to exert a high specific capacity and power density, respectively. In other words, nanomaterials for energy applications are required to have high energy density. To enhance their energy density, several nanomaterial candidates have been considered and synthesized. However, there are several difficulties in testing all the candidates due to time constraints and economic issues. Thus, for a more efficient development of the target nanomaterial, a process to screen the candidates is necessary, and reaction mechanistic studies can be conducted as additional processes to advance real experiments. These studies facilitate maximization of energy density in nanomaterials from investigation of thermodynamically and kinetically efficient reaction pathway and comparison of energy surfaces among reaction intermediates. Moreover, theoretical methods can prove to be helpful for reaction mechanistic studies. In this doctoral dissertation, reaction mechanistic studies in energy applications of nanomaterials have been conducted *via* multi-scale molecular simulation technique, which can prove to be a powerful tool to understand the physico-chemical phenomena for the reaction mechanistic studies of nanomaterials in energy applications.

In Chapter 2, we theoretically tracked the reaction process of Ni-Al nanoalloys. Molecular dynamics simulations had been applied to investigate the characteristics depending on molar ratio of Ni and Al, the bilayer thickness of nanolayer, and ignition temperature. It was found that the variation of stoichiometry between Ni and Al had marginal effects on the overall process of reaction coordinates, however, the reaction rate and intermixing regions were different in each system. In addition, quantitative analysis on the reaction kinetics and thermodynamics were performed under different reaction and structural conditions. In this theoretical study, the reaction characteristics of Ni-Al nanolayers were quantified with systematic calculations. Therefore, it was expected to contribute to fabricate more advanced Ni-Al nanolayer products.

In Chapter 3, we investigated the explosion characteristics of a nanobomb. In a nanobomb, nitromethane is constantly protected from the external environment due to stable mechanical and thermal properties of carbon nanotube (CNT) and is confined with the built-up pressure. After injection of thermal energy into confined nitromethane (NM) at various densities, the nanobomb was completely

decomposed along the bursting process. The results show that the explosion time was reduced at a higher density and initial temperature. While NM was being decomposed into intermediates, Stone-Wales (SW) defects or high-order rings were randomly constructed at both the cap and side wall of CNT. Subsequently, carbon atoms at defect sites were functionalized by the reaction intermediates, where nanoholes were generated and burst at the end of bursting phenomena.

Next, physicochemical modification of CNT was considered to improve the performance of the nanobomb. Chirality, nitrogen-doping, and monovacancy defect were introduced into CNT. All types of modifications on CNT brought time reduction in bursting of nanobomb although there was similarity on overall bursting mechanism. Among modifications on CNT, monovacancy defect exhibited the most striking effects on the enhancement of bursting. This suggests that chemical reactivity increased drastically around the defect sites. To intensively study the reason for this difference, SW defect formation energy and the adsorption energies of radical products on CNT were calculated for each modification. Both the formations of SW defects and bindings of the products were more favorable on monovacancy defect and nitrogen-doping site than the sites in pristine CNT. Furthermore, two heating methods were examined (*e.g.* electric spark and electromagnetic induction) as the additional external shocks on nanobomb. Bursting of nanobomb with electromagnetic induction occurs much rapidly due to oscillating frequency under a continuous electric field.

Additionally, synergistic effects on the bursting of nanobombs with NM-detonating molecule mixed inside CNT were investigated. Detonating molecule candidates were initially filtered by comparing detonation velocity and pressure derived from Kamlet–Jacobs (K–J) equations. When bulk mixtures which contain NM and detonating molecules were constructed and decomposed at high temperatures, HMX or RDX showed a faster decomposition rate than that of NM and supported acceleration in NM decomposition rate. Furthermore, nanobombs in which HMX or RDX is confined with NM in CNT were heated by thermal energy from CNT, and their decomposition processes were compared with pure NM nanobomb. After the confined molecules were heated, detonating molecules were decomposed prior to NM and contributed to enhanced decomposition of NM. Eventually, CNT with the detonating molecule burst by continuous functionalization of reaction intermediates in much short time than pure NM nanobomb. We believe that our theoretical explorations to improve the explosion performance of nanobomb enable much feasible manipulation of nanostructured HEMs.

In Chapter 4, reaction pathways in quinary molten-salt electrolyte-based Li$-$CO$_2$ battery with Ru catalyst were theoretically estimated, in which nitrate-based molten salt and Ru catalyst were introduced. This led to a significantly improved performance compared to previous Li$-$CO$_2$ batteries. Additionally, the number of battery cycles that can be operated was increased, but the reasonable electrochemical reaction behind its charge and discharge process was still veiled. From DFT calculation, three plausible

reaction pathways in charge processes depending on operation temperature of battery cell were derived. For the discharge process, each free energy diagram with and without Ru surface was compared to probe the catalytic role of Ru nanoparticle. Consequently, Ru surface strongly reduced the energy in thermodynamic barrier of discharge process, and this was because movement of electrons from CO_2^- to Ru surface energetically stabilized CO_2^-. We believe that mechanistic understanding of electrochemical reactions in charge and discharge processes will provide significant information for further development of Li−CO_2 battery cell.

Contents

List of Tables

List of Figures

Chapter 2

Chapter 3

Chapter 4

Chapter 1. Introduction

1.1 General Introduction

At the present time, witnessing the 4th industrial revolution, the development of new materials is the most important factor in the various fields of industrial manufacturing. In particular, the development of nanomaterials has been one of the important issues in the last few decades since nanomaterials can exert novel properties that are superior to conventional macroscopic materials. Among applications of nanomaterials, their energy applications are especially important due to the increase in the demands of energies under the current circumstances of depletion of fossil fuels (*e.g.* crude oil and coal) (**Figure 1.1**).[1] Nanomaterials can be utilized in energy applications such as energy generation (*e.g.* thermoelectric, piezoelectric, and triboelectric materials),[2-4] energy conversion (*e.g.* fuel cells and solar cells),[5,6] energy source (*e.g.* supercapacitors and batteries),[7,8] energy transmission (*e.g.* superconductivity and insulating materials),[9,10] and energy saving (*e.g.* nanolubricants, nanorefrigerants, and smart windows)[11-13] with high energy efficiency and enhanced performance (**Figure 1.2**).[14] Although nanomaterials have been widely applied in various fields of energy engineering, the level of development is still very low to meet the commercial demands. Therefore, the development of nanomaterials with improved performance and efficiency is continuously required.
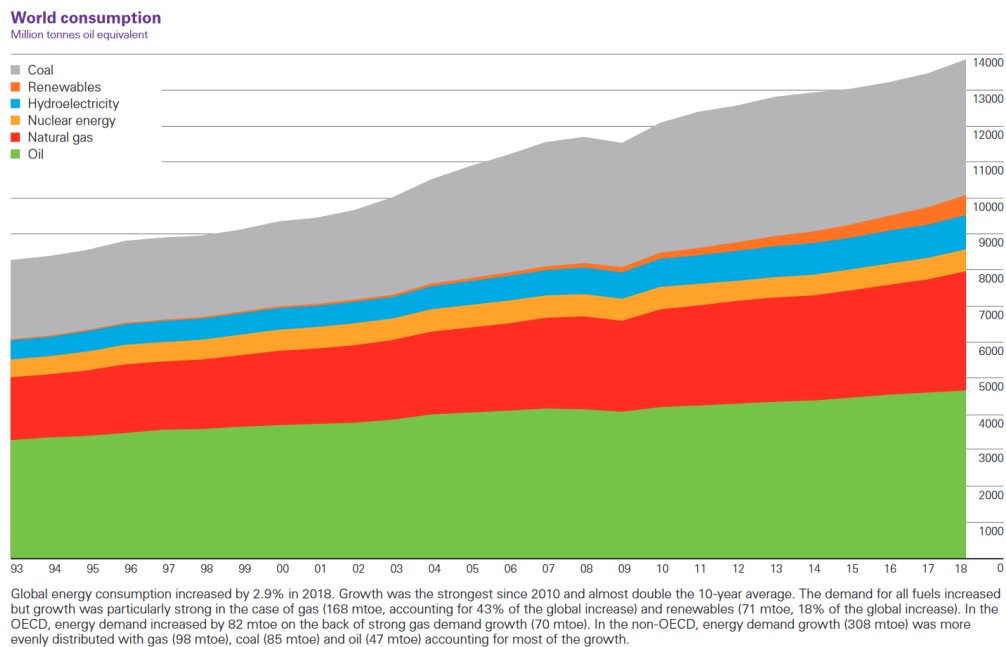
Figure 1.1 World consumption of energies reported in 2018. Culled from BP Statistical Review of World Energy.[1]
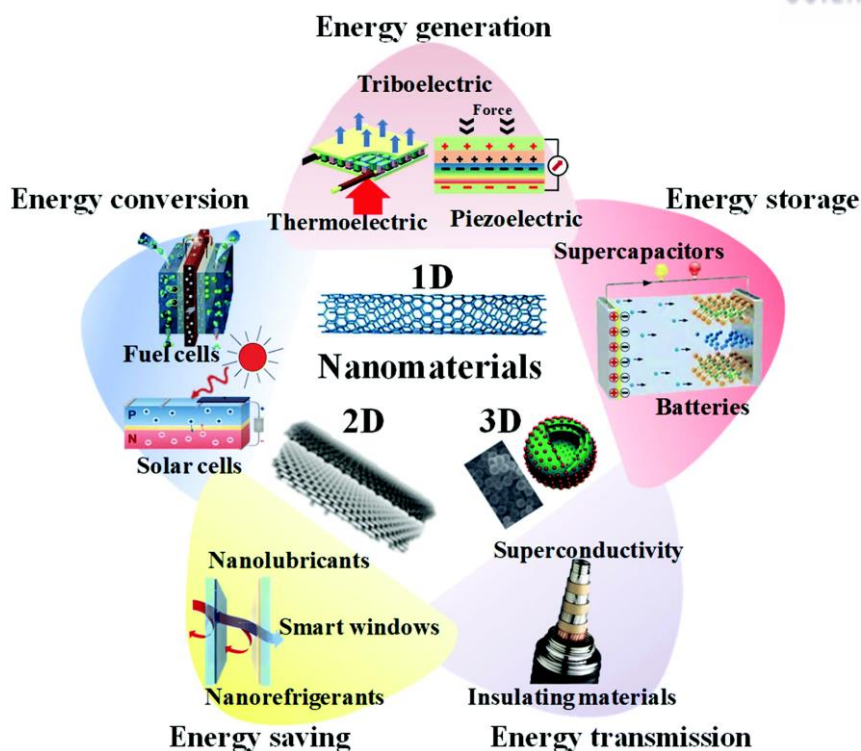
Figure 1.2 Various energy applications, such as energy generation, energy conversion, energy storage, energy saving and energy transmission. Reproduced from ref. 14 with permission from The Royal Society of Chemistry. Copyright © 2020, Royal Society of Chemistry.

1.2 Energetic Applications of Nanomaterials

As mentioned above, nanomaterials can be applied to various energy applications to increase energy efficiency of commercial devices. Among them, in this dissertation, energetic nanomaterials and Li−air batteries, which are the representative cases of nanomaterials in energy applications, will be covered in detail in **Chapter 1.2**.

1.2.1 Energetic Nanomaterials

Energetic materials are materials that can show exothermic properties when reacted with thermal or mechanical external stimuli.[15-18] However, the conventional energetic materials have some shortcomings as they have a relatively low energy density by limited enthalpy from their restricted size and form of species. Therefore, in order to maximize reaction enthalpy, energetic materials or energetic nanomaterials, at the nanoscale, have been developed in the recent decades. Energy density of devices with energetic nanomaterials can be maximized to 50 MJ/kg, which is much higher than those in classical energetic materials.[19] Additionally, the burning rate in the combustion of energetic

nanomaterials is extremely rapid compared to conventional materials.[20] For the fabrication of energetic nanomaterials with enhanced high energy density and kinetics, it is necessary to understand the reaction characteristics of energetic nanomaterials in detail. Recently, with the advancement of experimental equipment, analysis methods have been applied to observe the reaction process and structural analysis of phases generated during the reaction.[21,22] However, it is still quite complex to interpret reaction characteristics (*e.g.* mass and thermal diffusion, phase transformation) of energetic nanomaterials *via* experimental methods at the atomic level. To complement this, theoretical interpretation methods, especially molecular simulation approaches, can be promising.
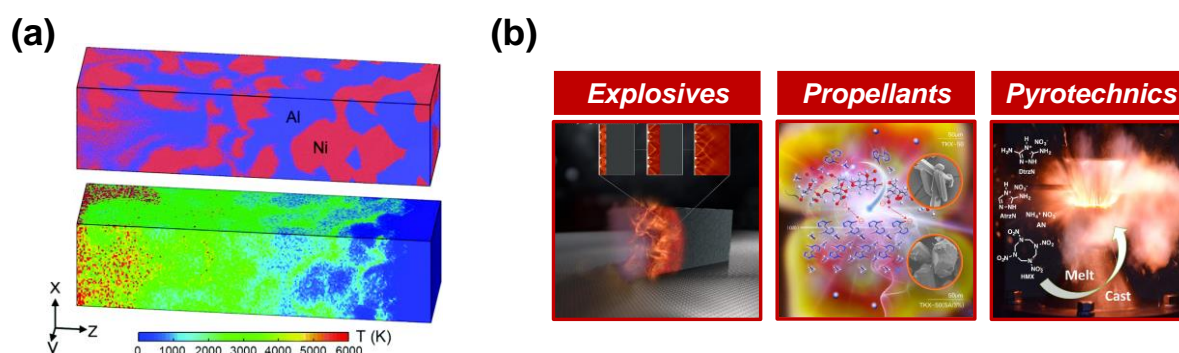
Figure 1.3 Energetic nanomaterials. (a) reactive multilayer nanofoil (b) HEMs. Reproduced from ref. 15 with permission from the PCCP Owner Societies and from ref. 16, 17, and 18 with permission from John Wiley and Sons, respectively. Copyright © 2019, The Royal Society of Chemistry. Copyright © 2018, John Wiley and Sons. Copyright © 2019, Wiley-VCH Verlag GmbH & Co. KGaA, Weinheim.

1.2.2 Li-CO$_2$ Battery

Rechargeable battery cells, represented by Li−ion batteries, are prospective materials that can perform in products by cutting-edge technologies such as portable electronic devices, electric motor vehicles, and energy storage systems.[23-25] However, the energy densities of ordinary Li−ion batteries are insufficient to handle the rapidly increasing demand for commercial use.[26] Therefore, rechargeable batteries with a much higher energy density are required. Li−air battery is the next-generation rechargeable battery that can meet the commercial demand, and Li−O$_2$ battery is one of the representative Li−air batteries (**Figure 1.4**).[27] Li−O$_2$ batteries have ultra-high energy density (3860 mAh g^{-1})[28] and are exceedingly light in weight because gas cathode consists of the battery, compared to those in the pre-existing Li−ion battery. However, as the battery cells continue to operate, by-products (*e.g.* lithium carbonate (Li$_2$CO$_3$)) from unintended reaction accumulate, reducing the capability and deteriorating the chemical stability of the battery cell.[29-31]
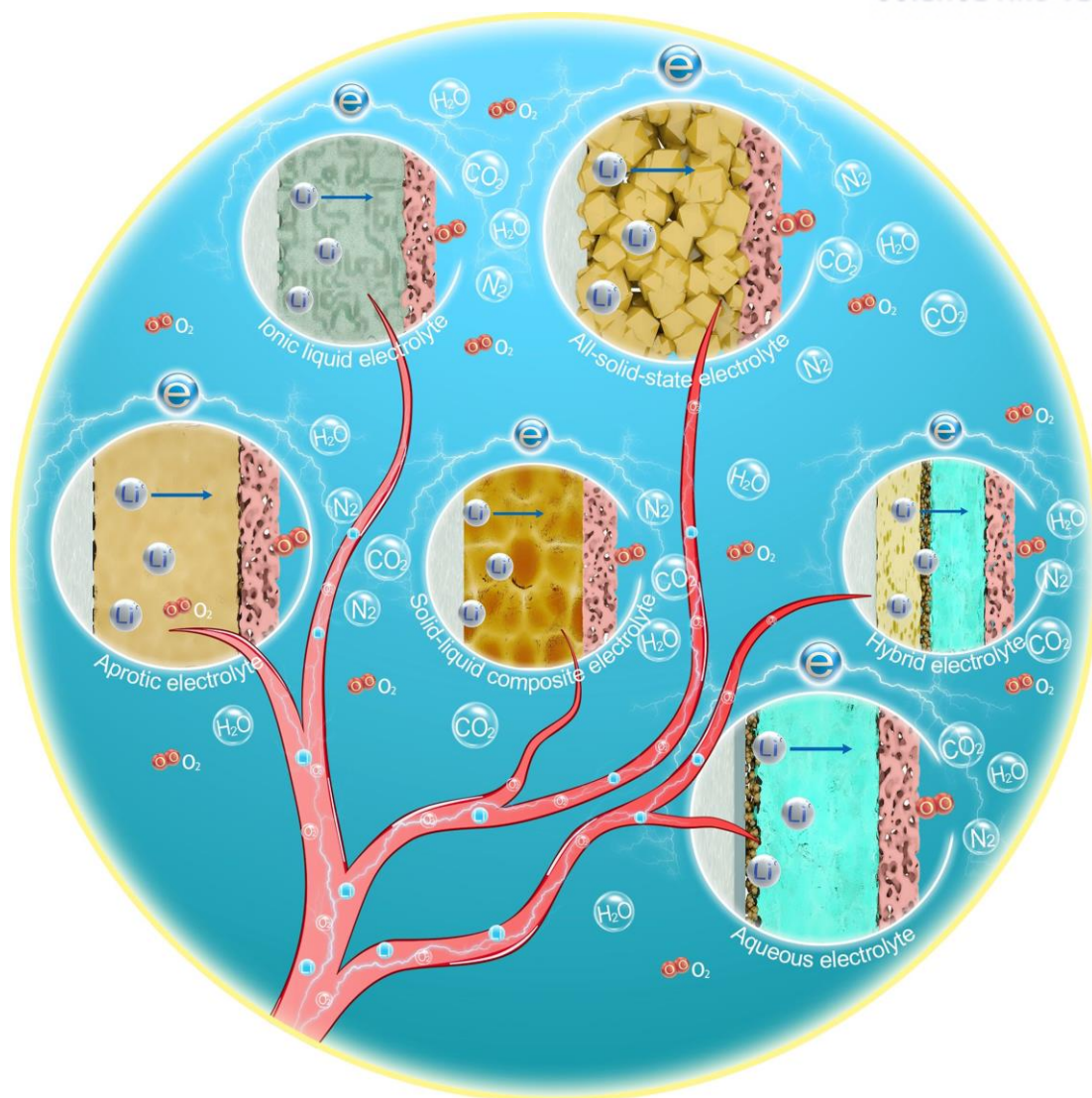
Figure 1.4 Rechargeable lithium−air batteries. Reproduced from ref. 27 with permission from John Wiley and Sons. Copyright © 2019, Wiley-VCH Verlag GmbH & Co. KGaA, Weinheim.

In order to overcome these shortcomings, lithium-carbon dioxide (Li−CO$_2$) batteries that can be charged and discharged through the decomposition and formation process of Li$_2$CO$_3$, unlike Li−O$_2$ batteries, have been recently developed (**Figure 1.5**).[32] Li−CO$_2$ batteries are advantageous as they have a high energy density and are eco-friendly since they can capture carbon dioxide (CO$_2$), which is a cause of global warming, as they operate.[33] Despite these promising advantages, Li−CO$_2$ batteries have a limitation that they are forced to operate at a low current density due to their insulating properties and the insolubility of lithium carbonate, when aprotic solvent is used as electrolyte inside the battery. In addition, unwanted parasitic reactions occur, leading to a decrease in the efficiency of battery performance.[34-37] In this respect, a smart design of a Li−CO$_2$ batteries is essential to maintain their high energy density and avoid side reactions. For this, theoretical research on the reaction mechanistic domains on charge/discharge process of Li−CO$_2$ battery cells is essential.
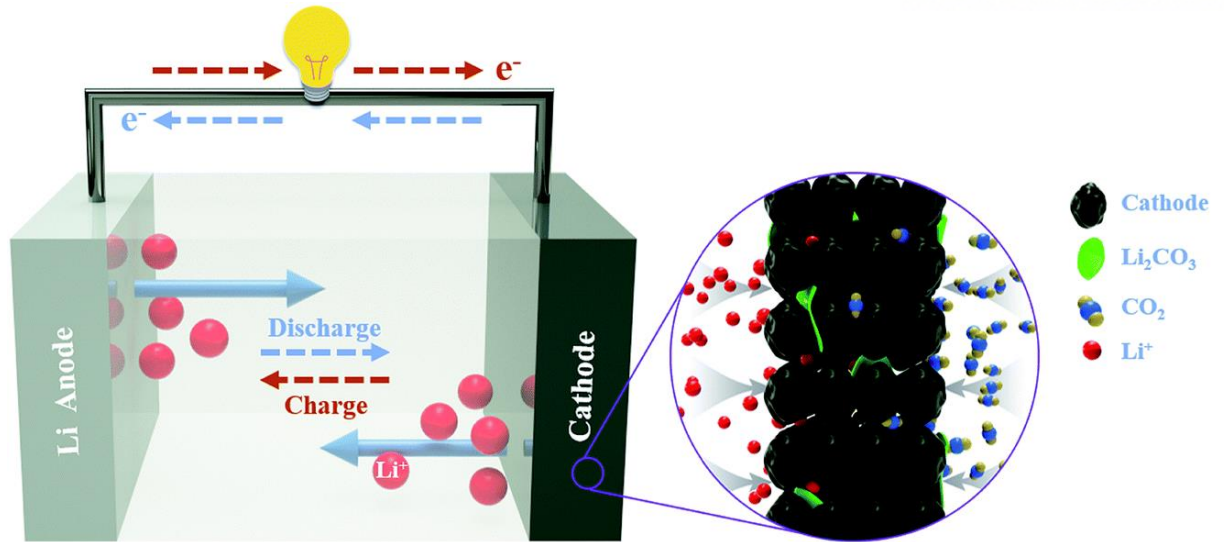
Figure 1.5 Schematic illustration of Li−CO$_2$ battery. Reproduced from ref. 32 with permission from The Royal Society of Chemistry. Copyright © 2019, Royal Society of Chemistry.

1.3 Multi-Scale Molecular Simulation Approach

Solutions with computational simulations play a very powerful role in the development of nanomaterials for energy applications, with the connection between dramatic increase in computational performance and hardened theories over time. These solutions cannot only select nanomaterial candidates prior to production, but also screen the candidates that exhibit the most suitable physical and chemical properties, according to the product needs. In addition, they can be applied to trace backwards through the process of nanomaterials synthesis or fabrication through experiments. Among these theoretical approaches, multi-scale molecular simulation approach is an optimized method to investigate the physicochemical phenomena of nanomaterials at the atomic level based on quantum mechanics and statistical mechanics. Multi-scale molecular simulation approaches include density functional theory, molecular dynamics simulation, and reactive molecular dynamics simulation (**Figure 1.6** and **Table 1.1**). More details will be covered in the sub-sections below.
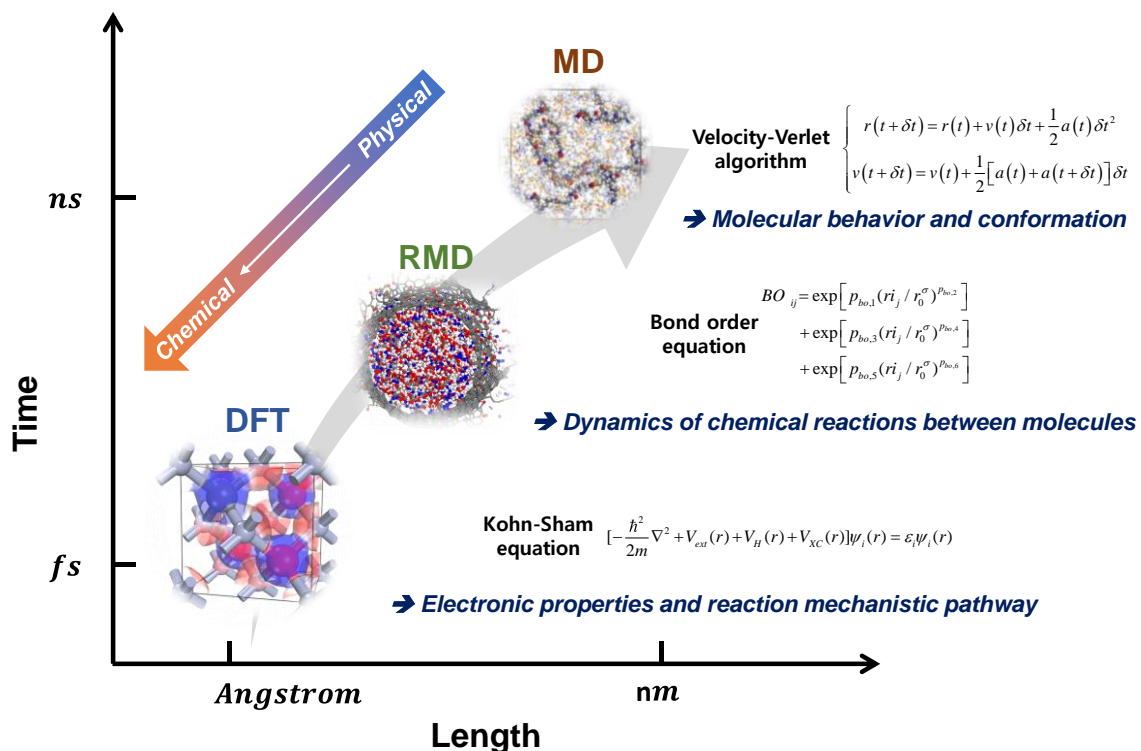
Figure 1.6 Multi-scale molecular simulation approach on time and length scale.

Table 1.1. Multiscale simulation methods, applications, and simulation codes.

Simulation methods	Applications	Simulation codes
Density functional theory (DFT) (LDA, GGA, hybrid functional, etc.)	Analysis of electronic structure and energy states of molecules	ADF, CASTEP, DMol³, Gaussian, Quantum Espresso, VASP, etc.
Molecular dynamics (MD) (Universal, COMPASS II, AMBER, OPLS, EAM, MEAM, etc.)	Thermodynamics properties and collective dynamic properties	FORCITE, GROMACS, GULP, LAMMPS, etc.
Reactive molecular dynamics (RMD) (ReaxFF, AIREBO, etc.)	Tracking of chemical reactions between molecules	ADF, LAMMPS, GULP, etc.

1.3.1 Density Functional Theory

Density functional theory (DFT) is one of the first principle calculation methods based on quantum mechanics. DFT calculation is based on the principle of finding the initial electron density using the wave function of the electrons, calculating each potential term, and finally solving the Kohn-Sham equation from the given potential to find the electron density that minimizes the total energy of the system. The Kohn-Sham equation can be written as follows:

$$[-\frac{\hbar^2}{2m}\nabla^2 + V_{ext}(r) + V_H(r) + V_{XC}(r)]\psi_i(r) = \varepsilon_i\psi_i(r) \tag{1.1}$$

where $\psi_i(r)$ is Kohn-Sham's orbital, $\hbar$ is Planck's constant, m is the mass of an electron, $V_{ext}(r)$ is external potential, $V_H(r)$ is Hartree potential, $V_{XC}(r)$ is exchange-correlation potential, and $\varepsilon_i(r)$ is eigenvalue.[38] DFT calculation is an excellent analytical technique for predicting the stable structure of a system and analyzing chemical reactions because it can grasp the electronic structure of atoms. In the energy application of nanomaterials, DFT calculation can provide specific information, such as direct electron structure (*e.g.* molecular orbitals and density of states (DOS)) of the system. In addition, analysis on energetics can be done by comparing surface energy for stable plane of crystal and binding energy between different sets of molecules. Moreover, reaction mechanism can be predicted with the calculation of relative energy of reactants, intermediates, and products in each reaction pathway.

1.3.2 Molecular Dynamics

Molecular dynamics (MD) simulation is a theoretical approach that calculates the forces acting on atoms and predicts their positions by integrating over time based on Newton's equation of classical mechanics, that is, the velocity-Verlet algorithm. MD simulation describes the interaction between atoms through the difference of interatomic potentials, or a force field. Formalism of force field consists of the following terms,[39,40]

$$E_{\text{total}} = E_{\text{valence}} + E_{\text{non-bond}} \tag{1.2}$$

where E_{valence} is the potential energy in bonded interactions and $E_{\text{non-bond}}$ is the potential energy in non-bond interactions, respectively. E_{valence} can be expressed as,

$$E_{\text{valence}} = E_{\text{bond}} + E_{\text{angle}} + E_{\text{torsion}} + E_{\text{inversion}} \tag{1.3}$$

where E_{bond} is the energy for bond stretch, E_{angle} is the energy for angle bend, E_{torsion} is the energy for torsion, and $E_{\text{inversion}}$ is the energy for inversion, respectively. $E_{\text{non-bond}}$ can be expressed as,

$$E_{\text{non-bond}} = E_{\text{vdW}} + E_{\text{Coulomb}} \tag{1.4}$$

where E_{vdW} is the energy for van der Waals (vdW) interactions, and E_{Coulomb} is the energy for electrostatic interactions (Coulombic interactions), respectively.

Through MD simulation, it is possible to measure atomic momentum and to obtain thermodynamic properties and collective dynamic properties (*e.g.* mass diffusion, viscosity, and thermal conductivity) over time by integrating the position and velocity of the atoms constituting the nanomaterial. Additionally, in the force field called embedded atom method (EAM), total potential energy is expressed as follows,

$$E_{total} = F_{S_i}\left(\sum_{i \neq j} \bar{\rho}_i\right) + \frac{1}{2}\sum_{i \neq j} V_{S_i S_j}(r_{ij}) \tag{1.5}$$

where F_{S_i} is the embedding energies of atom i into the host electron density, $\bar{\rho}_i$ is the host electron density, and $V_{S_i S_j}(r_{ij})$ is the pair interactions between atom i and j with chemical species S_i and S_j.[41]

MD calculations based on EAM are mainly applied to the examination of physical and chemical properties of pure metal or metal alloy systems. With EAM force field, reaction properties of system can be additionally investigated with the mixing of atoms.

1.3.3 Reactive Molecular Dynamics

Reactive molecular dynamics (RMD) simulation is a type of MD simulation, but unlike classical MD, it is possible to observe and track the reaction of molecules regardless of the initial connectivity of the atoms. In particular, in RMD simulation based on force field called ReaxFF, the formation and dissociation a of chemical bond can be observed. This is because ReaxFF is based on the bond order of covalent bonds between atoms and the information is updated by each simulation time step. Total potential energy of ReaxFF can be described as shown in equation (1.6),[42-44]

$$E_{\text{total}} = E_{\text{bond}} + E_{\text{over}} + E_{\text{angle}} + E_{\text{tors}} + E_{\text{vdWaals}} + E_{\text{Coulomb}} + E_{\text{specific}} \qquad (1.6)$$

where E_{bond} is the bond energy, E_{over} is an energy penalty to prevent over-coordination of each atom according to the rules of atomic valence, E_{angle} is the valence angle energy, E_{tors} is the torsional angle energy, E_{vdWaals} is the vdW energy, E_{Coulomb} is the electrostatic energy, and E_{specific} is the compensation energy for specific system, respectively. To be specific, the concept, bond order can be introduced as follows,

$$BO_{ij} = \exp[p_{bo,1} \cdot (r_{ij} / r_0^{\sigma})^{P_{bo,2}}] + \exp[p_{bo,3} \cdot (r_{ij} / r_0^{\sigma})^{P_{bo,4}}] + \exp[p_{bo,5} \cdot (r_{ij} / r_0^{\sigma})^{P_{bo,6}}] \qquad (1.7)$$

where BO is the bond order between atom i and j, r_{ij} is the interatomic distance between atom i and j, r_0 is the distance in equilibrium state, and p is the empirical parameter, respectively. According to this equation, since the bond order of each single bond (sigma bond), double bond (pi bond), or triple bond (double pi bond) depending on the distance between atoms is calculated at every time step, updated bond order affects bonded interactions and thus chemical reactions can be effectively tracked. For nanomaterials, RMD simulation can be used to grasp complex reactions *in-silico* over time which can occur on their surfaces and interfaces. Particularly, since explosive reactions in harsh conditions can also be simulated, reaction trajectories and following thermodynamic properties in energetic materials with high energy density (*e.g.* explosives) can be examined.

1.4 Outline of Dissertation

Identifying and examining the reaction mechanistic domain of nanomaterials are one of the essential elements toward the development of advanced nanomaterials for energy applications. This doctoral dissertation includes a reaction mechanistic study of energetic nanomaterials and $Li-CO_2$ battery through a multi-scale molecular simulation approach. In **Chapter 2**, the reaction characteristics of Ni-Al nanolayers were theoretically quantified. In **Chapter 3**, we investigated explosion dynamics of nanobomb, where NM is encapsulated in CNT nanocontainer, under several conditions such as packing density of NM and ignition temperature, physicochemical modification of nanocontainer and external shocks, co-encapsulation of detonator and NM. In **Chapter 4**, we studied electrochemical reaction mechanism in each charge and discharge process of rechargeable $Li-CO_2$ battery.

1.5 References

1   BP Statistical Review of World Energy; London, **2019**.

2.   Wang, L.; Zhang, Z.; Geng, L.; Yuan, T.; Liu, Y.; Guo, J.; Fang, L.; Qui, J.; Wang, S. Solution-printable fullerene/TiS_2 organic/inorganic hybrids for high-performance flexible n-type thermoelectrics. *Energy Environ. Sci.* **2018,** 11, 1307-1317.

3.   Xu, K.; Li, J.; Lv, X.; Wu, J.; Zhang, X.; Xiao, D.; Zhu, J. Superior Piezoelectric Properties in Potassium–Sodium Niobate Lead-Free Ceramics. *Adv. Mater.* **2016,** 28, 8519-8523.

4.   Liu, J.; Goswami, A.; Jiang, K.; Khan, F.; Kim, S.; Mcgee, R.; Li, Zhi.; Hu, Z.; Lee, J.; Thundat, T. Direct-current triboelectricity generation by a sliding Schottky nanocontact on MoS_2 multilayers. *Nat. Nanotechnol.* **2018,** 13, 112-116.

5.   Li, Y.; Nguyen, T. V. Core-shell rhodium sulfide catalyst for hydrogen evolution reaction / hydrogen oxidation reaction in hydrogen-bromine reversible fuel cell. *J. Power Sources* **2018,** 382, 152–159.

6.   Li, Z.; Wang, R.; Xue, J.; Xing, X.; Yu, Ch.; Huang, T.; Chu, J.; Wang, K.-L.; Dong, C.; Wei, Z.; Zhao, Y.; Wang, Z.-K.; Yang, Y. Core–Shell $ZnO@SnO_2$ Nanoparticles for Efficient Inorganic Perovskite Solar Cells. *J. Am. Chem. Soc.* **2019,** 141, (44), 17610–17616.

7.   Zhao, Y.; Hu, L.; Zhao, S.; Wu, Z. Preparation of $MnCo_2O_4@Ni(OH)_2$ Core–Shell Flowers for Asymmetric Supercapacitor Materials with Ultrahigh Specific Capacitance. *Adv. Funct. Mater.* **2016,** 26, 4085–4093.

8.   Chong, W. G.; Xiao, Y.; Huang, J.-Q.; Yao, S.; Cui, J.; Qin, L.; Gao, C.; Kim. J.-K. Highly conductive porous graphene/sulfur composite ribbon electrodes for flexible lithium–sulfur batteries. *Nanoscale.* **2018,** 10, 21132-21141.

9.   Xu, C.; Song, S.; Liu, Z.; Chen, L.; Wang, L.; Fan, D.; Kang, N.; Ma, X.; Cheng, H.-M.; Ren, W. Strongly Coupled High-Quality Graphene/2D Superconducting Mo_2C Vertical Heterostructures with Aligned Orientation. *ACS Nano* **2017,** 11, (6), 5906–5914.

10.   Pallon, L. K. H.; Hoang, A. T.; Pourrahimi, A. M.; Hedenqvist, M. S.; Nilsson, F.; Gubanski, S.; Gedde, U. W.; Olsson, R. T. The impact of MgO nanoparticle interface in ultra-insulating polyethylene nanocomposites for high voltage DC cables. *J. Mater. Chem. A* **2016,** 4, 8590-8601.

11.   Sharif, M. Z.; Azmi, W. H.; Redhwan, A. A. M.; Mamat, R.; Najafi, G. Energy saving in automotive air conditioning system performance using SiO_2/PAG nanolubricants. *J. Therm. Anal. Calorim.* **2019,** 135,1285-1297.

12.   Sadri, R.; Hosseini, M.; Kazi, S. N.; Bagheri, S.; Abdelrazek, A. H.; Ahmadi, G.; Zubir, N.; Ahmad, R.; Abidin, N. I. Z. A facile, bio-based, novel approach for synthesis of covalently functionalized graphene nanoplatelet nano-coolants toward improved thermo-physical and heat transfer properties. *J. Colloid Interface Sci.* **2018**, 509, 140–152.

13. Koo, B.-R.; Kim, K.-H.; Ahn, H.-J. Novel tunneled phosphorus-doped WO$_3$ films achieved using ignited red phosphorus for stable and fast switching electrochromic performances. *Nanoscale* **2019,** 11, 3318-3325.

14. Wang, H.; Liang, X.; Wang, J.; Jiao, S.; Xue, D. Multifunctional inorganic nanomaterials for energy applications. *Nanoscale.* **2020,** 12, 14-42.

15. Xiong, Y.; Li, X.; Xiao, S.; Deng, H.; Zhu, W.; Hu, W. Molecular dynamics simulations of shock loading of nearly fully dense granular Ni–Al composites. *Phys. Chem. Chem. Phys.* **2019,** 21, 20252-20261.

16. Leonard, P. W.; Chavez, D. E.; Bowden, P. R.; Francois, E. G. Nitrate Salt Based Melt Cast Materials. *Propellants, Explos., Pyrotech.* **2018**, 43, 11-14.

17. Springer, H. K.; Bastea, S.; Nichols, III, A. L.; Tarver, C. M.; Reaugh, J. E. Modeling The Effects of Shock Pressure and Pore Morphology on Hot Spot Mechanisms in HMX. *Propellants, Explos., Pyrotech.* **2018**, 43, 805-817.

18. Dong, W.; Chen, S.; Jin, S.; Chen, M.; Yan, Bo.; Chen, Yu. Effect of Sodium Alginate on the Morphology and Properties of High Energy Insensitive Explosive TKX-50. *Propellants, Explos., Pyrotech.* **2019**, 44, 413-422.

19. Zarko, V.; Gromov, A. *Energetic Nanomaterials: Synthesis, Characterization, and Application*, Elsevier B.V, **2016**; Chapter One; pp 1-20.

20. Becker, C. R.; Apperson, S.; Morris, C. J.; Gangopadhyay, S.; Currano, L. J.; Churaman, W. A.; Stoldt, C. R. Galvanic Porous Silicon Composites for High-Velocity Nanoenergetics. *Nano. Lett.* **2011**, 11, (2), 803-807.

21. Bahrami, M.; Taton, G.; Conédéra, V.; Salvagnac, L.; Tenailleau, C.; Alphonse, P.; Rossi, C. Magnetron Sputtered Al-CuO Nanolaminates: Effect of Stoichiometry and Layers Thickness on Energy Release and Burning Rate. *Propellants, Explos., Pyrotech.* **2014**, 39, 365-373.

22. Rossi, C. Engineering of Al/CuO Reactive Multilayer Thin Films for Tunable Initiation and Actuation. *Propellants, Explos., Pyrotech.* **2019**, 44, 94-108.

23. Tarascon, J. M.; Armand, M. Issues and challenges facing rechargeable lithium batteries. *Nature* **2001**, 414, 359–367.

24. Chu, S.; Majumdar, A. Opportunities and challenges for a sustainable energy future. *Nature* **2012**, 488, 294–303.

25. Cabana, J.; Monconduit, L.; Larcher, D.; Palacin, M. R. Beyond intercalation-based Li-ion batteries: the state of the art and challenges of electrode materials reacting through conversion reactions. *Adv. Mat.* **2010**, 22, E170–E192.

26. Aurbach, D.; McCloskey, B. D.; Nazar, L. F.; Bruce, P. G. Advances in Understanding Mechanisms Underpinning Lithium-Air Batteries. *Nat. Energy* **2016,** 1, 16128.

27. Lai, J.; Xing, Y.; Chen, N.; Li, L.; Wu, F.; Chen, R. Electrolytes for Rechargeable Lit

hium–Air Batteries. *Angew. Chem. Int. Ed.* **2020,** 59, 2974-2997.

28. Lu, J.; Park, J.-B.; Sun, Y.-K.; Wu, F.; Amine, K. Aprotic and aqueous Li–O2 batteries. *Chem. Rev.* **2014,** 114, (11), 5611–5640.

29. McCloskey, B. D.; Speidel, A.; Scheffler, R.; Miller, D. C.; Viswanathan, V.; Hummelshøj, J. S.; Nørskov, J. K.; Luntz, A. C. Twin problems of interfacial carbonate formation in nonaqueous Li–O2 batteries. *J. Phys. Chem. Lett.* **2012,** 3, (8), 997–1001.

30. Ottakam Thotiyl, M. M.; Freunberger, S. A.; Peng, Z.; Bruce, P. G. The carbon electrode in nonaqueous Li–O_2 cells. *J. Am. Chem. Soc.* **2013,** 135, (1), 494–500.

31. McCloskey, B. D.; Bethune, D. S.; Shelby, R. M.; Mori, T.; Scheffler, R.; Sherwood, M.; Luntz, A. C. Limitations in Rechargeability of Li–O_2 Batteries and Possible Origins. *J. Phys. Chem. Lett.* **2012,** 3, (20), 3043–3047.

32. Hu, A.; Shu, C.; Xu, C.; Liang, R.; Li, J.; Zheng, R.; Li, M.; Long, J. Design strategies toward catalytic materials and cathode structures for emerging Li–CO_2 batteries. *J. Mater. Chem. A* **2019,** 7, 21605–21633.

33. Qiao, Y.; Yi, J.; Wu, S.; Liu, Y.; Yang, S.; He, P.; Zhou, Haoshen. Li–CO_2 electrochemistry: a new strategy for CO_2 fixation and energy storage. *Joule* **2017,** 1, 359–370.

34. Zhang, X.; Zhang, Q.; Zhang, Z.; Chen, Y.; Xie, Z.; Wei, J.; Zhou, Z. Rechargeable Li–CO_2 batteries with carbon nanotubes as air cathode. *Chem. Commun.* **2015,** 51, 14636–14639.

35. Qie, L.; Lin, Y.; Connell, J. W.; Xu, J.; Dai, L. Highly Rechargeable Lithium-CO_2 Batteries with a Boron- and Nitrogen-Codoped Holey-Graphene Cathode. *Angew. Chem. Int. Ed.* **2017,** 56, 6970–6974.

36. Li, C.; Guo, Z.; Yang, B.; Liu, Y.; Wang, Y.; Xia, Y. A Rechargeable Li-CO_2 Battery with a Gel Polymer Electrolyte. *Angew. Chem. Int. Ed.* **2017,** 56, 9126–9130.

37. Zhang, Z.; Wang, X.-G.; Zhang, X.; Xie, Z.; Chen, Y.-N.; Ma, L.; Peng, Z.; Zhou, Z. Verifying the rechargeability of Li–CO_2 batteries on working cathodes of Ni nanoparticles highly dispersed on N-doped graphene. *Adv. Sci.* **2018,** 5, 1700567.

38. Kohn, W.; Sham, L. J. Self-Consistent Equations Including Exchange and Correlation Effects. *Phys. Rev.* **1965,** 140, A1133-A1138.

39. Rappe, A. K.; Casewit, C. J.; Colwell, K. S.; Goddard, W. A. III.; Skiff, W. M. UFF, a Full Periodic Table Force Field for Molecular Mechanics and Molecular Dynamics Simulations. *J. Am. Chem. Soc.* **1992**, 114, (25), 10024–10035.

40. Cornell, W. D.; Cieplak, P.; Bayly, C. I.; Gould, I. R.; Merz, K. M.; Ferguson, D. M.; Spellmeyer, D. C.; Fox, T.; Caldwell, J. W.; Kollman, P. A. A Second Generation Force Field for the Simulation of Proteins, Nucleic Acids, and Organic Molecules. *J. Am. Chem. Soc.* **1995**, 117, (19), 5179–5197.

41. Daw, M. S.; Baskes, M. I. Embedded-atom method: Derivation and application to impurities,

surfaces, and other defects in metals. *Phys. Rev. B* **1984**, 29, 6443–6453.

42. van Duin, A. C. T.; Dasgupta, S.; Lorant, F.; Goddard, W. A. III. Embedded-atom method: ReaxFF: A Reactive Force Field for Hydrocarbons. *J. Phys. Chem. A* **2001**, 105, (41), 9396–9409.

43. Chenoweth, K.; van Duin, A. C. T.; Goddard, W. A. III. ReaxFF Reactive Force Field for Molecular Dynamics Simulations of Hydrocarbon Oxidation. *J. Phys. Chem. A* **2008**, 112, (5), 1040–1053.

44. Senftle, T. P.; Hong, S.; Islam, M. M.; Kylasa, S. B.; Zheng, Y.; Shin, Y. K.; Junkermeier, C.; Engel-Herbert, R.; Janik, M. J.; Aktulga, H. M.; Verstraelen, T.; Grama, A.; van Duin, A. C. T. The Reaxff reactive force-field: development, applications and future directions. *NPJ. Comput. Mater.* **2016,** 2, 15011.

Chapter 2. Reactive Process of Ni-Al Alloys

This chapter includes the following content:

2.1 Introduction

Reactive multilayer foils are exothermal materials self-propagated and reacted by thermal or mechanical stimuli from external environment.[1-4] The reactive multilayer foils, which consist of alternating layers of two or more solid reactants, are manufactured by vapor deposition methods via sputtering,[5-7] mechanical processing techniques such as rolling,[8-10] compacting,[11] and etc. They exhibit specific characteristics of large heat of mixing, fast burn rate, and high power,[12] thus have many potential applications in military and industrial fields such as eco-friendly lead-free primers and detonators,[13,14] projectiles,[15,16] welding or joining,[17,18] soldering,[19] heat source for clinical usage,[20] and etc. There have been many studies including fundamental ones because of their complex reaction pathways involving melting, mass and thermal diffusions, and phase transition in initiation and progression of self-propagating exothermic reactions.[21] In particular, Ni-Al systems have attracted much attention because of high thermal and acidic stabilities in the formation process of intermetallic phase.[22,23] Recently, several experiments made significant progresses of the layer systems in nanoscale in terms of heat of reactions and speed of reaction by using high-end characterization methods such as differential scanning calorimetry (DSC) and in-situ XRD.[24-26]

However, experimental approach to the nanoscale system still has a limit to interpret the reaction phenomena originated from the atomistic level. In that respect, molecular simulation approach came into play; MD simulation is a suitable computational technique to observe physical and chemical phenomena in the atomic scale. In particular, by using the EAM potential developed by Purija and Mishin,[27] fundamental mechanism of Ni-Al multilayer system was actively studied. For example, Zhao et al. elucidated a mechanism of shock-induced alloying reaction involving pore effects.[20] Cherukara et al. studied exothermicity, reaction speed, and structural change in terms of temperature, periodic length, and defects.[28] A few important factors such as stoichiometry and ignition temperature have a strong influence on reaction but still crucial data are largely deficient in this area. Especially, the quantitative correlation between structural properties and reaction characteristic is very much critical information yet missing.

There are representative phases in Ni-Al binary systems, which are Ni_3Al, NiAl, and $NiAl_3$.[29] Out of them, *B2*-NiAl phase is energetically the most stable while Al-rich $NiAl_3$ is unstable.[27] Thus, by the change of stoichiometry, the product phase is expected to be varied. In this study, therefore, we set up the Ni-Al bulk nanolayers to have three stoichiometric ratios of NiAl (1:1), Ni_3Al (3:1), and $NiAl_3$ (1:3), where the bilayer thickness are changed, under the variation of ignition temperature. The reaction thermodynamics of model systems was explored in terms of the heat of reaction, which was obtained by estimating the enthalpy change in the reaction process. Also, the reaction kinetics was investigated by estimating the reaction time and diffusion coefficients as a function of ignition temperature and bilayer thickness. In summary, the reaction kinetics and thermodynamics were quantitatively investigated in terms of the variation of ignition temperature, stoichiometry, and bilayer thickness in Ni-Al nanolayers.

2.2 Simulation Details

Figure 2.1 shows the model systems of Ni-Al nanolayers used in the MD simulations. The Ni-Al nanolayers were constructed to confront the most stable (111) surfaces of Ni and Al.[30] Two supercells of Ni 6×10×1 and Al 5×9×1 were first put together in order to minimize the lattice mismatch (*i.e.* ~ 2 %). Then, by controlling the number of atoms, three different stoichiometric systems (*i.e.* NiAl, Ni_3Al, and $NiAl_3$) were modelled to have the different values of bilayer thickness (*i.e.* 10, 20, and 30 nm) in *z*-direction, which contain from 17280 to 63360 atoms. Note that all lengths in *x*- and *y*-directions were kept for 5.1 nm. The basic information of the model systems used in MD simulation is provided in **Table 2.1**.
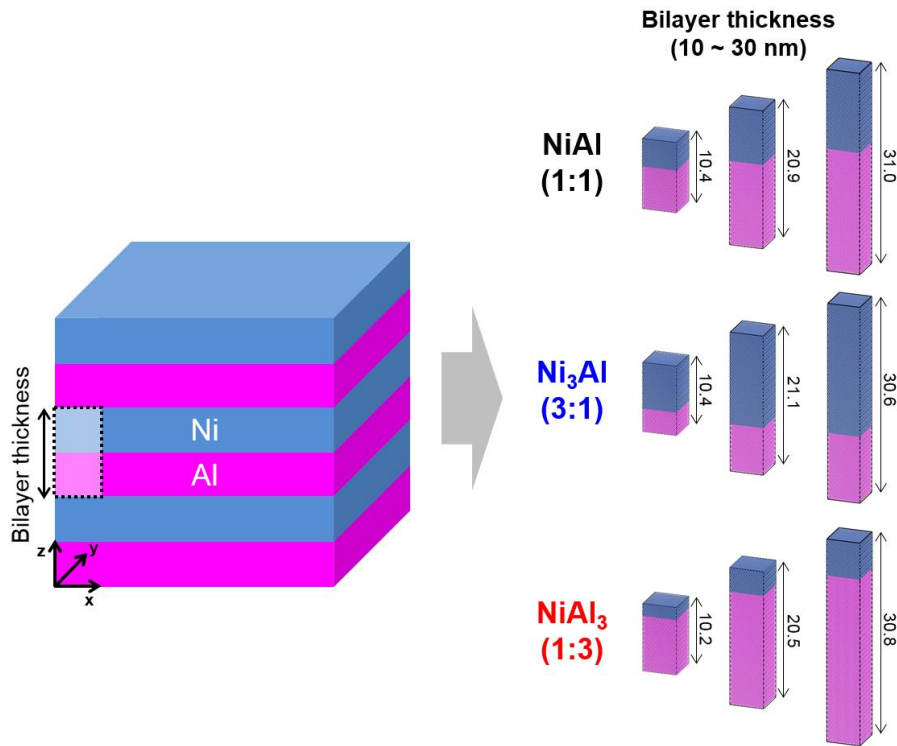
Figure 2.1 Schematics of model systems used in MD simulations. Three stoichiometric ratios (*i.e.* NiAl, Ni$_3$Al, and NiAl$_3$) with the variation of bilayer thickness (*i.e.* 10, 20, and 30 nm) were considered. Ni and Al atoms are colored as dark blue and pink, respectively. Copyright © 2017, The Korean Society of Industrial and Engineering Chemistry. Published by Elsevier B.V.

For MD simulation, we have used EAM potential developed by Purija and Mishin[27] in the LAMMPS package.[31] In order to mimic heating and igniting processes, *NVT* (*i.e.* canonical – constant temperature) and *NVE* (*i.e.* microcanonical – constant energy) ensembles were consecutively applied in the MD simulation. First, MD with *NVT* ensemble was run for initial 5 ps at 1000, 1400, and 1700 K. This step can be considered as a thermal shock, starting from no mixing at the interface. The Nose-Hoover thermostat with coupling constants of 0.1 ps was used to control the temperature. Next, MD with *NVE* ensemble was run until the temperature and pressure values converged, indicating the alloying reaction was completed. In this calculation process, thermal energy accumulated in Ni and Al atoms in the heating (*NVT* MD) process was transformed into kinetic energy, which in turn triggers mixing of Ni and Al atoms, at conserved total energy. The time step for all MD simulation was set to be 1 fs.

When thermal shock is applied to the Ni-Al nanolayers, temperature rises by mixing of Ni and Al, which undergoes phase transition from solid to liquid. In order to quantify the reaction kinetics, the reaction time (τ) was estimated at the point where a constant final temperature was reached, which is

the average temperature for last 0.1 ns during MD simulation. Subsequently, the τ's were compared by varying the ignition temperature, bilayer thickness, and stoichiometry.

Table 2.1 Summary of model systems used in MD simulations. Three stoichiometric ratios (*i.e.* NiAl, Ni$_3$Al, and NiAl$_3$) with the variation of bilayer thicknesses (*i.e.* 10, 20, and 30 nm) and ignition temperatures (*i.e.* 1000, 1400, and 1700 K) were considered. Copyright © 2017, The Korean Society of Industrial and Engineering Chemistry. Published by Elsevier B.V.

No.	Ignition temperature (T_i, K)	Stoichiometry	Final temperature (T_f, K)	Cell dimensions (nm^3)	Total number of atoms
1			1955.6	$5.1 \times 5.1 \times 10.4$	19320
2		NiAl	1986.5	$5.1 \times 5.1 \times 20.9$	38640
3			2030.1	$5.1 \times 5.1 \times 31.0$	57600
4			1701.3	$5.1 \times 5.1 \times 10.4$	21720
5	1000	Ni$_3$Al	1452.2	$5.1 \times 5.1 \times 21.1$	43440
6			1273.0	$5.1 \times 5.1 \times 30.6$	63360
7			1520.8	$5.1 \times 5.1 \times 10.2$	17280
8		NiAl$_3$	1551.9	$5.1 \times 5.1 \times 20.5$	34560
9			1577.7	$5.1 \times 5.1 \times 30.8$	51840
10			2371.1	$5.1 \times 5.1 \times 10.4$	19320
11		NiAl	2416.7	$5.1 \times 5.1 \times 20.9$	38640
12			2431.8	$5.1 \times 5.1 \times 31.0$	57600
13			2067.6	$5.1 \times 5.1 \times 10.4$	21720
14	1400	Ni$_3$Al	2064.7	$5.1 \times 5.1 \times 21.1$	43440
15			2042.4	$5.1 \times 5.1 \times 30.6$	63360
16			1917.2	$5.1 \times 5.1 \times 10.2$	17280
17		NiAl$_3$	1940.1	$5.1 \times 5.1 \times 20.5$	34560
18			1980.0	$5.1 \times 5.1 \times 30.8$	51840
19			2784.6	$5.1 \times 5.1 \times 10.4$	19320
20		NiAl	2718.3	$5.1 \times 5.1 \times 20.9$	38640
21			2734.5	$5.1 \times 5.1 \times 31.0$	57600
22			2366.0	$5.1 \times 5.1 \times 10.4$	21720
23	1700	Ni$_3$Al	2356.5	$5.1 \times 5.1 \times 21.1$	43440
24			2281.8	$5.1 \times 5.1 \times 30.6$	63360
25			2316.3	$5.1 \times 5.1 \times 10.2$	17280
26		NiAl$_3$	2261.1	$5.1 \times 5.1 \times 20.5$	34560
27			2299.9	$5.1 \times 5.1 \times 30.8$	51840

2.3 Results and Discussion

2.3.1 Reaction Mechanism by Stoichiometry

Figure 2.2 shows the mixing behaviour in the reaction process of NiAl 20 nm system with the ignition temperature of 1000 K. A series of snapshots from *NVE* MD simulation are shown in **Figure 2.2(a)**, and the time evolution of overall temperature and pressure in the system is shown in **Figure 2.2 (b)**. As reported in previous studies,[32-34] the exothermic reaction pathway of Ni-Al nanolayers can be discretely divided into several reaction steps. Initially, the mixing between Ni and Al occurred at the interface and during this stage, the temperature and pressure changed very slowly. In the second stage (from 3.15 ns), the Al region began to melt with a continuous rise in temperature and the rapid increase in pressure. Note that since the total volume of the system is fixed, the structural expansion by melting induces the pressure to increase, as previously reported by Zhao et al..[34] At 5.35 ns, a sudden dip of temperature and a pronounced peak of pressure were observed, indicating the melting transition in the Al region.

In the next step, as the Ni atoms gradually diffused into the liquid Al region, the alloying reaction was significantly accelerated, confirmed by a rapid rise in temperature and a sharp decrease in the pressure. Simultaneously, a stable *B2*-NiAl phase (*i.e.* ordered equiatomic bcc phase) was locally formed at the interface and served as a barrier to prevent the diffusion of Ni into Al (~ 7.73 ns). However, a continuous temperature rise due to alloying reaction caused the solid Ni and *B2*-NiAl phases to melt. At 8.16 ns, the interdiffusion of Ni and Al occurred in the liquid state, leading to the more rapid increases in temperature. Finally, at 10 ns, it was confirmed that the fully mixed state of NiAl liquid phase was generated by convergence of temperature and pressure values.

Figure 2.2(c) shows the time evolution of relative changes in total internal energy (ΔE_{tot}), potential energy (ΔE_{pot}), kinetic energy (ΔE_{kin}), and enthalpy (ΔH). In the *NVE* ensemble, since the total internal energy and the volume of system are fixed, the pressure changes dependently with energy release. The relative changes of the potential energy and kinetic energy in the reaction process decreased and increased by exactly the same amount ($\Delta E_{pot} = -\Delta E_{kin}$). In addition, the enthalpy change was apparently depended on the pressure ($\Delta H = V\Delta P$) and showed a negative change indicating the exothermic reaction, which was estimated as the heat of reactions (to be discussed later).
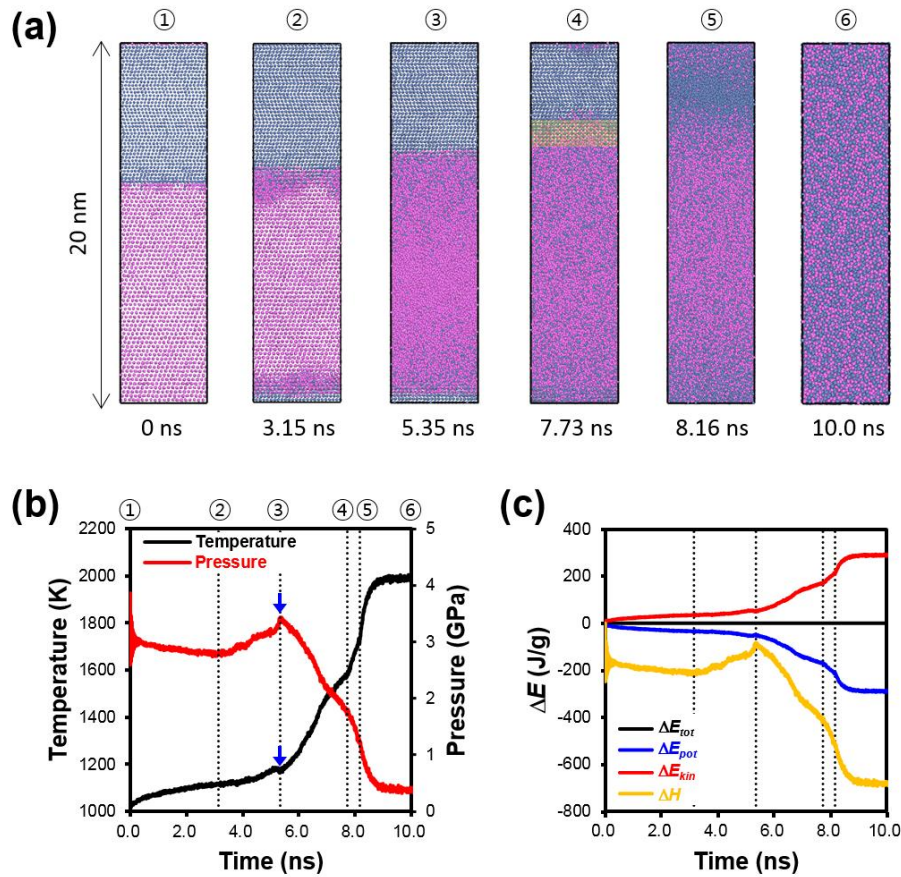
Figure 2.2 (a) MD simulation snapshots for NiAl stoichiometric system with 20 nm bilayer thickness at the ignition temperature of 1000 K. Light yellow region at 7.73 ns represents the *B2*-NiAl crystalline phase at the interface. (b) The time evolution of temperature and pressure of NiAl system during MD simulation for 10 ns. The blue arrows represent the sudden dip and pronounced peak in temperature and pressure, respectively. (c) The time evolution of relative changes in total internal energy (ΔE_{tot}), potential energy (ΔE_{pot}), kinetic energy (ΔE_{kin}), and enthalpy (ΔH) of NiAl stoichiometric system during the reaction. Copyright © 2017, The Korean Society of Industrial and Engineering Chemistry. Published by Elsevier B.V.

Figure 2.3 shows the mixing behaviour in the reaction process of Ni- and Al-rich systems of Ni-Al nanolayers (*i.e.* Ni$_3$Al and NiAl$_3$) with the ignition temperature of 1000 K. In analogous with NiAl stoichiometry, the overall alloying reaction was discretely divided into a series of reaction steps and followed a similar sequence of reactions. After the initial mixing occurred at the interface, the Al layer fully melted, followed by diffusion of Ni atoms into liquid Al, formation of *B2*-NiAl boundary, and interdiffusion of Ni and Al in the liquid state.
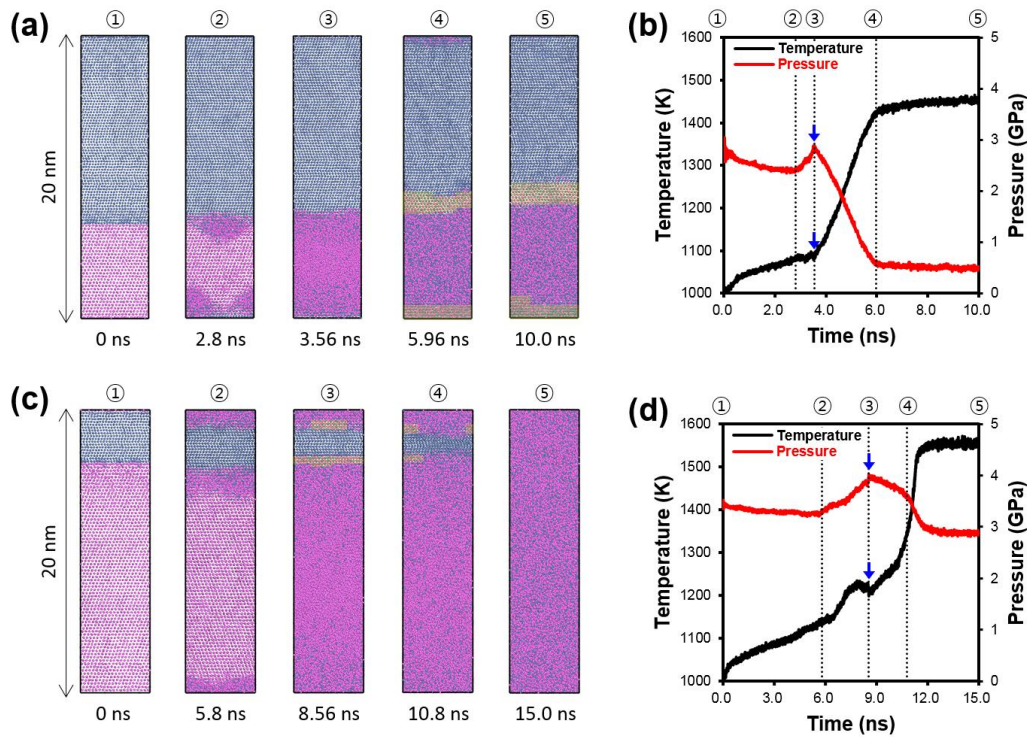
Figure 2.3 (a) MD simulation snapshots for Ni$_3$Al stoichiometric system with 20 nm bilayer thickness at the ignition temperature of 1000 K. (b) The time evolution of temperature and pressure of Ni$_3$Al system during MD simulation for 10 ns. The blue arrows represent the sudden dip and pronounced peak in temperature and pressure, respectively. Light yellow regions at 5.96 and 10.0 ns represent the *B2*-NiAl crystalline phase at the interface. (c) MD simulation snapshots for NiAl$_3$ stoichiometric system with 20 nm bilayer thickness at the ignition temperature of 1000 K. Light yellow regions at 8.56 and 10.8 ns represent the *B2*-NiAl crystalline phase at the interface. (d) The time evolution of temperature and pressure of NiAl$_3$ system during MD simulation for 15 ns. Copyright © 2017, The Korean Society of Industrial and Engineering Chemistry. Published by Elsevier B.V.

For Ni-rich system (*i.e.* Ni$_3$Al), the sudden dip and pronounced peak in the temperature and pressure were found early (3.56 ns), indicating the melting transition of Al layer (**Figure 2.3(a), (b)**). Note that since the Al ratio was not large, the induction time required to Al melting process was much shorter. Subsequently, Ni diffused into the liquid Al, but the reaction rate was relatively slow due to large portion of Ni. As a result, the local stoichiometric ratio at the interface became closer to equiatomic, resulting in the crystallization of *B2*-NiAl boundary all across the interface (5.96 ns). After all, Ni diffusion failed to proceed and finally the alloying reaction was terminated with partially mixed state (10 ns).

For Al-rich system (*i.e.* NiAl$_3$), the induction time required for Al melting was prolonged due to the high amount of Al, confirmed by a late occurrence of sudden dip of temperature and pronounced peak of pressure (8.56 ns). However, unlike the case of Ni-rich system, the *B2*-NiAl boundary was only locally formed at the interface due to faster reaction rate, and thus the diffusion of Ni into Al occurs unceasingly, reaching a fully mixed state of the NiAl$_3$ liquid phase (15 ns). Therefore, it is found that the exothermic reaction in the Ni-Al nanolayers proceeds through similar reaction pathways irrespective of stoichiometry. However, the reaction rate and extents of reaction truly changed by stoichiometry even at the same ignition temperature.

2.3.2 Reaction Characteristics by Ignition Temperature and Bilayer thickness

Figure 2.4(a)-(c) show the time evolution of temperature for three stoichiometric systems of Ni-Al nanolayers with 20 nm bilayer thickness by varying the ignition temperature (*i.e.* 1000, 1400, and 1700 K). Overall, the largest increase of reaction temperature was found for NiAl while similar increases were found for Ni$_3$Al and NiAl$_3$ with different reaction speeds. At 1000 K (**Figure 2.4(a)**), the reaction times were remarkably slow due to the existence of induction time required for Al melting. On the other hand, at above 1400 K (**Figure 2.4(b), (c)**), since Al layer melted rapidly at the early stage, the alloying reaction was easily accelerated by interdiffusion of Ni and Al in the liquid state. **Figure 2.4(d)** shows the reaction time (τ) as a function of the reciprocal values of ignition temperature ($1/T_i$). As expected, the reaction time decreased rapidly with increasing ignition temperature. Interestingly, for Al-rich NiAl$_3$ system, the reaction time was the slowest at 1000 K due to the longer induction time for Al melting, but at above 1400 K, it became faster than other stoichiometric systems due to the greater diffusivity of Al. Thus, as the Al ratio became larger, the variation width of reaction time with respect to the temperature gradually increased.
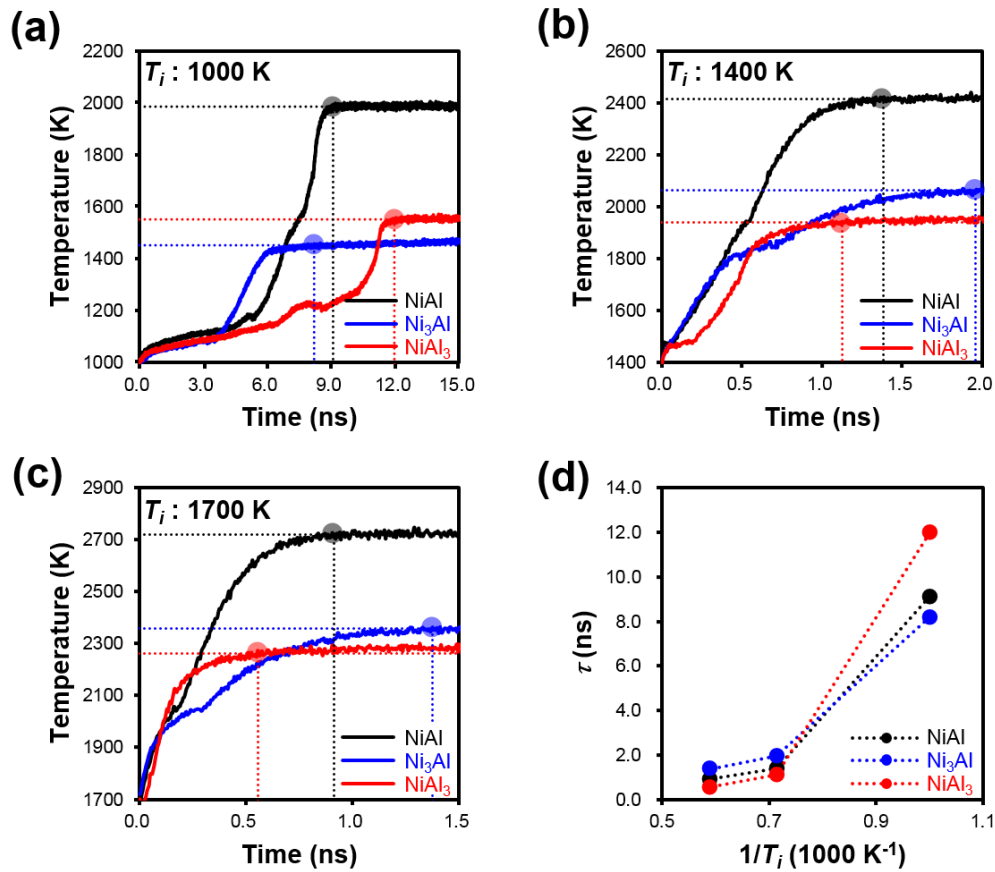
Figure 2.4. (a)-(c) The time evolution of temperature for three stoichiometric Ni-Al nanolayers (*i.e.* NiAl, Ni_3Al, and $NiAl_3$) with 20 nm bilayer thickness at different ignition temperatures (T_i) of (a) 1000 K, (b) 1400 K, and (c) 1700 K. Dotted lines and circles represent the reaction times estimated at the asymptotic final temperatures. (d) The reaction time (τ) as a function of reciprocal values of ignition temperature ($1/T_i$) for three stoichiometric Ni-Al nanolayers with 20 nm bilayer thickness. Copyright © 2017, The Korean Society of Industrial and Engineering Chemistry. Published by Elsevier B.V.

Figure 2.5(a)-(c) show the time evolution of temperature for three stoichiometric systems of Ni-Al nanolayers by varying the bilayer thickness (*i.e.* 10, 20, and 30 nm) at the ignition temperature of 1000 K. Except for Ni_3Al, the temperature rise was similar for all ranges of bilayer thickness. Note that in Ni_3Al, as the bilayer thickness increased, the temperature rise was considerably reduced since the fraction of unreacted Ni region increased due to the formation of *B2*-NiAl boundary. **Figure 2.5(d)** shows the reaction time as a function of bilayer thickness. The reaction time gradually increased with increasing bilayer thicknesses due to the increasing amount of Ni and Al in the system. However, it was difficult to corroborate the quantitative relationship between reaction time and stoichiometry at 1000 K since the reaction time of Ni_3Al might be underestimated due to the partially mixed state. Thus, we also

23

compared the reaction time as a function of bilayer thicknesses at above 1400 K (**Figure 2.6**). As a result, the reaction time was found to be shorter in order of increasing Al ratio, due to higher diffusivity of Al compared to Ni.[28]
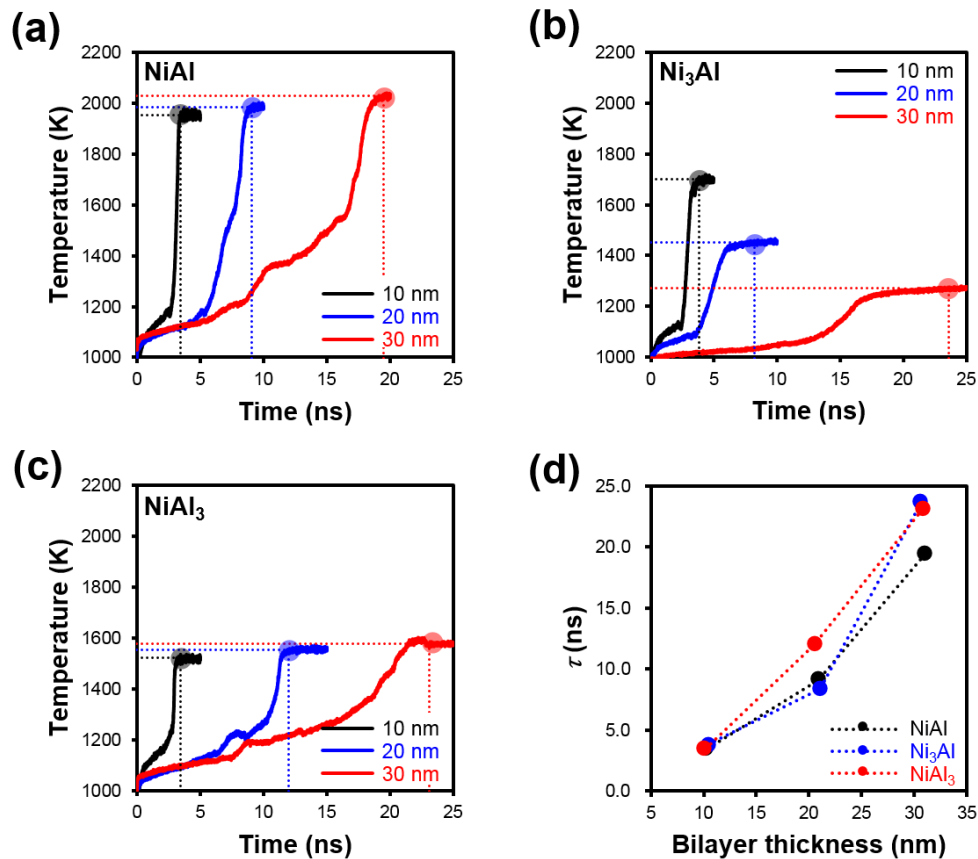
Figure 2.5 (a)-(c) The time evolution of temperature for three stoichiometric systems of Ni-Al nanolayers including (a) NiAl, (b) Ni_3Al, and (c) $NiAl_3$ by varying the bilayer thicknesses (*i.e.* 10, 20, and 30 nm). Dotted lines and circles represent the reaction times estimated at the asymptotic final temperatures. (d) The reaction time (τ) as a function of bilayer thickness of three stoichiometric Ni-Al nanolayers at the ignition temperature of 1000 K. Copyright © 2017, The Korean Society of Industrial and Engineering Chemistry. Published by Elsevier B.V.
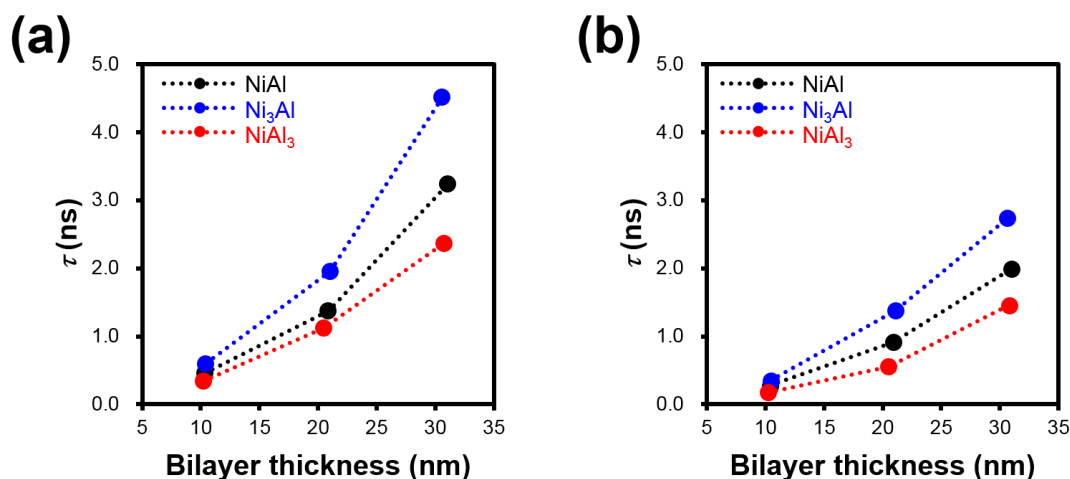
Figure 2.6 The reaction time (τ) as a function of bilayer thickness for three stoichiometric systems of Ni-Al nanolayers at the ignition temperature of (a) 1400 K and (b) 1700 K. Copyright © 2017, The Korean Society of Industrial and Engineering Chemistry. Published by Elsevier B.V.

2.3.3 Reaction Thermodynamics and Kinetics

To investigate the reaction thermodynamics of Ni-Al nanolayers, we compared the heats of reactions with different bilayer thicknesses and ignition temperatures (**Figure 2.7**). The heats of reactions ($-\Delta H$) were determined by estimating the absolute changes in total enthalpy during reactions in the *NVE* MD simulations. Several features have been deduced from the thermodynamic analysis of various temperatures and structural conditions. First, the general tendency of heats of reactions with stoichiometry was found in the order of NiAl, Ni_3Al, and $NiAl_3$. It was also agreed well with the trends of formation energy for crystalline phases corresponding to each stoichiometric ratio, as previously calculated by Purija and Mishin (*i.e.* -0.61 eV for *B2*-NiAl, -0.45 eV for *L1₂*-Ni_3Al, and -0.27 eV for *L1₂*-$NiAl_3$, respectively).[27] Note that the formation energies were represented as the dotted lines in **Figure 2.7** by converting the units to J/g. Further, the heats of reactions exhibited relatively similar values irrespective of ignition temperature and bilayer thicknesses, except for Ni_3Al. It implied that energy release during exothermic reaction was more directly affected by stoichiometric change than the variation of thickness or temperature. Notably, for Ni_3Al systems at the ignition temperature of 1000 K (**Figure 2.7(a)**), the heats of reaction were substantially reduced with increasing bilayer thickness since the extents of reaction decreased due to the crystallization of *B2*-NiAl boundary at the interface.
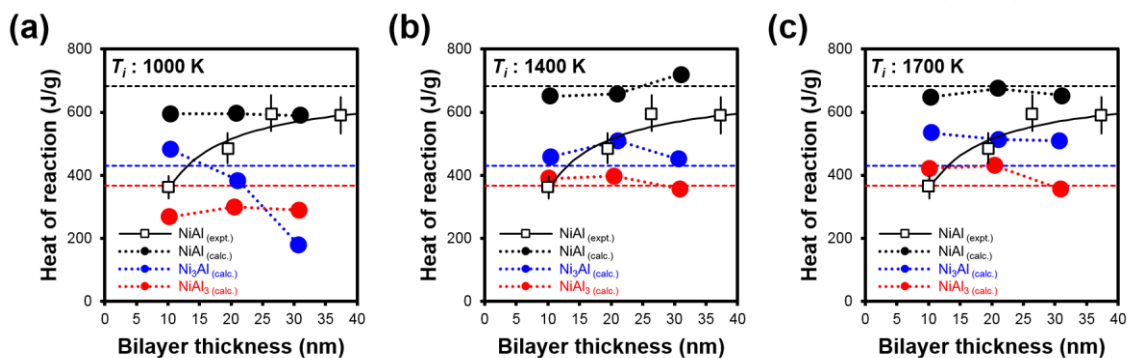
Figure 2.7 The heats of reactions for three stoichiometric systems of Ni-Al nanolayers (*i.e.* NiAl, Ni_3Al, and $NiAl_3$) with different ignition temperatures at (a) 1000 K, (b) 1400 K, and (c) 1700 K. 'NiAl $_{(expt.)}$' denotes the reference values from experimental DSC traces,[24] represented as white boxes with an error bar. The black solid lines represent the fitting lines of experimental values. Note that the experimental values were normalized by factor 2 to be compared with same scale in the MD simulation. 'NiAl $_{(calc.)}$', 'Ni_3Al $_{(calc.)}$', and '$NiAl_3$ $_{(calc.)}$' denotes the calculated values from our MD simulations for three stoichiometric systems. The black, blue, and red dotted lines represent the formation energies of crystalline phases corresponding to each stoichiometric ratio, previously calculated by Purija and Mishin[27] (*i.e.* -0.61 eV for *B2*-NiAl, -0.45 eV for *L1₂*-Ni_3Al, and -0.27 eV for *L1₂*-$NiAl_3$, respectively). Copyright © 2017, The Korean Society of Industrial and Engineering Chemistry. Published by Elsevier B.V.

When we compared the heats of reactions from our MD simulations with those from experimental DSC traces,[24] the increasing tendency with increasing bilayer thickness was found in the experimental values (available data was found only for NiAl). The reason of this increasing trend is due to the existence of premixed regions that forms during deposition, which reduces the overall exothermicity of alloying reaction.[24] As the bilayer thickness decreased, the volume fraction of premixed region became larger, resulting in the increasing trends for heat of reaction. Although the heat of reactions of NiAl obtained from MD simulations were relatively larger than experimental values, it is reasonable to speculate that they were within in a similar range considering the premixed region was not employed in the MD simulation.

Next, in order to quantify the reaction kinetics of Ni-Al nanolayers, the reaction times of three stoichiometric systems were estimated for different ignition temperatures and bilayer thicknesses. The reaction time (τ) can be expressed as a function of the square of transport distance (λ^2), which is a half of bilayer thickness, by following the equation reported by Cherukara et al.,[28]

$$\lambda^2 = D * \tau^{\gamma} \qquad\qquad (2.1)$$

where D is the diffusion coefficient and γ is an exponent value which is close to 1. By fitting the MD simulation data to above equation, the correlation plots between τ and λ^2 were obtained (**Figure 2.8(a)-(c)**). In general, the reaction time (τ) increases as T_i decreases and λ^2 increases. In addition, the exponent γ exhibited similar values with 1 (between 1.05 and 1.28), indicating the transport nature was not severely affected by stoichiometry. It became more closer to 1 when the T_i increased, implying that the mass diffusion behaviour occurred more ideally at higher temperature.

From the slope between τ and λ^2, the diffusion coefficients (D) can be obtained, while fixing the exponent $\gamma = 1$.[28] Also, D can be described by following Arrhenius relation,

$$D = D_0 \exp\left(\frac{-E_a}{kT}\right) \qquad\qquad (2.2)$$

where E_a is the activation energy, k is the Boltzmann constant, T is the absolute temperature, and D_0 is the Arrhenius pre-exponential factor. **Figure 2.8(d)** shows the Arrhenius plot between the reciprocal values of ignition temperatures ($1/T_i$) and diffusion coefficient in log scale ($\ln D$). Overall, as the portion of Al ratio becomes larger, the diffusivity becomes faster. However, at the same time, the variation width of diffusivity with respect to temperature became much larger, leading to the higher activation energy to react (*i.e.* 56.5 kJ/mol for NiAl$_3$, 46.0 kJ/mol for NiAl, and 44.8 kJ/mol for Ni$_3$Al, respectively). This result is attributed to the induction time during Al melting process. At low temperature (1000 K), the longer induction time is required as the Al ratio becomes larger, slowing down the diffusivity of Al-rich system. Meanwhile, at higher temperature (>1400 K), the induction time becomes very short since the diffusion of liquid Al occurs immediately, leading to the higher diffusivity for Al-rich system. To sum up with the above results, for Ni-rich systems (*i.e.* Ni$_3$Al), the exothermicity can be hindered by the crystallization of *B2*-NiAl boundary at the interface. Meanwhile, for Al-rich system (*i.e.* NiAl$_3$), the reaction kinetics were limited by the induction time during Al melting process. Based on the results, NiAl was found to be the best stoichiometry in respect of both thermodynamic and kinetic points of view.
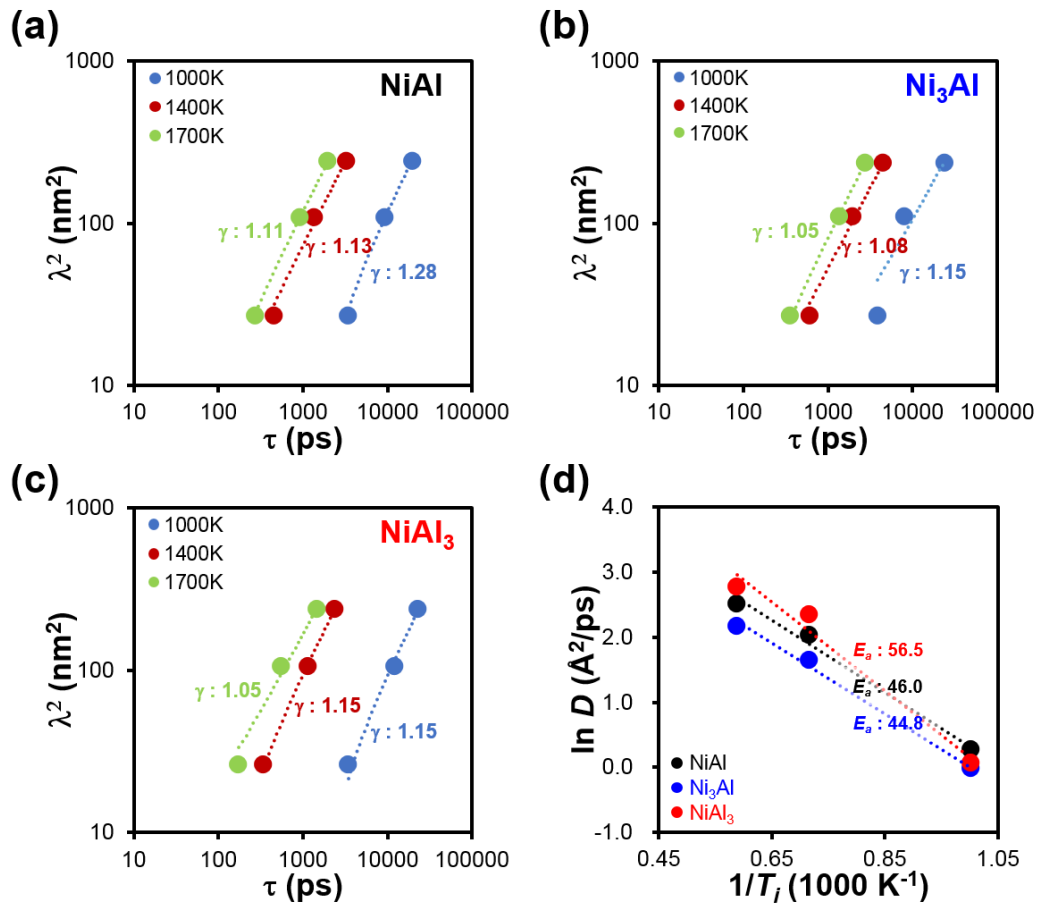
Figure 2.8 (a)-(c) The correlation plots between reaction time (τ) and squares of transport distance (λ^2) of three stoichiometric systems of Ni-Al nanolayers, including (a) NiAl, (b) Ni$_3$Al, and (c) NiAl$_3$. Three different ignition temperatures (*i.e.* 1000, 1400, and 1700 K) were considered. (d) Arrhenius plots between reciprocal values of ignition temperatures ($1/T_i$) and diffusion coefficients in a log scale (ln D). The activations energies from the slopes are labelled in the figure. Energy values are in kJ/mol. Copyright © 2017, The Korean Society of Industrial and Engineering Chemistry. Published by Elsevier B.V.

28

2.4 Conclusion

In this study, the reaction characteristics of Ni-Al nanolayers (*i.e.* temperature rise, reaction time, heat of reaction, diffusion coefficient, and activation energy) were theoretically investigated by MD simulation. First, we explored the reaction mechanisms of Ni-Al nanolayers by stoichiometry. Interestingly, the sequence of the overall reaction mechanism by stoichiometry was found to be similar, but the reaction rate and the extents of intermixing were changed even at the same ignition temperature. Next, we also compared the reaction characteristics by varying the ignition temperatures and bilayer thicknesses. While the temperature rises remained constant, the reaction times decreased with increasing ignition temperature or decreasing the bilayer thicknesses. Lastly, the reaction thermodynamics and kinetics in terms of heats of reactions, diffusion coefficients, and activation energies were investigated. The overall reaction thermodynamics was found to be more directly affected by stoichiometry than the changes of thickness or ignition temperatures. For reaction kinetics, since the temperature dependence of diffusivity was crucially related to the Al ratio, the activation energy was found to be maximized in the Al-rich system. Thus, in both thermodynamic and kinetic point of view, NiAl was found to be the best stoichiometry for Ni-Al nanolayers. In conclusion, the reaction characteristics of Ni-Al nanolayers were theoretically quantified by various structural and reaction conditions (*i.e.* stoichiometry, bilayer thickness, and ignition temperature). From these fundamental understanding about the underlying complex reaction phenomena, we expect that these theoretical quantification of reaction characteristics will provide an insight into manufacturing more advanced nanolayer systems.

2.5 References

1. Merzhanov, A. G. The chemistry of self-propagating high-temperature synthesis. *J. Mater. Chem.* **2004,** 14, 1779-1786.

2. Trenkle, J. C.; Wang, J.; Weihs, T. P.; Hufnagel, T. C. Microstructural study of an oscillatory formation reaction in nanostructured reactive multilayer foils. *Appl. Phys. Lett.* **2005,** 87, 153108.

3. Rogachev, A. S.; Vadchenko, S. G.; Mukasyan, A. S. Self-sustained waves of exothermic dissolution in reactive multilayer nano-foils. *Appl. Phys. Lett.* **2012,** 101, 063119.

4. Varma, A.; Mukasyan, A. S. Combustion Synthesis of Advanced Materials: Fundamentals and Applications. *Korean J. Chem. Eng.* **2004,** 21, 527-536.

5. Gavens, A. J.; Van Heerden, D.; Mann, A. B.; Reiss, M. E.; Weihs, T. P. Effect of intermixing on self-propagating exothermic reactions in Al/Ni nanolaminate foils. *J. Appl. Phys.* **2000,** 21, 1255-1263.

6. Wang, J.; Besnoin, E.; Duckham, A.; Spey, S. J.; Reiss, M. E.; Knio, O. M.; Weihs, T. P. Joining of stainless-steel specimens with nanostructured Al/Ni foils. *J. Appl. Phys.* **2004,** 95, 248-256.

7. Hong, J.; Kang, S. W. A metal sputtered waterproof coating that enhances hot water stability. *J. Ind. Eng. Chem.* **2012,** 18, 1496-1498.

8. Battezzati, L.; Pappalepore, P.; Durbiano, F.; Gallino, I. Solid state reactions in Al/Ni alternate foils induced by cold rolling and annealing. *Acta Mater.* **1999,** 47, 1901-1914.

9. Sieber, H.; Park, J. S.; Weissmuller, J.; Perepezko, J. H. Structural evolution and phase formation in cold-rolled aluminum–nickel multilayers. *Acta Mater.* **2001,** 49, 1139-1151.

10. Qiu, X.; Graeter, J.; Kecskes, L.; Wang, J. Exothermic reactions in cold-rolled Ni/Al reactive multilayer foils. *J. Mater. Res.* **2008,** 23, 367-1151.

11. Makino, A. Fundamental aspects of the heterogeneous flame in the self-propagating high-temperature synthesis (SHS) process. *Prog. Energ. Combust.* **2001,** 27, 1-74.

12. Zhu, P.; Shen, R. Q.; Ye, Y. H.; Zhou, X.; Hu, Y. Influence of Al/CuO reactive multilayer films additives on exploding foil initiator. *J. Appl. Phys.* **2011,** 110, 094505.

13. Giles, J. Collateral damage. *Nature* **2004,** 427, 580-581.

14. Higa, K. T. Energetic Nanocomposite Lead-Free Electric Primers. *J. Propul. Power,* **2007,** 23, 722-727.

15. Sorensen, B. High-Velocity Impact of Encased Al/PTFE Projectiles on Structural Aluminum Armor. *Procedia. Eng.* **2015,** 103, 569-576.

16. Wang, H.; Li, Y.; Feng, B.; Huang, J.; Zhang, S.; Fang, X. Compressive properties of PTFE/Al/Ni composite under uniaxial loading. *J. Mater. Eng. Perform.* **2017,** 26, 2331-2336.

17. Duckham, A.; Spey, S. J.; Wang, J.; Reiss, M. E.; Weihs, T. P.; Besnoin, E.; Knio, O. M. Reactive nanostructured foil used as a heat source for joining titanium. *J. Appl. Phys.* **2004,** 96, 2336-2342.

18. Swiston, A. J.; Besnoin, E.; Duckham, A.; Knio, O. M.; Weihs, T. P.; Hufnagel, T. C. Thermal and microstructural effects of welding metallic glasses by self-propagating reactions in multilayer foils. *Acta Mater.* **2005,** 53, 3713-3719.

19. Wang, J.; Besnoin, E.; Duckham, A.; Spey, S. J.; Reiss, M. E.; Knio, O. M.; Powers, M.; Whitener, M.; Weihs, T. P.; Hufnagel, T. C. Room-temperature soldering with nanostructured foils. *Appl. Phys. Lett.* **2003,** 83, 3987-3989.

20. Zhao, S.; Germann, T. C.; Strachan, A. Room-temperature soldering with nanostructured foils. *J. Chem. Phys.* **2006,** 125, 164707.

21. Kim, J. S.; LaGrange, T.; Reed, B. W.; Taheri, M. L.; Armstrong, M. R.; King, W. E.; Browning, N. D.; Campbell, G. H. Imaging of Transient Structures Using Nanosecond in Situ TEM. *Science* **2008,** 321, 1472-1475.

22. Barmak, K.; Michaelsen, C.; Lucadamo, G. Reactive phase formation in sputter-deposited Ni/Al multilayer thin films. *J. Mater. Res.* **1997,** 12, 133-146.

23. Gunduz, I. E.; Fadenberger, K.; Kokonou, M.; Rebholz, C.; Doumanidis, C. C.; Ando, T. Modeling of the self-propagating reactions of nickel and aluminum multilayered foils. *J. Appl. Phys.* **2009,** 105, 074903.

24. Knepper, R.; Snyder, M. R.; Fritz, G.; Fisher, K.; Knio, O. M.; Weihs, T. P. Effect of varying bilayer spacing distribution on reaction heat and velocity in reactive Al/Ni multilayers. *J. Appl. Phys.* **2009,** 105, 083504.

25. Trenkle, J. C.; Koerner, L. J.; Tate, M. W.; Gruner, S. M.; Weihs, T. P.; Hufnagel, T. C. Phase transformations during rapid heating of Al/Ni multilayer foils. *Appl. Phys. Lett.* **2008,** 93, 3081903.

26. Fadenberger, K.; Gunduz, I. E.; Tsotsos, C.; Kokonou, M.; Gravani, S.; Brandstetter, S.; Bergamaschi, A.; Schmitt, B.; Mayrhofer, P. H.; Doumanidis, C. C.; Rebholz, C. *In situ* observation of rapid reactions in nanoscale Ni–Al multilayer foils using synchrotron radiation. *Appl. Phys. Lett.* **2010,** 97, 144101.

27. Pun, G. P. P.; Mishin, Y. Development of an interatomic potential for the Ni-Al system. *Philos. Mag.* **2009,** 89, 3245-3267.

28. Cherukara, M. J.; Vishnu, K. G.; Strachan, A. Role of nanostructure on reaction and transport in Ni/Al intermolecular reactive composites. *Phys. Rev. B* **2012,** 86, 075470.

29. Rothhaar, U.; Oechsner, H.; Scheib, M.; Müller, R. Compositional and structural characterization of temperature-induced solid-state reactions in Al/Ni multilayers. *Phys. Rev. B* **2000,** 61, 974-979.

30. Shin, Y. K.; Kwak, H.; Zou, C. Y.; Vasenkov, A. V.; van Duin, A. C. T. Development and Validation of a ReaxFF Reactive Force Field for Fe/Al/Ni Alloys: Molecular Dynamics Study of Elastic Constants, Diffusion, and Segregation. *J. Phys. Chem. A* **2012,** 116, (49), 12163-12174.

31. Plimpton, S. J. Fast Parallel Algorithms for Short-Range Molecular Dynamics. *J. Comput. Phys.* **1995,** 117, 1-19.

32. Weingarten, N. S.; Mattson, W. D.; Yau, A. D.; Weihs, T. P.; Rice, B. M. A molecular dynamics study of the role of pressure on the response of reactive materials to thermal initiation. *J. Appl. Phys.* **2010,** 107, 093517.

33. Sandoval, L.; Campbell, G. H.; Marian, J. A molecular dynamics study of the role of pressure on the response of reactive materials to thermal initiation. *Modell. Simul. Mater. Sci. Eng.* **2014,** 22, 025022.

34. Zhao, S.; Germann, T. C.; Strachan, A. Melting and alloying of Ni∕Al nanolaminates induced by shock loading: A molecular dynamics simulation study. *Phys. Rev. B* **2007,** 76, 104105.

Chapter 3. Explosion Dynamics of Nanobomb

3.1 Effect of Packing Density of Nitromethane and Ignition Temperature

---

3.1.1 Introduction

Nitromethane (NM), which is the simplest type of nitro compound in high explosive energetic material (HE), has been used for years in explosion-related applications. Many researchers have conducted experimental and theoretical studies on, to name a few, optical[1] and thermal decompositions[2-8] as well as phase transitions including melting[9,10] and solidification[11] (or crystallization). Recently, specific interest was begun on the behavior of NM in confinement environment by focusing on the decomposition activity. For instances, Liu et al.[7] conducted *ab initio* molecular dynamics (AIMD) to show fast decomposition of NM between functionalized graphene sheets. Smeu et al.[12] showed the stabilizations of several HEs (*e.g.* FOX-7, RDX, HMX etc.) encapsulated in carbon nanotube (CNT) and graphene bilayer by DFT calculations. Especially, *via* MD, NM confined in CNT was found to undergo special intermolecular arrangement[13,14] and to have low activation energy for reaction.[15,16] In a way, the idea of nanobomb, which is composed of nanocontainer and enclosed HEs, has been already shown[17] but it was not concretely realized even in *in silico* studies. Under the encapsulation, HE is expected to be intact from outside by nanocontainer, which prohibits the change of chemical properties of confined molecules, at normal conditions. However, when in use, the effect of explosion would be enhanced by the built-up pressure (*i.e.* by decomposition of HE) inside before the burst of nanobomb.

In order to model the conceptual nanobomb, we define a nanocontainer, which is a small container and can encapsulate a few tens to hundreds of molecules. A promising nanocontainer, CNT, is a good candidate because of its excellent thermal and mechanical properties.[18] In particular, it can endure internally developed pressures of 30−100 GPa because of high axial tensile strength in intrinsic structural stability.[19] Furthermore, CNT with cap is expected to transport encapsulated materials safely by making isolated conditions.[20] In this study, therefore, we conceptually constructed a nanobomb with NM and CNT as the explosive and nanocontainer, respectively.

In general, thermal decompositions of HE materials follow very complex reaction mechanisms, which are very difficult to trace at harsh condition of high pressure and temperature under confined environment. Also, there have been few data of confined NM on fundamental knowledge of decomposition phenomena including detailed interaction mechanism and information on various intermediates and products. In order to capture the desired information, temporal and methodological limits of generic MD and DFT must be lifted. To do so, reactive force field (denoted as ReaxFF) developed by van Duin et al.[21] was considered for this study since it can handle reactive dynamics of atoms via the bond order information describing the interatomic pair force. So far, reactive behaviors of HEs such as NM,[5, 6] TNT,[22, 23] and RDX[24, 25] have been studied with ReaxFF. Strachan et al.[24] reported shock-induced decomposition mechanism of RDX thin layer. Han et al.[5] and Rom et al.[6] studied the decomposition pathway of compressed NM. Recently, compression-dependent decomposition product, namely Buckybomb (dodecanitrofullerene, $C_{60}(NO_2)_{12}$), was investigated by nonequilibrium reactive MD (NERMD) simulation.[26] In this regard, ReaxFF, which can provide details of dynamics of the reactive system, was adopted to the study of the nonequilibrium behavior of nanobomb.

3.1.2 Simulation Details

First, we have modeled an explosive nanocontainer, CNT, *via* generic MD and grand canonical Monte Carlo (GCMC) simulations (see **Chapter 3.1.2.1**), where COMPASS force field[27,28] was used *via* Materials Studio 2016.[29] Especially, GCMC was employed to confirm the number of NMs that can be stably packed into the CNT by computing required energies for the insertion and deletion of NMs (**Table 3.1.1**). After the preparation of nanobomb including NM and CNT, NERMD simulation with ReaxFF was conducted for the decomposition of initially heated system. For this calculation, we used LAMMPS program.[30,31] Potential energy parameters were taken from Rom et al.'s work.[6] The internal density of NM in the nanocontainer and initial heating temperature were varied to investigate their effects on the explosion, where the decomposition mechanism and bursting phenomena were investigated. The bursting mechanism of the nanobomb was confirmed by investigating all configurations, which were generated during simulation. The procedure of the theoretical study is discussed in more detail below.

3.1.2.1 Criteria of Proper Diameter of Nanobomb

As an initial step prior to system modeling, we chose the appropriate size (radius or chiral index) of the CNT to contain enough NM molecules to be ruptured itself by the heat released from the internally contained NM. The number of NM loaded in the unit length of CNT with each radius was confirmed through the GCMC simulation, and the maximum heat of reaction was calculated. Reaction enthalpy of NM was estimated when NM was exactly decomposed in the form of gas molecules.[6]

$$CH_3NO_2 \rightarrow CO \; + \; \tfrac{1}{2}N_2 \; + \; H_2O \; + \; \tfrac{1}{2}H_2 \qquad \Delta H_{Rxn} = \text{-67 kcal/mol} \qquad (3.1.1)$$
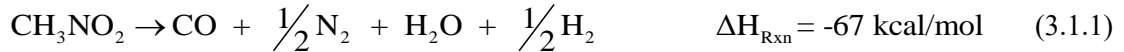
Bond dissociation energy (BDE) of the C-C bond in CNT was calculated using following form of the overall reaction

$$CNT \; + \; O_2 \rightarrow CNT^* \; + \; CO_2 \qquad \Delta H_{Rxn} = \text{-63.703 kcal/mol} \qquad (3.1.2)$$

CNT* referred to the CNT that one carbon was removed, and the above heat of reaction was obtained from DFT calculation using generalized gradient approximation (GGA) and Perdew−Burke−Ernzerhof (PBE)[32] functional. The BDE of the O=O bond in O_2 and the C-O bond in CO_2 are known as 117.577 kcal/mol and 353.919 kcal/mol, respectively. Thus, the above equation can be separated into the following three elementary reactions.

$$
\begin{aligned}
O_2 &\rightarrow 2O & \Delta H_{Rxn} &= \; 117.577 \text{ kcal/mol} \\
C \; + \; 2O &\rightarrow CO_2 & \Delta H_{Rxn} &= \text{-707.838 kcal/mol} \qquad (3.1.3) \\
CNT &\rightarrow CNT^* \; + \; C & \Delta H_{Rxn} &= 3 \times BDE_{c-c} \text{ kcal/mol}
\end{aligned}
$$
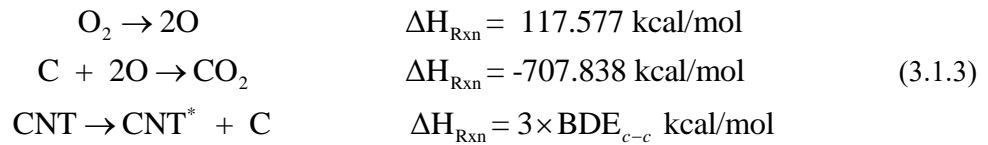
Since three C-C bonds are broken when one carbon atom is separated from the CNT, the BDE of the C-C bond of CNT is calculated to be about 218 kcal/mol. This means that 218 kcal/mol is required to cut one side of the armchair CNT with a width of one C-C bond in the zigzag direction. The number of NM that can be loaded into CNT with one C-C bond width for each chiral index is estimated by GCMC simulation, and the maximum reaction heat of each number is calculated (**Table 3.1.1**). From our calculation, over (17,17) armchair CNT can be self-decomposed by the heat emitted from encapsulated NM. However, in a real system, decomposition takes place through various pathways, and a product having a high energy can be generated as a final product, so the total heat of reaction is expected to be reduced. Therefore, (20,20) CNT was selected as the nanocontainer that encapsulates proper amount of NM in this study.

Table 3.1.1. GCMC results for system modeling. Copyright © 2017, American Chemical Society.

Chiral index	# of loaded NM (/1 bond CNT)	Ideal heat of reaction
(6, 6)	0.209	13.984
(7, 7)	0.278	18.611
(8, 8)	0.389	26.056
(9, 9)	0.659	44.183
(10, 10)	0.884	59.224
(11, 11)	1.156	77.471
(12, 12)	1.485	99.491
(13, 13)	1.813	121.482
(14, 14)	2.189	146.663
(15, 15)	2.567	171.996
(16, 16)	2.996	200.747
(17, 17)	3.650	244.550
(18, 18)	4.037	270.469
(19, 19)	4.690	314.200
(20, 20)	5.335	357.472

3.1.2.2 Modeling of nanocontainer

From the result of GCMC, (20,20) CNT has been selected as a nanocontainer for the nanobomb system. Since we have defined the nanocontainer as an isolated molecule with a finite length that can completely enclose a few hundreds of NM, it is necessary to consider the cap structure, which has been frequently ignored in other study due to the high aspect ratio of CNT.[33,34] For finding the right cap structure, the isolated pentagon rule is the most applicable one, which indicates whether the arrangement of adjacent pentagons is energetically favored or not. There have been previous studies using this rule[33-38] and among them, the solution of Thomson problem[38] was employed to construct the reasonable cap of the CNT. In a brief introduction of Thomson's method, it is called tube Thomson point (N_T^{tube}) if the Thomson point is located at CNT wall. The other one is cap Thomson point (N_T^{cap}), which is located at the arbitrary hemisphere-shaped surface. In this study, we have set 215 N_T^{cap} 's to model the cap structure of the (20, 20) CNT. Stable configuration comprising N_T^{cap} 's was obtained by following Robinson et al.'s work,[38] where the energy minimization and optimization were performed for the arrangement of cap Thomson points. The capped CNT was then built by locating carbon atoms on the lattice points, which were obtained by the intersection points of the vertical bisector of the triangulated Thomson points (*i.e.* connecting all of Thomson points to nearest neighbors) (**Figure 3.1.1**).

Side view   Front view
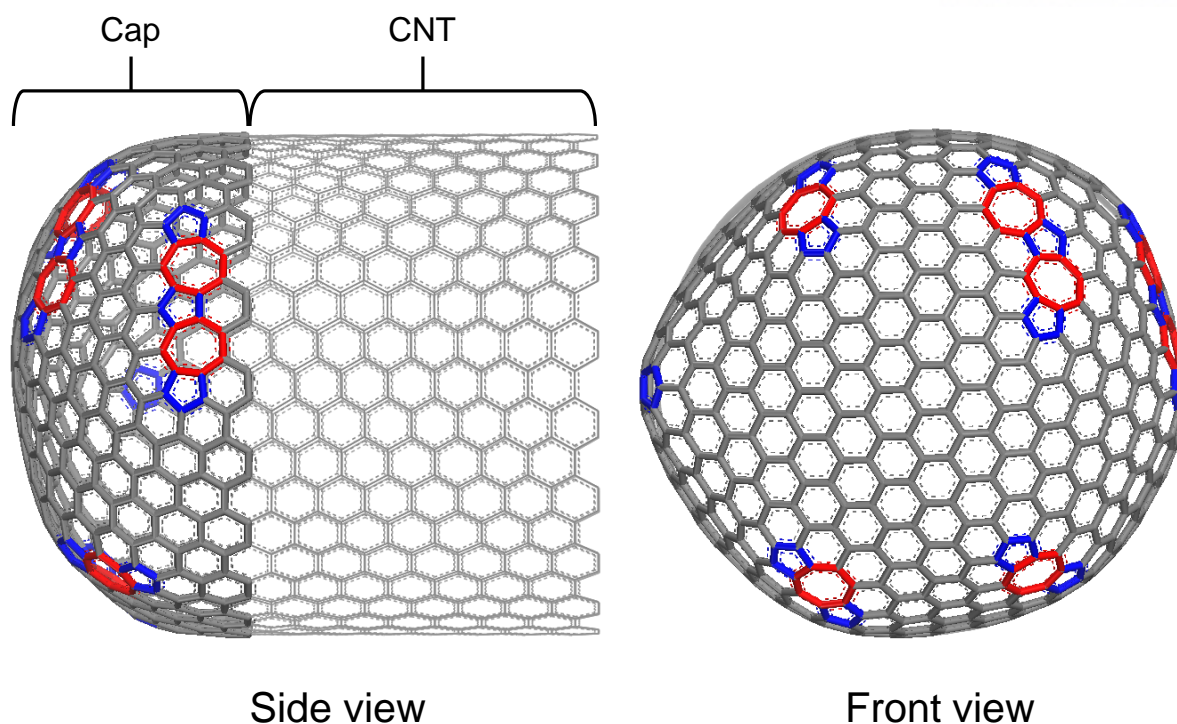
Figure 3.1.1 CNT cap model constructed in this study using the solution of Thomson problem. 5-7 carbon atoms rings are colored as blue and red lines, respectively. Copyright © 2017, American Chemical Society.

3.1.2.3 Construction of Nanobomb System

To control the internal density of NM in nanocontainer, the cavity volume of the capped CNT was calculated by obtaining Connolly surface (**Figure 3.1.2**). Note that a probe atom with certain radius (*i.e.* 1.0 Å in diameter) rolls on the van der Waals surface of the target system and the sum of probed trajectories produces Connolly surface.[39] Default packing density of NM was selected as 1.137 g/cm^3 and higher densities (*i.e.* 1.2, 1.3, 1.5, and 1.7 g/cm^3) of compressed NM were also considered for further simulations. Number of NM molecules corresponding to density (**Table 3.1.2**) was randomly packed inside the CNT. To prevent undesired decomposition during relaxation simulation, generic MD simulation was conducted to stabilize the systems by annealing at temperatures between 300 K and 500 K with the time step of 1 fs. The relaxed NM-encapsulated nanocontainer is shown in **Figure 3.1.3**.

(a)

(b)
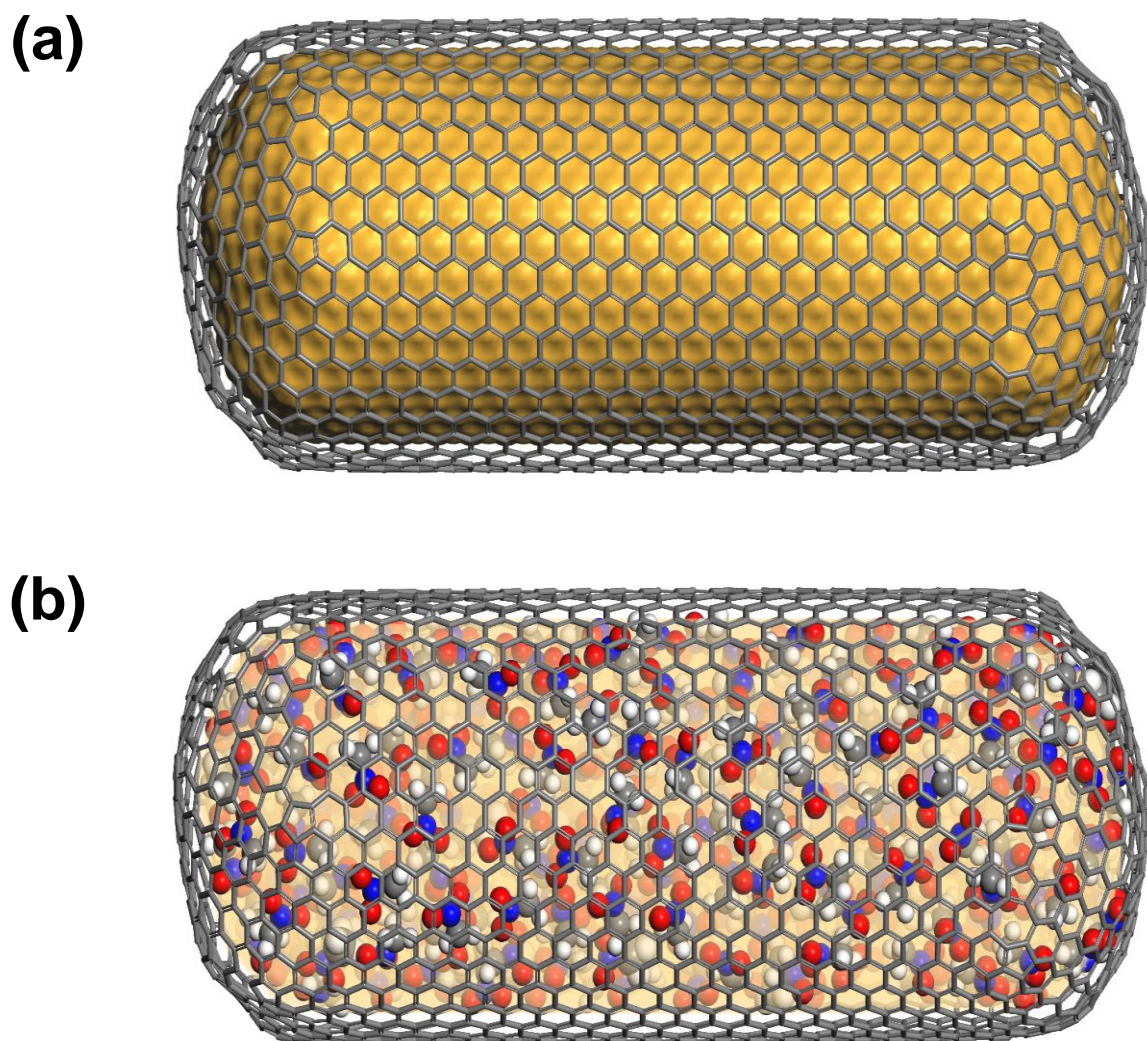
Figure 3.1.2 Connolly surface and cavity volume of CNT container. (a) Gold area is the Connolly surface of CNT container. (b) Cavity volume of nanobomb, which is the enclosed region of Connolly surface drawn as the shaded yellow. NM molecules are packed in the shaded yellow region. Copyright © 2017, American Chemical Society.

Table 3.1.2 Density and the number of confined NMs in capped (20, 20) CNT used in explosion dynamics simulation. Inner volume was estimated by Connolly volume calculation. Copyright © 2017, American Chemical Society.

Density (g/cm^3)	Inner volume (Å^3) of CNT	no. of NM
1.137		323
1.200		340
1.300	28750	369
1.500		425
1.700		482
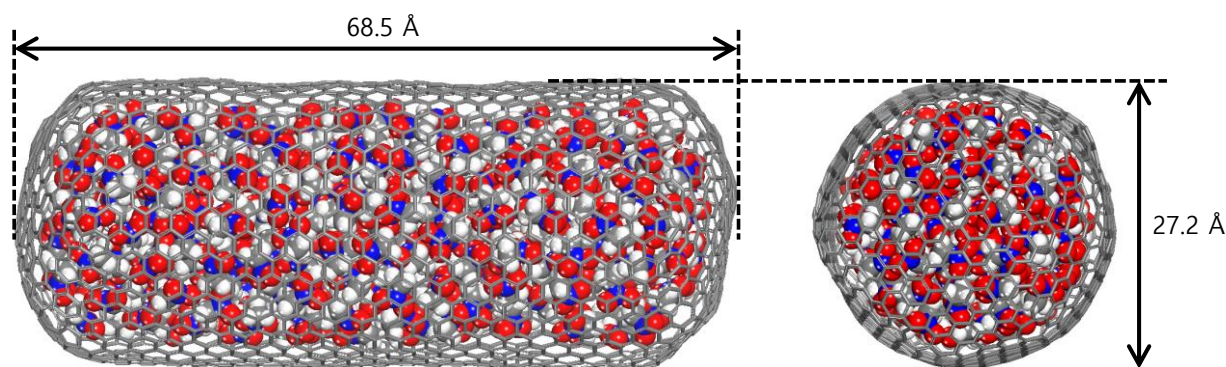
Figure 3.1.3 Side (left) and front (right) views of NM encapsulated (density = 1.137 g/cm^3) (20, 20) armchair CNT model with caps, which were constructed by following the solution of Thomson problem. Copyright © 2017, American Chemical Society.

3.1.2.4 Reactive Dynamics Simulation

Unlike MD using classical force fields, ReaxFF takes into account the dynamic bond order, which is renewed at each simulation step, to calculate the bond and non-bond energies.[21] For atomic partial charges, electronegativity equalization method (EEM),[40,41] which reflects the influence of the electrostatic field by the neighboring atoms, is employed and the atomic charge was updated at every time step, which was set to 0.1 fs. Berendsen thermostat was used to keep temperature constant. We have performed three steps for the reactive dynamics. The detailed procedure of the simulation is listed below.

Relaxation: The energy of the nanobomb system (*i.e.* NM-encapsulated CNT), which was relaxed with MD, was minimized once again *via* ReaxFF with conjugate gradient algorithm. Then, NVT simulation at room temperature was performed during 50 ps of simulation time

while preventing initial reaction due to high internal energy.

Heat-up: The temperature of each system was rapidly raised to the target temperature (*i.e.* 2500 K, 3000 K, 3500 K and 4000 K) within a short period of time (100 fs) to impose similar effect of heating the system through the detonation wave. In this step, some portions of NM were decomposed.

Thermal decomposition: In this step, NERMD was applied to nanobomb system during 200 ps. We observed that the energy released from the decomposition of NM contributed to the additional rise of the system temperature, resulting in the explosion phenomena. Note that the time step employed in this step was adequate to ensure the conservation of the total energy (maximum 3.6% variation in **Table 3.1.3**).

Table 3.1.3 Energy conservation test from non-equilibrium reactive MD simulation for 200 ps. Copyright © 2017, American Chemical Society.

Model system		Initial (kcal/mol)	Max. energy (kcal/mol)	diff (%)	Min. energy (kcal/mol)	diff (%)
Density (g/cm^3)	Initial heating temperature					
1.137	2500	-615263.170	-607067.470	1.332	-615276.150	0.002
	3000	-602429.720	-587248.200	2.520	-602510.150	0.013
	3500	-589173.600	-569645.290	3.315	-589242.210	0.012
	4000	-574882.670	-558511.100	2.848	-574973.550	0.016
1.2	2500	-624571.900	-615250.190	1.492	-624574.180	0.000
	3000	-610880.390	-592457.540	3.016	-610887.000	0.001
	3500	-597690.250	-576010.330	3.627	-597725.730	0.006
	4000	-583722.720	-573991.810	1.667	-583818.540	0.016
1.3	2500	-639339.010	-628286.480	1.729	-639349.130	0.002
	3000	-625412.870	-603669.090	3.477	-625426.940	0.002
	3500	-611041.450	-596486.970	2.382	-611121.260	0.013
	4000	-597139.620	-586345.130	1.808	-597209.490	0.012
1.5	2500	-667982.730	-658170.830	1.469	-667993.600	0.002
	3000	-652376.690	-637216.170	2.324	-652419.040	0.006
	3500	-636864.430	-628365.290	1.335	-636901.740	0.006
	4000	-621000.440	-611432.000	1.541	-621049.940	0.008
1.7	2500	-695501.820	-684883.790	1.527	-695517.480	0.002
	3000	-679307.440	-669631.650	1.424	-679316.560	0.001
	3500	-662427.870	-654184.330	1.244	-662467.830	0.006
	4000	-644397.430	-634575.360	1.524	-644427.130	0.005

3.1.3 Results and Discussion

3.1.3.1 Decomposition Behavior of Confined NM

Five NM systems at different densities were run with NERMD simulations after introducing initial heating at four different temperatures. We analyzed two aspects of thermal decomposition; decomposition behavior of internal species and bursting mechanism of the nanocontainer over time. Since there is no concept on explicit bond in ReaxFF, the species generated from the reaction were recognized by the bond order, for which their cut-off value for each atom pair were presented in **Table 3.1.4**. The numbers of molecules (molecular fragments) during NERMD simulation were normalized by the initial number of NM molecules with respect to each NM density.

Table 3.1.4 Bond order cut-off value for species analysis. Copyright © 2017, American Chemical Society.

Bond	Cut off
C-N	0.30
C-C	0.55
C-O	0.80
C-H	0.40
O-O	0.65
N-O	0.55
O-H	0.40
H-H	0.55
H-N	0.55
N-N	0.55

3.1.3.1 Decomposition behavior of confined NM

Figure 3.1.4 shows the decomposition rate of NMs as a function of time during thermal decomposition simulation. Clearly, the decomposition occurred earlier as the initial temperature became higher. In terms of density, the decomposition rate at the initial stage was relatively slow at high NM density. This trend was similar to the case of uni-molecular reaction described in Rom et al.'s work,[6] which explained the heat removal of neighboring molecules working as a thermal bath, so that the reaction rate was decelerated at high density. However, at a later stage, the reaction rate at high densities of NM was reversed. Interestingly, as the initial temperature increased, the decomposition of NM at

initial stage was faster for the confined NM compared to liquid NM in bulk.[6] We conjecture that CNT played a role to induce high thermal vibration for NM, where the confined system at low density was highly influenced, to exhibit the large decomposition at initial stage.
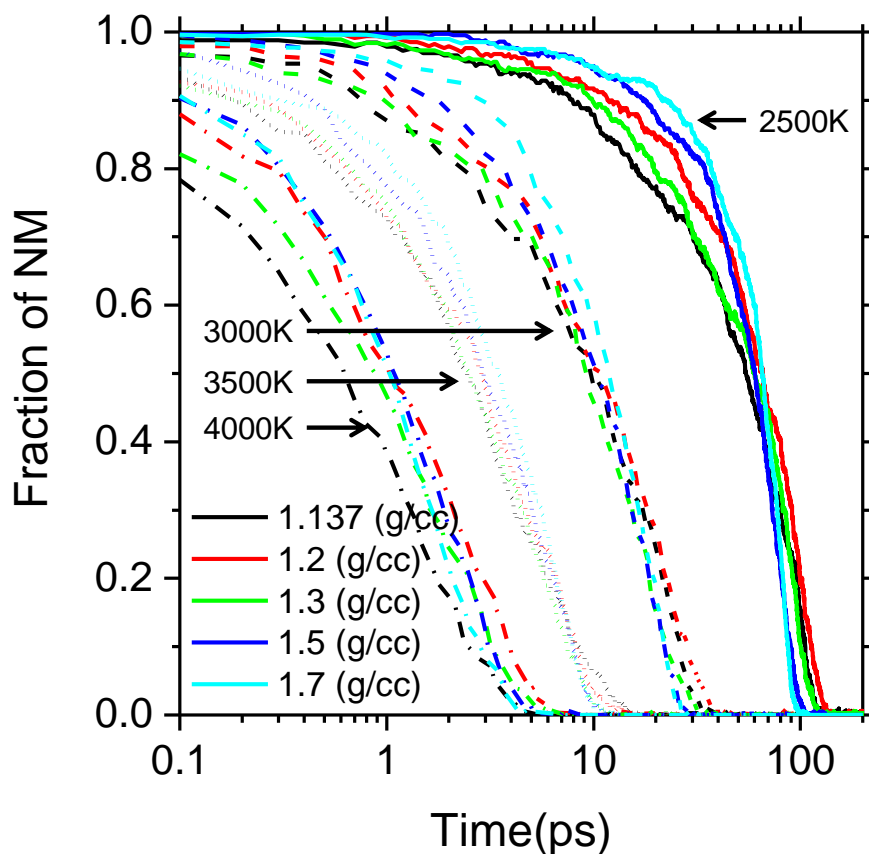
Figure 3.1.4 Molar fraction of NM by the decomposition during NERMD simulation vs. simulation time for 200 ps. Temperatures indicate initially given temperatures. Copyright © 2017, American Chemical Society.

Variations of kinetic and potential energies and temperature over time were also analyzed to observe detailed information on decomposition reaction. During NERMD simulation, the potential energy was converted into the kinetic energy (see **Figure 3.1.5** for the variation of potential energy), which was directly related to the temperature elevation (**Figure 3.1.6**). We observed three distinctive signatures in the temperature profile, *i.e.* slight drop at initial, gradual increase at middle, and sudden

increase at final stage. The temperature changes were directly related to the reactions inside and outside the nanocontainer. For all systems, temperatures were slightly dropped down at the beginning of the reaction. This phenomenon was driven by the following three endothermic reactions, which were suggested by previous experimental work[2] and also confirmed from the observation of the dominant species in the simulation results (**Figure 3.1.7 – 3.1.11**).

$$CH_3NO_2 \rightarrow CH_3 + NO_2 \qquad (3.1.4)$$

$$CH_3NO_2 \rightarrow H_2C=O + HNO \qquad (3.1.5)$$

$$CH_3NO_2 \rightarrow CH_3NO + O \qquad (3.1.6)$$
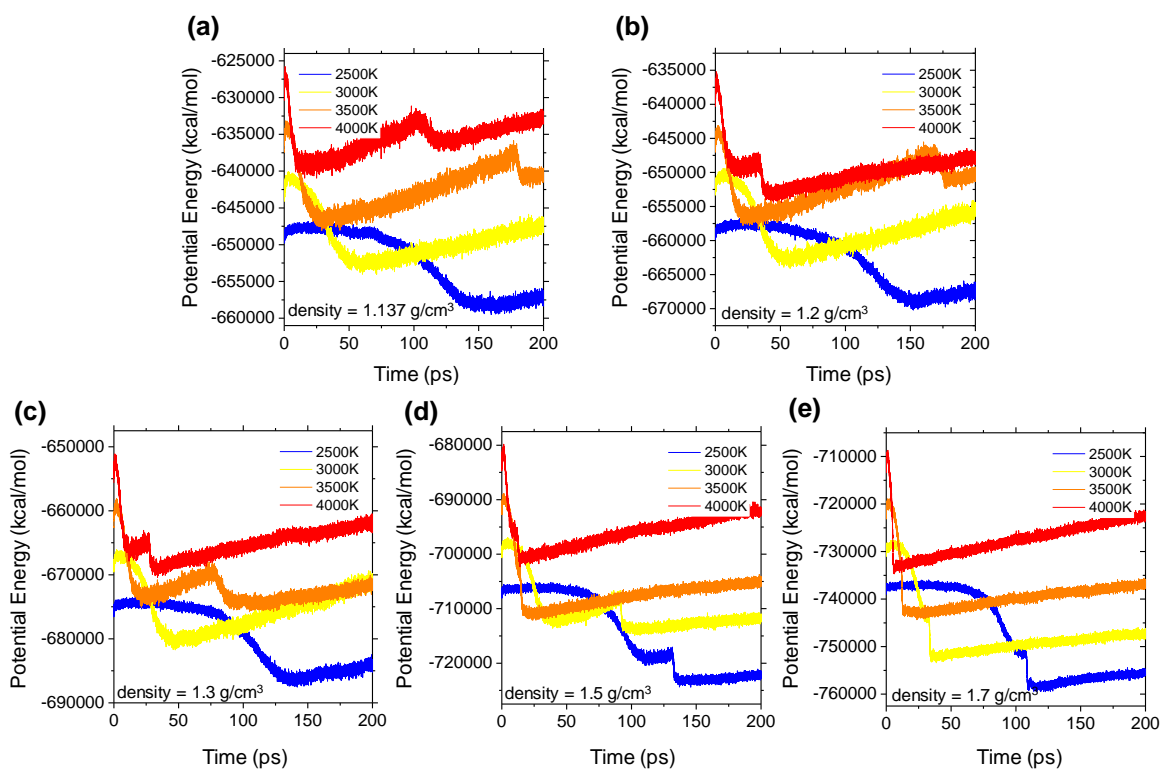
Figure 3.1.5 Potential energy profile of the system at density of (a) 1.137 g/cm^3, (b) 1.2 g/cm^3, (c) 1.3 g/cm^3, (d) 1.5 g/cm^3, and (e) 1.7 g/cm^3, respectively. Copyright © 2017, American Chemical Society.

43
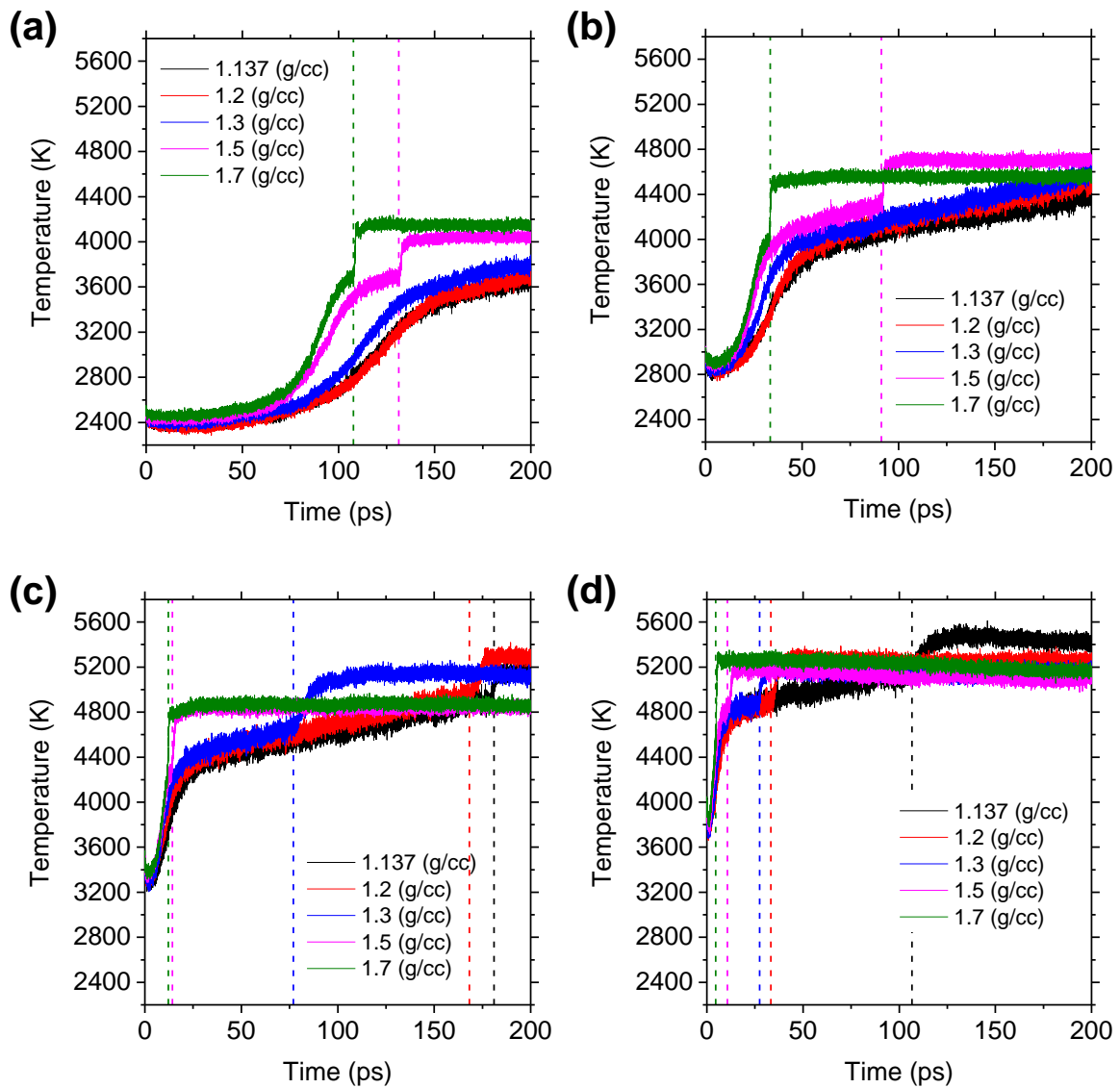
Figure 3.1.6 Temperature profiles at different densities vs. simulation time for 200 ps. Initial temperature is (a) 2500 K, (b) 3000 K, (c) 3500 K and (d) 4000 K. Vertical dashed-lines indicate the time of the burst of CNT. Copyright © 2017, American Chemical Society.
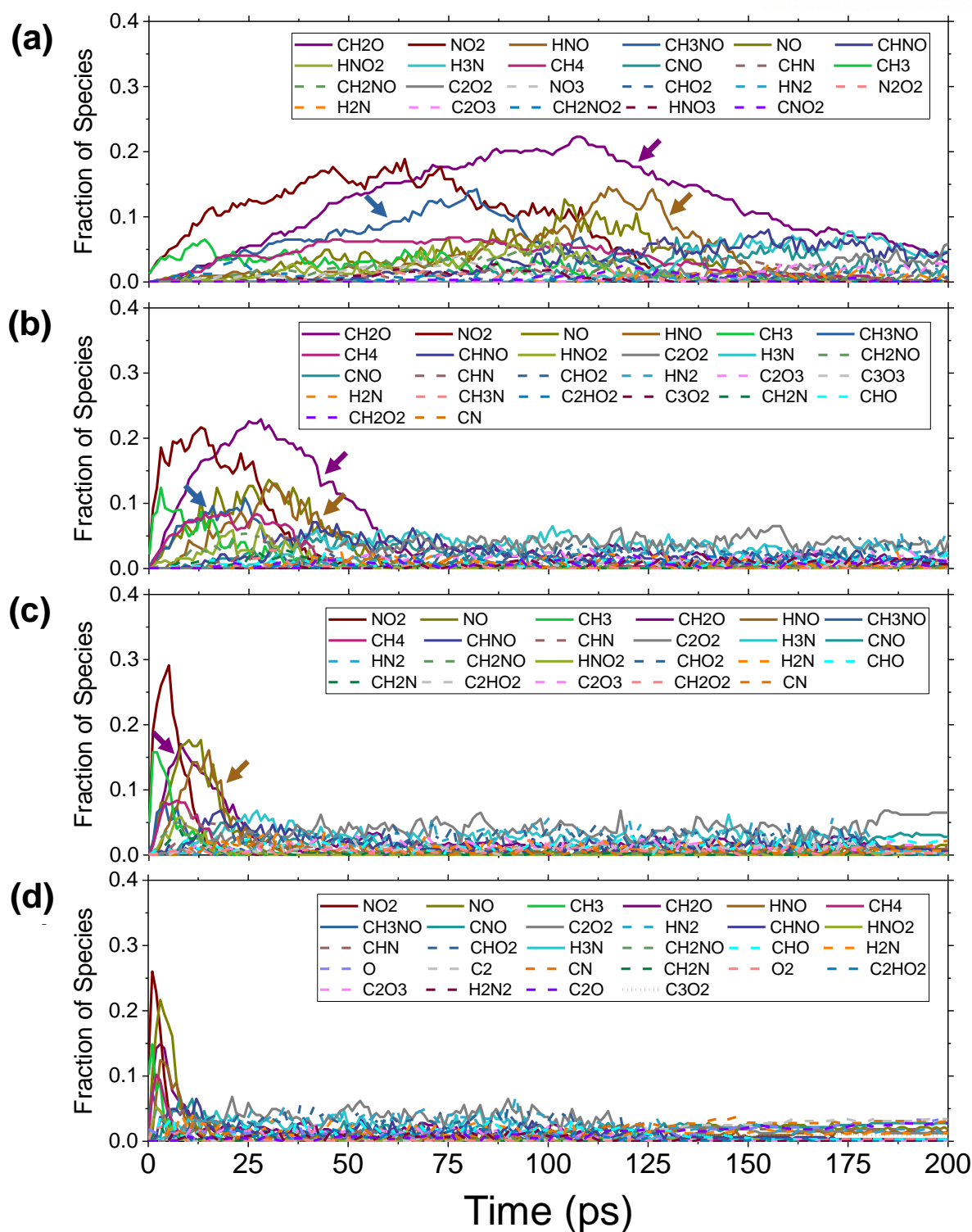
Figure 3.1.7 Reaction intermediates at density = 1.137 g/cm^3 with initial heating temperature of (a) 2500 K, (b) 3000 K, (c) 3500 K, and (d) 4000 K, respectively. Arrows in each figure indicate the relevant same color of lines for three main initial intermediates, *i.e.* CH$_2$O for purple, CH$_3$NO for deep blue, and HNO for light brown, respectively. Copyright © 2017, American Chemical Society.
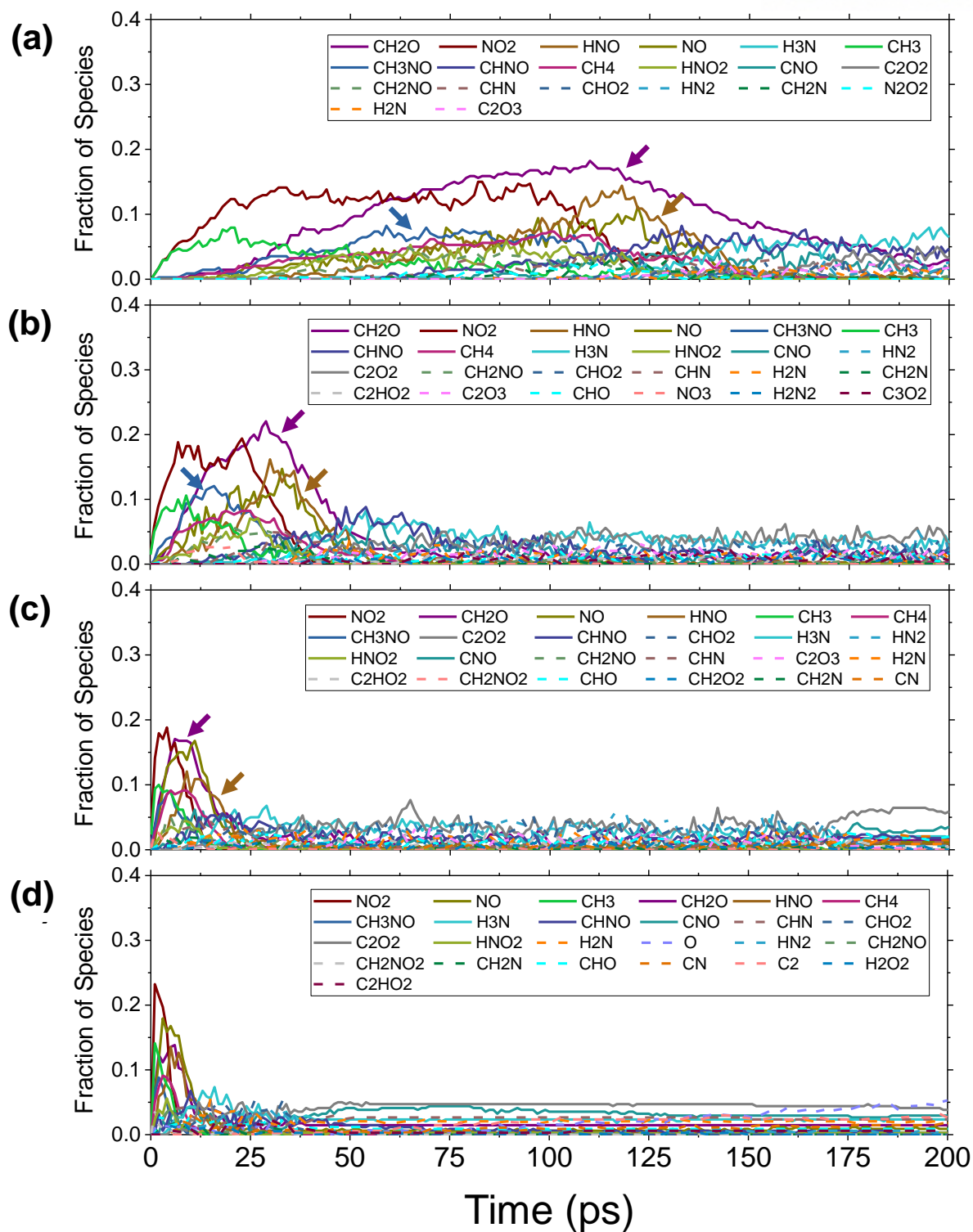
Figure 3.1.8 Reaction intermediates at density = 1.2 g/cm^3 with initial heating temperature of (a) 2500 K, (b) 3000 K, (c) 3500 K, and (d) 4000 K, respectively. Arrows in each figure indicate the relevant same color of lines for three main initial intermediates, *i.e.* CH$_2$O for purple, CH$_3$NO for deep blue, and HNO for light brown, respectively. Copyright © 2017, American Chemical Society.
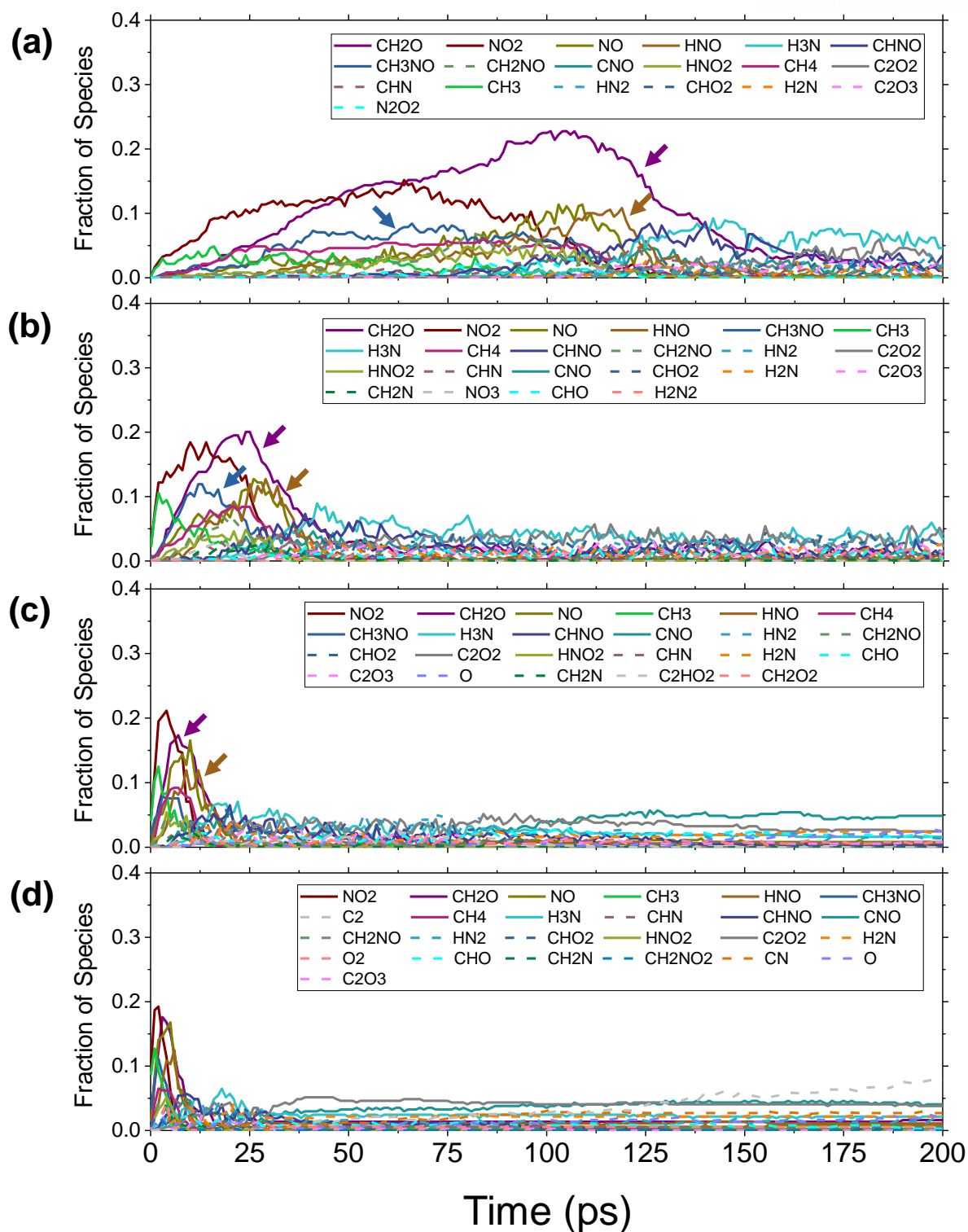
Figure 3.1.9 Reaction intermediates at density = 1.3 g/cm^3 with initial heating temperature of (a) 2500 K, (b) 3000 K, (c) 3500 K, and (d) 4000 K, respectively. Arrows in each figure indicate the relevant same color of lines for three main initial intermediates, *i.e.* CH$_2$O for purple, CH$_3$NO for deep blue, and HNO for light brown, respectively. Copyright © 2017, American Chemical Society.
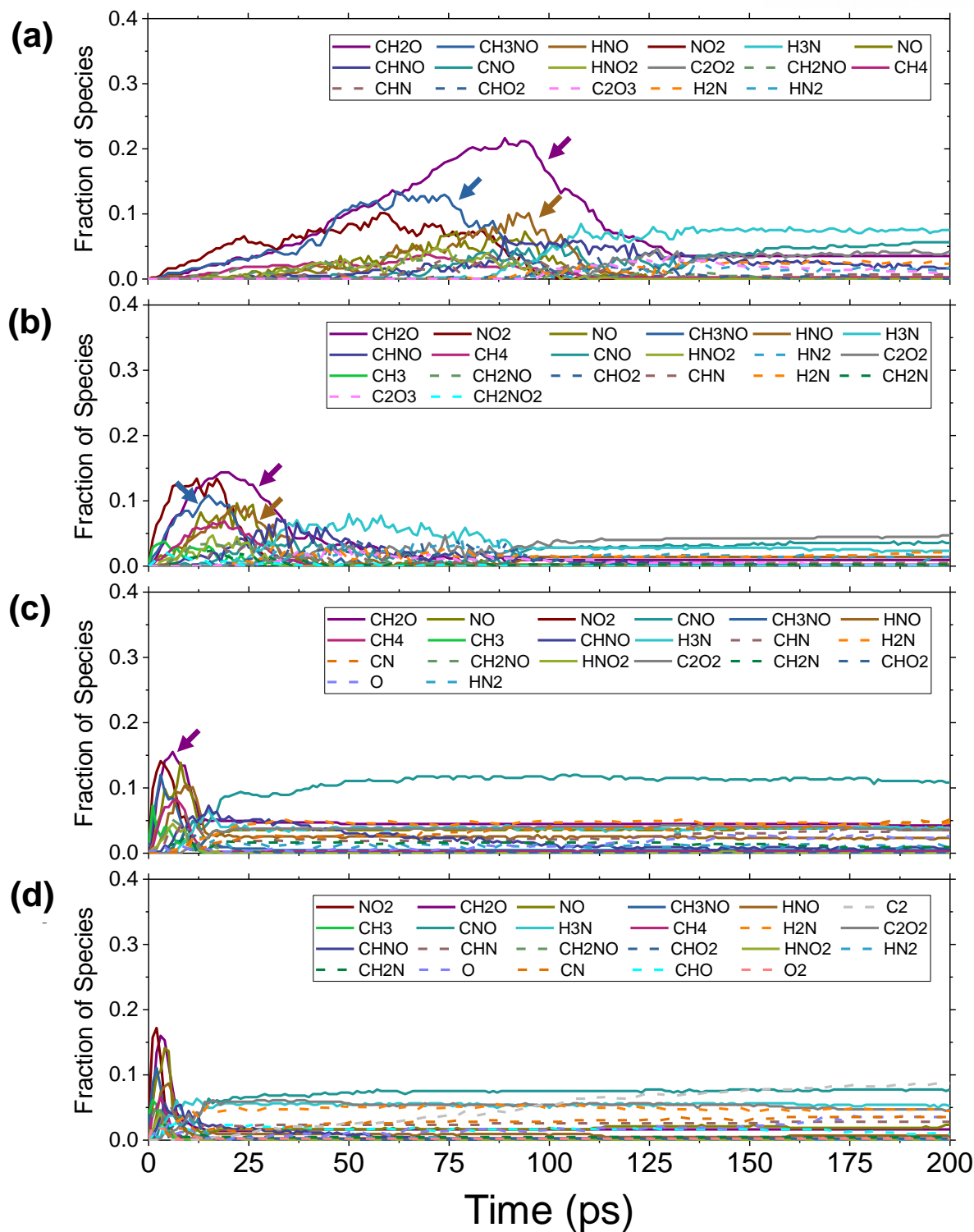
Figure 3.1.10 Reaction intermediates at density = 1.5 g/cm³ with initial heating temperature of (a) 2500 K, (b) 3000 K, (c) 3500 K, and (d) 4000 K, respectively. Arrows in each figure indicate the relevant same color of lines for three main initial intermediates, *i.e.* CH₂O for purple, CH₃NO for deep blue, and HNO for light brown, respectively. Copyright © 2017, American Chemical Society.

48
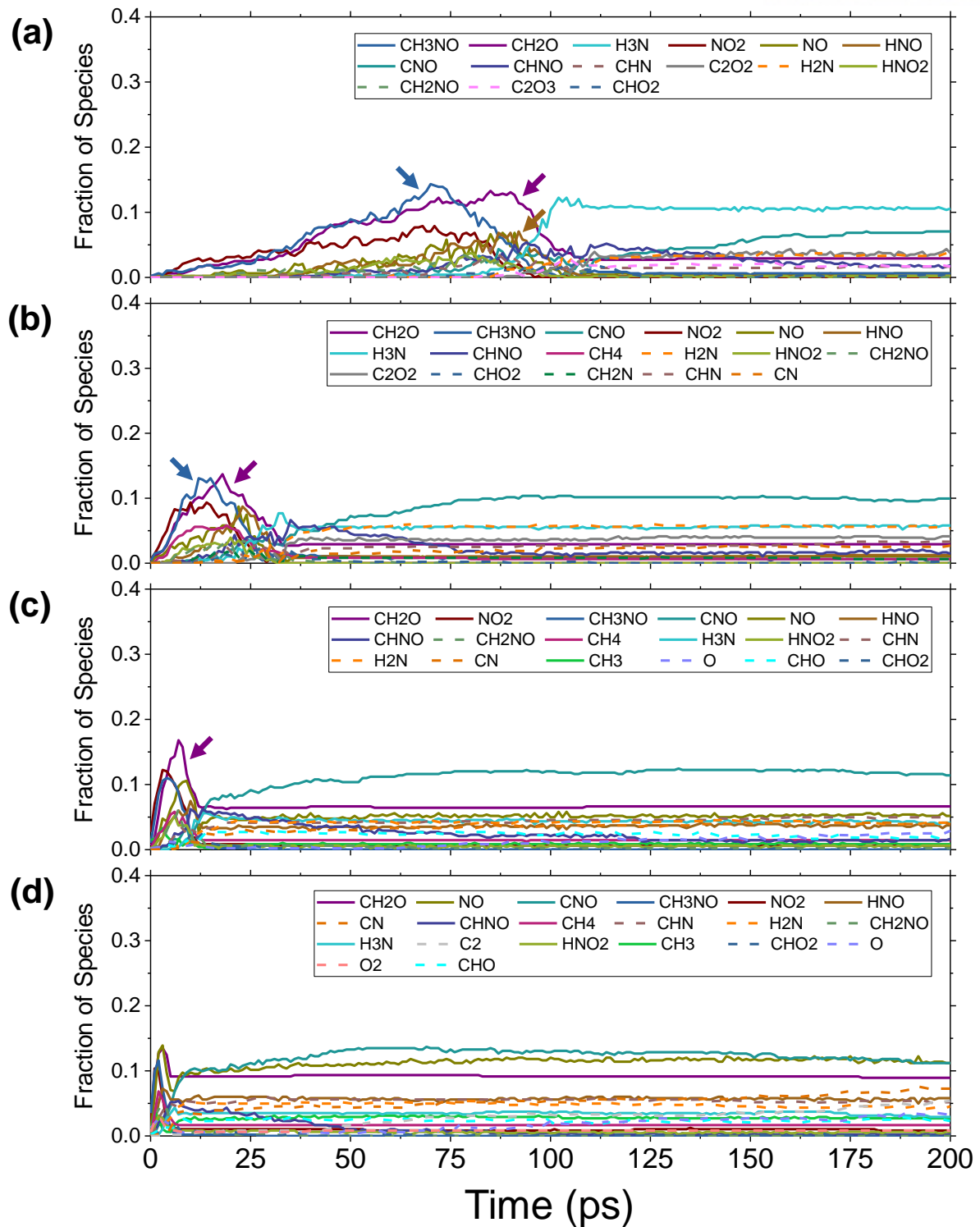
Figure 3.1.11 Reaction intermediates at density = 1.7 g/cm^3 with initial heating temperature of (a) 2500 K, (b) 3000 K, (c) 3500 K, and (d) 4000 K, respectively. Arrows in each figure indicate the relevant same color of lines for three main initial intermediates, *i.e.* CH$_2$O for purple, CH$_3$NO for deep blue, and HNO for light brown, respectively. Copyright © 2017, American Chemical Society.

49

In general, the breakage of C–N bond (equation (3.1.4)) dominantly occurred in all systems, but concerted molecular elimination (equation (3.1.5)) and oxygen atom elimination (equation (3.1.6)) took place more frequently as the density of NM inside the CNT increased.

The species in the process of the decomposition of NM were checked in order to see the effect by the confinement of CNT and temperature rise. We examined all species, which have been produced over 3% of the initial NM, from initial to certain period of simulation time (**Figure 3.1.7 – 3.1.16**). We could not observe significant change in the type of reaction intermediates by the confinement, but the amount and production time of products were reduced because of elevated temperature during NERMD simulation. CH_3 (green line) and NO_2 (brown line) were generated from the break of C-N bond in NM at the initial stage of the reaction (~10 ps). Those were converted into another species in further reaction. Interestingly, because of high molecular stability, the life time of NO_2 was relatively longer than that of CH_3. Thus, the amount of NO_2 was sustained up to 15 % at 100 ps of 2500 K.

As the temperature of each system was increased, the number of C–N bond-breaking was increased. As a result, the amounts of CH_3 and NO_2 at initial state were also increased. However, their maximum composition was not highly increased above 3500 K because of the rapid reaction inducing the occurrence of subsequent reaction. Oppositely, it was shown that the formations of CH_2O (purple line), CH_3NO (deep blue line), and HNO (light brown line) species were decreased. In terms of density, as the internal density of NM in the CNT increased, the compositions of products (*i.e.* CH_3NO, CH_2O) generated from bimolecular reactions were increased. In particular, the amount and formation rate of CH_2O and CH_3NO were greater than those of CH_3 at 1.5 and 1.7 g/cm^3 and 2500 K. Note that similar trend of the decomposition of liquid NM in bulk[6] was also observed in our simulation except the explosion phenomenon of the nanocontainer.

After the initial period, cascading release of the potential energy resulted in the significant rise of the reaction temperature, which induced the acceleration of the decomposition of NM. It was conjectured that there was a correlation between temperature and the amount of water, which was one of the most stable products formed from the decomposition of intermediates such as CH_3NO and CH_2O. Since the interval between temperature rise and the time of rapid formation of water coincided, the formation reaction of water was considered as a major contributing factor to the increase in temperature (**Figure 3.1.6** and **3.1.12–3.1.16**). As the NM density increased, the production rate of water was accelerated and the rate of temperature elevation also quickened.
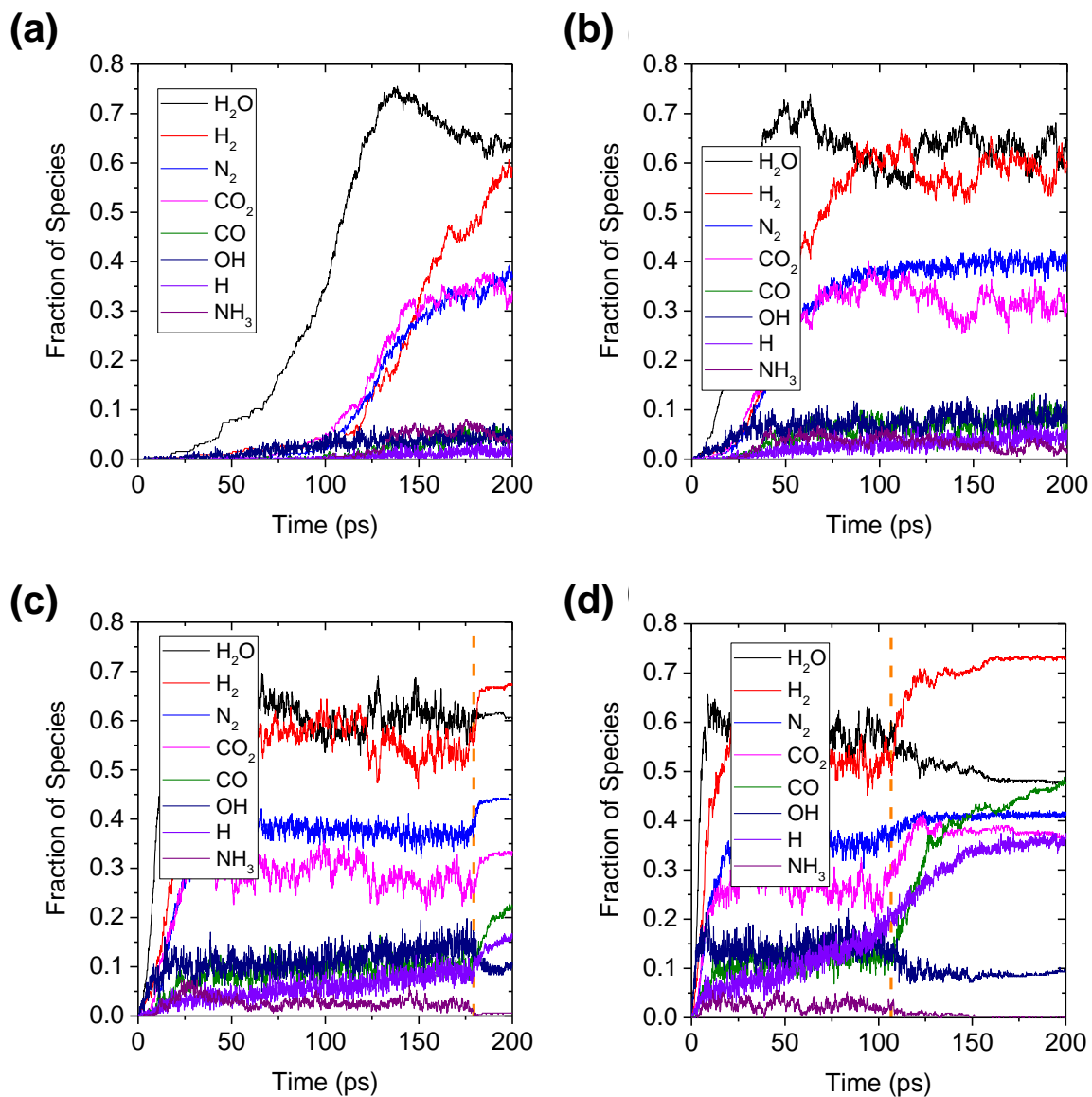
Figure 3.1.12 Stable products at density = 1.137 g/cm^3 at initial heating temperature of (a) 2500 K, (b) 3000 K, (c) 3500 K, and (d) 4000 K, respectively. Orange dashed-line represents the bursting time. Copyright © 2017, American Chemical Society.
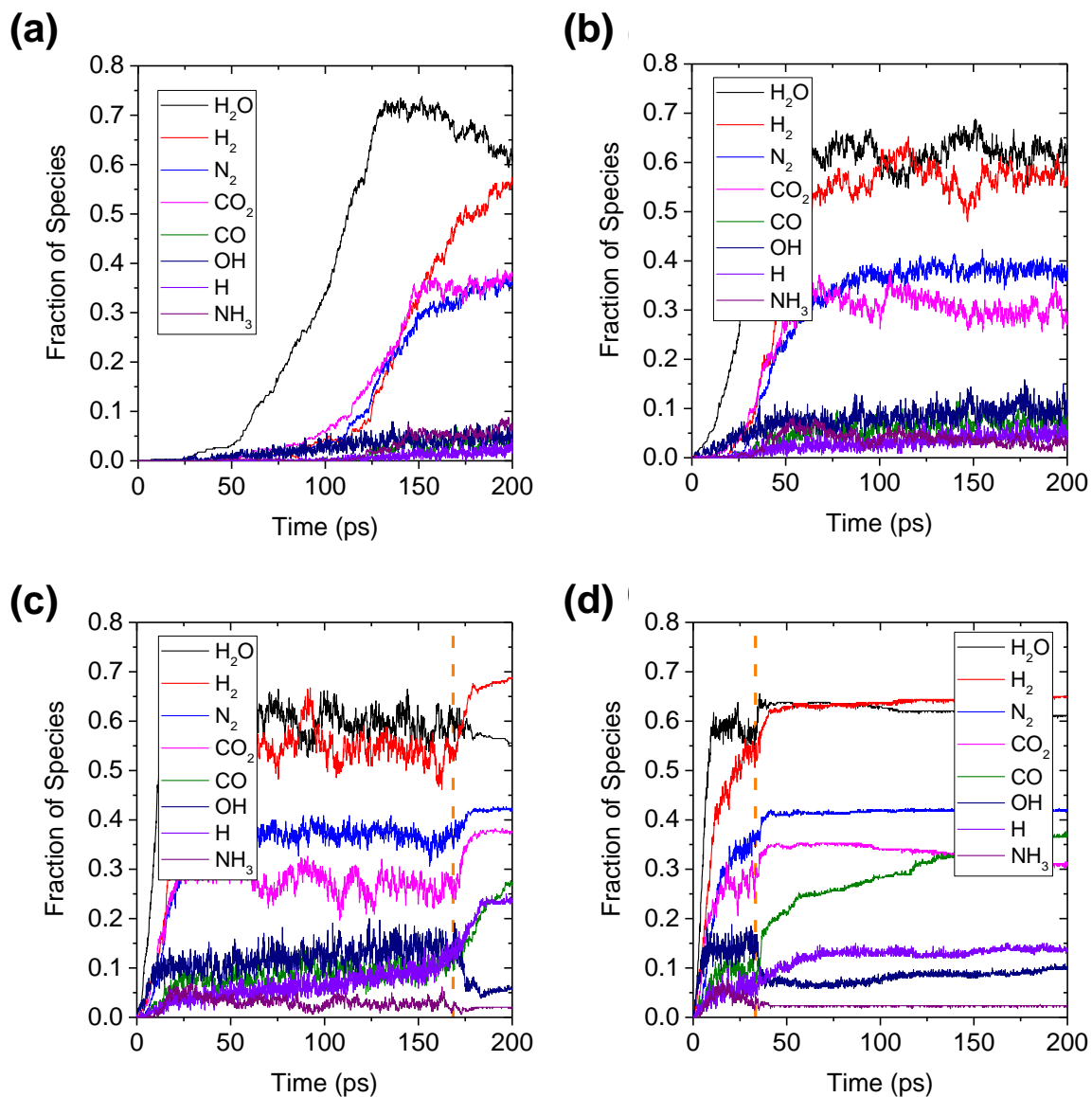
Figure 3.1.13 Stable products at density = 1.2 g/cm^3 at initial heating temperature of (a) 2500 K, (b) 3000 K, (c) 3500 K, and (d) 4000 K, respectively. Orange dashed-line represents the bursting time. Copyright © 2017, American Chemical Society.
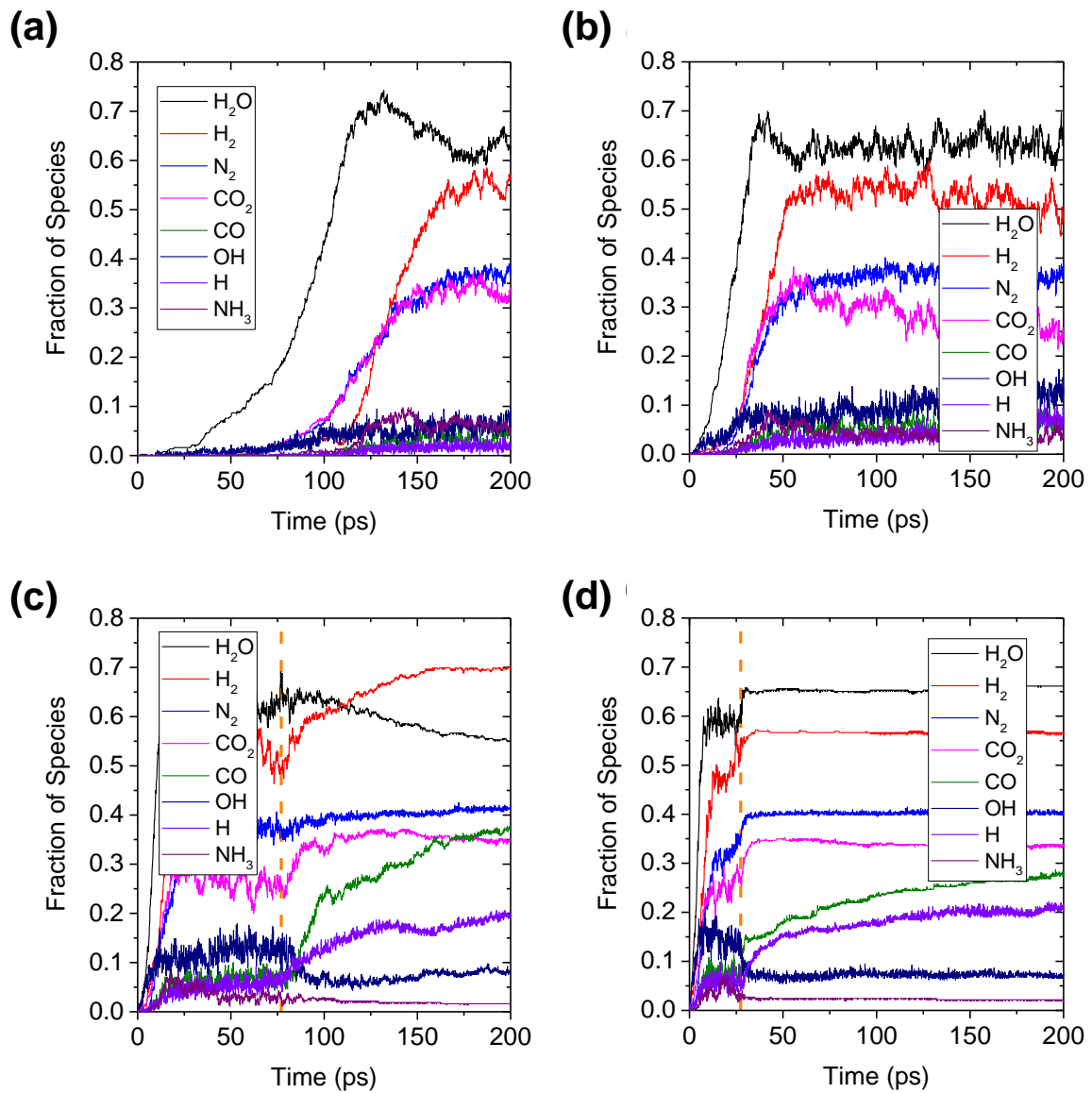
Figure 3.1.14 Stable products at density = 1.3 g/cm^3 at initial heating temperature of (a) 2500 K, (b) 3000 K, (c) 3500 K, and (d) 4000 K, respectively. Orange dashed-line represents the bursting time. Copyright © 2017, American Chemical Society.
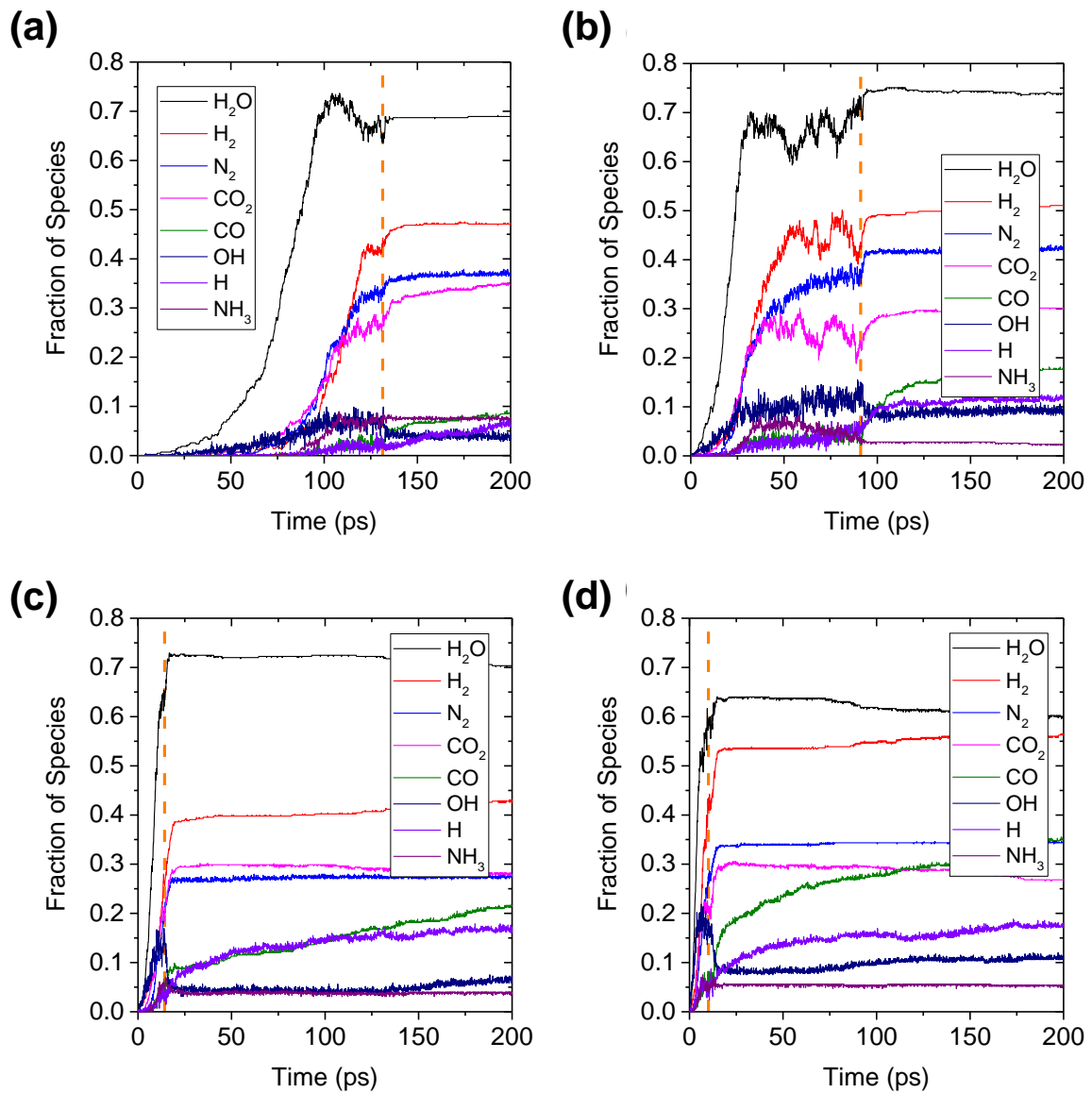
Figure 3.1.15 Stable products at density = 1.5 g/cm^3 at initial heating temperature of (a) 2500 K, (b) 3000 K, (c) 3500 K, and (d) 4000 K, respectively. Orange dashed-line represents the bursting time. Copyright © 2017, American Chemical Society.

(a)

(b)

(c)

(d)
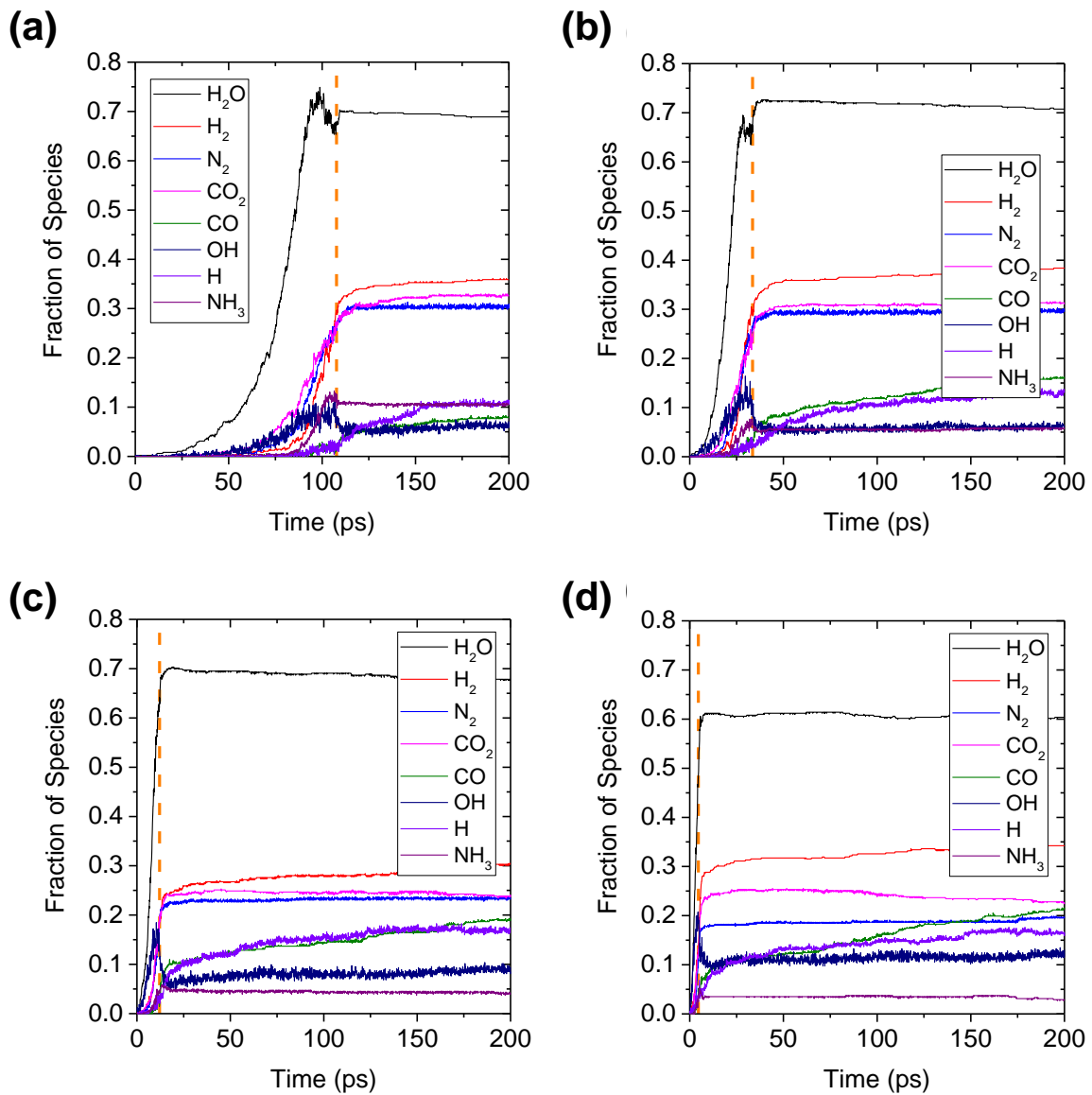
Figure 3.1.16 Stable products at density = 1.7 g/cm^3 at initial heating temperature of (a) 2500 K, (b) 3000 K, (c) 3500 K, and (d) 4000 K, respectively. Orange dashed-line represents the bursting time. Copyright © 2017, American Chemical Society.

At the final stage of the decomposition reaction, the burst of CNT (*i.e.* explosion), indicated by the sudden increase of temperature, was observed (see **Table 3.1.4** for the bursting time). Interestingly, the explosive power determined by the density affected the composition of final species, making a difference in the rate of temperature rise. The rate of temperature elevation at the density of NM above 1.5 g/cm^3 was greater than that at lower density. They showed explosive bursting, so there was no loss of internal species in high density systems. On the contrary, internal species appeared to be weakly released from torn CNT at low densities. At this point, the decomposition of H_2O into another species such as H_2 and CO occurred as indicated by the change in composition after the orange dashed-line shown in **Figure 3.1.12–3.1.14**. Therefore, the decomposition of water during the weak explosion at low density induced the slow increase of the temperature.

Table 3.1.4 Simulation time (ps) of the burst of CNT from each system. The time is the same as the dashed-lines shown in **Figure 3.1.6.** Copyright © 2017, American Chemical Society.

NM density	Initial Temperature (K)			
(g/cm^3)	2500	3000	3500	4000
1.137	-	-	179.4	106.7
1.200	-	-	168.5	33.3
1.300	-	-	77.0	27.4
1.500	131.4	91.1	14.2	10.1
1.700	107.7	33.5	12.1	4.6

We further identified the differences in the intermediates and final products due to the change in the reaction path originated from temperature and internal density. The final numbers of stable species from each system are shown in **Figure 3.1.17**. Overall reaction was terminated with relieving accumulated pressure when CNT burst, and final products were mainly composed of hydrogen and water molecules in most cases. Water was generated with the regular amount of 60−70 % from any density conditions also as confirmed from Rom et al.'s work.[6] Meanwhile, a large number of hydrogen molecules were originated from the excess number of intermolecular collisions between intermediates under confinement inside the nanocontainer. In addition, there was a characteristic change in the proportion of the radical products when nanobomb burst, which was similar to the sudden increase in the temperature profile (**Figure 3.1.6**). Unstable radical products such as H and CO, which were less produced from bulk decomposition reaction, were more created (see **Figure 3.1.12−3.1.16** for time-dependent amounts of radical species). Conversely, OH radicals and NH_3 molecules were slightly decreased right after the bursting. It was observed that OH and NH_3 combined with torn CNT containers

56

because they were easily functionalized on the walls of the container. Therefore, the portion of final products except water, OH and NH_3 were increased after the explosion.

From **Figure 3.1.17(c)** and **3.1.17(d),** it is noteworthy that the number of COs in the final product was significantly increased from our result compared to previous study,[6] where CO was produced less than 10% of initial NM. In order to clarify this phenomenon, we traced carbon atoms during simulation. **Figure 3.1.18** describes the number of carbon atoms in CNT, which was originally composed of 2336 C atoms, and CO molecules during NERMD simulation. Since the numbers of two species oppositely changed, it was considered that CO was created by the reaction between oxygen atom from NM and carbon atoms of torn CNT container. In addition, when NM molecules were decomposed, some intermediates were attached to the container wall as demonstrated in previous studies.[7,8] Thus, the total number of carbon atoms in CNT can be seen to be slightly increased, but its number was significantly reduced after the explosion of nanobomb due to the generation of CO.
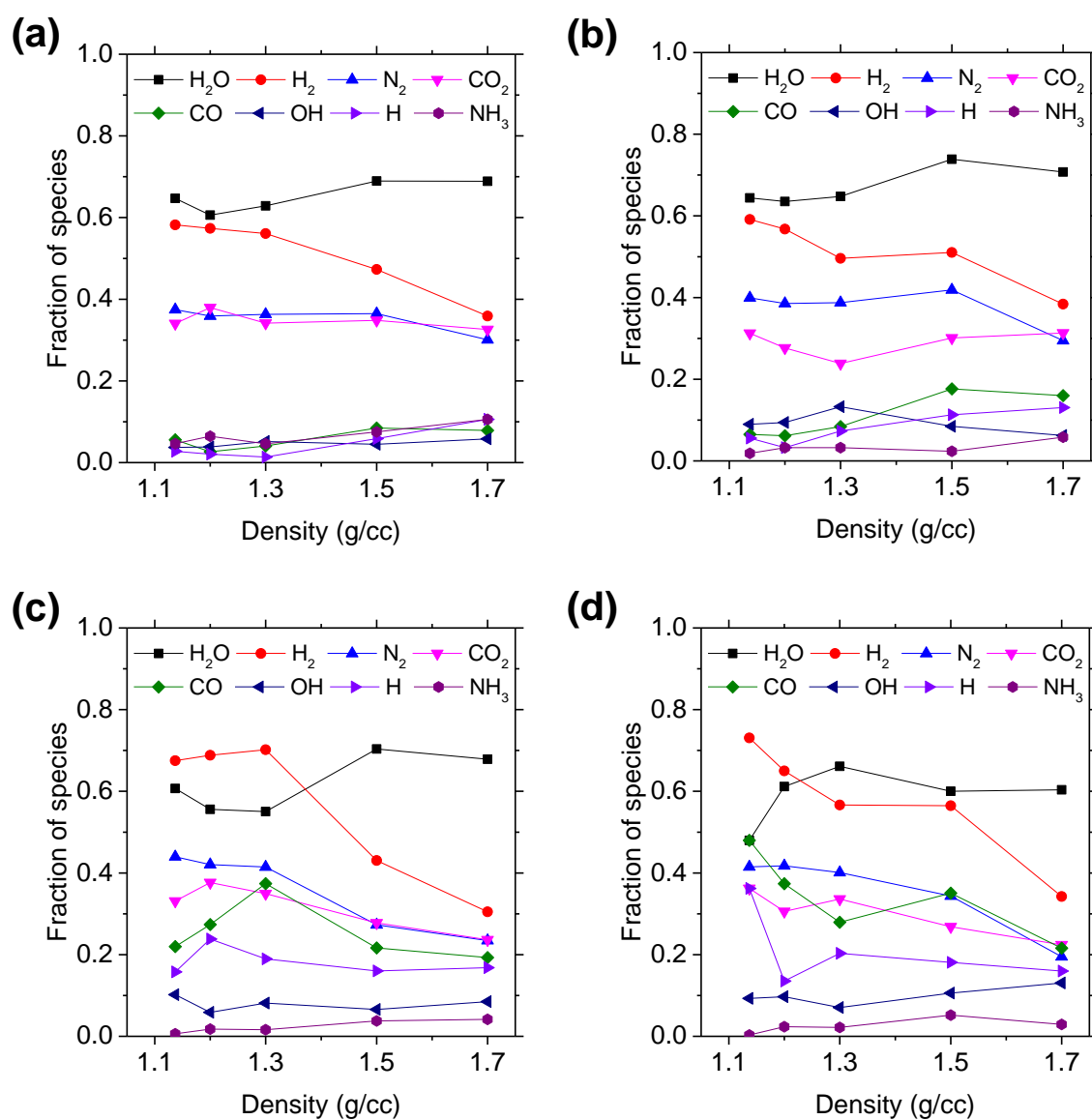
Figure 3.1.17 Final amount of stable species acquired at each density. Initial temperature is (a) 2500, (b) 3000, (c) 3500, and (d) 4000 K. Copyright © 2017, American Chemical Society.
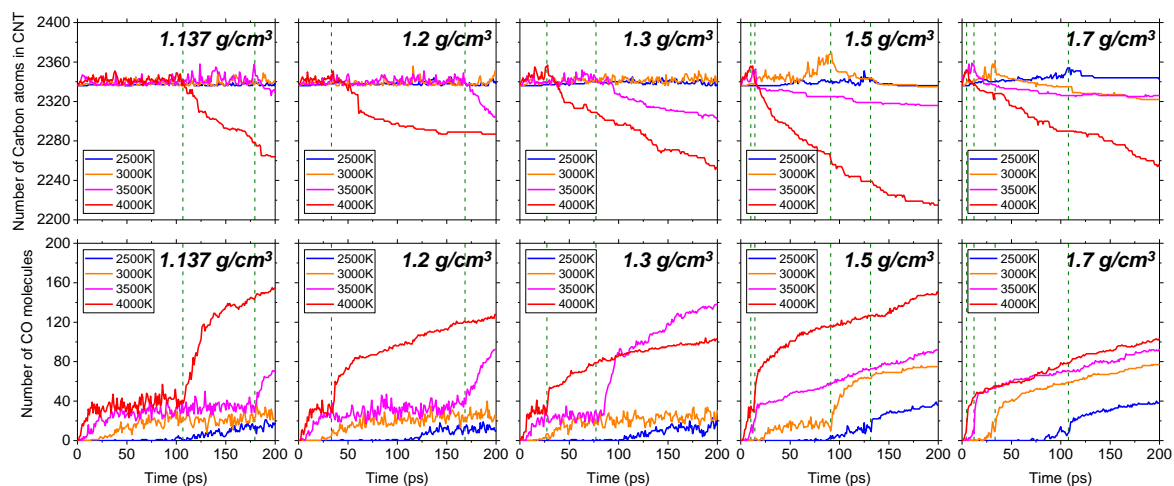
Figure 3.1.18 The number of carbon atoms in CNT (upper panel) and CO (lower panel) during simulation time for each system. Green dashed-line represents the bursting time. Copyright © 2017, American Chemical Society.

3.1.3.2 Bursting Mechanism of Nanobomb

From the results shown above, we realized that the bursting of CNT and decomposed product and intermediate were related. Thus, the bursting mechanisms of nanocontainer of all systems were compared to draw a general view. Even though each of the systems showed different processes of the tearing of the container depending on the temperature and density, there existed a common mechanism of bursting of the CNT. In addition, the effect of vacancy defects on the CNT wall was investigated in terms of explosiveness. We have modeled the vacancy defective system by randomly removing 0.5% of the carbon atoms from the container, which was packed with the density (1.137 g/cm^3) of NM, and compared the result of the system with pristine CNT container.

Figure 3.1.19 shows four representative models at the initiation stage of the CNT bursting. The bursting of CNT began with a transformation from two hexagonal 6 carbon atoms ring to one 5−7 carbon atoms ring, which is referred to as the Stone−Wales (SW) defect.[43] The deformation of carbon atoms ring occurred spontaneously because of the high temperature of the system[44] and/or the functionalization of the reaction intermediates. The starting point of the explosion reaction was found for one of four cases, which are summarized below,

59

(1) Transformation from 6 carbon atoms ring to 5−7 carbon atoms ring due to the functionalization of intermediate from NM at the cap junction of CNT

(2) Spontaneous conversion of the ring structure from two 6 carbon atoms rings to 5−7 carbon atoms rings

(3) Production of two 7 carbon atoms ring caused by the attachment of CH from intermediate of NM into the CNT wall

(4) Functionalization of the CNT wall by NH and OH groups
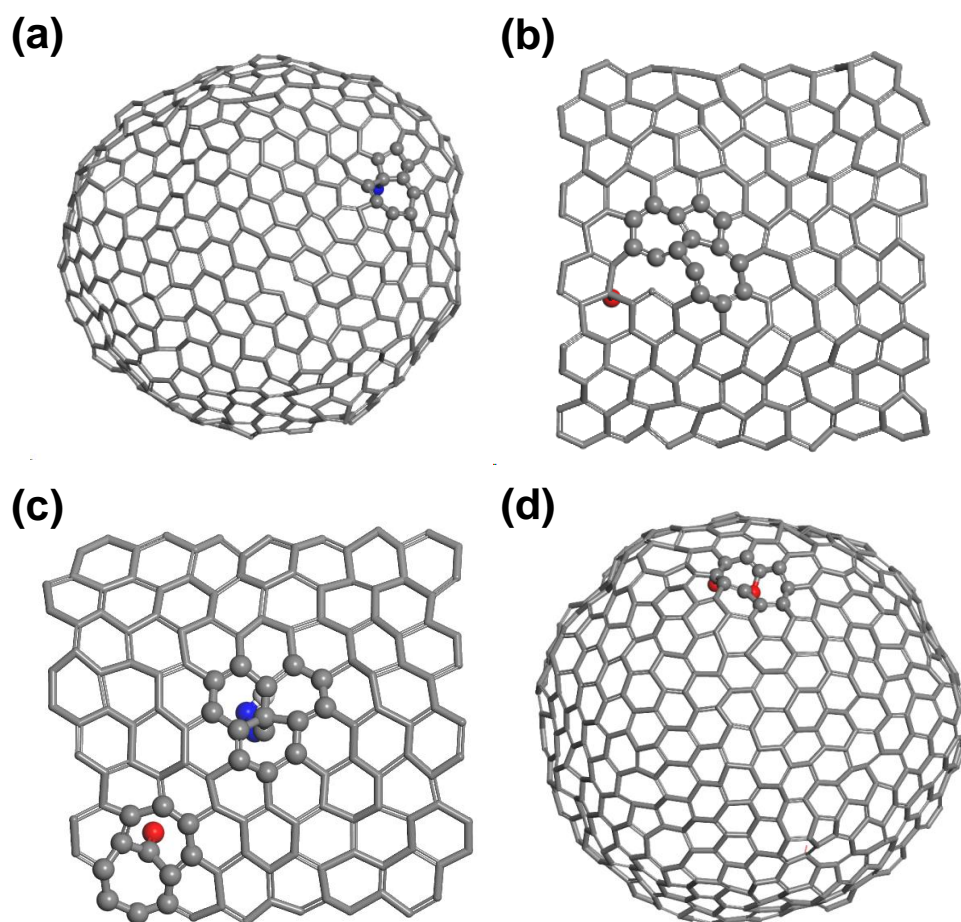
Figure 3.1.19 Initial 5−7 carbon atoms ring generation stage of the CNT bursting mechanism. Carbon, hydrogen, oxygen, and nitrogen atoms are colored gray, white, red, and blue, respectively. Copyright © 2017, American Chemical Society.

Through four paths as described above, the SW defect, which was energetically less stable, was commonly generated, and the bursting phenomenon of nanocontainer occurred. Defect generation and decomposition of these unstable rings simultaneously and randomly occurred at multiple sites of the container.

Overall mechanism of the bursting is illustrated by the representative system with respect to simulation time (**Figure 3.1.20**). The nanobomb systems at 53.2 ps (**Figure 3.1.20(a)**) and at 15.3 ps (**Figure 3.1.20(b)**) show unstable sites of the CNT. After the initiation state, the reaction intermediates, such as OH, H_2O, CO, and NH, functionalized $5-7$ carbon atoms rings and unstable rings of carbon atoms consisting of more than 8 atoms as shown at 53.6 ps (**Figure 3.1.20(a)**) and 20.1 ps (**Figure 3.1.20(b)**). These intermediates prevented the recombination of cleaved $C-C$ bonds at the rings. The broken $C-C$ bond contributed to cleave other adjacent bonds and triggered the formation of small nanopore on the CNT wall. After that, the sizes of these pores became larger with cleaving $C-C$ bond by additional functionalization of the unstable species. When the diameter of the nanopore was increased to 8 Å, light gases (*e.g.* H, H_2, N_2, H_2O etc.) were outpoured from the pores. In this step, the pore edge was saturated by the intermediates to form $-OH$, $-H$ and $=O$ groups.

To be more specific, the mechanism for the bursting of nanocontainer was separately investigated by the location of the generated nanopore, where the ejection of intermediates took place. For type 1 (**Figure 3.1.20(a)**), which showed a nanopore on the container cap, remaining gas molecules were ejected regardless of the species after the diameter of nanopore was expanded to 15 Å (77.7 ps). The pore was not grown further after the diameter reached to about 20 Å, where the ejection of interior materials occurred while the terminal of pore edge was detached in forms of C=C, CO, and H_2O (94.8 ps). When the outpouring was almost completed, $C-C$ bonds, which were cleaved by bursting, were restored despite of loss of 20 carbon atoms from the container. At 198.9 ps, the bursting was terminated and the pore size was gradually reduced. For type 2 (**Figure 3.1.20(b)**), which showed a nanopore on the side of the container, neighboring nanopores were merged and the container was sharply torn about a half in the zigzag direction (27.3 ps). Note that CNT is mechanically fragile in that direction.[45] In this type, the pore with much larger size (*i.e.* about 10 Å × 25 Å) permitted encapsulated materials to eject freely. Unlike type 1, we observed that the pore was enlarged continuously up to $50-60$ Å and the functional groups attached to the pore edges were detached as small molecular fragments like C=C, CO, H_2O and etc. (28.4 ps). At 150.1 ps, the recombination of the broken $C-C$ bonds was largely observed at the termination of the outpouring.
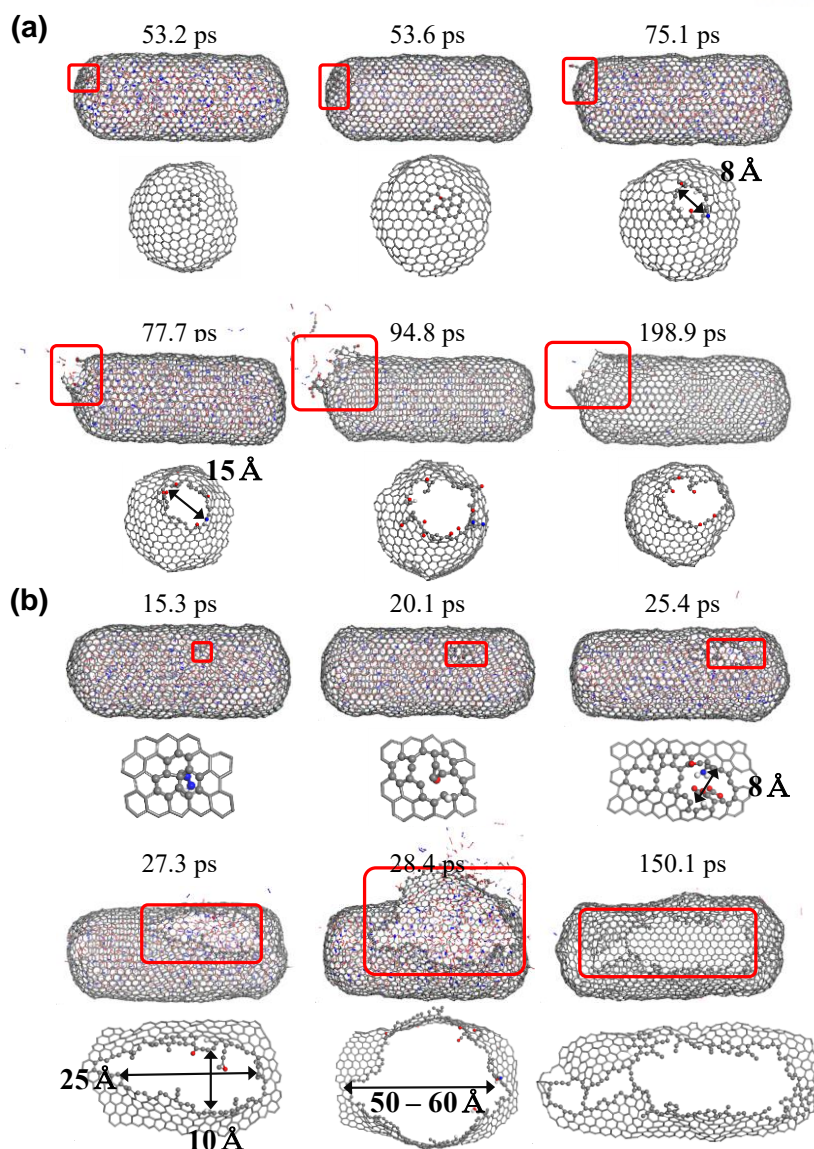
Figure 3.1.20 Mechanistic model of CNT bursting (a) near the CNT cap, and (b) at the CNT side. Representative pictures and times are taken from (a) 1.3 g/cm^3 at 3500 K and (b) 1.3 g/cm^3 at 4000 K. Color scheme is the same as in **Figure 3.1.19**. Red solid boxes represent the location of bursting. For a), the reaction mechanism was depicted with unstable sites in the cap at 53.2 ps, functionalization of reaction intermediate to unstable carbon atoms ring at 53.6 ps, generation of nanopore up to 8 Å by the outpouring of light gas molecules at 75.1 ps, growth of nanopore up to 15 Å by the ejecting products at 77.7 ps, detachment of the pore edge at 94.8 ps, and termination of bursting at 198.9 ps. For b), the reaction mechanism was depicted with formation of 5−7 carbon atoms ring at 15.3 ps, functionalization of reaction intermediate to 5−7 carbon atoms ring at 20.1 ps, generation of nanopore by the outpouring of light gas molecules at 25.4 ps, tearing of CNT about 10 Å × 25 Å in zigzag direction along with detachment of the pore edge at 27.3 ps, enlargement of pore width about 50 Å at 28.4 ps, and termination of bursting at 150.1 ps. Copyright © 2017, American Chemical Society.

Lastly, we considered the effect of vacancy defect on the explosion of nanocontainer. Vacancy defect, which can change mechanical properties of CNT, is inevitably generated during the synthesis of the CNT. From our simulation results, the bursting of defective CNT required low initial heating, for example, at 3000 K, whereas the pristine CNT required initial heating at 3500 K (**Figure 3.1.21**). Nevertheless, the bursting mechanism of defective CNT was similar to that of pristine CNT, where SW defect was generated. For direct comparison, simplified bursting mechanisms of pristine and defective CNTs were examined at 3500 K (**Figure 3.1.22**). It took less than 30 ps for the defective CNT to burst in comparison to 179.4 ps for the pristine CNT. Neighboring vacancy defects spontaneously induced 5－7 carbon atoms rings during the heat-up process as analogous to the case shown in **Figure 3.1.19(b)**, and nanopore was generated after the attachment of hydrogen or oxygen atoms. Thereafter, the ejection of intermediates was observed at 30.6 ps in defective CNT, which was a considerably earlier time compared to that of pristine CNT.
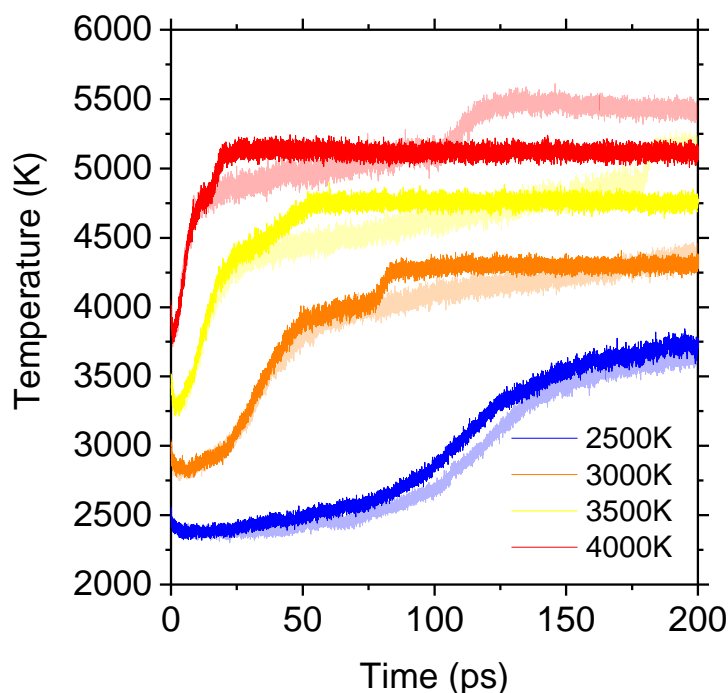
Figure 3.1.21 Temperature profile for reactive dynamics with and without point defect for density = 1.137 g/cm^3. Light color ones represent the results from non-defective system, and deep ones are the result from 0.5% point defect systems. Copyright © 2017, American Chemical Society.

(a)　　　　　　　　　　**(b)**

| Initial | 5 ps | Initial | 160 ps |

| 15.2 ps | 30.6 ps | 174 ps | 178 ps |
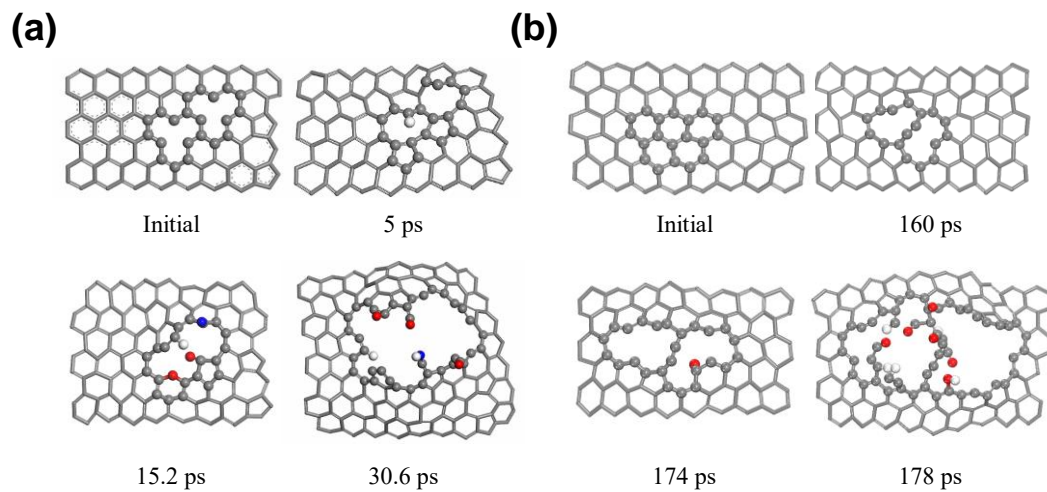
Figure 3.1.22 CNT bursting mechanism of (a) defective and (b) pristine container at 1.137 g/cm^3 3500 K. For (a) and (b), initial state before thermal decomposition process, consolidation of 5$-$7 carbon atoms ring defects (5 ps for (a) and 160 ps for (b)), nanopore formation step (15.2 ps for (a) and 174 ps for (b)), and nanopore extension and emission of the product (30.6 ps for (a) and 178 ps for (b)). Copyright © 2017, American Chemical Society.

3.1.4 Conclusion

In this study, the nanobomb architecture including NM and nanocontainer was theoretically modeled and investigated by NERMD simulations on the explosion dynamics. Along with the decomposition of NM, the explosiveness has been traced in terms of reaction temperature by varying initial density and initial heating temperature. In all cases, the reaction temperature was elevated more than 1000 K from the initial temperature, maximally from 2500 to 4200 K at 1.7 g/cm^3 of NM and from 4000 to 5600 K at 1.137 g/cm^3. During simulation for 200 ps, we observed three distinct signatures in temperature profile, which represented the endothermic reaction at initial stage, the formation of intermediates at middle stage, and the explosion of the nanobomb followed by isothermal process from middle to final stage. Notably, the CNT nanocontainer started forming defects of SW type (5－7 carbon atoms ring) or high order rings at the middle stage. Then, the defects worked as seeds to form nanoholes, where the generated intermediates functionalized unstable carbon atoms. Finally, the nanocontainer burst when nanohole was larger than about 8 Å. As inspired by this phenomenon on the pristine CNT nanocontainer, we further investigated defective CNT nanocontainer, which enabled to reduce the explosion time, and demonstrated high efficiency to explode the nanobomb. NM-encapsulated CNT nanocontainer modeled in this theoretical study is simply one of many similar types, which might open a new field for the application study of nanoscale explosion.

3.1.5 References

1. Nelson, T.; Bjorgaard, J.; Greenfield, M.; Bolme, C.; Brown, K.; McGrane, S.; Scharff, R. J.; Tretiak, S. Ultrafast Photodissociation Dynamics of Nitromethane. *J. Phys. Chem. A* **2016**, *120*, 519−526.

2. Hu, W.-F.; He, T.-J.; Chen, D.-M.; Liu, F.-C. Theoretical Study of the CH_3NO_2 Unimolecular Decomposition Potential Energy Surface. *J. Phys. Chem. A* **2002**, *106*, 7294−7303.

3. Manaa, M. R.; Reed, E. J.; Fried L. E.; Galli, G.; Gygi, F. Early Chemistry in Hot and Dense Nitromethane: Molecular Dynamics Simulations. *J. Chem. Phys* **2004**, *120*, 10146–10153.

4. Chang, J.; Lian, P.; Wei, D.-Q.; Chen, X.-R.; Zhang, Q.-M.; Gong, Z.-Z. Thermal Decomposition of the Solid Phase of Nitromethane: *Ab Initio* Molecular Dynamics Simulations. *Phys. Rev. Lett.* **2010**, *105*, 188302.

5. Han, S.-p.; van Duin, A. C. T.; Goddard, W. A. III.; Strachan, A. Thermal Decomposition of Condensed-Phase Nitromethane from Molecular Dynamics from ReaxFF Reactive Dynamics. *J. Phys. Chem. B* **2011**, *115*, 6534–6540.

6. Rom, N.; Zybin, S. V.; van Duin, A. C. T.; Goddard, W. A. III.; Zeiri, Y.; Katz, G.; Kosloff, R. Density-Dependent Liquid Nitromethane Decomposition: Molecular Dynamics Simulations Based on ReaxFF. *J. Phys. Chem. A* **2011**, *115*, 10181–10202.

7. Liu, L.-M.; Car, R.; Selloni, A.; Dabbs, D. M.; Aksay, I. A.; Yetter, R. A. Enhanced Thermal Decomposition of Nitromethane on Functionalized Graphene Sheets: *Ab Initio* Molecular Dynamics Simulations. *J. Am. Chem. Soc.* **2012**, *134*, 19011−19016.

8. Zhang, C.; Wen, Y.; Xue, X. Self-Enhanced Catalytic Activities of Functionalized Graphene Sheets in the Combustion of Nitromethane: Molecular Dynamic Simulations by Molecular Reactive Force Field. *ACS Appl. Mater. Interfaces* **2014**, *6*, 12235−12244.

9. Agrawal, P. M.; Rice, B. M.; Thompson, D. L. Molecular Dynamics Study of the Melting of Nitromethane. *J. Chem. Phys.* **2003**, *119*, 9617−9627.

10. Zheng, L.; Luo, S.-N.; Thompson, D. L. Molecular Dynamics Simulations of Melting and the Glass Transition of Nitromethane. *J. Chem. Phys.* **2006**, *124*, 154504.

11. Siavosh-Haghighi, A.; Sewell, T. D.; Thompson, D. L. Molecular Dynamics Study of the Crystallization of Nitromethane from the Melt. *J. Chem. Phys.* **2010**, *133*, 194501.

12. Smeu, M.; Zahid, F.; Ji, W.; Guo, H.; Jaidann, M.; Abou-Rachid, H. Energetic Molecules Encapsulated inside Carbon Nanotubes and between Graphene Layers: DFT Calculations. *J. Phys. Chem. C* **2011**, *115*, 10985–10989.

13. Liu, Y.; Lai, W.; Yu, T.; Ge, Z.; Kang, Y. Structural Characteristics of Liquid Nitromethane at the Nanoscale Confinement in Carbon Nanotubes. *J. Mol. Model.* **2014**, *20*, 2459.

14. Liu, Y.; Lai, W.; Yu, T.; Kang, Y.; Ge, Z. Interactions of Carbon Nanotubes with the Nitromethane−Water Mixture Governing Selective Adsorption of Energetic Molecules from Aqueous Solution. *Phys. Chem. Chem. Phys.* **2015**, *17*, 6995–7001.

15. Wang, L.; Xu, J.; Yi, C.; Zou, H.; Xu, W. Theoretical Study on the Thermal Decomposition of Nitromethane Encapsulated inside Single-Walled Carbon Nanotubes. *J. Mol. Struct.: THEOCHEM* **2010**, *940*, 76–81.

16. Wang, L.; Yi, C.; Zou, H.; Xu, J.; Xu, W. Rearrangement and Thermal Decomposition of Nitromethane Confined inside an Armchair (5,5) Single-Walled Carbon Nanotube. *Chem. Phys.* **2010**, *367*, 120–126.

17. Bae, S. W.; Cho, S. G. Molecular Dynamics Study of the Behavior of Nitromethanes Enclosed Inside Carbon Nanotube Containers. *J. Mol. Model.* **2016**, *22*, 147.

18. Tasis, D.; Tagmatarchis, N.; Bianco, A.; Prato, M. Chemistry of Carbon Nanotubes. *Chem. Rev.* **2006**, *106*, 1105−1136.

19. Chen, N.; Xu, Q.; Ye, X. Single-Walled Carbon Nanotubes as High Pressure Nanocontainer. *Int. J. Mod. Phys. B* **2014**, *28*, 1450074.

20. Hilder, T. A.; Hill, J. M. Modeling the Loading and Unloading of Drugs into Nanotubes. *Small* **2009**, *5*, 300−308.

21. van Duin, A. C. T.; Dasgupta, S.; Lorant, F.; Goddard, W. A. III. ReaxFF: A Reactive Force Field for Hydrocarbons. *J. Phys. Chem. A* **2001**, *105*, 9396−9409.

22. Rom, N.; Hirshberg, B.; Zeiri, Y.; Furman, D.; Zybin, S. V.; Goddard, W. A. III.; Kosloff, R. First-Principles-Based Reaction Kinetics for Decomposition of Hot, Dense Liquid TNT from ReaxFF Multiscale Reactive Dynamics Simulations. *J. Phys. Chem. C* **2013**, *117*, 21043−21054.

23. Guo, D.; An, Q.; Zybin, S. V.; Goddard, W. A. III; Huang, F.; Tang, B. The Co-Crystal of TNT/CL-20 Leads to Decreased Sensitivity toward Thermal Decomposition from First Principles Based Reactive Molecular Dynamics. *J. Mater. Chem. A* **2015**, *3*, 5409–5419.

24. Strachan, A.; van Duin, A. C. T.; Chakraborty, D.; Dasgupta, S.; Goddard, W. A. III. Shock Waves in High-Energy Materials: The Initial Chemical Events in Nitramine RDX. *Phys. Rev. Lett.* **2003**, *91*, 98301.

25. Xue, X.; Wen, Y.; Long, X.; Li, J.; Zhang, C. Influence of Dislocations on the Shock Sensitivity of RDX: Molecular Dynamics Simulations by Reactive Force Field. *J. Phys. Chem. C* **2015**, *119*, 13735−13742.

26. Chaban, V. V.; Fileti, E. E.; Prezhdo, O. V. Buckybomb: Reactive Molecular Dynamics Simulation. *J. Phys. Chem. Lett.* **2015**, *6*, 913−917.

27. Sun, H.; Ren, P.; Fried, J. R. The COMPASS Force Field: Parameterization and Validation for Phosphazenes. *Comput. Theor. Polym. Sci.* **1998**, *8*, 229−246.

28. Sun, H. COMPASS: An *ab Initio* Force-Field Optimized for Condensed-Phase Applications Overview with Details on Alkane and Benzene Compounds. *J. Phys. Chem. B* **1998**, *102*, 7338−7364.

29. Materials Studio 2016; BIOVIA Inc., San Diego, CA, 2016. http://www.materials-studio.com/ (accessed March 7, 2017).

30. Plimpton, S. Fast Parallel Algorithms for Short-Range Molecular Dynamics. *J. Comput. Phys.* **1995**, *117*, 1−19.

31. Aktulga, H. M.; Fogarty, J. C.; Pandit, S. A.; Grama, A. Y. Parallel Reactive Molecular Dynamics: Numerical Methods and Algorithmic Techniques. *Parallel Comput.* **2012**, *38*, 245−259.

32. Perdew, J. P.; Burke, K.; Ernzerhof, M. Generalized Gradient Approximation Made Simple. *Phys. Rev. Lett.* **1996**, *77*, 3865−3868.

33. Melle-Franco, M.; Brinkmann, G.; Zerbetto, F. Modeling Nanotube Caps: The Relationship Between Fullerenes and Caps. *J. Phys. Chem. A* **2015**, *119*, 12839−12844.

34. Reich, S.; Li, L.; Robertson, J. Structure and Formation Energy of Carbon Nanotube Caps. *Phys. Rev. B* **2005**, *72*, 165423.

35. Brinkmann, G.; Fowler, P. W.; Manolopoulos, D. E.; Palser, A. H. R. A Census of Nanotube Caps. *Chem. Phys. Lett.* **1999**, *315*, 335−347.

36. Lair, S. L.; Herndon, W. C.; Murr, L. E.; Quinones, S. A. End Cap Nucleation of Carbon Nanotubes. *Carbon* **2006**, *44*, 447−455.

37. Peszke, J.; Stobinski, L.; Tomasik, P.; Kurzydlowski, K. J. Designing Patterns of the Isomeric Carbon Nanotube Caps. *Phys. Status Solidi A* **2011**, *208*, 1801−1803.

38. Robinson, M.; Suarez-Martinez, I.; Marks, N. A. Generalized Method for Constructing the Atomic Coordinates of Nanotube Caps. *Phys. Rev. B* **2013**, *87*, 155430.

39. Connolly, M. L. Solvent-Accessible Surfaces of Proteins and Nucleic Acids. *Science* **1983**, *221*, 709-713.

40. Mortier, W. J.; Ghosh, S. K.; Shankar, S. Electronegativity-Equalization Method for the Calculation of Atomic Charges in Molecules. *J. Am. Chem. Soc.* **1986**, *108*, 4315−4320.

41. Janssens, G. O. A.; Baekelandt, B. G.; Toufar, H.; Mortier, W. J.; Schoonheydt, R. A. Comparison of Cluster and Infinite Crystal Calculations on Zeolites with the Electronegativity Equalization Method (EEM). *J. Phys. Chem.* **1995**, *99*, 3251−3258.

42. Melius, C. F. Thermochemistry and Reaction Mechanisms of Nitromethane Ignition. *J. Phys. IV* **1995**, *5*, 535−552.

43. Stone, A. J.; Wales, D. J. Theoretical Studies of Icosahedral C_{60} and Some Related Species. *Chem. Phys. Lett.* **1986**, *128*, 501−503.

44. Zhou, L. G.; Shi, S.-Q. Formation Energy of Stone−Wales Defects in Carbon Nanotubes. *Appl. Phys. Lett.* **2003**, *83*, 1222−1224.

45.   Zhao, H.; Min, K.; Aluru, N. R. Size and Chirality Dependent Elastic Properties of Graphene Nanoribbons under Uniaxial Tension. *Nano Lett.* **2009**, *9*, 3012−3015.

3.2 Effect of Physicochemical Modification of Nanocontainer and External Shocks

This chapter includes the published contents:

3.2.1 Introduction

The development of high-energy materials (HEMs) and improving their performance are important undertakings for the development of defense technology. HEMs can be classified into propellants, explosives, and pyrotechnics depending on their application and performance. Explosives are characterized by a rapid reaction rate and ability to detonate.[1] Ideal explosives should have a high detonation velocity and pressure, while having low sensitivity to external stimuli such as heat, impact, and friction. In other words, it is necessary for explosive to improve sensitivity parameter to ensure safety, while still maintaining high explosion performance. In order to overcome this challenge, several groups, for example, Pagoria, Chavez, and Klapötke have been made efforts to synthesize new HEM molecules.[2-4] However, these groups have mainly focused on varying molecular structure itself. The explosion performance and sensitivity of explosives also can be significantly improved depending on how they are assembled on a nanoscale, *i.e.* nanoenergetic materials. Some groups have attempted to make nanoenergetic materials composed of a typical HEM having a controlled nanostructure. Bolton et al. succeeded to synthesize cocrystal consisting of CL-20:HMX, which kept low sensitivity and much improved detonation properties compared to pure *β*-HMX.[5] Liu et al. showed that the impact sensitivity of nanonitramine explosives could be reduced to less than half of that of conventional nitramine explosives.[6] In another case, an energetic metal−organic framework (MOF), containing an energetic material as a linker that provided a platform for making various nanostructures, was found to exhibit excellent structural stability and produce a large amount of heat energy.[7]

In a previous study, we applied *in silico* design to a nanobomb composed of NM and carbon nanotubes (CNTs).[8] A nanobomb is a new type of nanoenergetic material system, where a few tens to hundreds of NM molecules are confined in a nanometer-sized CNT. Nanobombs reportedly stabilized NM because of the stable thermal and mechanical properties of the CNTs that acted as nanocontainers. In the nanobomb, NM is isolated from the external environment under normal conditions, but when the

nanobomb is stimulated by thermal shock, the built-up pressure due to the CNT nanocontainer results in enhanced explosive power. Further, when NM or other HEMs were associated with CNTs or graphene sheets, unique structural arrangements and positive effects on the explosion reaction were achieved. Smeu et al. theoretically showed that several HEMs were stabilized by confinement between CNTs and a graphene bilayer.[9] Liu et al.[10] and Zhang et al.[11] theoretically predicted that the decomposition of NM molecules could be accelerated by functionalized graphene sheets. In addition, Um et al. experimentally synthesized a CNT-RDX (*i.e.* 1,3,5-trinitroperhydro-1,3,5-triazine) composite. They reported increased release of energy during explosion.[12] With this background, the aim of the present study is to investigate and to improve the explosion performance (temperature elevation, decomposition of NM, and bursting time) of a nanobomb by physicochemical modification of the CNT component based on chirality, doping with heteroatoms (*i.e.* nitrogen), and defects (*i.e.* monovacancy). The method of synthesis significantly influences the mechanical[13,14] and electrical properties,[15,16] as well as the reactivity,[17,18] of the CNTs.

To assess the effect of the properties of the nanocontainer on the performance and reactivity of the nanobomb, appropriate detonation methods for initiating the explosion reaction should also be taken into account. In many previous studies, the decomposition reaction was triggered by applying intensified physical or chemical shock to the HEM, such as thermal energy,[19–23] mechanical impact,[24] an electric spark,[25] electromagnetic induction,[26,27] or compressive shear.[28] Herein, the nanobombs with CNT nanocontainers having different mechanical and electrical properties are subjected to thermal shock-induced decomposition to evaluate the effect of the type of physicochemical modification on the decomposition rate and mechanism. To mimic the transfer of heat energy from the detonator during thermal shock-induced bursting, the decomposition paths of the nanobombs exposed to an external heat source are investigated through NERMD simulation and DFT calculations. In addition, the effects of an electric spark and electromagnetic induction on the decomposition reaction of the nanobomb exposed to an electric field were evaluated.

3.2.2 Simulation Details

For the simulations of interest, classical MD simulations were conducted with the COMPASS II force field[29] in the Materials Studio 2019 package.[30] NERMD simulations were conducted with the ReaxFF force field, which was previously used by Rom et al.,[21] in the LAMMPS[31] package. DFT calculations were performed with the DMol^3 program.[32,33]

3.2.2.1 Model Systems

Considering the high aspect ratio of CNTs synthesized *via* the conventional approach,[34−37] the CNT container was modeled as having infinite length in the z-direction by applying the periodic boundary condition. The physicochemical modifications considered in this work are changes in the chirality, nitrogen-doping, and introduction of monovacancy defects (**Figure 3.2.1**). Nitrogen-doping was expected to facilitate charge transfer between NM and the CNTs during decomposition of the NM molecules. To verify our expectation, preliminary DFT calculations were conducted with the carbon-cluster model (see **Chapter 3.2.2.4** for the detailed modeling procedure and **Figure 3.2.2** for the cluster models). It was found that N-doping could enhance the feasibility of electron transfer (see **Chapter 3.2.2.2** and **Figure 3.2.3**).

According to our previous study, the armchair (20,20) CNT configuration is large enough to undergo explosion due to the heat of reaction of NM confined in the inner volume.[8] To investigate the effect of chirality, two CNT containers (*i.e.* armchair (20,20) and zigzag (35,0)) with the same diameter were modeled. For the models with nitrogen-doping and monovacancy defects, considering the experimental concentrations of doping[38] and defect sites,[39] 1% and 2% nonvicinal carbon atoms in the CNTs were randomly substituted with nitrogen atoms or removed, respectively. In addition, to compare the effect of hydrogenation on the defective sites, hydrogenated monovacancy systems, where carbon atoms with dangling bonds were saturated with additional hydrogen atoms, were considered. To reduce the strain effect in the periodic direction, the modeled CNTs were relaxed by the following procedures. First, the structures were consecutively relaxed using the COMPASS II force field and ReaxFF force field used by Rom et al.[20] Subsequently, RMD simulations were carried out at 298 K for 50 ps with the $NP_{zz}T$ ensemble, in which the x- and y- axes of the system box were fixed to 500 Å for nonperiodicity of the CNT model, and only 1 atm pressure was applied to the z axis through a Berendsen[40] thermostat and barostat (see **Chapter 3.2.2.3** for a detailed description of the RMD simulation).
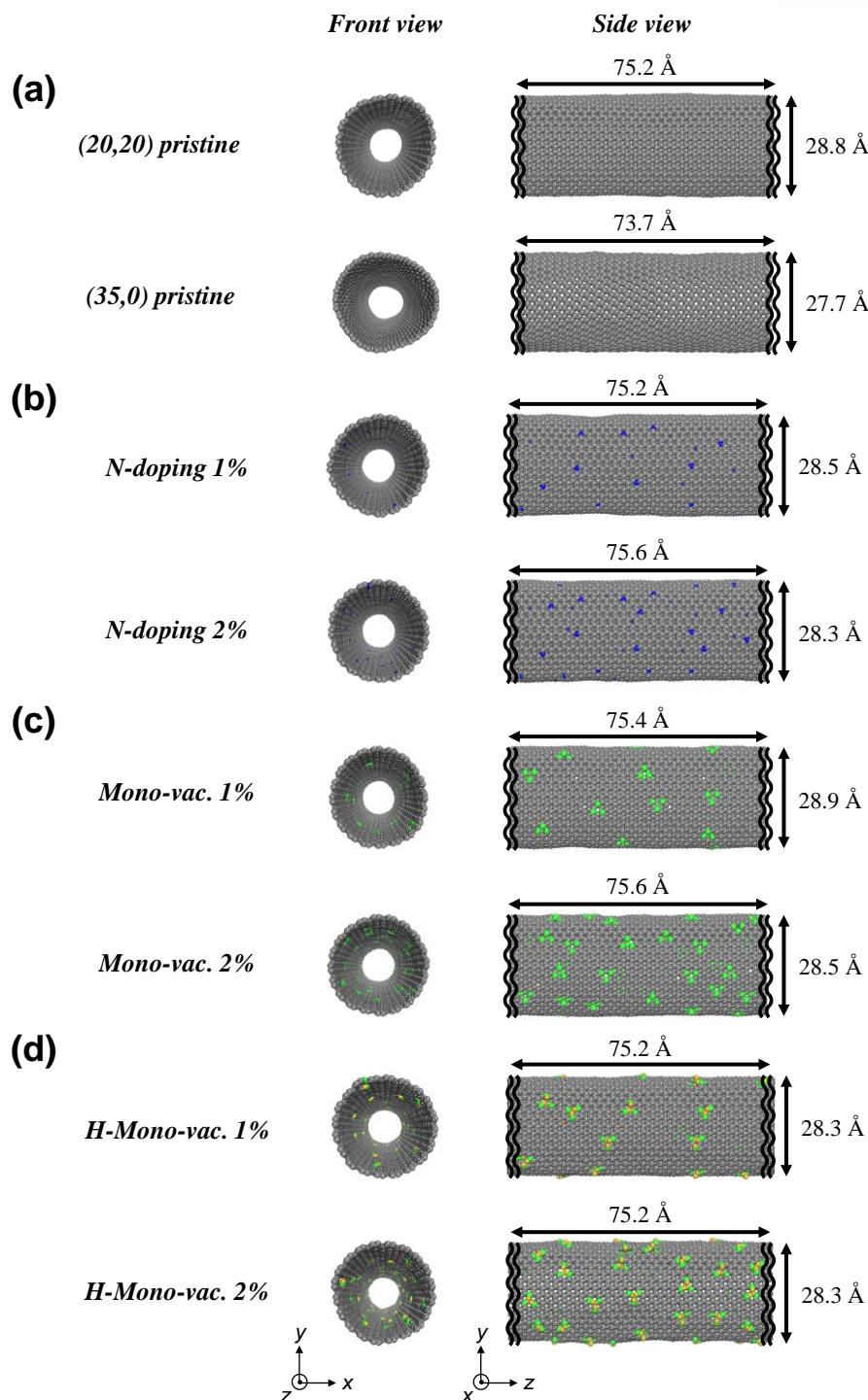
Figure 3.2.1 Relaxed CNT models with (a) chirality modification, (b) N-doping modification, (c) monovacancy modification, and (d) monovacancy modification with hydrogenation. For each CNT model, front and side views are represented, respectively. The values of diameter and periodic length of each CNT are written on the side view with arrows. The carbon, nitrogen, and hydrogen atoms are colored in gray, blue, and orange, respectively and carbon atoms constituting monovacancy defect are colored in green. Copyright © 2020, American Chemical Society.
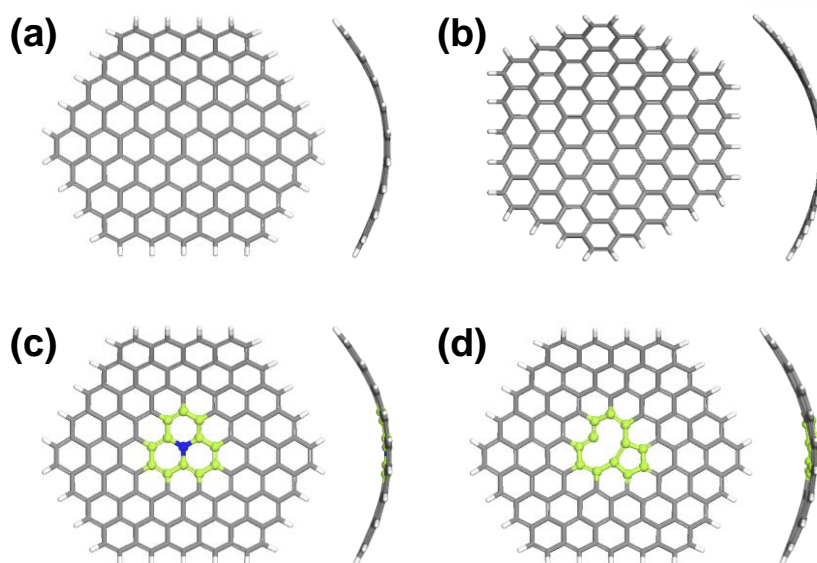
Figure 3.2.2 Carbon cluster models for (a) (20,20) pristine, (b) (35,0) pristine, (c) N-doped, and (d) monovacancy CNTs. For the clear view, carbon atoms around the doped N (blue ball) or vacant site are shown by green ball-and-sticks. Except these atoms, carbon and hydrogen atoms are colored in gray and white sticks, respectively. Copyright © 2020, American Chemical Society.

The nanobomb was constructed by packing NM inside the CNT obtained through the relaxation process. NM molecules were randomly packed into the void space determined by Connolly surface calculation according to the vdW radius of the carbon or nitrogen atoms. Note that a probe atom with a diameter of 1.0 Å was used to produce the Connolly surface, which was rolled on the van der Waals surface of the CNT.[41] The density of NM confined in the CNT of each model system was set to 1.3 g cm^{-3}, which is slightly larger than the density of liquid NM under ambient conditions (*i.e.* 1.1 g cm^{-3}), because the density of the confined fluid increases to some extent. **Table 3.2.1** shows the modeling information for each system. The numbers of NMs encapsulated in the CNTs with N-doping, monovacancy defects, and hydrogenated monovacancy defects were set to the same value of NMs in the pristine (20,20) CNT ($N = 453$) ignoring the marginal differences caused by the N-dopant atoms and vacant sites.

After the nanobomb systems were modelled, thermal annealing simulation was conducted in the temperature range of 300−500 K for 100 ps with classical MD to relax the systems. Finally, classical MD simulation with the *NVT* (*i.e.* isothermal) ensemble was performed for 100 ps at 298 K to complete the relaxation of each system. **Figure 3.2.4** shows the schematics of the relaxed nanobomb systems with the physicochemically modified CNTs.

Table 3.2.1 Modeling information of nanobomb systems depending on physicochemical modifications of CNT. Copyright © 2020, American Chemical Society.

Type of structural modification		Inner volume of CNT (Å^3)	no. of atoms in CNT	no. of NM
Chiral index	(20,20)	35337.0	2400	453
	(35,0)	35387.8	2380	454
Nitrogen-doping	1.0%		2376	
	2.0%	35337.0	2352	453
Monovacancy defect	1.0%		2376	
	2.0%		2352	
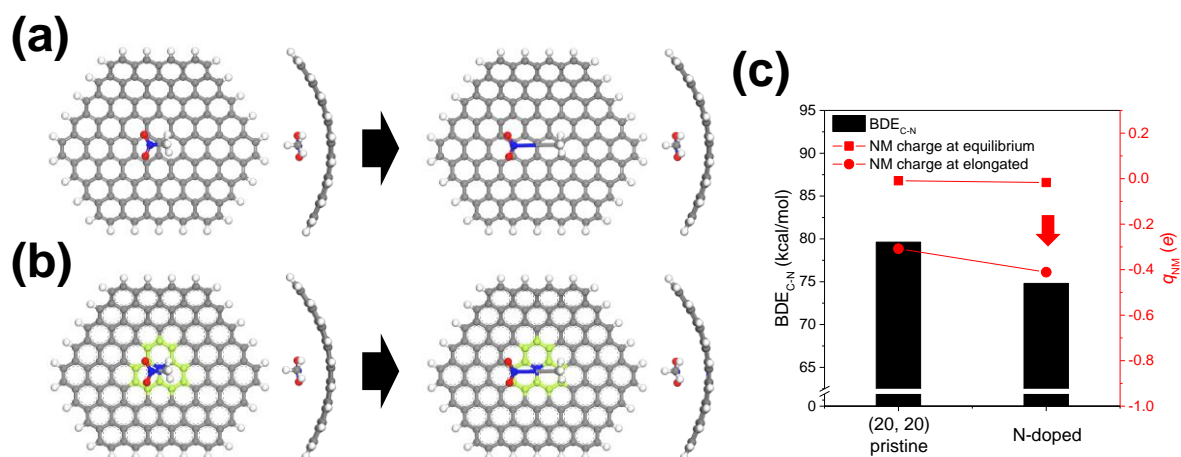
Figure 3.2.3 DFT calculations for bond dissociation energy of C−N bonds in NM molecule. Calculation models for (a) (20,20) pristine, (b) N-doping. The carbon, oxygen, nitrogen, and hydrogen atoms are colored in gray, red, white, and blue, respectively. (c) Bond dissociation energy (BDE_{C-N}) and charge of NM molecule (q_{NM}) with each carbon-cluster model. For the clear view, carbon atoms around the doped N site are shown by green ball-and-sticks. Copyright © 2020, American Chemical Society.
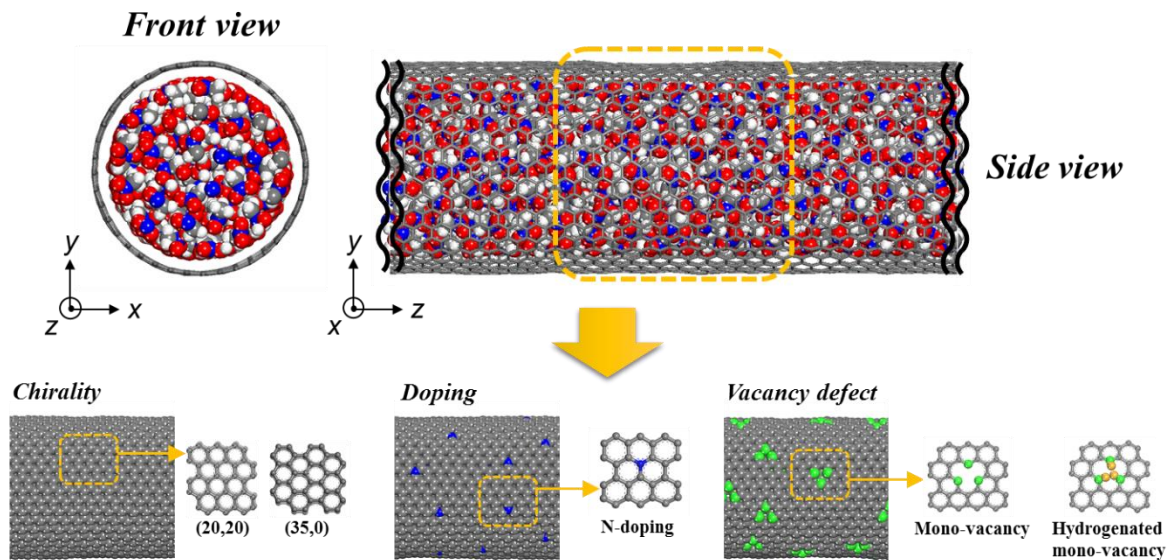
Figure 3.2.4 Schematic modeling of NM encapsulated in periodic CNT (upper figures) and types of physicochemical modifications of CNT (lower figures). Representative image in the upper figure corresponds to a nanobomb system with (20,20) pristine CNT. (35,0) pristine CNTs were considered to investigate the effect of the chirality; 1% and 2% nitrogen-doping and monovacancies and hydrogenated monovacancies were considered to investigate the effect of the concentration of the dopant and vacancies, respectively. The carbon, nitrogen, and hydrogen atoms of the CNT are represented by gray, blue, and orange, respectively and carbon atoms constituting the monovacancy defects are indicated by green. The carbon, nitrogen, oxygen, and hydrogen of NM are represented by gray, blue, red, and white, respectively. Copyright © 2020, American Chemical Society.

3.2.2.2 Bond Dissociation Energy of C−N Bond

The C-N bond dissociation energy (BDE_{C-N}) of NM molecule at around the CNT wall was estimated with and without nitrogen atom at cluster model (**Figures 3.2.3(a)** and **(b)**). When NM molecule was adsorbed on the CNT, trace amount of electron was transferred to the NM molecule, while transferred electron was increased as the C-N bond was elongated to about 4.5 Å. As expected, electron transfer was more active in the N-doped carbon-cluster model, which resulted in less energy required for bond dissociation from 79.6 kcal/mol to 74.8 kcal/mol (**Figures 3.2.3(c)**).

3.2.2.3 RMD Simulation

RMD simulations were conducted using the ReaxFF force field, where the bond is automatically calculated based on the bond order determined by the distance between the atoms, and the atomic charge is updated at each time-step *via* the EEM.[42] The RMD simulation using ReaxFF is widely used to study HEMs because the reaction of molecules can be analyzed under various conditions.[8,11,19,20,22–26,28,42–51] In the current study, ReaxFF was employed to investigate the shock-induced bursting of the modified nanobombs. Berendsen thermostat was used with a time step of 0.1 fs. Before induction of the nanobomb reaction by external shock, the nanobomb system was relaxed by *NVT*-RMD simulation for 100 ps at 298 K. Thereafter, the RMD simulations were independently performed with three shock-induced methods based on the type of external shock applied. First, to mimic actual decomposition in explosive device, where decomposition of explosive is initiated by external heat source, we defined CNT and contents as "hot" and "cold" regions following Zhou et al.'s work.[52] The temperature of the CNT was maintained at 2000, 2250, and 2500 K using *NVT* ensemble, whereas NM molecules were naturally heated by the hot CNT using *NVE* ensemble (*i.e.* heat up period of 39−57 ps). Thereafter, NERMD simulations (*i.e.* decomposition period) were conducted with the heated system using the *NVE* ensemble for 300 ps (350 ps for the (20,20) pristine nanobomb at 2500 K). Second, to realize an electric spark, constant electrical field was applied to the whole system along the x-direction, which was perpendicular to the principal axis of the CNT, under *NVE* ensemble until the temperature reached the decomposition temperature following Li et al.'s work.[25] The electric field was then removed, and the NERMD simulation was conducted. To determine proper range of the electric field strength to be applied to the nanobomb, electric-field-associated DFT calculation of the dissociation of the C−N bond in NM was conducted, and it was found that an electric field of at least 25 V nm^{-1} was required as the material was in the gas phase. However, at that electric field strength, it was found that the nanobomb would burst within a few picoseconds, which was much shorter than the time in the thermal shock method. Therefore, for the RMD simulations using the electric field to run on a time scale similar to thermal shock, a few strengths of electric field less than 10 V nm^{-1} were considered. The strengths of

the applied electric field were set to 6, 7, and 8 V nm^{-1}, which were within the range of the values employed by Li et al.[25]

Further, to simulate the electromagnetic induction according to the Wood et al.'s work,[26] the following equation was employed to apply oscillating electric field to the whole system by modulating the strength and direction of electric field with the simulation time:

$$E_x = E_0 \sin(\omega t) \tag{3.2.1}$$

where E_x is the electrical field applied in the x-direction, E_0 is the strength of the electric field, ω is the frequency of the electric field, and t is the simulation time (in ps unit). The electric field strengths were the same as those applied for the electric spark (*i.e.* E_0 = 6, 7, and 8 V nm^{-1}). The frequency of the oscillating field was set to correspond to the vibrational frequency of the C−N bond stretch in NM (659.5 cm^{-1}), which was derived by calculating the infrared (IR) spectrum of the bulk NM system using RMD simulation at room temperature. To identify molecular species from the RMD simulation, the bond cutoff values were taken from the data reported by Rom et al.[21]

3.2.2.4 DFT Calculations

DFT calculations were carried out to quantitatively compare the effects of the modified CNTs on bursting of the nanobomb. For the model systems, the curved carbon cluster model was used to reflect the curvatures of each CNT model (**Figure 3.2.2**). A carbon-cluster with a radius of ~10 Å was adopted for the (20,20) CNT, and the terminal carbon atoms were hydrogenated. Specifically, the positions of the hydrogen atoms were determined by optimization, while the carbon atoms were fixed. The positions of the carbon atoms were subsequently recalculated with fixed hydrogen atoms, which were previously optimized. To construct the cluster model of the zigzag CNT, the same procedure was applied to the (35,0) CNT. For the monovacancy defect and N-doping models, one C atom at the center of the (20,20) cluster model was removed or substituted with a N atom.

The electron exchange-correlation energy was calculated with the GGA and PBE[53] functional with the DNP 4.4 basis set. The Tkatchenko−Scheffler (TS) dispersion correction[54] was applied to consider van der Waals interaction of the molecule during adsorption on the carbon cluster. The convergence criteria for the energy, force, and displacement were set to 1.0×10^{-5} Ha, 0.002 Ha Å^{-1}, and 0.005 Å, respectively. To investigate the transition state involved in formation of the SW defect, the linear synchronous transit (LST) and quadratic synchronous transit (QST) methods[55,56] were applied until the convergence criteria of the root-mean-square (rms) force, which was set as 0.002 Ha Å^{-1}, were met. The binding energy ($\Delta E_{B.E.}$) of the molecule adsorbed on the cluster model was calculated as follows:

$$\Delta E_{B.E.} = E_{adsorbed} - E_{cluster} - E_{molecule} \qquad (3.2.2)$$

where $E_{adsorbed}$, $E_{cluster}$, and $E_{molecule}$ are the total energies of the intermediate-adsorbed carbon cluster, carbon cluster, and intermediate atom or molecule, respectively.

3.2.3 Results and Discussion

For thermal shock-induced bursting of the nanobomb, the confined NM molecules were heated through the CNT container that was exposed to thermal energy. The radial distribution of the temperature of the (20,20) nanobomb system is shown in **Figure 3.2.5.** With the progress of time, the temperature of the NM molecules reached the temperature of the CNT container by absorbing heat energy from the CNT container. Over the total simulation time, including heat up and decomposition period, the average temperature of the contents inside the nanobomb (*i.e.* NM and decomposed product) increased, with slight changes in the slopes of the profiles depending on the progress of decomposition (**Figure 3.2.6(a)**). The temperature increased during the heat up period, where only a small fraction of NM was decomposed (**Figure 3.2.6(b)**). When the temperature of the nanobomb system reached the target temperature, the *NVE* MD simulation was conducted. Thereafter, the NM molecules were heavily decomposed. For the systems subjected to high temperature, a rapid rise of the temperature was observed due to the formation of water molecules, which was the most exothermic reaction in the NM decomposition mechanism, as reported in our previous work (**Figure 3.2.6(c)**).[8] Note that even though water molecules were produced when the system was heated at 2000 K, the highest fraction of water molecules produced was ~0.1. At the final stage of nanobomb decomposition, the nanobomb heated to 2500 K exhibited a sudden temperature rise at around 350 ps, where the CNT container was ruptured.
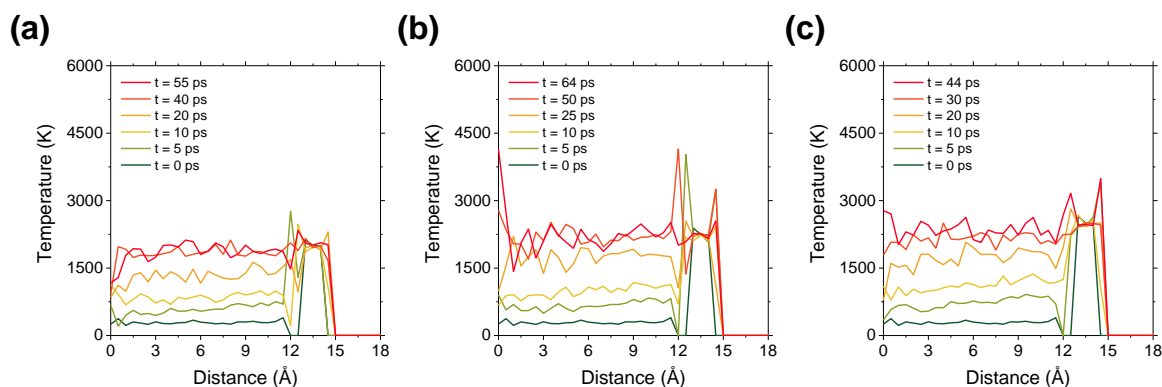
Figure 3.2.5 Radial temperature distributions for NM in (20,20) pristine nanobomb during the heating-up period at (a) 2000K, (b) 2250K, (c) 2500K over time. Radius of CNT is about 12~15 Å. Copyright © 2020, American Chemical Society.
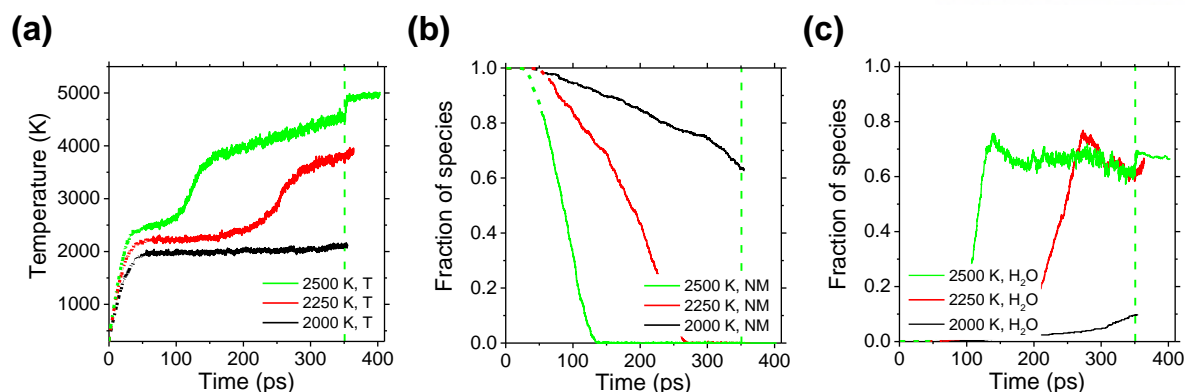
Figure 3.2.6 (a) Temperature profiles of NM, molar fractions of (b) NM and (c) H_2O in (20,20) pristine nanobomb during NERMD simulation vs simulation time depending on heat up temperature. Heat up period and decomposition period are shown by dashed line and solid line respectively. Vertical dashed lines indicate the time of the burst of CNT heated to 2500 K. Copyright © 2020, American Chemical Society.

To define the overall trend due to the effects of CNT modification (*i.e.* chirality, N-doping, and monovacancy defects), five independent simulations were carried out for the systems heated at 2500 K. The bursting times from five simulations for each modification type were averaged, and the results (*i.e.* bursting time and mechanism) of the simulation, of which bursting time was closest to the averaged value, were analyzed depending on the type of CNT modification (see **Table 3.2.2** for bursting time of reproduction simulations). **Figure 3.2.7** shows the results, where focus was placed on the changes in temperature (including bursting time), decomposition of NM, and water formation. The fraction of species in **Figure 3.2.7** represents the relative amount of species to the initial number of NM molecules ($N_{NM,0}$) inside the CNT container, *i.e.* $N_{NM,0} = 453$ for (20,20) pristine, N-doped, and monovacancy CNTs, and $N_{NM,0} = 454$ for (35,0) pristine CNT. Three temperature spikes were observed for the pristine (20,20) nanobomb system, where the formation of water molecules contributed to the second temperature spike and the NM molecules were completely decomposed within 150 ps. Eventually, the nanobomb systems burst, as indicated by the sharp temperature change. The effect of chirality on bursting of the nanobomb is shown in **Figures 3.2.7(a)–(c)**. Due to the slightly inferior mechanical properties of the (35,0) CNT relative to that of the (20,20) CNT,[57,58] the bursting time, indicated by vertical dashed lines in the temperature profile, was shorter for the (35,0) nanobomb. Except for the difference in the bursting time, however, changing the chirality had little effect on the bursting phenomenon. Nitrogen-doping of the CNTs also led to quite small changes in the rate of NM decomposition and water formation, while the bursting time was consistently shortened by increasing the concentration of the N-dopant atoms (**Figures 3.2.7(d)–(f)**).

Table 3.2.2 Bursting time of five independent simulations for each physicochemical modification type. According to our criteria, *i.e.* simulation trial of which bursting time is the closest to the average bursting time, trial 5 for (20,20) pristine nanobomb, trial 2 for (35,0) pristine nanobomb, trial 3 for N-doping 1% nanobomb, trial 3 for N-doping 2% nanobomb, trial 1 for monovacancy defect 1% nanobomb, trial 4 for monovacancy defect 2% nanobomb, trial 4 for monovacancy defect 1% with hydrogenation nanobomb, and trial 2 for monovacancy defect 2% with hydrogenation nanobomb were employed, respectively. Copyright © 2020, American Chemical Society.

Type of structural modification		Bursting time (ps)					
		trial 1	trial 2	trial 3	trial 4	trial 5	average
Chirality	(20,20)	292.7	351.1	397.6	308.0	350.7	340.0 ± 36.9
	(35,0)	222.0	305.5	300.4	363.4	342.4	306.7± 48.4
Nitrogen -doping	1.0 %	278.3	270.5	318.7	337.8	338.8	308.8 ± 29.1
	2.0 %	287.7	279.6	234.0	190.2	229.1	244.1 ± 35.8
Monovacancy defect	1.0 %	160.7	146.7	180.6	148.1	149.5	157.1 ± 12.7
	2.0 %	136.2	138.5	170.3	155.9	137.5	147.7 ± 13.4
Hydrogenated monovacancy defect	1.0 %	158.1	203.6	200.3	179.1	172.6	182.7 ± 17.1
	2.0 %	160.1	159.8	144.4	150.4	161.2	155.2 ± 6.6
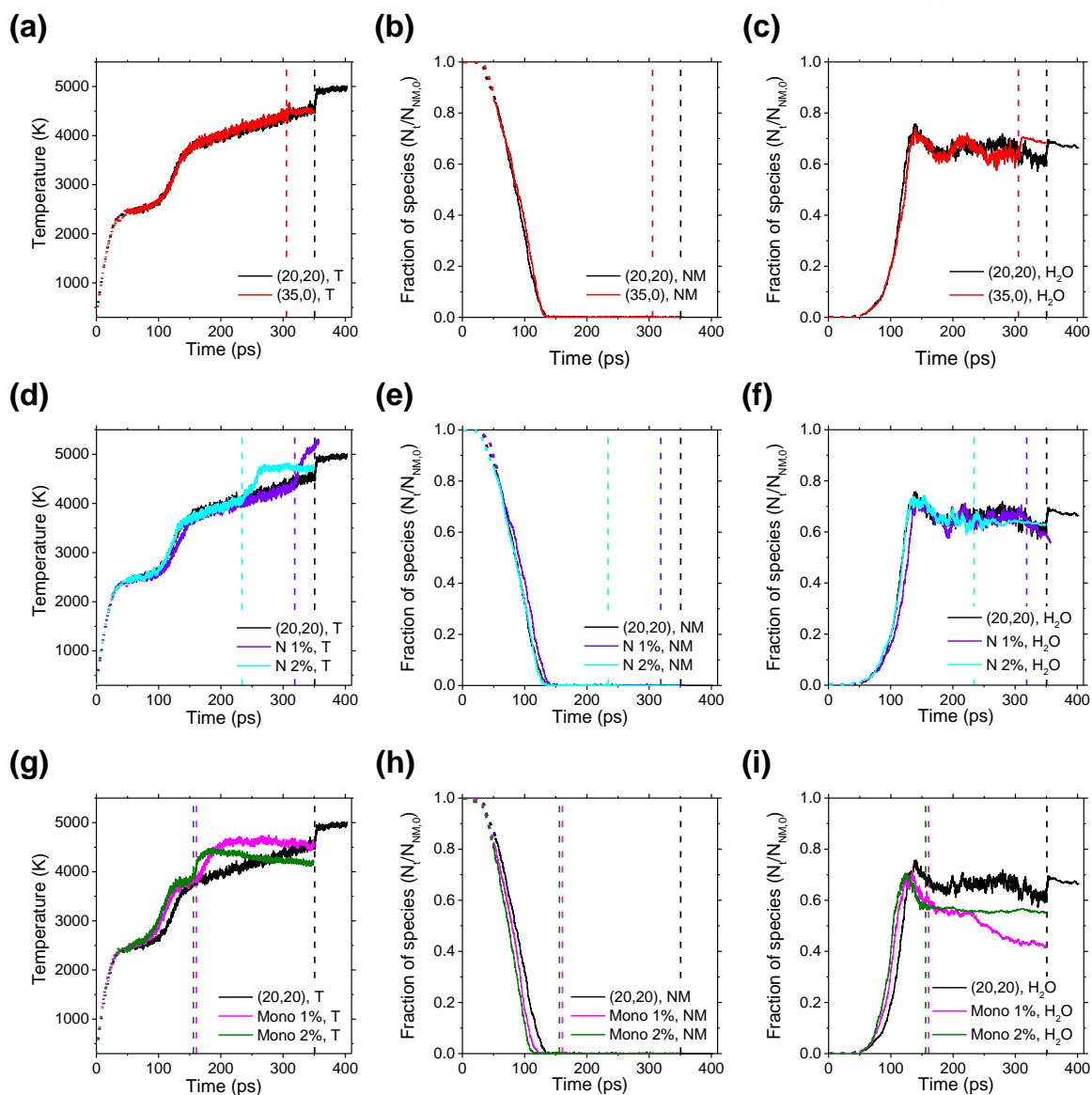
Figure 3.2.7 NERMD simulation data for nanobomb with physicochemical modifications at the heating temperature of 2500 K. (a) Temperature profiles of NM, molar fractions of (b) NM and (c) H_2O in nanobomb with chirality modification, respectively. (d) Temperature profiles of NM, molar fractions of (e) NM and (f) H_2O in nanobomb with N-doping modification, respectively. (g) Temperature profiles of NM, molar fractions of (h) NM and (i) H_2O in nanobomb with monovacancy defect modification, respectively. (20,20), (35,0), N 1%, N 2%, Mono 1%, and Mono 2% represent the (20,20) pristine nanobomb, (35,0) pristine nanobomb, nitrogen-doped nanobombs with 1% and 2% dopant concentration, and monovacancy nanobombs with 1% and 2% vacancy concentration, respectively. The heat up period and decomposition period are indicated by dashed line and solid line, respectively. Vertical dashed lines indicate the time required for the CNT to burst for each system. Copyright © 2020, American Chemical Society.

The most noticeable difference was achieved with the monovacancy defect-based nanobomb (**Figure 3.2.7(g)**–**(i)**). The monovacancy defect brought about a promising result: the higher the concentration of monovacancy defects, the faster the decomposition of NM and the formation of H_2O. Notably, bursting occurred within 170 ps for the monovacancy systems. To assess the effect of the chemical reactivity of the nanocontainer with monovacancy defects on bursting of the nanobomb, a hydrogenated nanobomb, where the defective carbons were stabilized by functionalization with hydrogen atoms, was also considered (**Figure 3.2.8**). The rates of NM decomposition and H_2O formation were accelerated even for the hydrogenated monodefective nanobomb, where the bursting time of the hydrogenated nanobomb was slightly longer than that of the non-hydrogenated monodefective nanobomb. The bursting time was shortened when the concentration of defects increased. Thus, the reactivity of the defect vacancy is thought to be a relevant factor for nanobomb bursting.
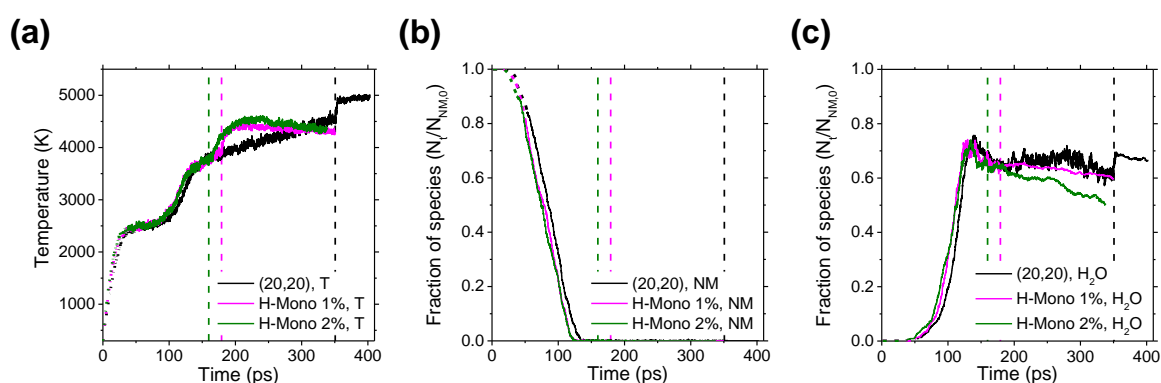
Figure 3.2.8 (a) Temperature profiles of NM, molar fractions of (b) NM and (c) H_2O in nanobomb with hydrogenated monovacancy modification during NERMD simulation vs simulation time at the heating temperature of 2500 K. (20,20), H-Mono 1%, and H-Mono 2% represent for (20,20) pristine nanobomb, and hydrogenated monovacancy nanobombs with 1% and 2% concentration, respectively. Heat up period and decomposition period are shown by dashed line and solid line respectively. Vertical dashed lines indicate the time of the burst of CNT for each system. Copyright © 2020, American Chemical Society.

For the intermediates, we analyzed the changes in the amount of CO, H, and OH species, which are highly reactive radicals among the numerous products.[8] The products generated by NM decomposition as a function of the simulation time for the nanobombs with different CNT modifications are shown in **Figure 3.2.9**. CO and H species were formed and gradually increased in line with the time domain of water formation (~100 ps), while the OH species were formed as early as within the time domain of initial NM decomposition (~50 ps). This trend was similar for all the modified systems, including that with the hydrogenated defect vacancy (**Figure 3.2.10**). After bursting was achieved for each modified system, the amount of CO increased sharply and the amount of H species also increased, whereas the concentration of OH species decreased sharply. It is proposed that consumption of the oxygen-containing species, including the OH species, was associated with the increase in the CO and H species. Interestingly, the concentration of OH increased steadily after the sudden drop due to reactions between the confined products. The relative amount of CO was larger than that of H due to reaction between the torn CNT and oxygen-containing species. In the case of the system with 2% N-doping, before nanobomb bursting, H atoms were formed at a faster rate than in the other systems. This is because the H atoms could be detached from the small torn sites in the CNT prior to bursting of the nanobomb, rather than remaining attached to the CNT.
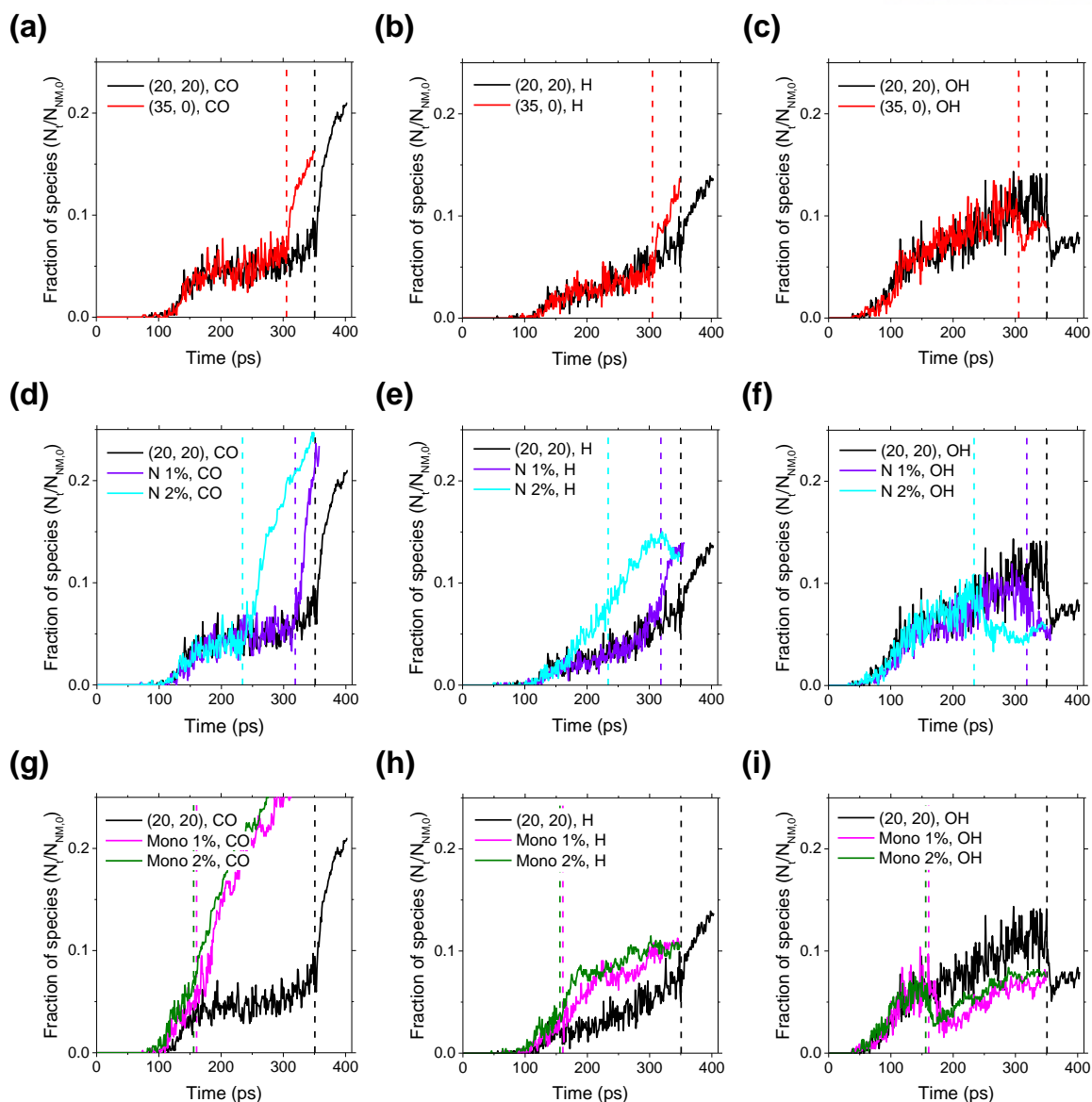
Figure 3.2.9 Molar fractions of CO, H, and OH in nanobomb with physicochemical modifications during NERMD simulation vs simulation time. (a) CO, (b) H, and (c) OH profiles for nanobomb with chirality modification. (d) CO, (e) H, and (f) OH profiles for nanobomb with N-doping modification. (g) CO, (h) H, and (i) OH profiles for nanobomb with monovacancy modification. (20,20), (35,0), N 1%, N 2%, Mono 1%, and Mono 2% represent the (20,20) pristine nanobomb, (35,0) pristine nanobomb, nitrogen-doped nanobombs with 1% and 2% dopant concentration, and monovacancy nanobombs with 1% and 2% vacancy concentration, respectively. The heat up period and decomposition period are indicated by dashed line and solid line, respectively. Vertical dashed lines indicate the time required for the CNT to burst for each system. Copyright © 2020, American Chemical Society.

(a)

(b)

(c)
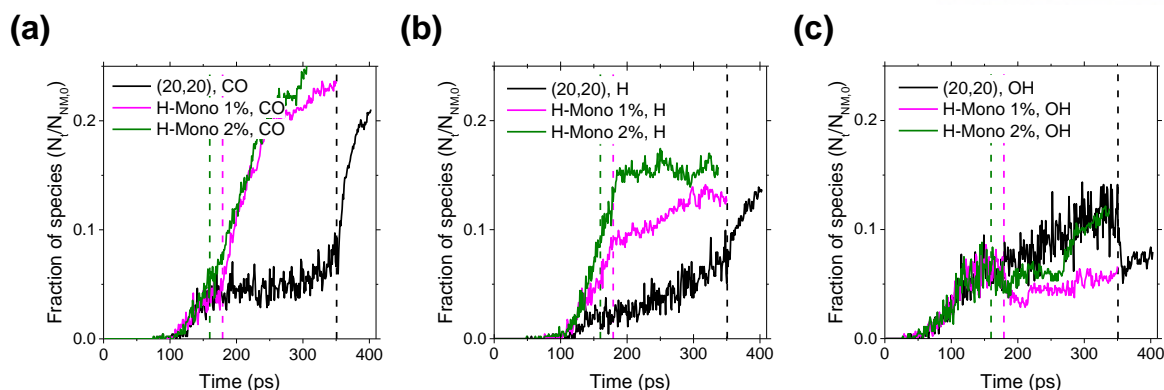
Figure 3.2.10 Molar fractions of (a) CO, (b) H, and (c) OH in nanobomb with hydrogenated monovacancy modification during NERMD simulation vs simulation time at the heating temperature of 2500 K. (20,20), H-Mono 1%, and H-Mono 2% represent for (20,20) pristine nanobomb, and hydrogenated monovacancy nanobombs with 1% and 2% concentration, respectively. Heat up period and decomposition period are shown by dashed line and solid line respectively. Vertical dashed lines indicate the time of the burst of CNT for each system. Copyright © 2020, American Chemical Society.

Thus, it was found that certain physicochemical modifications of the CNT nanocontainer induced fast decomposition of NM and early bursting of the system. For deeper evaluation, the bursting mechanism of the nanobomb after NM decomposition in each system was scrutinized. First, we analyzed the bursting mechanism of the (20,20) nanobomb (see **Figures 3.2.11(a)** and **3.2.12**). Bursting was initiated by internal functionalization of the reaction intermediate, which was mainly composed of carbon and oxygen atoms, to form an unstable carbon ring (*e.g.* a 7−7 ring as observed at 305.2 ps). The unstable ring evolved to form a nanopore by further functionalization of the intermediate (343.1 ps). Thereafter, the nanopore grew further by subsequent functionalization of other intermediates (349.8 ps). Finally, ejection of the reaction products was initiated at 350.8 ps, and the nanopore was torn rapidly from 352.1 to 398.2 ps. The bursting time was found to be closely related to the time when the internal compounds reacted with the CNT wall and the six rings of the CNT were deformed.

We also investigated the difference in the reaction mechanisms due to the effect of CNT modification on the reactivity of the CNT wall. Note that for the N-doped and monovacancy systems, the atomic trajectories of the 2% model systems were employed for comparison of the mechanism. **Figures 3.2.11(b)–(d)** show the bursting mechanism of the nanobombs with different CNT modifications. The reaction mechanisms were similar, regardless of the type of physicochemical modification. At the beginning of the reaction, the internal products attached to the CNT; it occurred at 291.2 ps for the (35,0) CNT (**Figure 3.2.11(b)**), 169.3 ps for the CNT with 2% N-doping (**Figure 3.2.11(c)**), and 77.3 ps for the CNT with 2% monovacancy (**Figure 3.2.11(d)**). Thereafter, the hexagonal carbon rings were deformed to generate a nanopore at 294.9, 220.9, and 134.1 ps, respectively. This pore gradually enlarged over time, and ejection of the encapsulated products was initiated at 305.5−307.4, 227.9−229.3, and 147.4−155.0 ps, respectively. From the temperature profile and bursting mechanism, the bursting time of the (35,0) nanobomb was faster than that of the (20,20) nanobomb. Nanopore formation on the (35,0) CNT container took about 3.7 ps, compared to 37.9 ps for the (20,20) container (**Figures 3.2.11(a)** and (**b**)). Moreover, for the N-doped and monovacancy systems, bursting proceeded more rapidly than for the systems with different chirality. These observations demonstrate that the reaction site of the CNT and the reaction time varied based on the modification. In the case of the N-doped system, radical species (*i.e.* hydrogen atoms) were generally adsorbed on the carbon around the doping sites at early time (**Figure 3.2.11(c)**). In the case of the monovacancy defect system, radical species (*i.e.* oxygen atoms) were strongly adsorbed on the defective sites, even before the thermal decomposition period, and additional radical oxygen atoms were further adsorbed around the defect sites (**Figure 3.2.11(d)**). Note that the preferential sites for the reacting radicals were further investigated *via* DFT calculations, as presented in the later paragraphs of this section. The adsorption of radical atoms accelerated the bursting phenomenon. In the hydrogenated monovacancy system, the CNT wall adopted two different configurations prior to nanopore formation. In one configuration, the hydrogen atom was detached from the defective site, after which a confined product such as a nitrogen atom from NM was attached to the dangling carbon atom (**Figure 3.2.13(a)**). For the other configuration, the carbons around the defect site were directly cleaved to form dangling bonds and a small nanopore (**Figure 3.2.13(b)**). Considering the structures, it is proposed that although the defect sites were stabilized by hydrogen, the defect characteristics were regenerated during the decomposition of NM, leading to rapid bursting.

(a)

(20,20)

| 305.2 ps | 343.1 ps | 349.8 ps | 350.8 ps |

(b)

(35,0)

| 291.2 ps | 294.9 ps | 305.5 ps | 307.4 ps |

(c)

N-doping 2%

| 169.3 ps | 220.9 ps | 227.9 ps | 229.3 ps |

(d)

Mono-vac. 2%

| 77.3 ps | 134.1 ps | 147.4 ps | 155.0 ps |
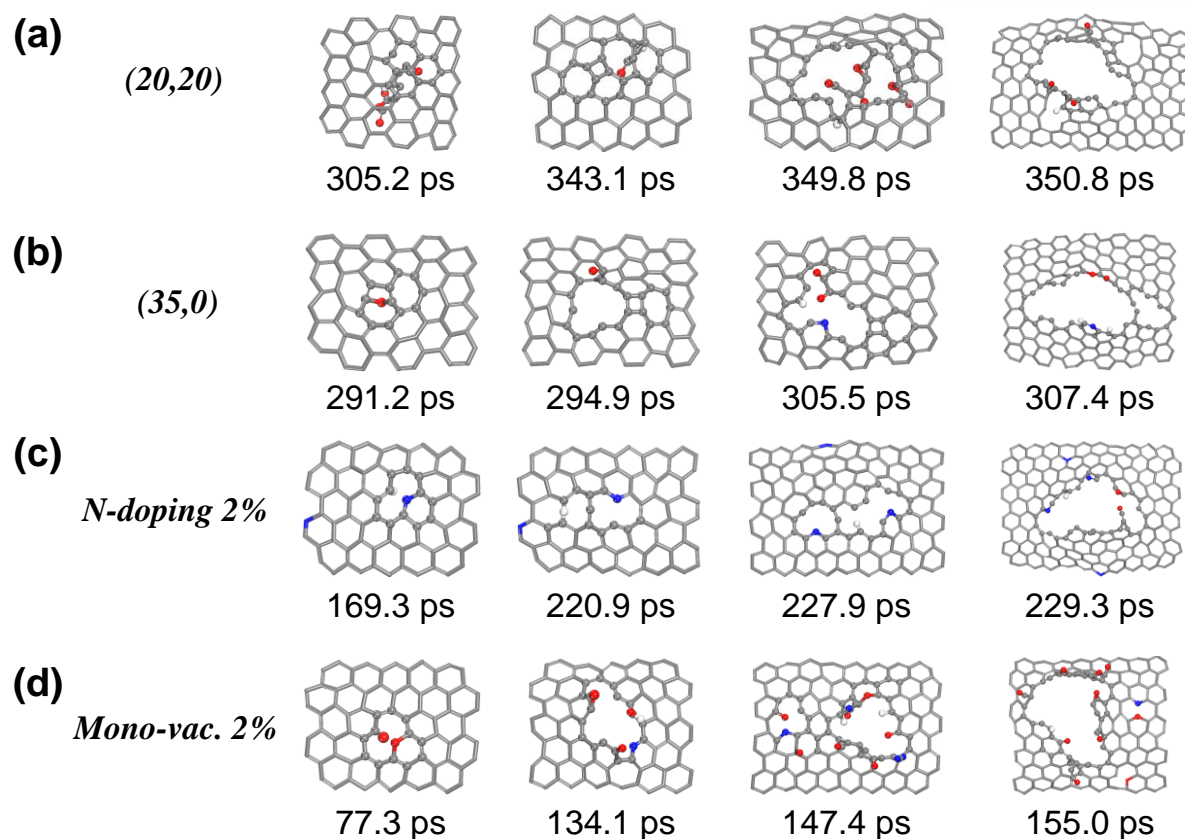
Figure 3.2.11 Mechanistic models of bursting for each physicochemical modification of CNT at the heating temperature of 2500 K. (a) (20,20) pristine nanobomb, (b) (35,0) pristine nanobomb, (c) N-doped nanobomb with 2% dopant, and (d) monovacancy nanobomb with 2% vacancy. The four simulation snapshots of each system show the moments of adsorption of the internal products, pore generation, pore expansion, and initial bursting, respectively, in time order. The carbon, oxygen, nitrogen, and hydrogen atoms are represented by gray, red, blue, and white, respectively. Copyright © 2020, American Chemical Society.

305.2 ps   343.1 ps   349.8 ps

350.8 ps   352.1 ps   398.2 ps
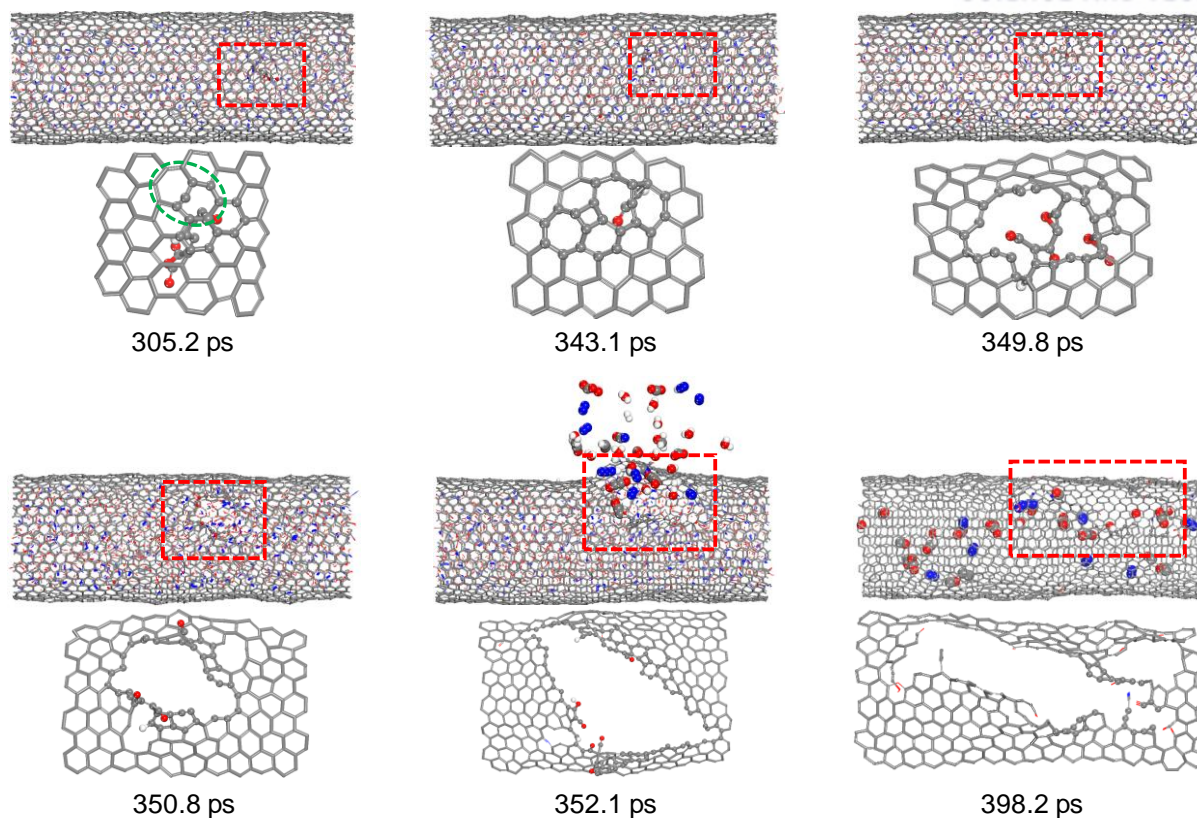
Figure 3.2.12 Bursting mechanistic models of nanobomb system. Representative snapshots with time evolution are taken from (20,20) nanobomb system at 2500 K. The carbon, oxygen, nitrogen, and hydrogen atoms are colored in gray, red, blue, and white, respectively. Red dashed boxes represent the location of bursting for the clear view. Green dashed-circle at 305.2 ps represents unstable 7$-$7 carbon atoms ring. The reaction mechanism was depicted with functionalization of reaction intermediate to unstable carbon atoms ring at 305.2 ps, generation of nanopore by the continuous functionalization of intermediate at 343.1 ps, growth of nanopore by the internal pressure at 349.8 ps, start of eruption with intermediate in nanopore at 350.8 ps, ejection of inner product and rapid tearing of nanopore at 352.1 ps, and termination of bursting at 398.2 ps. Copyright © 2020, American Chemical Society.

(a)   **(b)**
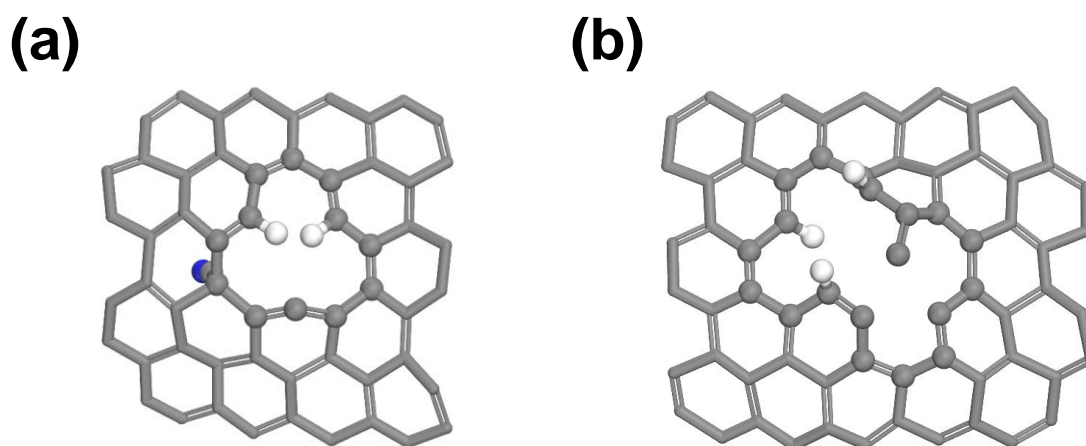
Figure 3.2.13 Simulation snapshots from the nanobomb with hydrogenated monovacancy defect modification at 95.2 ps. (a) Adsorption of internal products to deprotonated site. (b) C−C bond cleavage at bursting site. The carbon, nitrogen, and hydrogen atoms are colored in gray, blue, and white, respectively. Copyright © 2020, American Chemical Society.

To gain detailed insight into these phenomena, formation of the SW defect and adsorption of radical species to the curved cluster models for each physicochemical modification type were explored based on DFT calculations. Note that the SW defect was consistently formed in the period right after the functionalization of the internal products to the CNT wall. To construct the SW defect, two central carbon atoms were rotated by 90° (**Figure 3.2.14**). The activation energy was not significantly different for the armchair (20,20) pristine CNT and zigzag (35,0) pristine CNT (*i.e.* ~3.6 kcal mol^{-1}). The formation energy of the SW defect in the zigzag (35,0) pristine CNT was 13% larger than that of the armchair (20,20) pristine CNT due to the differences in the direction of curvature of the carbon atoms involved in forming the SW defect. For the curved cluster models with nitrogen-doping and monovacancy defects, the activation energy and formation energy were significantly lower than that of the (20,20) pristine CNT model. In particular, the vacancy defect exerted a more significant effect because of the reduced strain energy for rotating the carbon atoms around the vacancy defect. Formation of unstable rings on the CNT wall was less favored by modification of the chirality but was promoted by nitrogen-doping and monovacancy defects.
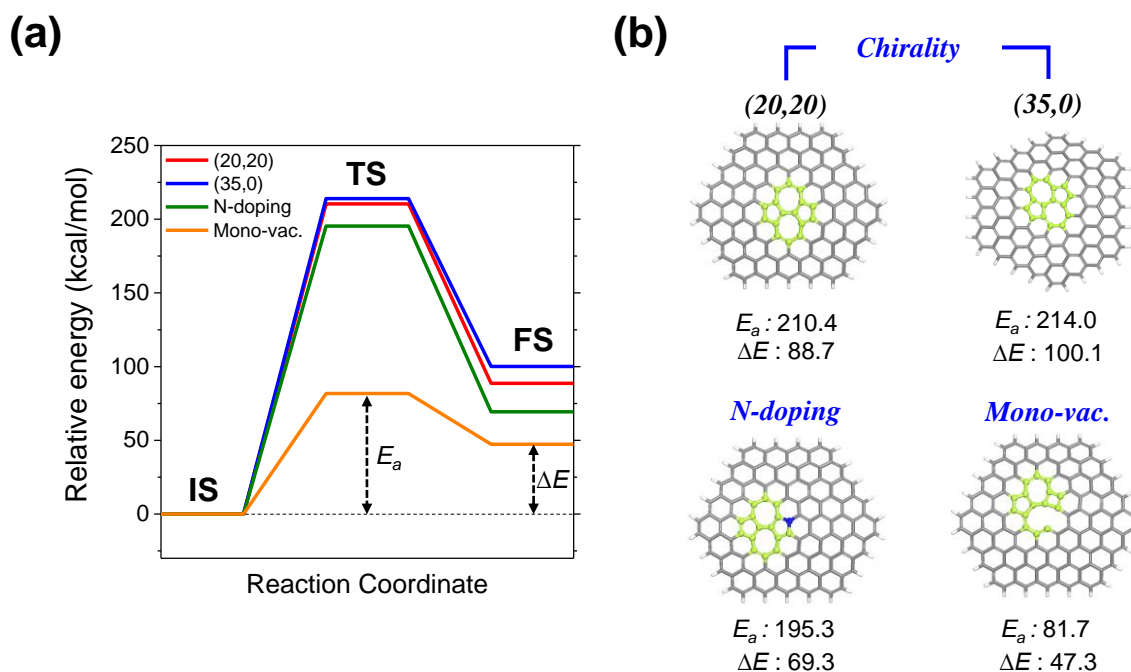
Figure 3.2.14 Mechanism of formation of SW defect on carbon cluster model. (a) Relative energy diagram according to reaction coordinates. (b) Optimized carbon clusters with single SW defect. At the bottom of each figure, E_a and ΔE denote the activation and formation energies (in units of kcal mol^{-1}) for the SW defect, respectively. For a clear view, the carbon atoms in the SW defect and doped nitrogen atoms are indicated by green and blue ball-and-sticks, respectively. The carbon and hydrogen atoms are represented by gray and white sticks, respectively. Copyright © 2020, American Chemical Society.

Additionally, to investigate the effect of physicochemical modification of the CNT on adsorption of the reaction intermediates after NM decomposition, the binding energies of O, OH, H, and CO on the CNT wall were compared. **Figure 3.2.15(a)** shows the optimized configuration of O, OH, H, and CO adsorbed on the curved cluster models for each physicochemical modification. Note that the radical or intermediate molecules were strongly adsorbed on the C atom nearest to the doping or defect sites. O and CO formed bidentate bonds with two C atoms. There was no difference in the binding energy due to modification of the chirality (**Figure 3.2.15(b)**). Nitrogen-doping and monovacancy defects enlarged the binding energy relative to that of the pristine cluster models, where the binding energy was lower for the monovacancy defect. Notably, for the monovacancy defect system, the adsorbed O atom could be inserted at the vacancy site (inset figure in **Figure 3.2.15(b)**), where the largest binding energy was obtained (*i.e.* -159.5 kcal mol^{-1}). Thus, nitrogen-doping and the monovacancy defect are expected

to facilitate binding between the intermediate and the CNT wall, thereby accelerating bursting of the nanobomb.
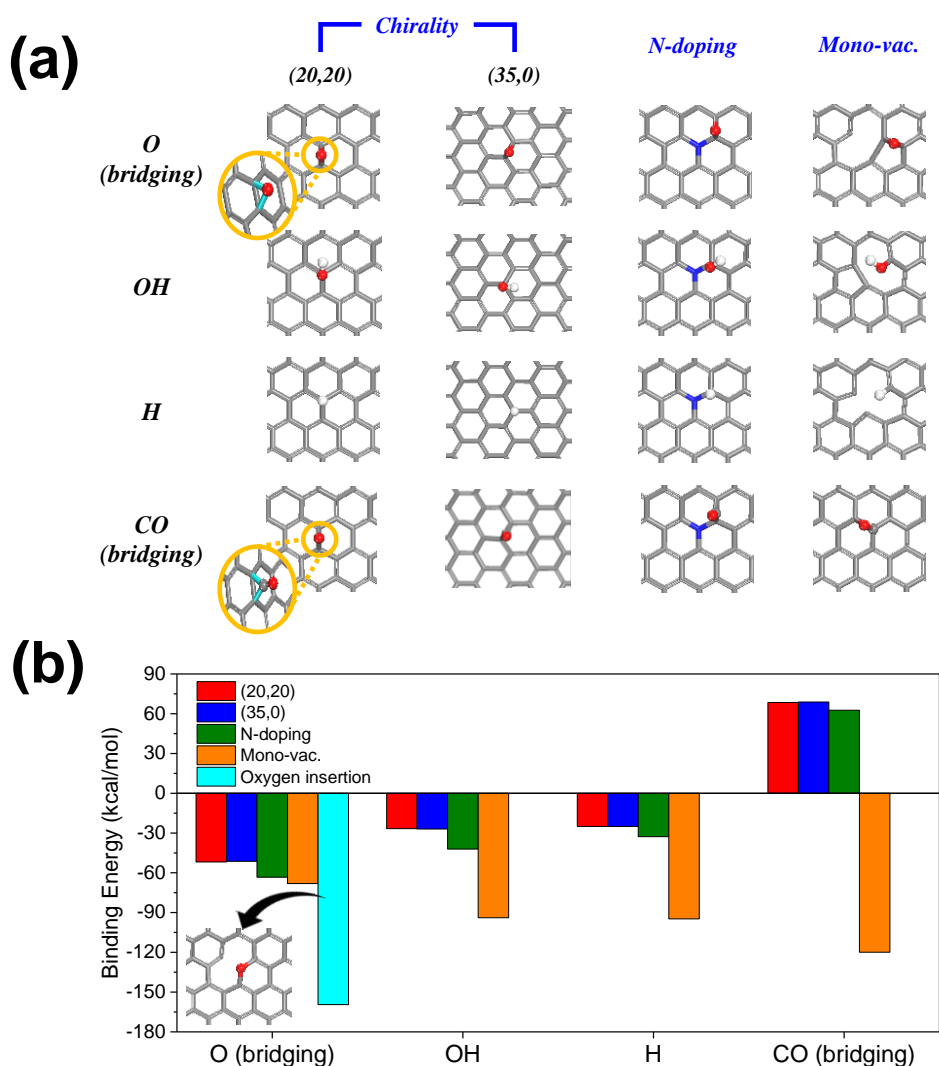
Figure 3.2.15 (a) Optimized carbon clusters with adsorbed products, *i.e.* O, OH, H, and CO, depending on CNT modifications. Colors of atoms are the same as those in **Figure 3.2.11**. Among the three products, each O and CO form a bridge with two carbon atoms on each carbon cluster (magnified for clear view). (b) Binding energies of products with carbon-cluster, calculated using optimized models in (a). Cyan-colored bar is the binding energy where O substitutes the monovacancy defect site of carbon-cluster, and the inset figure shows the corresponding optimized structure. Copyright © 2020, American Chemical Society.

The optimal method of triggering bursting (*e.g.* thermal shock, electric spark, or electromagnetic induction) was also of interest. Thus, in addition to investigating thermal shock-induced bursting of the nanobomb, we further investigated the effects of an electrical spark and electromagnetic induction on bursting of the nanobomb. To directly compare the electrical spark and electromagnetic induction with thermal shock-induced bursting, an electrical field was applied with and without sinusoidal variation of the field strength and direction until the temperature of NM reached 2500 K. Subsequently, *NVE* RMD simulation was implemented without applying an electrical field to observe bursting of the nanobomb system. Note that the (20,20) pristine CNT was chosen for this control simulation. The temporal evolution of the temperature, number of NM, and water molecules produced depending on the type and strength of the external shock are shown in **Figure 3.2.16**. During decomposition of the nanobomb systems upon application of an electric spark, the temperature increased in three stages, where the second stage was closely related to the formation of water. In the final stage, the nanobomb systems were ruptured, as indicated by the rapid temperature change (see vertical dashed line). This propagation of the decomposition reaction was almost the same as that observed for decomposition under thermal shock, and the time required for bursting after the heat up period was also similar to that in the systems heated by thermal shock. However, in the electric spark simulations, due to the overheating of NM compared to CNT by the strong electric field, the temperature declined slightly within a few picoseconds after the heat up period. On the other hand, in all of the nanobomb systems heated by the electromagnetic induction method, the time for heating the nanobomb was less than 3 ps. Due to the strong electromagnetic wave with a vibrational frequency corresponding to that of the C−N bond stretch in NM, the kinetic energy transferred to NM was much higher than that of the CNT during the heat up period. As the result, when the *NVE* RMD simulation was started, the entire system was temporarily quenched to 1600−1700 K, as the thermal energy of NM was transferred to the CNT within 30 ps. Thereafter, the temperature increased very slowly over the remaining simulation time due to limited decomposition of the NM molecules and retarded water formation.
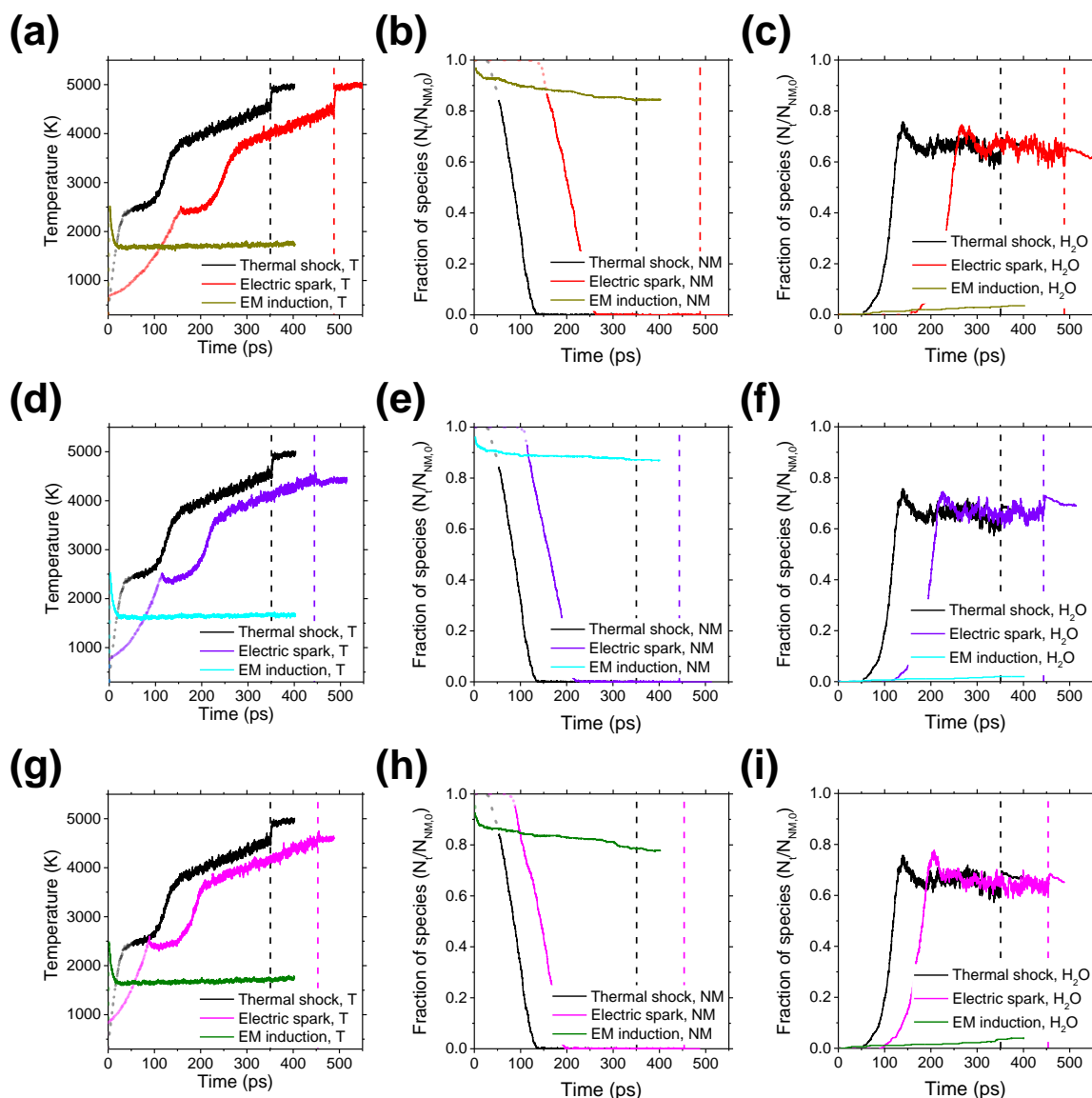
Figure 3.2.16 NERMD simulation data for nanobomb under electric spark and electromagnetic induction. (a) Temperature profiles of NM, molar fractions of (b) NM and (c) H_2O in nanobomb with 6 V nm^{-1} field strength, respectively. (d) Temperature profiles of NM, molar fractions of (e) NM and (f) H_2O in nanobomb with 7 V nm^{-1} field strength, respectively. (g) Temperature profiles of NM, molar fractions of (h) NM and (i) H_2O in nanobomb with 8 V nm^{-1} field strength, respectively. EM induction represent for electromagnetic induction. Heat up period and decomposition period are shown by dashed line and solid line respectively. Vertical dashed lines indicate the time of the burst of CNT for each system. Copyright © 2020, American Chemical Society.

When the two kinds of electric field-based shocks were applied, the time required for bursting after heating was similar or much longer than that induced by thermal shock. Nevertheless, we expected that if the electric field was continuously applied until the nanobomb burst, the electric field could accelerate decomposition by effectively influencing the arrangement and bond environment of the NM molecules (**Figure 3.2.17**).
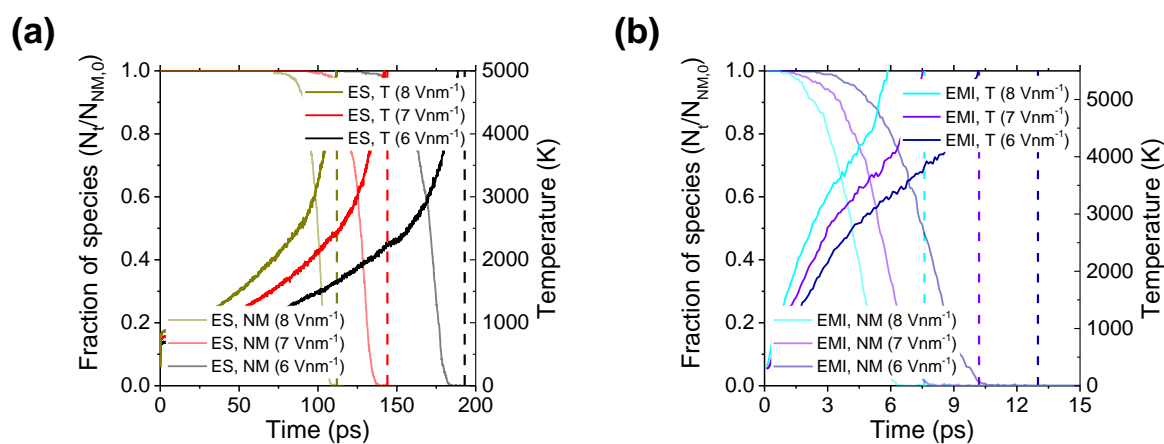
Figure 3.2.17. Molar fractions of NM and temperature profiles of NM in nanobomb with (a) electric spark and (b) electromagnetic induction during NERMD simulation vs simulation time. The strength of the electric field was set at 6, 7, and 8 V nm^{-1}. ES and EMI represent "electric spark" and "electromagnetic induction", respectively. The rate of NM decomposition in each nanobomb is represented by translucent solid line. Vertical dashed lines indicate the bursting time of the CNT for each system. Copyright © 2020, American Chemical Society.

For both electric spark and electromagnetic induction, the temperature increased quickly, and the time for bursting was reduced as the strength of electric field increased. For a given intensity of the electric field, the nanobomb systems subjected to electromagnetic induction were ruptured much faster than the system exposed to the electric spark. This significant difference in the bursting time could be explained by the different bursting mechanisms induced by the two types of external shock (**Figure 3.2.18**). In the case of the electric spark (**Figure 3.2.18(a)**), the NM molecules were aligned along the direction of the electric field, and decomposition was initiated. As the reaction progressed further, the oxygen- and hydrogen-containing reaction products segregated from each other inside the nanocontainer. Note that the CNT walls were partially functionalized at the opposite side from the

direction of the electric field where the oxygen-containing molecules were found to be concentrated. Finally, the nanobomb burst and the internal products were ejected, starting from tearing of the functionalized site. On the other hand, in the case of electromagnetic induction (**Figure 3.2.18(b)**), there was no observable alignment of the NM molecules induced by the electric field. Instead, the C−N bond dissociated rapidly due to the effect of the frequency of the electric field. Thus, the encapsulated reaction intermediates were randomly and immediately functionalized on the CNT walls, and rupture of the nanobomb occurred within 10 ps.

(a)

(b)
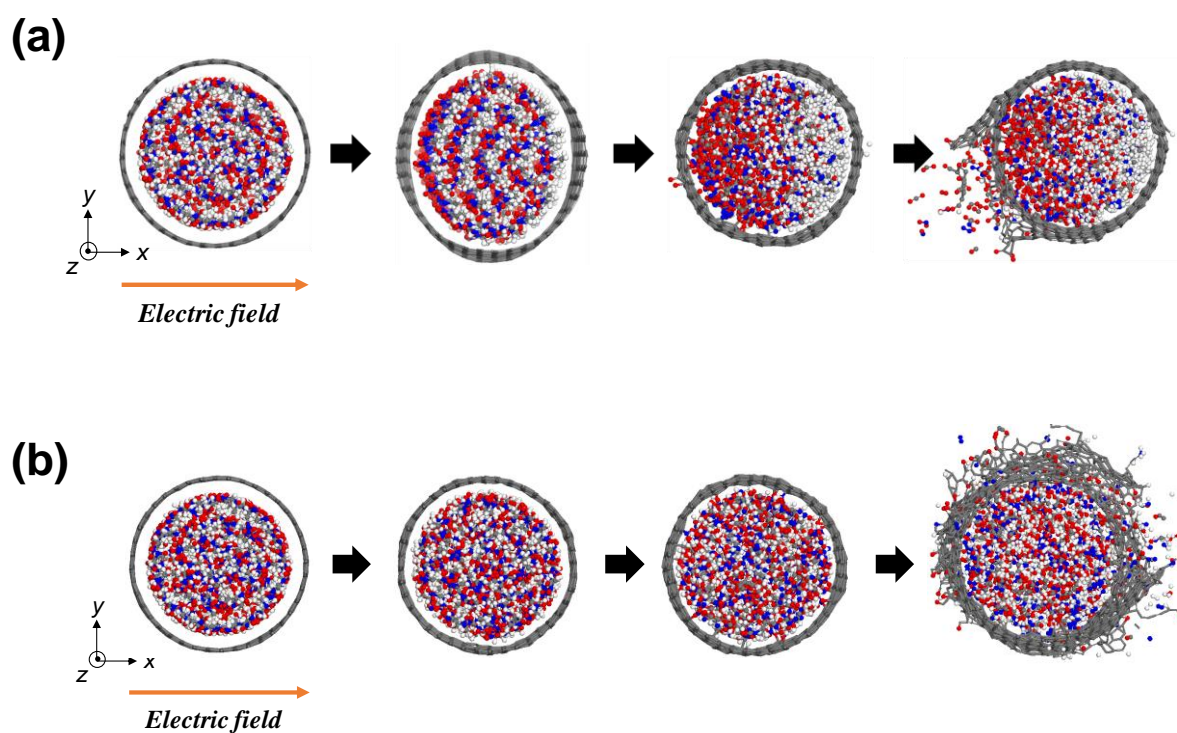
Figure 3.2.18 Schematic illustration of bursting mechanism of the (20,20) nanobomb under 6 Vnm^{-1} electric field. Bursting of nanobomb (a) under electric spark, and (b) under electromagnetic induction. The atoms in CNT and NM molecules are represented by stick and ball-and-stick models, respectively. The carbon, oxygen, nitrogen, and hydrogen atoms are colored in gray, red, blue, and white, respectively. The orange arrow represents the direction of electric field. Copyright © 2020, American Chemical Society.

3.2.4 Conclusion

Nanobomb systems were constructed by confining NM in CNT nanocontainers that were subjected to physicochemical modifications by changing the chirality, nitrogen-doping, and introducing a monovacancy. The systems were investigated by thermal shock-induced NERMD simulation and DFT calculations. The bursting properties of each nanobomb system were determined from the temperature profile, NM decomposition rate, intermediates, and reaction mechanism with respect to the simulation time. Even though the overall mechanism was similar for all modifications to that of pristine (20,20) CNT, CNT modifications generally accelerated bursting of the nanobomb. Changing the chirality of the CNT nanocontainer produced marginal differences in the bursting properties except for the reduced bursting time, which was expected to be associated with weak mechanical property of zigzag CNT. Nitrogen-doping on CNT also had a little effect on the bursting properties of the nanobomb, but earlier attachment of the confined products reduced the bursting time of nitrogen-doped nanobomb. Among physicochemical modifications of interest, monovacancy defect induced the most noticeable and concentration-dependent effect, where a higher concentration of monovacancy defects accelerated the decomposition of NM, the generation of H_2O, and the temperature increase before bursting. Due to high chemical reactivity around the defective sites, the most rapid bursting of nanobomb was achieved by facilitated attachment of reaction intermediates as observed in the nitrogen-doped nanobomb. When the mono-vacancies were saturated with hydrogen, bursting of the nanobomb was slightly retarded compared to that of the monovacancy nanobomb due to the reduced reactivity. However, because hydrogen desorption occurred over time, the saturated vacancies eventually exhibited a similar effect to that of the monovacancy defects. To analyze the reason for this difference, the energy related to SW defect formation and the binding energies of the confined products determined from DFT calculations were compared for the systems with different physicochemical modifications. Formation of SW defects and adsorption of the confined product at the nitrogen-doping site or monovacancy defect site were much easier than in the case of the pristine CNT.

The effects of electric spark and electromagnetic induction were examined by applying an electric field to the (20,20) nanobomb system. When the *NVE* RMD simulation was performed after the temperature was raised to 2500 K by application of the respective electric field-based shocks, the explosion characteristics of the nanobomb heated by the electric spark were similar to those subjected to the thermal shock, whereas the nanobomb heated by electromagnetic induction cooled rapidly and decomposed very slowly. However, when the electric field was continuously applied, both shocks induced significant changes in the explosion of the nanobomb. Continuous collision and decomposition of NM were induced by applying an electric spark to the nanobomb, and the temperature of the nanobomb gradually increased, resulting in bursting within 200 ps. Notably, in the case of

electromagnetic induction, the frequency of the electric field, which corresponded to the C−N bond stretch in NM, brought about rapid decomposition of NM, and the nanobombs exploded within 10 ps, which is much faster than the case with the electric spark.

3.2.5 References

1. Zhou, X.; Torabi, M.; Lu, J.; Shen, R. Q.; Zhang, K. L. Nanostructured Energetic Composites: Synthesis, Ignition/Combustion Modeling, and Applications. *ACS Appl. Mater. Interfaces* **2014**, 6, 3058−3074.

2. Pagoria, P.; Zhang, M-X.; Zuckerman, N.; Lee, G.; Mitchell, A.; DeHope, A.; Gash, A.; Coon, C.; Gallagher, P. Synthetic Studies of 2,6-Diamino-3,5-Dinitropyrazine- 1-Oxide (LLM-105) from Discovery to Multi-Kilogram Scale. *Propellants Explos. Pyrotech.* **2018**, 43, 15−27.

3. Johnson, E. C.; Bukowski, E. J.; Sabatini, J. J.; Sausa, R. C.; Byrd, E. F. C.; Garner, M. A.; Chavez, D. E. Bis(1,2,4-oxadiazolyl) Furoxan: A Promising Melt-Castable Eutectic Material of Low Sensitivity. *ChemPlusChem* **2019**, 84, 319−322.

4. Klapötke, T. M.; Krumm, B.; Unger, C. C. Energetic Metal and Nitrogen-Rich Salts of the Pentaerythritol Tetranitrate Analogue Pentaerythritol Tetranitrocarbamate. *Inorg. Chem.* **2019**, 58, 2881−2887.

5. Bolton, O.; Simke, L. R.; Pagoria, P. F.; Matzger, A. J. High Power Explosive with Good Sensitivity: A 2:1 Cocrystal of CL-20:HMX. *Cryst. Growth Des.* **2012**, 12, 4311−4314.

6. Liu, J.; Jiang, W.; Yang, Q.; Song, J.; Hao, G.-Z.; Li, F.-S. Study of Nano-Nitramine Explosives: Preparation, Sensitivity and Application. *Def. Technol.* **2014**, *10*, 184−189.

7. Qu, X. N.; Yang, Q.; Han, J.; Wei, Q.; Xie, G.; Chen, S.; Gao, S. High Performance 5-Aminotetrazole-Based Energetic MOF and its Catalytic Effect on Decomposition of RDX. *RSC Adv.* **2016**, *6*, 46212−46217.

8. Lee, J. H.; Kim, J. C.; Jeon, W. C.; Cho, S. G.; Kwak, S. K. Explosion Study of Nitromethane Confined in Carbon Nanotube Nanocontainer via Reactive Molecular Dynamics. *J. Phys. Chem. C* **2017**, *121*, 6415−6423.

9. Smeu, M.; Zahid, F.; Ji, W.; Guo, H.; Jaidann, M.; Abou-Rachid, H. Energetic Molecules Encapsulated Inside Carbon Nanotubes and between Graphene Layers: DFT Calculations. *J. Phys. Chem. C* **2011**, *115*, 10985–10989.

10. Liu, L.-M.; Car, R.; Selloni, A.; Dabbs, D. M.; Aksay, I. A.; Yetter, R. A. Enhanced Thermal Decomposition of Nitromethane on Functionalized Graphene Sheets: Ab Initio Molecular Dynamics Simulations. *J. Am. Chem. Soc.* **2012**, *134*, 19011−19016.

11. Zhang, C.; Wen, Y.; Xue, X. Self-Enhanced Catalytic Activities of Functionalized Graphene Sheets in the Combustion of Nitromethane: Molecular Dynamic Simulations by Molecular Reactive Force Field. *ACS Appl. Mater. Interfaces* **2014**, *6*, 12235−12244.

12. Um, J. E.; Yeo, T.; Choi, W.; Chae, J. S.; Kim, H. S.; Kim, W. J. Enhanced Energy Release from Homogeneous Carbon Nanotube-Energetic Material Composites. *Sci. Adv. Mater.* **2016**, *8*, 164−170.

13. Natsuki, T.; Tantrakarn, K.; Endo, M. Effects of Carbon Nanotube Structures on Mechanical Properties. *Appl. Phys. A: Mater. Sci. Process.* **2004**, *79*, 117−124.

14. Sammalkorpi, M.; Krasheninnikov, A.; Kuronen, A.; Nordlund, K.; Kaski, K. Mechanical Properties of Carbon Nanotubes with Vacancies and Related Defects. *Phys. Rev. B* **2004**, *70*, 245416.

15. Sawaya, S.; Akita, S.; Nakayama, Y. Correlation Between the Mechanical and Electrical Properties of Carbon Nanotubes. *Nanotechnology* **2007**, *18*, 035702.

16. Javey, A.; Tu, R.; Farmer, D. B.; Guo, J.; Gordon, R. G.; Dai, H. High Performance n-Type Carbon Nanotube Field-Effect Transistors with Chemically Doped Contacts. *Nano Lett.* **2005**, *5*, 345−348.

17. Maldonado, S.; Morin, S.; Stevenson, K. J. Structure, Composition, and Chemical Reactivity of Carbon Nanotubes by Selective Nitrogen Doping. *Carbon* **2006**, *44*, 1429−1437.

18. Wang, H.-M.; Wang, H.-X.; Chen, Y.; Liu, Y.-J.; Zhao, J.-X.; Cai, Q.-H.; Wang, X.-Z. Phosphorus-Doped Graphene and (8, 0) Carbon Nanotube: Structural, Electronic, Magnetic Properties, and Chemical Reactivity. *Appl. Surf. Sci.* **2013**, *273*, 302−309.

19. Han, S.-P.; van Duin, A. C. T.; Goddard, W. A. III.; Strachan, A. Thermal Decomposition of Condensed-Phase Nitromethane from Molecular Dynamics from ReaxFF Reactive Dynamics, *J. Phys. Chem. B*, **2011**, *115*, 6534−6540.

20. Liu, L.; Liu, Y.; Zybin, S.V.; Sun, H.; Goddard, W. A. III. ReaxFF-*l*g: Correction of the ReaxFF Reactive Force Field for London Dispersion, with Applications to the Equations of State for Energetic Materials. *J. Phys. Chem. A*, **2011**, *115*, 11016−11022.

21. Rom, N.; Zybin, S. V.; van Duin, A. C. T.; Goddard, W. A. III.; Zeiri, Y.; Katz, G.; Kosloff, R. Density-Dependent Liquid Nitromethane Decomposition: Molecular Dynamics Simulations Based on ReaxFF. *J. Phys. Chem. A* **2011**, *115*, 10181−10202.

22. Rom, N.; Hirshberg, B.; Zeiri, Y.; Furman, D.; Zybin, S. V.; Goddard, W. A. III.; Kosloff, R. First-Principles-Based Reaction Kinetics for Decomposition of Hot, Dense Liquid TNT from ReaxFF Multiscale Reactive Dynamics Simulations. *J. Phys. Chem. C* **2013**, *117*, 21043−21054.

23. Chaban, V. V.; Fileti, E. E.; Prezhdo, O. V. Buckybomb: Reactive Molecular Dynamics Simulation. *J. Phys. Chem. Lett.* **2015**, *6*, 913−917.

24. Strachan, A.; van Duin, A. C. T.; Chakraborty, D.; Dasgupta, S.; Goddard, W. A. III. Shock Waves in High-Energy Materials: The Initial Chemical Events in Nitramine RDX. *Phys. Rev. Lett.* **2003**, *91*, 098301.

25. Li, Z.; Huang, H.; Zhang, T.; Zhang, G.; Zhang, F. Electric-Field-Induced Structural and Electronic Changes and Decomposition of an Energetic Complex: A Computational Study on Zinc Carbohydrazide Perchlorate Crystals. *RSC Adv.*, **2015**, *5*, 22601−22608.

26. Wood, M.A.; van Duin, A. C. T.; Strachan, A. Coupled Thermal and Electromagnetic Induced Decomposition in the Molecular Explosive αHMX; A Reactive Molecular Dynamics Study, *J. Phys. Chem. A* **2014**, *118*, 885−895.

27. Wood, M.A.; Strachan, A. Nonequilibrium Reaction Kinetics in Molecular Solids, *J. Phys. Chem. C* **2016**, *120*, 542−552.

28. Guo, D.; An, Q.; Goddard, W. A. III.; Zybin, S. V.; Huang, F. Compressive Shear Reactive Molecular Dynamics Studies Indicating That Cocrystals of TNT/CL-20 Decrease Sensitivity. *J. Phys. Chem. C* **2014**, *118*, 30202–30208.

29. Sun, H.; Jin, Z.; Yang, C. W.; Akkermans, R. L. C.; Robertson, S. H.; Spenley, N. A.; Miller, S.; Todd, S. M. COMPASS II: Extended Coverage for Polymer and Drug-Like Molecule Databases. *J. Mol. Model.* **2016**, *22*, 47.

30. Materials Studio 2019; Dassault Systems BIOVIA, San Diego, 2018.

31. Plimpton, S. Fast Parallel Algorithms for Short-Range Molecular Dynamics. *J. Comput. Phys.* **1995**, *117*, 1−19.

32. Delley, B. An All-Electron Numerical Method for Solving the Local Density Functional for Polyatomic Molecules. *J. Chem. Phys.* **1990**, *92*, 508−517.

33. Delley, B. From molecules to Solids with the DMol[3] Approach. *J. Chem. Phys.* **2000**, *113*, 7756−7764.

34. Dervishi, E.; Li, Z.; Watanabe, F.; Saini, V.; Biris, A. R.; Xu, Y.; Biris, A. S. High-Aspect Ratio and Horizontally Oriented Carbon Nanotubes Synthesized by RF-cCVD. *Diam. Relat. Mater.* **2010**, *19*, 67−72.

35. Abu Al-Rub, R. K.; Ashour, A. I. Tyson, B. M. On the Aspect Ratio Effect of Multi-Walled Carbon Nanotube Reinforcements on the Mechanical Properties of Cementitious Nanocomposites. *Constr. Build. Mater.* **2012**, *35*, 647−655.

36. Lee, B.; Baek, Y.; Lee, M.; Jeong, D. H.; Lee, H. H.; Yoon, J.; Kim, Y. H. A Carbon Nanotube Wall Membrane for Water Treatment. *Nat. Commun.* **2015**, *6*, 7109.

37. Kim, H.-I.; Wang, M.; Lee, S. K.; Kang, J.; Nam, J.-D.; Ci, L.; Suhr, J. Tensile Properties of Millimeter Long Multi-Walled Carbon Nanotubes. *Sci. Rep.* **2017**, *7*, 9512.

38. Mawhinney, D. B.; Naumenko, V.; Kuznetsova, A.; Yates Jr, J. T.; Liu, J.; Smalley, R. E. Surface defect site density on single walled carbon nanotubes by titration. *Chem. Phys. Lett.* **2000**, *324*, 213−216.

39. Wiggins-Camacho, J. D.; Stevenson, K. J. Effect of Nitrogen Concentration on Capacitance, Density of States, Electronic Conductivity, and Morphology of N-Doped Carbon Nanotube Electrodes. *J. Phys. Chem. C* **2009**, 113, 19082−19090.

40. Berendsen, H. J. C.; Postma, J. P. M.; Vangunsteren, W. F.; Dinola, A.; Haak, J. R. Molecular-Dynamics with Coupling to an External Bath. *J. Chem. Phys.* **1984**, *81*, 3684−3690.

41. Connolly, M. L. Solvent-Accessible Surfaces of Proteins and Nucleic Acids. *Science* **1983**, *221*, 709−713.

42. van Duin, A. C. T.; Dasgupta, S.; Lorant, F.; Goddard W. A. III. ReaxFF: A Reactive Force Field for Hydrocarbons. *J. Phys. Chem. A* **2001**, *105*, 9396−9409.

43. van Duin, A. C. T.; Zeiri, Y.; Dubnikova, F.; Kosloff, R.; Goddard W. A. III. Atomistic-Scale Simulations of the Initial Chemical Events in the Thermal Initiation of Triacetonetriperoxide. *J. Am. Chem. Soc*. **2005**, *127*, 11053−11062.

44. Budzien, J.; Thompson, A. P.; Zybin, S. V. Reactive Molecular Dynamics Simulations of Shock Through a Single Crystal of Pentaerythritol Tetranitrate. *J. Phys. Chem. B* **2009**, *113*, 13142−13151.

45. Guo, F.; Cheng, X.; Zhang, H. Reactive Molecular Dynamics Simulation of Solid Nitromethane Impact on (010) Surfaces Induced and Nonimpact Thermal Decomposition. *J. Phys. Chem. A* **2012**, *116*, 3514−3520.

46. Wood, M. A.; van Duin, A. C. T.; Strachan, A. Coupled Thermal and Electromagnetic Induced Decomposition in the Molecular Explosive αHMX; A Reactive Molecular Dynamics Study. *J. Phys. Chem. A* **2014**, *118*, 885–895.

47. Zhang, C.; Wen, Y.; Xue, X. Self-Enhanced Catalytic Activities of Functionalized Graphene Sheets in the Combustion of Nitromethane: Molecular Dynamic Simulations by Molecular Reactive Force Field. *ACS Appl. Mater. Interfaces* **2014**, *6*, 12235−12244.

48. Guo, D.; An, Q.; Zybin, S. V.; Goddard, W. A. III; Huang, F.; Tang, B. The Co-Crystal of TNT/CL-20 Leads to Decreased Sensitivity Toward Thermal Decomposition from First Principles Based Reactive Molecular Dynamics. *J. Mater. Chem. A* **2015**, *3*, 5409−5419.

49. Kabbani, M. A.; Tiwary, C. S.; Autreto, P. A. S.; Brunetto, G.; Som, A.; Krishnadas, K. R.; Ozden, S.; Hackenberg, K. P.; Gong, Y.; Galvao, D. S.; Vajtai, R.; Kabbani, A. T.; Pradeep, T.; Ajayan, P. M. Ambient Solid-State Mechano-Chemical Reactions Between Functionalized Carbon Nanotubes. *Nat. Commun.* **2015**, *6*, 7291.

50. Wood, M. A.; Dalvit, D. A. R.; Moore, D. S. Nonlinear Electromagnetic Interactions in Energetic Materials. *Phys. Rev. Applied* **2016**, *5*, 014004.

51. Furman, D.; Dubnikova, F.; van Duin, A. C. T.; Zeiri, Y.; Kosloff, R. Reactive Force Field for Liquid Hydrazoic Acid with Applications to Detonation Chemistry. *J. Phys. Chem. C* **2016**, *120*, 4744−4752.

52. Zhou, T.; Song, H.; Liu, Y.; Huang F. Shock initiated thermal and chemical responses of HMX crystal from ReaxFF molecular dynamics simulation. *Phys. Chem. Chem. Phys*. **2014**, *16*, 13914−13931.

53. Perdew, J. P.; Burke, K.; Ernzerhof, M. Generalized Gradient Approximation Made Simple. *Phys. Rev. Lett.* **1996**, *77*, 3865−3868.

54. Tkatchenko, A.; Scheffler, M. Accurate Molecular van Der Waals Interactions from Ground-State Electron Density and Free-Atom Reference Data. *Phys. Rev. Lett.* **2009**, *102*, 073005.

55. Bell, S.; Crighton, J. S. Locating Transition-States. *J. Chem. Phys.* **1984**, *80*, 2464−2475.

56. Halgren, T. A.; Lipscomb, W. N. The Synchronous-Transit Method for Determining Reaction Pathways and Locating Molecular Transition-States. *Chem. Phys. Lett.* **1977**, *49*, 225−232.

57. Talukdar, K.; Agrawala, R.; Mitra, A. K. Dependence of Mechanical Characteristics and the Fracture and Buckling Behavior of Single-Walled Carbon Nanotubes on Their Geometry. *New Carbon Mater.* **2011**, *26*, 408–416.

58. Jensen, B. D.; Wise, K. E.; Odegard, G. M. The Effect of Time Step, Thermostat, and Strain Rate on ReaxFF Simulations of Mechanical Failure in Diamond, Graphene, and Carbon Nanotube. *J. Comput. Chem*. **2015**, *36*, 1587−1596.

3.3 Effect of Co-encapsulation of Nitromethane and Detonating Molecule

This chapter includes the published contents:

3.3.1 Introduction

In the defense industry, high-energy materials (HEMs) are steadily developed and applied for explosive, propellant, and pyrotechnic applications for their superior explosive properties. Among the HEMs, explosives are detonated by external impact, such as physical or chemical shock, and invoke subsequent explosive reactions, while generating an instantaneous shock wave. For practical and safe use, the sensitivity of HEMs to external stimuli should be sufficiently low. However, the stability and reactivity of explosive compete; if one property is improved, the other deteriorates. To overcome this limitation, up to these days, several researchers have attempted to synthesize new HEMs[1-3] or construct new types of composites, in which the structures of conventional HEMs are controlled at the nanoscale.[4,5]

The nanobomb is another type of nanostructured complex that can improve the explosion properties of HEMs. In our previous study, the nanobomb model, in which compressed NM was encapsulated inside a CNT vessel, was proposed to improve the explosion power and stability of NM.[6] In the nanobomb structure, synergistic effects between NM and CNT were expected such that the confined NM was not only stabilized at ambient condition,[7] but also decomposed rapidly at bursting.[8,9] However, owing to the increased stability of the surrounding container, the nanobomb required pressurized NM or high thermal-shock energy for bursting. Therefore, we have investigated alternative ways to improve the explosion characteristics by supporting the decomposition of NM. In general, an explosive device is equipped with detonator to trigger the explosive reaction the less-sensitive HEM. To mimic this concept at the molecular scale and consequently enhance the explosion performance of the nanobomb, we herein aim to propose a detonator-integrated nanobomb.

Detonators deliver reaction energy through their high pressure and velocity. Thus, when external stimuli are exerted on the explosive device, they first decompose and generate a shock wave to initiate the chain reaction. Until recently, several mixture models, in which explosive and detonating molecules coexist, have been suggested to improve explosion characteristics. Guo et al. showed that CL–20

exhibited excellent detonating properties with reduced sensitivity when co-crystallized with TNT, compared to those of pure crystal of CL–20.[10] Li and his coworkers found that RDX decomposed more completely than pure RDX at the same decomposition temperature when RDX existed as a composite with AlH$_3$ nanoparticles.[11] Other studies[12-15] have also shown that the coexistence of detonators and explosives could modulate the explosive power and sensitivity. Therefore, it would be possible to design new nanobomb with improved detonating speed of NM with guaranteed stability in CNT with NM loaded with a detonating molecule.

In this study, to improve the bursting kinetics of a nanobomb without the loss of structural stability of the container, we employed a molecular-scale detonator mixed with NM. To address the reaction characteristics of the nanobomb, we investigated how the nanobomb is decomposed by thermal shock according to the existence of detonators by tracking the reaction rate and investigating the bursting mechanism. First, the candidate detonating molecules were screened to check their applicability to nanobombs by estimating their detonating properties by DFT calculations. In addition, bulk mixtures of the NM and detonating molecule were prepared, and decomposed using NERMD at high temperatures. The changes in the energetics and species of molecules were compared to those in pure NM. After that, the detonating molecules were selected for the nanobomb as a mixture with NM. Their explosion kinetics were investigated depending on the composition of molecules and variation of heat-up temperature with NERMD simulations. Finally, we analyzed how the decomposed intermediates in the initial reaction mechanism affected the reaction kinetics of NM.

3.3.2 Simulation Details

3.3.2.1 DFT

The detonation velocity (D in km s^{-1} unit) and detonation pressure (P in GPa unit) of candidate material were calculated using Kamlet–Jacobs (K–J) equations, as follows[16]:

$$D = 1.01\left(N\bar{M}^{1/2}Q^{1/2}\right)^{1/2}(1+1.30\rho_0),$$
(3.3.1)

$$P = 1.558\rho_0^{\,2}N\bar{M}^{1/2}Q^{1/2},$$
(3.3.2)

where N is the moles of gas produced per gram of explosives, $\bar{M}$ is the average molar weight of detonation product (in g mol^{-1} unit), Q is the energy of detonation (in kJ g^{-1} unit) acquired from heat of formation, and ρ_0 is the packed density (in g cm^{-3} unit). According to the previous work done by Gui-xiang et al., N, $\bar{M}$, and Q could be estimated considering the elemental composition of the detonating molecules (**Table 3.3.1**).[17] For the detonating molecule composed of C, H, O, and N elements, the

amount and kinds of final products are varied by the stoichiometric ratio in the molecule. Oxygen, in particular, participates in producing several stable species, such as H_2O, CO_2, and O_2. Therefore, three stoichiometric conditions of oxygen (*i.e.* c in **Table 3.3.1**) compared to other elements were considered. To calculate the heat of formation, diamond, nitrogen gas, oxygen gas, and hydrogen gas were assumed as the reference products for each carbon, nitrogen, oxygen, and hydrogen atom, respectively. We considered NM and five species of detonating molecule (*i.e.* HMX, HNS, PETN, RDX, and TNT), which have excellent detonating properties, for DFT calculations, referring to the previous study (**Figure 3.3.1**).[18]

Table 3.3.1 Theoretical N, $\bar{M}$, and Q values depending on the stoichiometric ratio of detonating molecule composed of $C_aH_bO_cN_d$. Copyright © 2019, The Korean Society of Industrial and Engineering Chemistry. Published by Elsevier B.V.

Parameter	Range of stoichiometric ratio		
	$c \geq 2a + b/2$	$2a + b/2 \geq c \geq b/2$	$b/2 \geq c$
N	(b + 2c + 2d)/4M	(b + 2c + 2d)/4M	(b + d)/4M
$\bar{M}$	4M/(b + 2c + 2d)	(56d + 88c - 8c)/(b + 2c + 2d)	(2b + 28d + 32c)/(b + d)
$Q \times 10^{-3}$	(28.9b + 94.05a + 0.239$\Delta H_f°$)/M	[28.9b + 94.05(c/2 - b/4) + 0.239$\Delta H_f°$]/M	(57.8c + 0.239$\Delta H_f°$)/M

NM
(CH$_3$NO$_2$)

HMX
(C$_4$H$_8$N$_8$O$_8$)

HNS
(C$_{14}$H$_6$N$_6$O$_{12}$)

PETN
(C$_5$H$_8$N$_4$O$_{12}$)

RDX
(C$_3$H$_6$N$_6$O$_6$)

TNT
(C$_7$H$_5$N$_3$O$_6$)
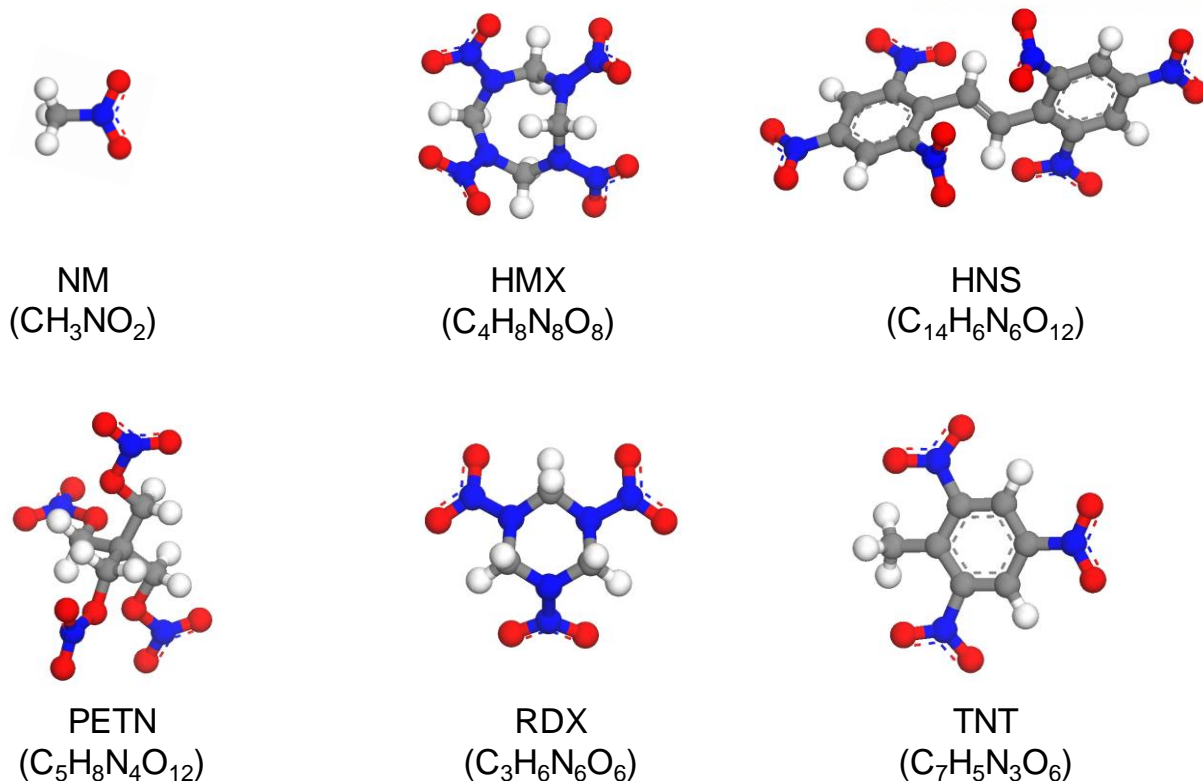
Figure 3.3.1 Explosive and detonating molecules considered in this study. The carbon, oxygen, nitrogen, and hydrogen atoms are colored in gray, red, blue, and white, respectively. Copyright © 2019, The Korean Society of Industrial and Engineering Chemistry. Published by Elsevier B.V.

DFT calculations were carried out to investigate the heat of formation of the detonating molecules using Dmol^3 program[19,20] in Materials Studio 2019 package[21]. For the DFT calculations, we employed PBE[22] exchange–correlation functional and DNP 4.4 basis set with all-electron core treatment. To consider van der Waals interactions of detonating molecules, TS dispersion correction[23] was applied. The convergence criteria for the energy, force, and displacement were set to 1×10^{-5} Ha, 0.002 Ha/Å, and 0.005 Å, respectively.

3.3.2.2 RMD

To evaluate the detonators' enhancing effects on nanobomb, RMD simulations were conducted on LAMMPS package[24] using bulk liquid mixture systems and nanobomb systems. In this study, ReaxFF parameters, which were used for the simulation of the decomposition reaction of the bulk NM at different densities[25], were applied for RMD simulations. For the bulk system, 200 NM molecules with some portion of additional detonating molecules were randomly packed in a cubic simulation cell. The compositions of NM and detonating molecules were considered in two weight ratios (*i.e.* 75:25 and 50:50) (**Figure 3.3.2**), and their equilibrium densities were acquired *via* 50 ps of NPT-MD simulation at ambient condition. After the detonating molecules are selected through assessment of the bulk systems, periodic (20, 20) pristine CNT (the number of carbon atoms in CNT: 2400) was relaxed in the first step of nanobomb construction. To reduce the strain effect in the periodic direction of CNT, the models were relaxed by COMPASS II force field[26] and ReaxFF force field, consecutively. Next, RMD simulations were conducted for 50 ps at 298 K and 1 atm *via* $NP_{zz}T$ ensemble while fixing the length of the x and y axes of each system. Then, pure NM or mixtures of NM and detonating molecules were randomly packed inside the CNT considering the equilibrium density. To relax the nanobomb system, the entire structure was optimized, followed by *NVT*–RMD simulation for 100 ps at 298 K (**Figure 3.3.3**).

To observe the decomposition phenomena of bulk and nanobomb systems, two different simulation procedures were considered. For the bulk system, the temperature of each system was rapidly raised to the target temperature (*i.e.* 2000, 2500, and 3000 K) within a short simulation time (100 fs). After that, the *NVT*–NERMD simulation was conducted for 200 ps. In contrast, for the nanobomb system, thermal shock was applied to nanobomb. In the thermal-shock-induced bursting, the NM and detonating molecules were indirectly heated by the CNT nanocontainer, which was assumed to be a heat source. The heating process continued until the average temperature of the contents reached to the target temperature (*i.e.* heat-up period). Next, the *NVE*–NERMD simulation was conducted for 300 ps in total while conserving the total energy of the system (*i.e.* decomposition period). Time step for all RMD simulations was set to 0.1 fs.
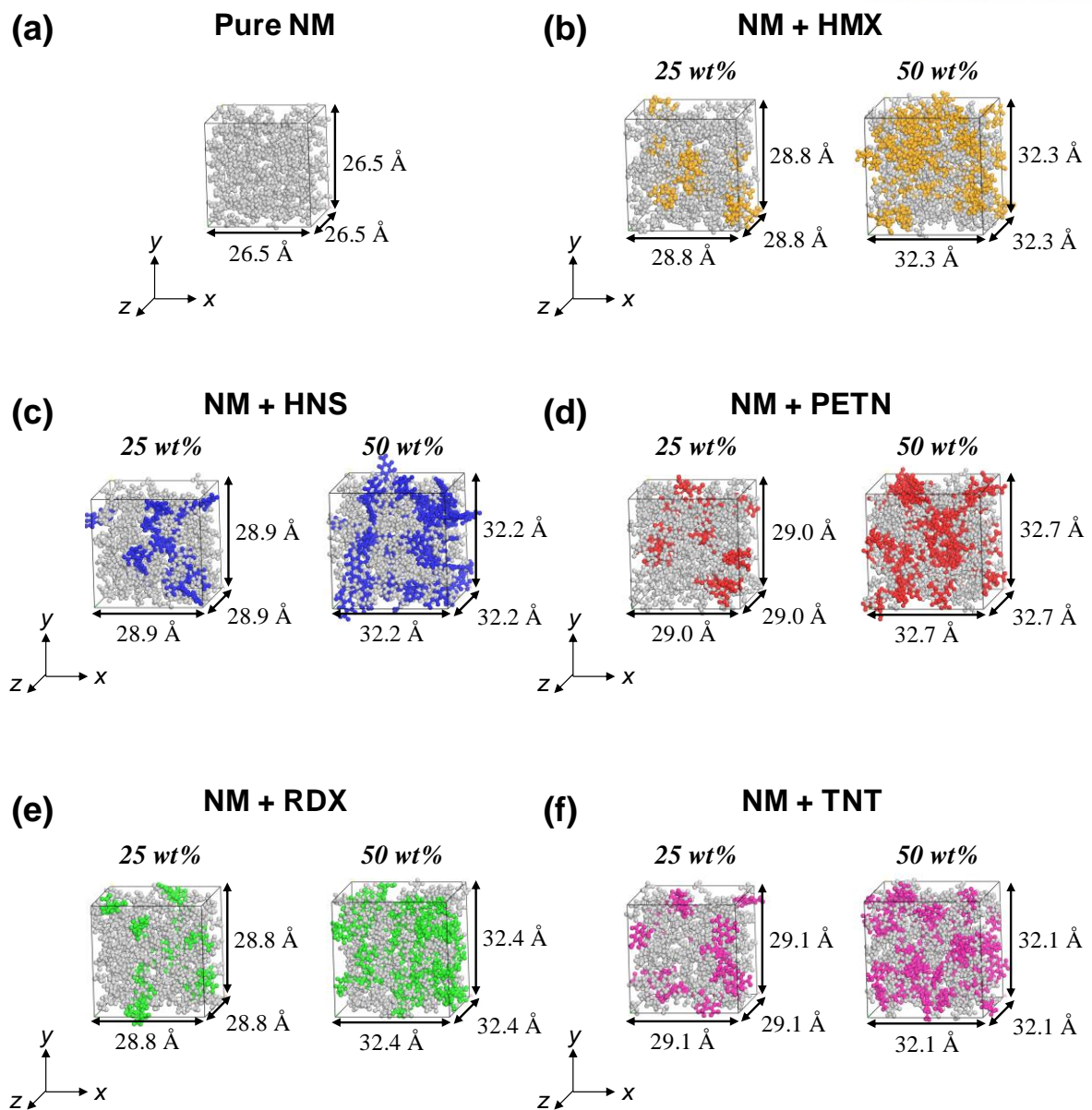
Figure 3.3.2 Relaxed bulk systems of pure NM and mixtures. (a) Pure NM bulk system. (b) HMX-mixed bulk systems. (c) HNS-mixed bulk systems. (d) PETN-mixed bulk systems. (e) RDX-mixed bulk systems. (f) TNT-mixed bulk systems. The values of lattice parameter are written with arrows. NM, HMX, HNS, PETN, RDX, and TNT are colored in light gray, orange, blue, red, green, and magenta, respectively. Copyright © 2019, The Korean Society of Industrial and Engineering Chemistry. Published by Elsevier B.V.

(a) *Pure NM*

75.2 Å

28.8 Å

(b) *25 wt % HMX*

(c) *50 wt % HMX*
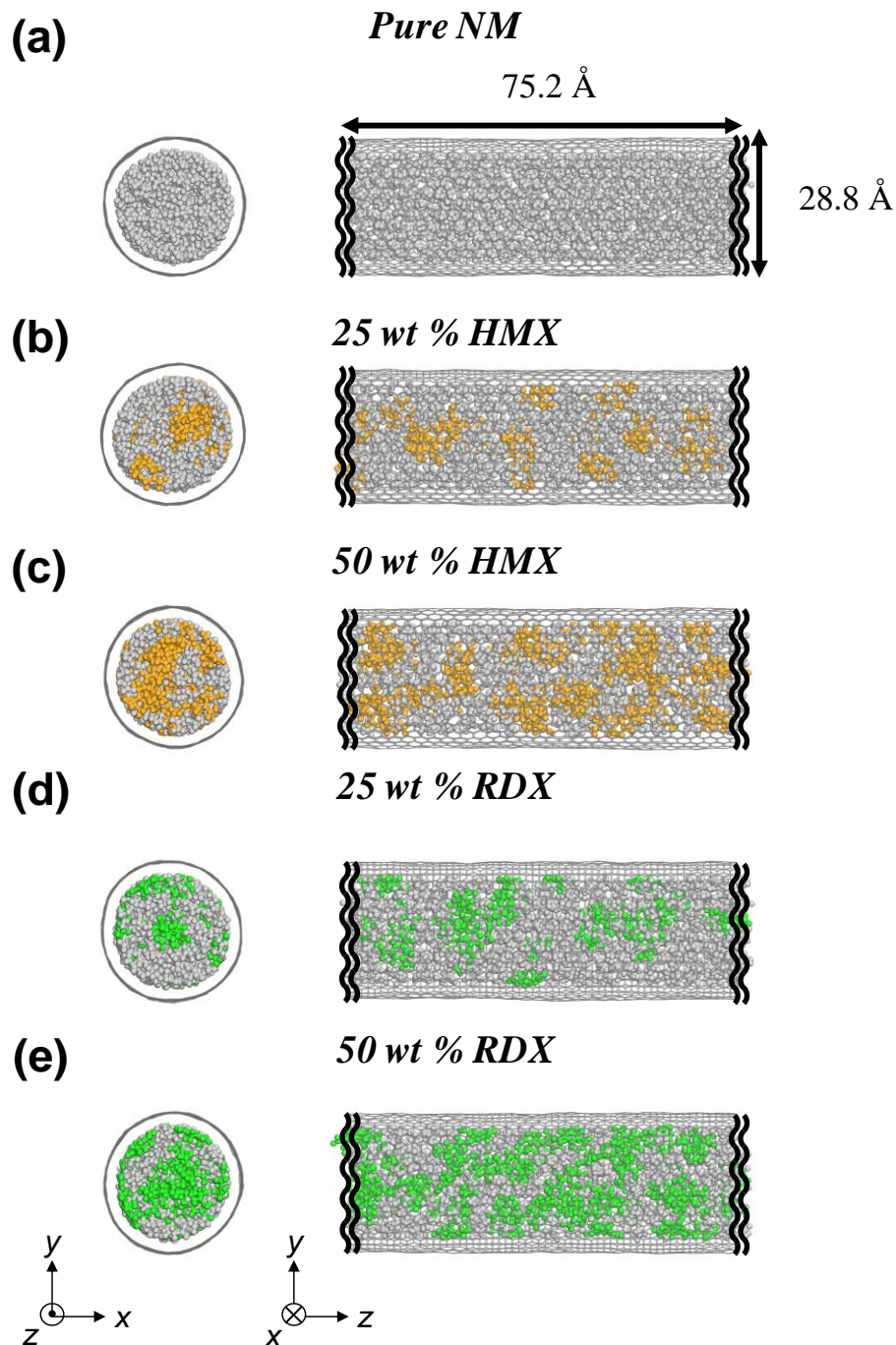
(d) *25 wt % RDX*

(e) *50 wt % RDX*

Figure 3.3.3 Front (left) and side views (right) of relaxed nanobomb models. (a) Pure NM nanobomb. (b) 25 wt% HMX-mixed nanobomb. (c) 50 wt% HMX-mixed nanobomb. (d) 25 wt% RDX-mixed nanobomb. (e) 50 wt% RDX-mixed nanobomb. The values of diameter and periodic length of CNT are written on the side view of (a), and the others are identical to (a). CNTs are colored in dark gray depicted with line and NM, HMX, and RDX are colored in light gray, orange, and green depicted with ball-and-stick. Copyright © 2019, The Korean Society of Industrial and Engineering Chemistry. Published by Elsevier B.V.

3.3.3 Results and Discussion

3.3.3.1 Selection of Detonating Molecule

To improve the bursting performance of the nanobomb, the appropriate detonating molecule must be chosen and encapsulated inside the CNT nanocontainer. The most important criteria for evaluating the performance of detonating molecule are the detonation velocity (D in km s^{-1} unit) and pressure (P in GPa unit). D and P are the velocity and pressure emitted from shock wave energy when the external shock is applied to the detonating molecules. Detonating molecules with high D and P values become quickly spread out and release strong shock wave energy. Therefore, they can promote the activation of surrounding explosives, improving explosion performance. Several widely employed explosives composed of CHON elements were chosen from literature[18], and their detonation properties were calculated *via* the DFT method. **Table 3.3.2** summarizes the calculated results of D and P, as well as the molecular properties employed in the K–J equation. Among the detonating molecules, molecules with aromatic ring (*i.e.* HNS and TNT) exhibited relatively low and weak D and P values, whereas saturated ring molecules containing nitrogen (*i.e.* RDX and HMX) had high and strong D and P values. Based on the theoretical detonation properties, RDX and HMX were expected to enhance the bursting performance of the nanobomb when mixed with NM.

Table 3.3.2 Thermodynamic and detonating properties of detonating molecules employed in this study. Copyright © 2019, The Korean Society of Industrial and Engineering Chemistry. Published by Elsevier B.V.

Detonating molecule	ΔH_f° (kJ/mol)	ρ_0 (g/cm^3)	N	$\overline{M}$ (g/mol)	Q (kJ/g)	D (km/s)	P (GPa)
NM	-11.98	1.137	0.0368	23.1	1406.14	6.451	13.384
HMX	157.13	1.91	0.0338	27.2	1542.62	9.249	39.312
HNS	144.01	1.70	0.0233	32.0	1401.64	7.203	22.239
PETN	-102.95	1.77	0.0316	30.4	1332.72	8.411	32.078
RDX	131.21	1.86	0.0338	27.2	1521.69	9.039	36.948
TNT	-276.50	1.65	0.0253	28.5	1192.67	6.874	19.901

Before we apply detonating molecules to the nanobomb, the enhancing effects were investigated on a bulk liquid mixture with NM. Liquid mixtures of NM and detonating molecules were modeled by considering two composition ratios (*i.e.* 75:25 and 50:50 weight ratio in the total system), and were relaxed at room temperature to acquire the equilibrium density of mixture (**Table 3.3.3**). Decomposition phenomena were observed by heating the bulk systems to 2000, 2500, and 3000 K, respectively, using *NVT*–NERMD simulations. **Figure 3.3.4** shows the decomposition rate of NM in the bulk systems depending on the temperature and composition ratio. The decomposition of NM was accelerated in most mixture systems due to the fast reaction of the detonating molecule compared to NM (**Table 3.3.4**). In contrast to almost intact NM molecules at 2000 K, for example, HMX was completely decomposed within 6 ps. As expected in the detonation properties *via* DFT calculations, the decomposition rates of NM, as well as those of the detonating molecule itself, were observed in the order of HMX, RDX, PETN, HNS, and TNT. Note that under the high-temperature heating, all species, regardless of NM and detonating molecule, were rapidly decomposed by excessive heat energy.

Table 3.3.3 Number of molecules (N_{t0}) and density of bulk mixture systems at the initial step. Copyright © 2019, The Korean Society of Industrial and Engineering Chemistry. Published by Elsevier B.V.

Model system (wt%)		N_{t0}		Density (g/cm^3)
		NM	Detonating molecule	
Pure NM		200	-	1.0837
HMX	25	200	14	1.1373
	50	200	41	1.1986
HNS	25	200	9	1.1196
	50	200	27	1.2175
PETN	25	200	13	1.1102
	50	200	39	1.1611
RDX	25	200	18	1.1289
	50	200	55	1.1924
TNT	25	200	18	1.1017
	50	200	54	1.2255

Figure 3.3.4 Molecular fraction of NM in the bulk systems over simulation time for 200 ps. (a)–(c) Decomposition of 25 wt% mixture at (a) T = 2000 K, (b) T = 2500 K, and (c) T = 3000 K. (d)–(f) Decomposition of 50 wt% mixture at (d) T = 2000 K, (e) T = 2500 K, and (f) T = 3000 K. Copyright © 2019, The Korean Society of Industrial and Engineering Chemistry. Published by Elsevier B.V.

Table 3.3.4 Time (in ps unit) for the detonating molecule to be completely decomposed from each bulk mixture system. Copyright © 2019, The Korean Society of Industrial and Engineering Chemistry. Published by Elsevier B.V.

Model system (wt%)		T = 2000 K	T = 2500 K	T = 3000 K
HMX	25	2.8	0.4	0.1
	50	5.7	1.2	<0.1
HNS	25	174.2	16.7	6.8
	50	177.3	34.8	12.9
PETN	25	8.5	1.2	0.2
	50	9.8	2.4	0.6
RDX	25	3.8	1.0	0.3
	50	3.5	1.4	0.5
TNT	25	>200	39.9	16.4
	50	>200	42.9	11.7

To directly compare the effect of the detonator on the energy-emitting performance, time evolutions of the total potential energy (PE) were investigated (**Figure 3.3.5**). Because of the initial endothermic reaction and following exothermic reactions, the PE curves increased slightly and then decreased significantly with time. In contrast to the rates of NM decomposition, which were similar to each other regardless of detonator at high temperature heating, changes in PE curve were prominently different depending on the types of detonating molecule. HMX- and RDX-containing systems exhibited huge heat release during decomposition and differences increased as the composition of detonating molecule increased. On the other hand, mixture systems with HNS and TNT showed similar heat of reaction with pure NM system at 2000 and 2500 K and showed much lower heat release at 3000 K. These differences increased as the composition of detonating molecule increased. For the PETN, even though the D and P values were similar to those of HMX and RDX, weak heat was released from the mixture system compared to that of HMX- and RDX-containing systems.
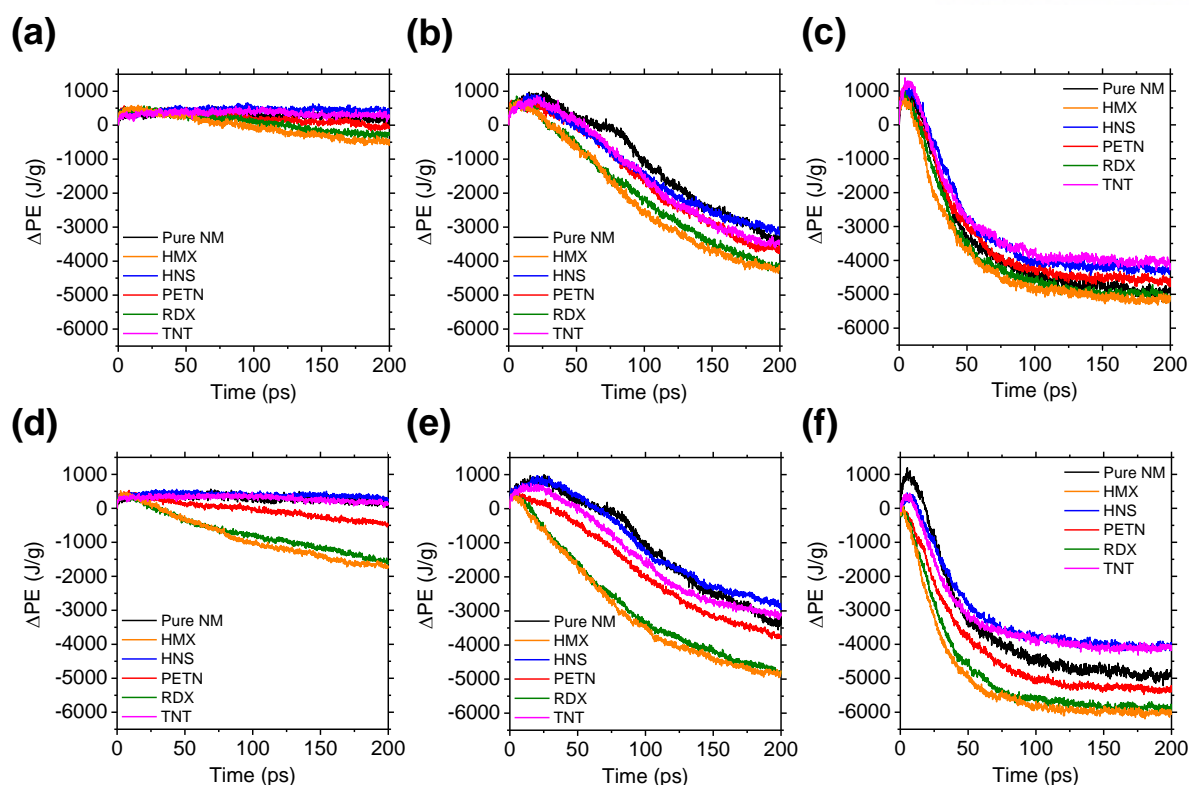
Figure 3.3.5 PE curves of the bulk systems by the simulation time for 200 ps. (a)–(c) Decomposition of 25 wt% mixture at (a) T = 2000 K, (b) T = 2500 K, and (c) T = 3000 K. (d)–(f) Decomposition of 50 wt% mixture at (d) T = 2000 K, (e) T = 2500 K, and (f) T = 3000 K. Copyright © 2019, The Korean Society of Industrial and Engineering Chemistry. Published by Elsevier B.V.

As in the PE curves depending on the type of detonating molecule, these differences were also observed in the time evolution of the formation of water molecules. In our previous study,[6] the formation of water molecules among several reaction products made from pure NM was found to be closely related to the heat of reaction. For the mixture of detonating molecules, this trend was also applied, as depicted in **Figure 3.3.6**. The amount of water produced was scaled by the total weight of each mixture system. At the conditions of 2000 K and 25 wt% detonating molecule, water molecules were produced rapidly when NM was mixed with HMX, RDX, and PETN. As the ratio of detonating molecules was increased to 50 wt%, prominent increments at HMX and RDX were observed. These trends were more remarkable at 2500 K. However, note that as the reaction progressed further at 3000 K, the relative amount of water in all mixture systems was less than that in the pure NM system. Furthermore, at the conditions of 3000 K, the water slightly decomposed after it reached its maximum quantity due to further reaction to other products.
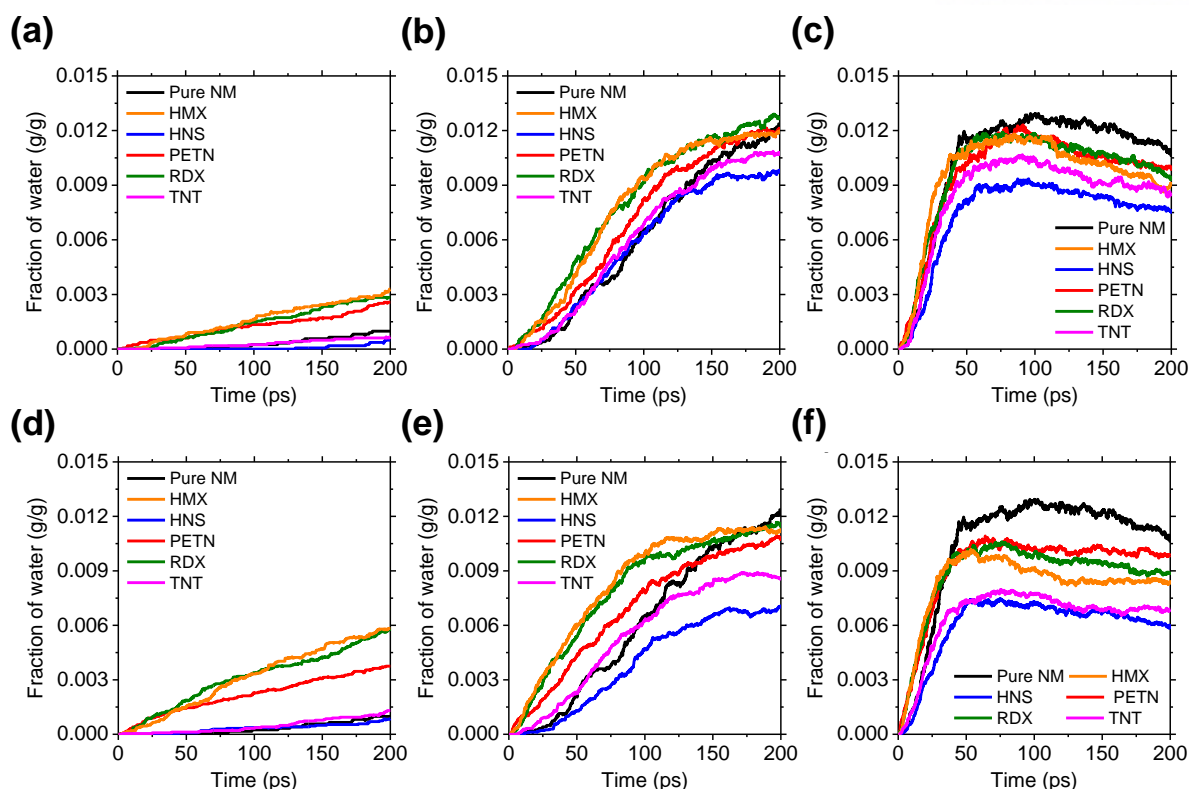
Figure 3.3.6 Fractions of produced water from the bulk systems by the simulation time for 200 ps. Decomposition of 25 wt% mixture at (a) T = 2000 K, (b) T = 2500 K, and (c) T = 3000 K. Decomposition of 50 wt% mixture at (d) T = 2000 K, (e) T = 2500 K, and (f) T = 3000 K. Copyright © 2019, The Korean Society of Industrial and Engineering Chemistry. Published by Elsevier B.V.

3.3.3.2 Construction of Detonator-integrated Nanobomb

Considering the enhancement effect of HMX and RDX in the bulk mixture, nanobombs encapsulating HMX and RDX with NM together were constructed, respectively. Improved nanobombs were also constructed with two composition ratios, and their packing densities inside the nanocontainer were obtained from the *NPT*–MD simulation of each mixture at room temperature (**Table 3.3.5**). To evaluate the enhancement effect on the bursting performance of nanobombs, thermal-shock-induced bursting was studied. From the heat-up period to the decomposition period, the temperature of the contents (*i.e.* NM and detonating molecule) continuously increased with some changes in slope with the propagation of the simulation (**Figure 3.3.7**). In the first stage of the temperature profile, via numerous collisions of contents to the CNT, the thermal energy of the container was transferred to the contents to be heated from room temperature to the reaction temperature, accompanying some fraction of decomposition of the explosives. Then, by implementing *NVE* simulation to the nanobomb, the NM

and detonating molecules were decomposed to produce many water molecules as well as other species, and their PE was converted to thermal energy to increase the system temperature (second stage). In the final stage of the reaction, for the system heated to 3000 K, a sudden increase in temperature occurred due to the bursting nanobomb with the expulsion of reaction intermediates.

Table 3.3.5 Number of molecules (N_{t0}) and density of the contents in nanobomb systems at the initial step. Copyright © 2019, The Korean Society of Industrial and Engineering Chemistry. Published by Elsevier B.V.

Model system (wt%)		N_{t0}		Density (g/cm^3)
		NM	Detonating molecule	
Pure NM		374	-	1.0837
HMX	25	296	21	1.1373
	50	210	43	1.1986
RDX	25	299	27	1.1289
	50	209	57	1.1924
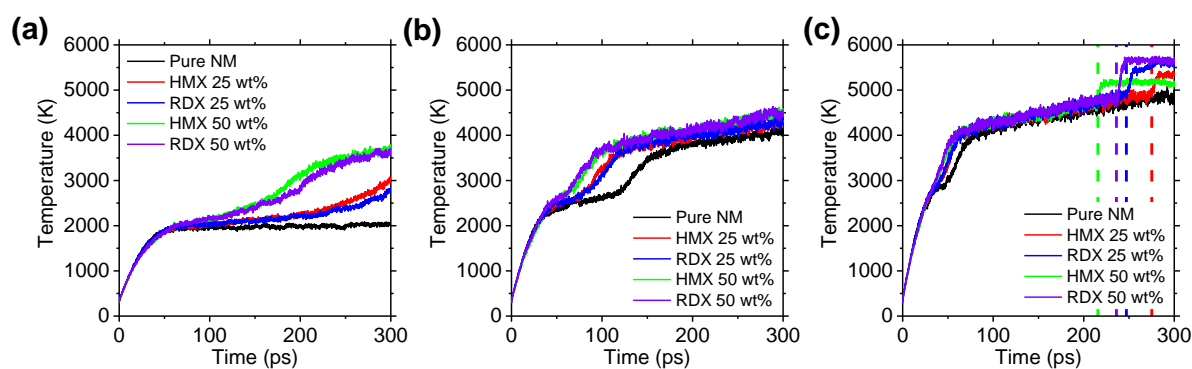
Figure 3.3.7 Temperature profiles of the contents in nanobomb systems for heating temperatures of (a) T = 2000 K, (b) T = 2500 K, and (c) T = 3000 K. Vertical dashed lines in (c) represent the bursting time. Copyright © 2019, The Korean Society of Industrial and Engineering Chemistry. Published by Elsevier B.V.

To further investigate the detonator-induced change in reaction mechanism, reaction intermediates produced during the heat-up period were scrutinized. As observed in the bulk liquid mixture, while the contents were heated from room temperature to bursting temperature, the detonator-mixed nanobomb exhibited an accelerated decomposition rate of NM due to the fast decomposition rate of the detonating molecule compared to that of NM (**Figure 3.3.8－3.3.10**). Within the heat-up period, HMX and RDX were completely decomposed, whereas half of NM molecules were reacted at most. Note that the effect of the detonating molecule mixing was pronounced at low temperature, but the higher the temperature, the less the effect of mixing due to the excessively high temperature.
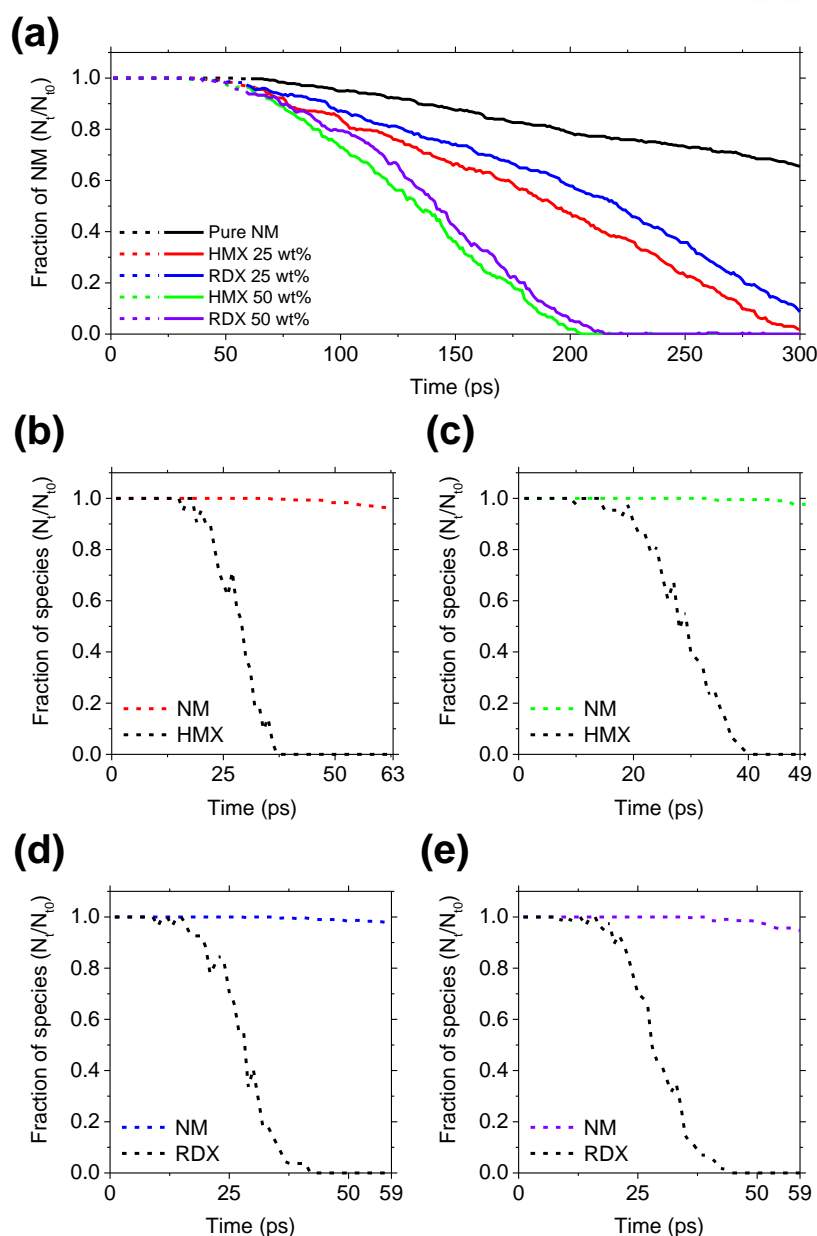
Figure 3.3.8 Fractions of the contents in nanobomb at a heating temperature of 2000 K. (a) Fractions of NM during decomposition simulation (*i.e.* heat-up and decomposition periods). Fractions of NM and HMX of (b) 25 wt% and (c) 50 wt% HMX-mixed nanobomb during the heat-up period. Fractions of NM and RDX of (d) 25 wt% and (e) 50 wt% RDX-mixed nanobomb during the heat-up period. For clarity, the heat-up and decomposition periods are represented by dashed and solid lines, respectively. Copyright © 2019, The Korean Society of Industrial and Engineering Chemistry. Published by Elsevier B.V.
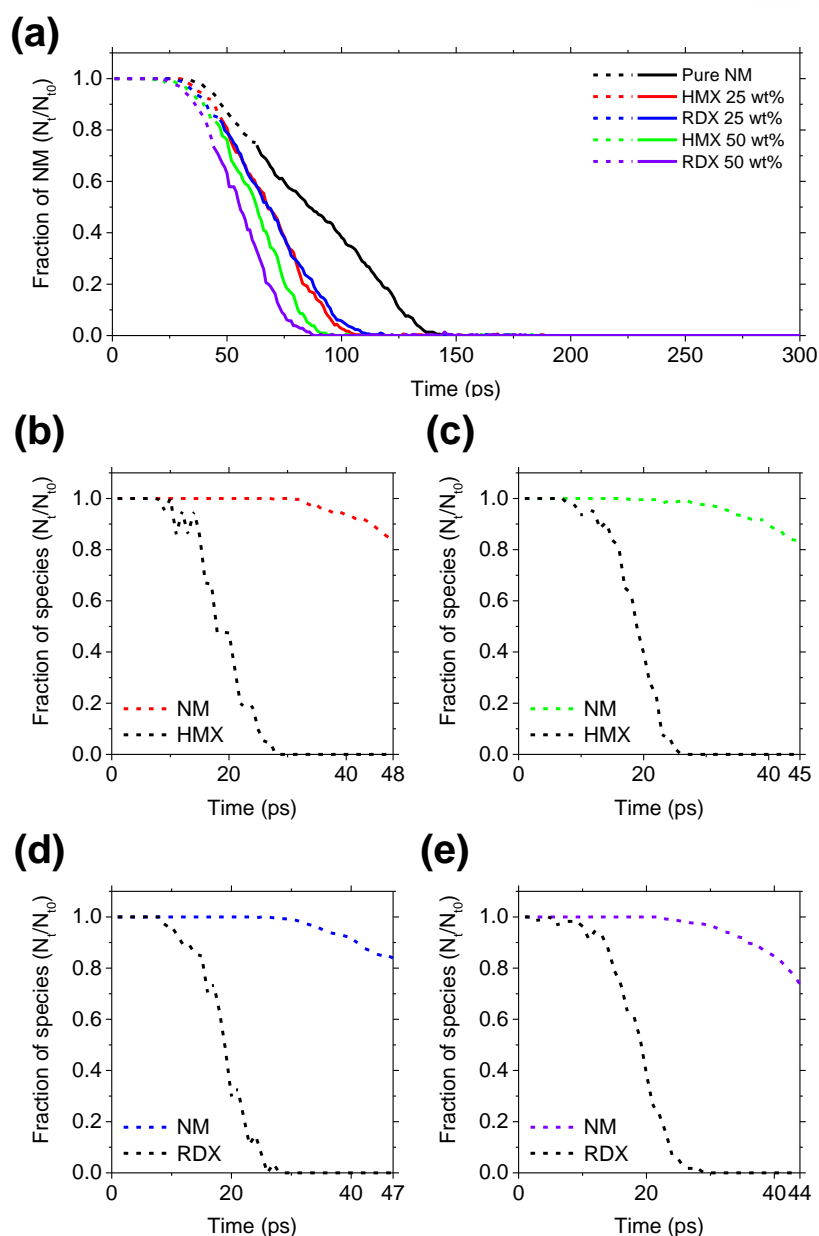
Figure 3.3.9 Fractions of the contents in nanobomb at a heating temperature of 2500 K. (a) Fractions of NM during decomposition simulation (*i.e.* heat-up and decomposition periods). Fractions of NM and HMX of (b) 25 wt% and (c) 50 wt% HMX-mixed nanobomb during the heat-up period. Fractions of NM and RDX of (d) 25 wt% and (e) 50 wt% RDX-mixed nanobomb during the heat-up period. For clarity, the heat-up and decomposition periods are represented by dashed and solid lines, respectively. Copyright © 2019, The Korean Society of Industrial and Engineering Chemistry. Published by Elsevier B.V.
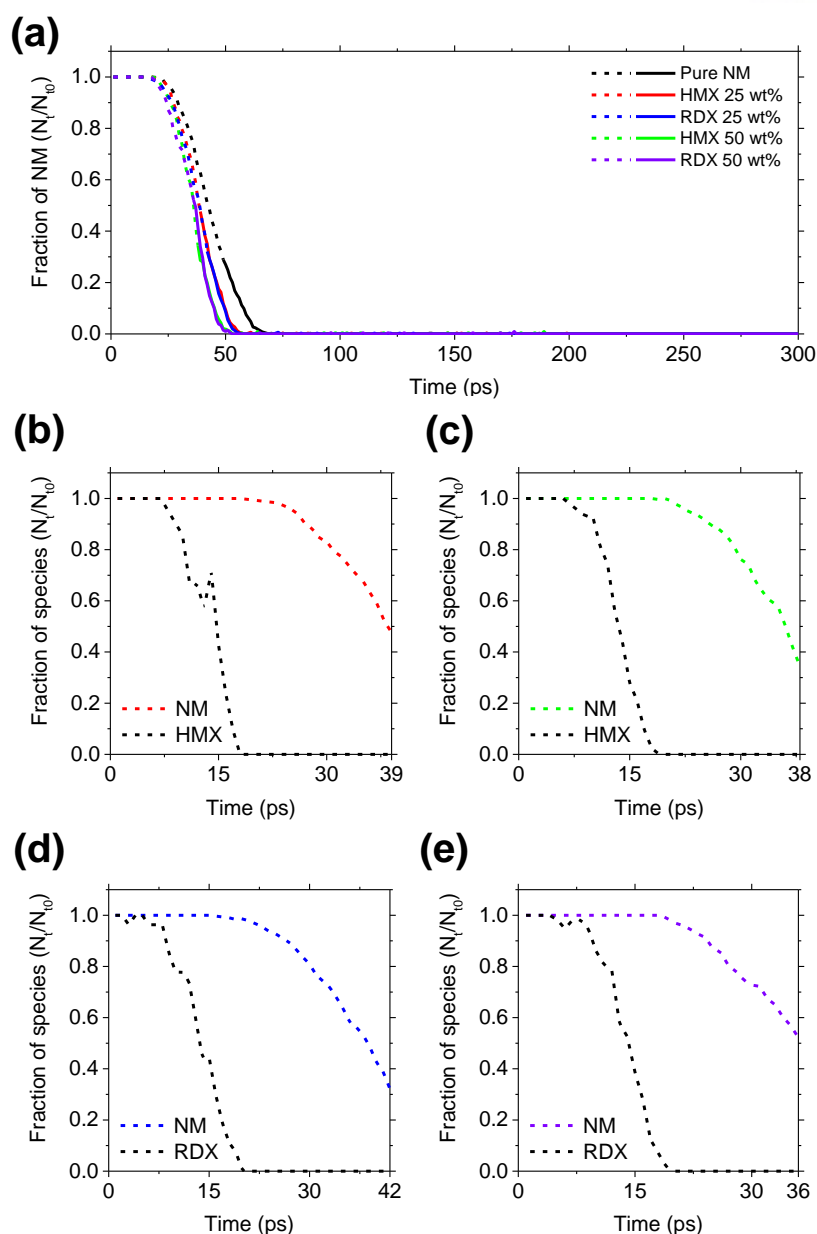
Figure 3.3.10 Fractions of the contents in nanobomb at a heating temperature of 3000 K. (a) Fractions of NM during decomposition simulation (*i.e.* heat-up and decomposition periods). Fractions of NM and HMX of (b) 25 wt% and (c) 50 wt% HMX-mixed nanobomb during the heat-up period. Fractions of NM and RDX of (d) 25 wt% and (e) 50 wt% RDX-mixed nanobomb during the heat-up period. For clarity, the heat-up and decomposition periods are represented by dashed and solid lines, respectively. Copyright © 2019, The Korean Society of Industrial and Engineering Chemistry. Published by Elsevier B.V.

In the reaction intermediate, the most obvious change when the HMX and RDX were added to the nanobomb was the fast and large formation of NO_2 and CH_2N molecules, which were made by dissociation of the N–N and C–N bonds of each detonating molecule (see the following equations and **Figure 3.3.11** and **3.3.12**), consistent with the RDX decomposition mechanism in previous studies.[27,28]

$$HMX(C_4H_8N_8O_8) \rightarrow C_4H_8N_7O_6 + NO_2 \rightarrow \cdots \rightarrow 4CH_2N + 4NO_2 \qquad (3.3.3)$$

$$RDX(C_3H_6N_6O_6) \rightarrow C_3H_6N_5O_4 + NO_2 \rightarrow \cdots \rightarrow 3CH_2N + 3NO_2 \qquad (3.3.4)$$

According to our observation, the NO_2 molecule was initially isolated from each detonating molecule. Then, through cascading decomposition reactions, CH_2N and NO_2 molecules were formed largely during the heat-up period. After hydrogen transfer from CH_2N to NO_2, as-made HNO_2 was further decomposed to NO and OH, which are reactive radical molecule to decompose NM. Note that even though OH was observed to form during the heat-up period, owing to its fast reaction time, the number of OH was very small and thus it was not seen in **Figure 3.3.11** and **3.3.12**. As depicted in **Figure 3.3.13**, NM molecules packed with detonating molecules inside the CNT were facilitatively reacted with radical intermediates (*i.e.* NO molecule made from HMX), and decomposed into NO_2, NO, and CH_2. Thus, it was noteworthy that the decomposition reaction of NM was assisted by reaction intermediates directly made from the detonating molecule.
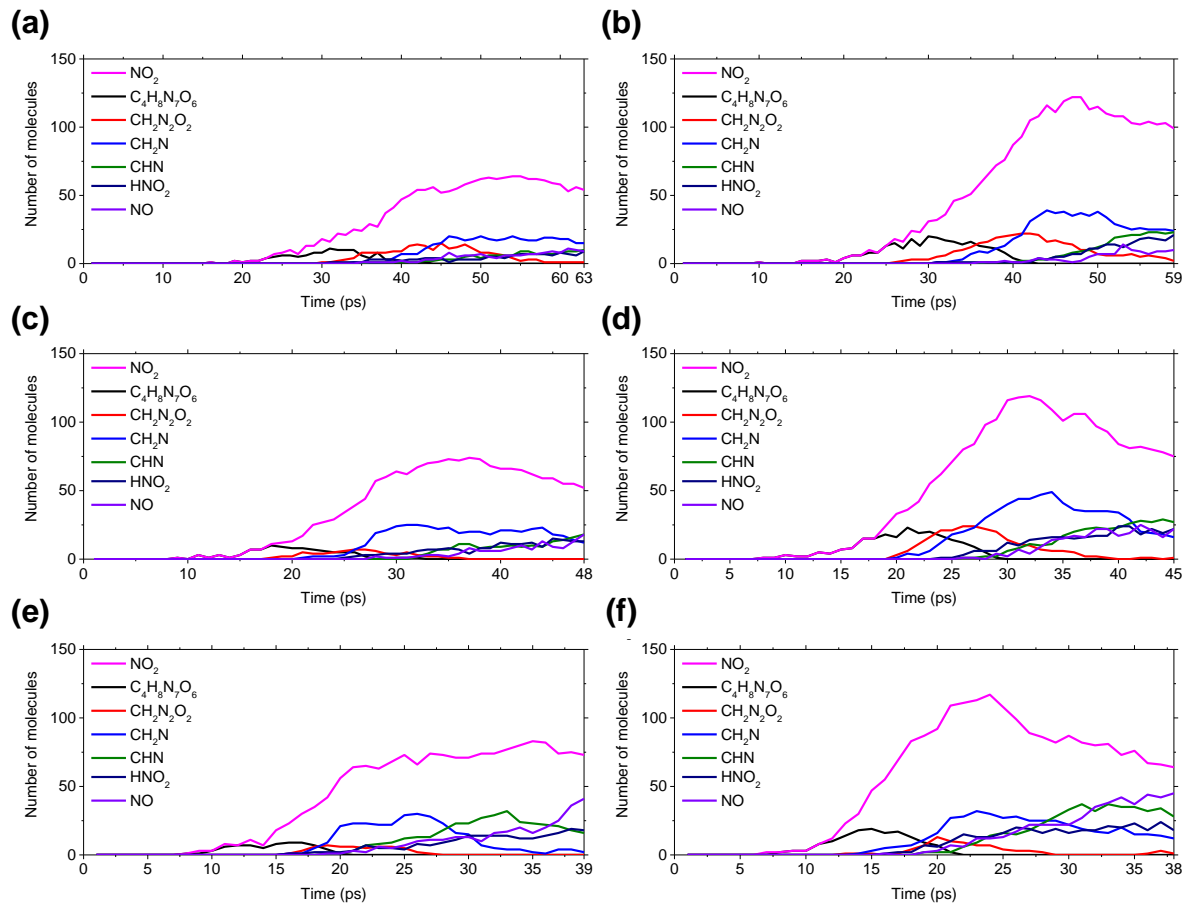
Figure 3.3.11 Number of major reaction intermediates observed during the heat-up period in HMX-mixed nanobombs. (a) 25 wt% HMX-mixed nanobomb with 2000 K heating. (b) 50 wt% HMX-mixed nanobomb with 2000 K heating. (c) 25 wt% HMX-mixed nanobomb with 2500 K heating. (d) 50 wt% HMX-mixed nanobomb with 2500 K heating. (e) 25 wt% HMX-mixed nanobomb with 3000 K heating. (f) 50 wt% HMX-mixed nanobomb with 3000 K heating. Copyright © 2019, The Korean Society of Industrial and Engineering Chemistry. Published by Elsevier B.V.
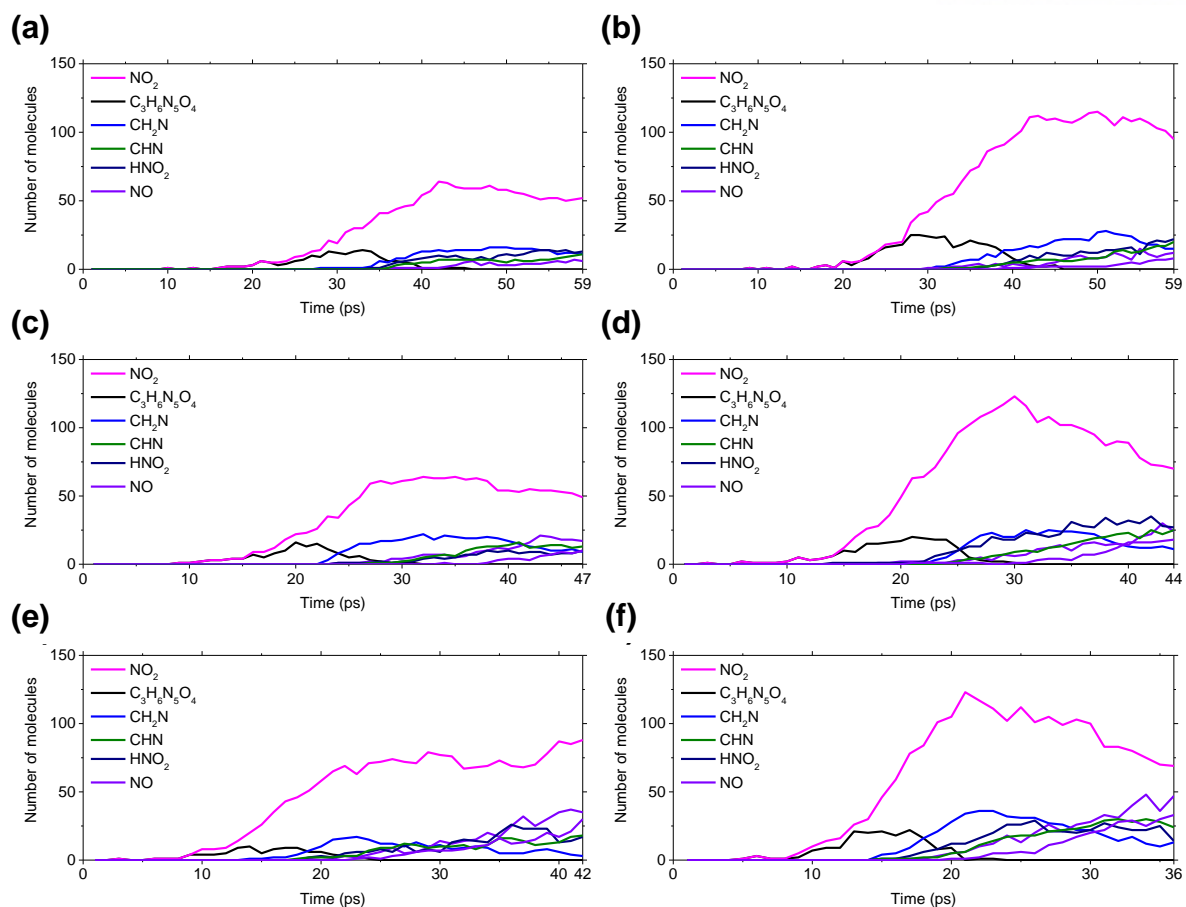
Figure 3.3.12 Number of major reaction intermediates observed during the heat-up period in RDX-mixed nanobombs. (a) 25 wt% RDX-mixed nanobomb with 2000 K heating. (b) 50 wt% RDX-mixed nanobomb with 2000 K heating. (c) 25 wt% RDX-mixed nanobomb with 2500 K heating. (d) 50 wt% RDX-mixed nanobomb with 2500 K heating. (e) 25 wt% RDX-mixed nanobomb with 3000 K heating. (f) 50 wt% RDX-mixed nanobomb with 3000 K heating. Copyright © 2019, The Korean Society of Industrial and Engineering Chemistry. Published by Elsevier B.V.
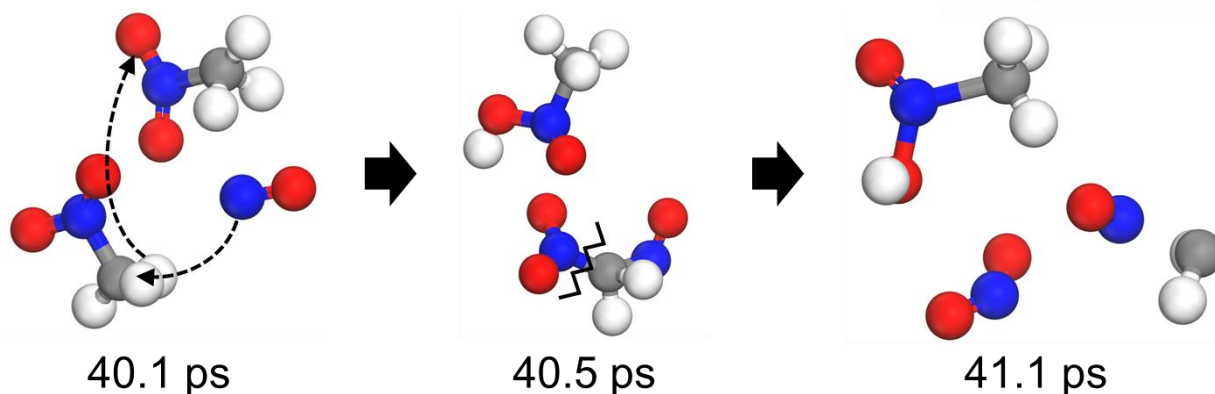
Figure 3.3.13 Mechanistic snapshots of NM and reactive intermediate (NO) made from HMX observed in reactive MD simulation. The number below each figure represents the simulation time obtained from the 50 wt% HMX-mixed nanobomb under a heating temperature of 2500 K. Color scheme is same as **Figure 3.3.1**. Copyright © 2019, The Korean Society of Industrial and Engineering Chemistry. Published by Elsevier B.V.

In the temperature profiles over simulation time, the most noticeable difference between the original and improved nanobombs due to incorporating detonating molecules was observed at the second elevation of temperature. Particularly for the decomposition under a heating temperature of 2000 K, the difference between HMX and RDX was not significant, but with increasing quantities of detonating molecules, the temperature-elevation rate increased in this period. In contrast, nanobomb without detonating molecule did not exhibit second temperature elevation during 300 simulation time even though about 40% of NM molecules were decomposed as shown in **Figure 3.3.8(a)**. We speculated that the absence of a temperature increase was due to the slow reaction rate of the pure-NM nanobomb. According to our previous study on nanobomb, the temperature of the nanobomb after heat-up period was dominantly affected by the formation of water, which was the largest exothermic reaction in the NM decomposition reaction. In **Figure 3.3.14**, the numbers of produced water molecules were compared depending on the number of detonating molecules. For the decomposition of the pure-NM nanobomb heated to 2000 K, only about 10% of the largest number of water formation compared to the other systems (≈ 280) was produced, whereas the 50 wt%-mixed nanobomb already reached maximum point at 200 ps NERMD simulation time. For the higher heating temperature, due to the high thermal energy, the difference between pure NM, 25 wt%-mixed, and 50 wt%-mixed systems at second temperature elevation period was diminished. At 3000 K, nanobomb systems were initially burst within 300 ps simulation time, which was identified by sudden increase in temperature, except for the pure-NM nanobomb. The difference in bursting time of each system was obvious, representing that HMX-mixed nanobomb is more effective in bursting performance.
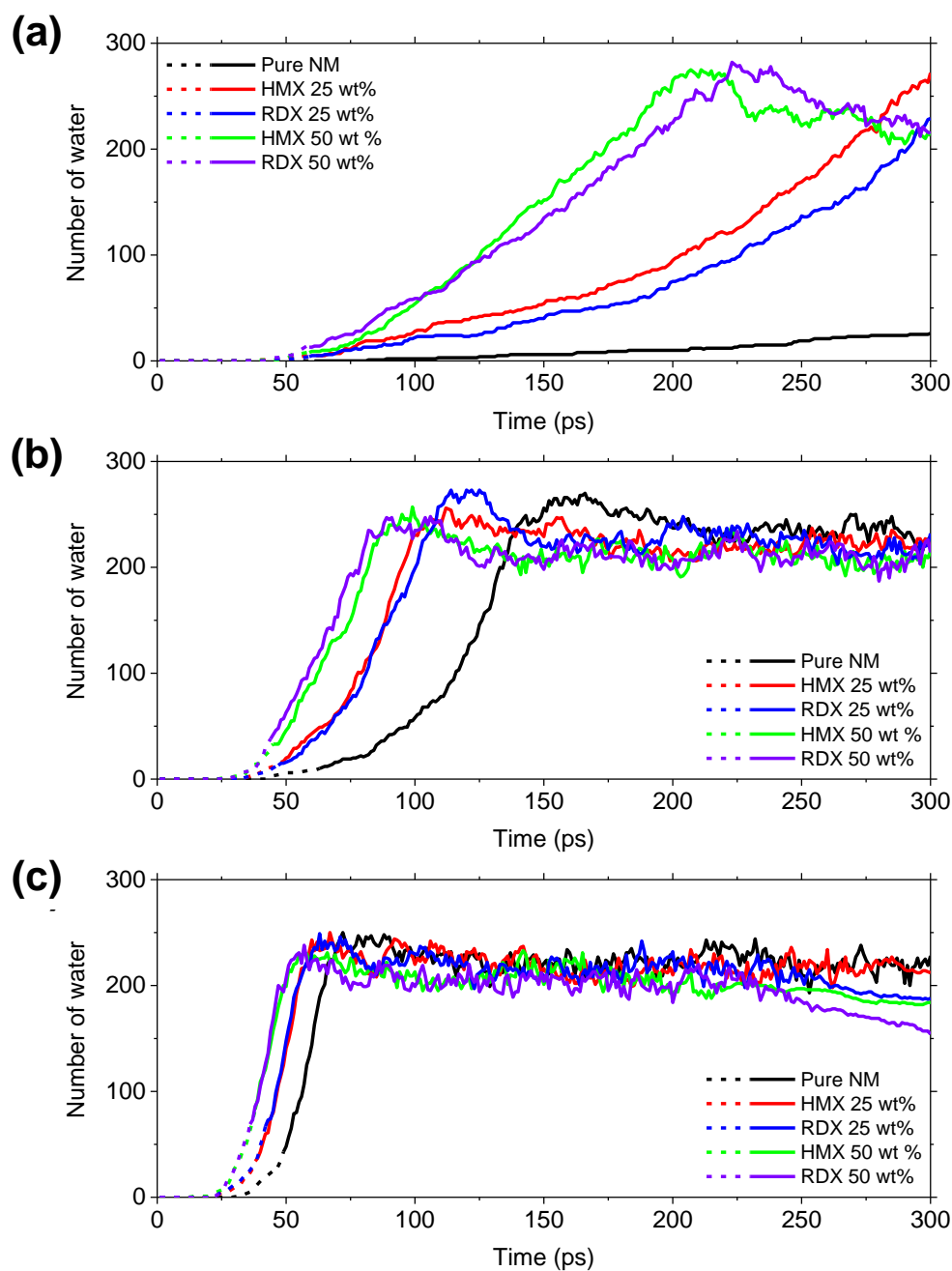
Figure 3.3.14 Number of water molecules produced from the nanobomb under heating temperatures of (a) 2000 K, (b) 2500 K, and (c) 3000 K. For the clear view, heat-up and decomposition periods are presented by dashed and solid lines, respectively. Copyright © 2019, The Korean Society of Industrial and Engineering Chemistry. Published by Elsevier B.V.
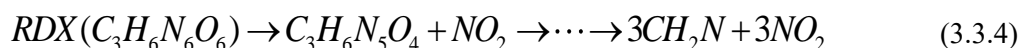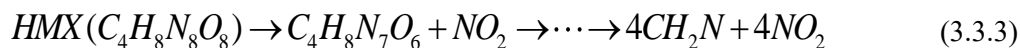
By considering the relation between the bursting time and reactivity of the CNT wall in our previous studies, we also compared the differences in reaction mechanisms to analyze the cause of the difference in bursting time depending on the detonating molecule. For the nanobomb systems containing detonating molecules, 50 wt% detonator-mixed nanobomb systems under the heating temperature of 3000 K were employed to compare the mechanism. Because the pure-NM nanobomb did not burst within 300 ps, short additional simulation was conducted to observe the precise bursting time and mechanism. A similar reaction mechanism was observed regardless of the species of detonating molecules (**Figure 3.3.15**). More specifically, at the beginning of the nanobomb decomposition, the internal products attached to the inside wall of the CNT, as observed at the beginning of the bursting mechanism for the pure-NM nanobomb in our previous studies.[6] At the same time, the hexagonal carbon atoms rings were deformed to make 7–7 carbon atom rings or 5–7 carbon atom rings (SW defect), at 307.1 ps (**Figure 3.3.15(a)**), 126.6 ps (**Figure 3.3.15(b)**), and 213.1 ps (**Figure 3.3.15(c)**). Then, a nanopore was formed by bond cleavage between carbon atoms around the deformed carbon ring at 327.8 ps (**Figure 3.3.15(a)**), 206.9 ps (**Figure 3.3.15(b)**), and 231.7 ps (**Figure 3.3.15(c)**). This pore gradually enlarged over time, and intermediates started to be ejected (*i.e.* burting of nanobomb started) at 336.0 ps (**Figure 3.3.15(a)**), 212.6 ps (**Figure 3.3.15(b)**), and 234.3 ps (**Figure 3.3.15(c)**). According to the bursting mechanism and temperature-profile analysis, the bursting time of the nanobomb systems with HMX and RDX was earlier than that of the pure-NM nanobomb. This difference was speculated to be due to the expedited attachment of reaction intermediates as well as the decomposition of NM by the addition of detonating molecules.
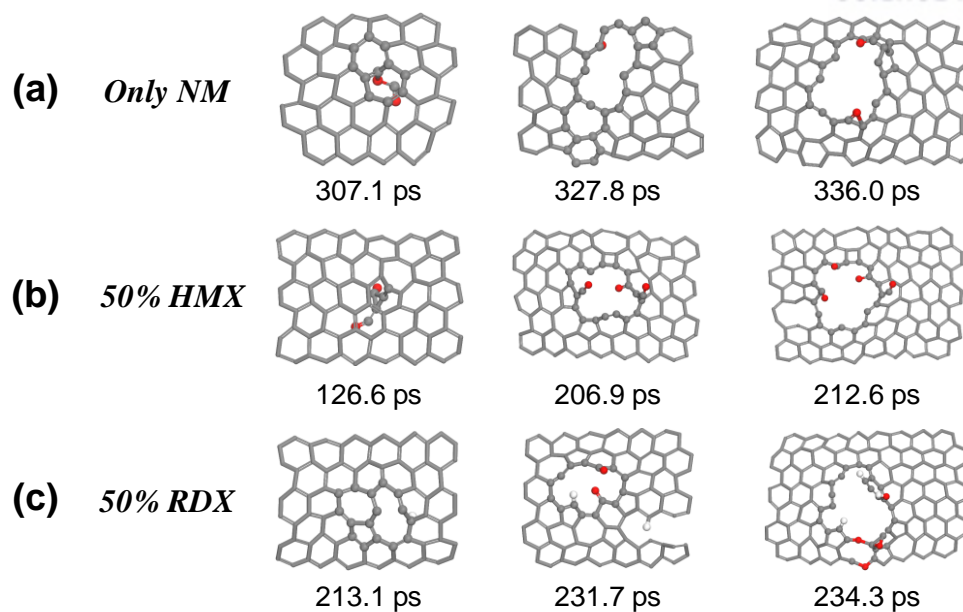
Figure 3.3.15 Mechanistic models in bursting with each physicochemical modification of CNT at the heating temperature of 3000 K: (a) pure-NM nanobomb, (b) 50 wt% HMX-mixed nanobomb, (c) 50 wt% RDX-mixed nanobomb. The three simulation snapshots in each system show the moments of the adsorption of internal products, pore generation, and expansion of the pore to burst, in chronological order. The carbon, oxygen, nitrogen, and hydrogen atoms are colored gray, red, blue, and white, respectively. Copyright © 2019, The Korean Society of Industrial and Engineering Chemistry. Published by Elsevier B.V.

3.3.4 Conclusion

In this study, to improve the bursting performance of nanobombs, a detonating molecule, which was calculated to achieve superior detonation velocity and pressure by DFT calculation, was incorporated in the nanobomb system. Their enhanced performance was investigated by NERMD simulations. The detonation velocity and pressure were calculated for five well-known explosive molecules (*i.e.* RDX, HMX, TNT, PTEN, and HNS) using the K–J equation, and the effects of mixing the NM and detonating molecule were observed at the bulk liquid mixture. As the result, RDX and HMX were observed not only to have high detonation velocity and pressure, but also to accelerate the NM decomposition in the bulk liquid mixture. These quickened reaction kinetics were more apparent at higher concentrations of the detonating molecule. Finally, to verify the enhancement of the bursting kinetics of the improved nanobombs, where HMX or RDX were encapsulated with NM together inside the CNT, NERMD simulations were conducted. All detonating molecules were first broken by the transferred heat from the CNT during the heat-up period, and eventually decomposed into NO and OH molecules. These reactive intermediates directly reacted with NM to promote rapid decomposition. According to the bursting mechanism observed from atomic trajectories during NERMD simulation, even though detonators helped the nanobomb decompose rapidly (*i.e.* fast decomposition of NM, formation of water, and bursting of nanobomb), the overall mechanisms of bursting were similar to each other because of the same atomic composition in the detonating molecule as NM. In conclusion, it has been observed that injecting a detonator, which was expected to have high D and P values in DFT calculation, inside the molecular bomb was effective in improving the performance of the molecular bomb.

3.3.5 References

1. Thottempudi, V.; Yin, P.; Zhang, J.; Parrish, D. A.; Shreeve, J. M. 1,2,3-Triazolo[4,5,-*e*]furazano[3,4,-*b*]pyrazine 6-Oxide—A Fused Heterocycle with a Roving Hydrogen Forms a New Class of Insensitive Energetic Materials. *Chem. Eur. J.* **2014**, 20, 542−548.

2. Zhang, J.; Zhang, Q.; Vo, T. T.; Parrish, D. A.; Shreeve, J. M. Energetic Salts with π-Stacking and Hydrogen-Bonding Interactions Lead the Way to Future Energetic Materials. *J. Am. Chem. Soc.* **2015**, 137, 1697−1704.

3. Zhang, J.; Mitchell, L. A.; Parrish, D. A.; Shreeve, J. M. Enforced Layer-by-Layer Stacking of Energetic Salts towards High-Performance Insensitive Energetic Materials. *J. Am. Chem. Soc.* **2015**, 137, 10532−10535.

4. Liu, J.; Jiang, W.; Yang, Q.; Song, J.; Hao, G.-Z.; Li, F.-S. Study of nano-nitramine explosives: preparation, sensitivity and application. *Def. Technol.* **2014**, 10, 184−189.

5. Qu, X.; Yang, Q.; Han, J.; Wei, Q.; Xie, G.; Chen, S.; Gao, S. High performance 5-aminotetrazole-based energetic MOF and its catalytic effect on decomposition of RDX. *RSC Adv.* **2016**, 6, 46212−46217.

6. Lee, J. H.; Kim, J. C.; Jeon, W. C.; Cho, S. G.; Kwak, S. K. Explosion Study of Nitromethane Confined in Carbon Nanotube Nanocontainer via Reactive Molecular Dynamics. *J. Phys. Chem. C* **2017**, 121, 6415−6423.

7. Smeu, M.; Zahid, F.; Ji, W.; Guo, H.; Jaidann, M.; Abou-Rachid, H. Energetic Molecules Encapsulated Inside Carbon Nanotubes and between Graphene Layers: DFT Calculations. *J. Phys. Chem. C* **2011**, 115, 10985−10989.

8. Liu, L.-M.; Car, R.; Selloni, A.; Dabbs, D. M.; Aksay, I. A.; Yetter, R. A. Enhanced Thermal Decomposition of Nitromethane on Functionalized Graphene Sheets: Ab Initio Molecular Dynamics Simulations. *J. Am. Chem. Soc.* **2012**, 134, 19011−19016.

9. Zhang, C.; Wen, Y.; Xue, X. Self-Enhanced Catalytic Activities of Functionalized Graphene Sheets in the Combustion of Nitromethane: Molecular Dynamic Simulations by Molecular Reactive Force Field. *ACS Appl. Mater. Interfaces* **2014,** 6, 12235–12244.

10. Guo, D.; An, Q.; Goddard, W. A. III.; Zybin, S. V.; Huang, F. Compressive Shear Reactive Molecular Dynamics Studies Indicating That Cocrystals of TNT/CL-20 Decrease Sensitivity. *J. Phys. Chem. C* **2014**, 118, 30202−30208.

11. Li, C.-F.; Mei, Z.; Zhao, F.-Q.; Xu, S.-Y.; Ju, X.-H. Molecular dynamic simulation for thermal decomposition of RDX with nano-AlH$_3$ particles. *Phys. Chem. Chem. Phys.* **2018,** 20, 14192−14199.

12. Zhang, J.-Q.; Xu, Y.-L.; Jia, Q.; Zhang, S.-J.; Liu, N.; Gao, H.-X.; Hu, R.-Z. Nonisothermal decomposition and safety parameters of HNIW/TNT cocrystal. *RSC Adv.* **2018,** 8, 31028−31036.

13. Mei, Z.; An, Q.; Zhao, F.-Q.; Xu, S.-Y.; Ju, X.-H. Reactive molecular dynamics simulation of thermal decomposition for nano-aluminized explosives. *Phys. Chem. Chem. Phys.* **2018,** 20, 29341−29350.

14. Vuppuluri, V. S.; Samuels, P. J.; Caflin, K. C.; Gunduz, I. E.; Son, S. F. Detonation Performance Characterization of a Novel CL-20 Cocrystal Using Microwave Interferometry. *Propellants Explos. Pyrotech.* **2018,** 43, 38–47.

15. Zhao, L.; Yin, Y.; Sui, H.; Yu, Q.; Sun, S.; Zhang, H.; Wang, S.; Chen, L.; Sun, J. Kinetic model of thermal decomposition of CL-20/HMX co-crystal for thermal safety prediction. *Thermochim. Acta* **2019,** 674, 44–51.

16. Kamlet, M. J.; Jacobs, S. J. Chemistry of Detonations. I. A Simple Method for Calculating Detonation Properties of C–H–N–O Explosives. *J. Chem. Phys.* **1968,** 48, 23–35.

17. Gui-xiang, W.; Chun-hong, S.; Xue-dong, G.; He-ming, X. Theoretical Investigation on Structures, Densities, Detonation Properties, and the Pyrolysis Mechanism of the Derivatives of HNS. *J. Phys. Chem. A* **2009,** 113, 1318–1326.

18. Politzer, P.; Murray, J. S. Some perspectives on estimating detonation properties of C, H, N, O compounds. *Cent. Eur. J. Energ. Mater.* **2011,** 8, 209–220.

19. Delly, B. An all-electron numerical method for solving the local density functional for polyatomic molecules. *J. Chem. Phys.* **1990,** 92, 508–517.

20. Delly, B. From molecules to solids with the DMol^3 approach. *J. Chem. Phys.* **2000,** 113, 7756–7764.

21. *Materials Studio 2019*; Dassault Systems BIOVIA, San Diego, CA, 2019.

22. Perdew, J. P.; Burke, K.; Ernzerhof, M. Generalized Gradient Approximation Made Simple. *Phys. Rev. Lett.* **1997,** 77, 3865–3868.

23. Tkatchenko, A.; Scheffler, M. Accurate Molecular Van Der Waals Interactions from Ground-State Electron Density and Free-Atom Reference Data. *Phys. Rev. Lett.* **2009,** 102, 073005.

24. Plimpton, S. Fast Parallel Algorithms for Short-Range Molecular Dynamics. *J. Comput. Phys.* **1995,** 117, 1–19.

25. Rom, N.; Zybin, S. V.; van Duin, A. C. T.; Goddard, W. A. III.; Zeiri, Y.; Katz, G.; Kosloff, R. Density-Dependent Liquid Nitromethane Decomposition: Molecular Dynamics Simulations Based on ReaxFF. *J. Phys. Chem. A* **2011,** 115, 10181–10202.

26. Sun, H.; Jin, Z.; Yang, C.; Akkermans, R. L. C.; Robertson, S. H.; Spenley, N. A.; Miller, S.; Todd, S. M. COMPASS II: extended coverage for polymer and drug-like molecule databases. *J. Mol. Model.* **2016,** 22, 47.

27. Chakraborty, D.; Muller, R. P.; Dasgupta, S.; Goddard, W. A. III. The Mechanism for Unimolecular Decomposition of RDX (1,3,5-Trinitro-1,3,5-triazine), an ab Initio Study. *J. Phys. Chem. A* **2000,** 104, 2261–2272.

28. Swadley, M. J.; Li, T. L. Reaction Mechanism of 1,3,5-Trinitro-*s*-triazine (RDX) Deciphered by Density Functional Theory. *J. Chem. Theory Comput.* **2007,** 3, 505–2272.

Chapter 4. Reaction Mechanism in Charge/Discharge Process of Rechargeable Li-CO₂ Battery

This chapter includes the following content:

Baek, K.[†]; Jeon, W. C.[†]; Woo, S.; Kim, J. C.; Lee, J. G.; An, K.; S. K. Kwak.; Kang, S. J., *Nat. Commun.* **2020** 11:456 (**†: equally contributed**). Reproduced with permission from Springer Nature. Copyright © 2020, Springer Nature.

4.1 Introduction

Rechargeable alkali metal-gas cells have drawn attention as high energy storage system and ultra-lightweight due to their air cathodes.[1-8] For the case of Li−O₂ battery, which is the representative alkali metal-gas cell, specific energy of the battery cell can reach to about 3860 m Ah g^{-1}, which is extremely higher value than that in existing Li ion batteries.[1-3] However, an unintended side reaction evoked by the carbon current collector and the aprotic electrolyte heavily lowers down the performance of Li−O₂ battery.[9–11] In addition, even in the Li−O₂ battery with nitrate-based molten salt electrolyte, although detrimental side reactions were reduced and the operation of battery cycle was prolonged, there is still one critical problem; the accumulation of the parasitic product Li_2CO_3 in repeating discharge-charge process.[9,12] Formation of Li_2CO_3 creates a useless space inside the battery cell and continuously induces overpotential, which eventually reduces the limit of capability in battery cycle.

To tide over these issues, researchers have succeeded in proposing a Li−CO₂ cell and showed the importance of its application as both a rechargeable secondary battery and CO₂ capture device to retard global warming[5,13–20]. However, although the Li-CO₂ cell effectively captures CO₂ gas during the discharge process, the high charge over-potential caused by the insulating and insoluble characteristics of Li_2CO_3 in the aprotic electrolyte should be reduced to prevent the severe parasitic reaction[7,13,14,21]. Moreover, the sluggish electron transfer enforce the Li−CO₂ cells operates on mild current densities, which can't meet the demands of high-performance battery for commercial purpose. Thus, recent researches are focusing on enhancing performance of Li−CO₂ cells by reducing the charge over-potential and extending the cycle ability, which enables the battery operation on high current densities.

In this regards, in-depth study on electrochemical reactions in Li−CO₂ battery is essential for battery cell design to step forward. The electrochemical reaction in Li−CO₂ battery, in general, CO₂ reduction reaction (CO₂RR), is known as follows; $4Li^+ + 3CO_2 + 4e^- \rightarrow 2Li_2CO_3 + C$ (2.80 V vs. Li/Li$^+$)[5]. This electrochemical reaction has been verified through experimental analysis[5,22], and reaction

mechanism analysis through DFT calculation[23]. However, CO_2RR would differ depending on the battery operating temperature[22], and is established on the most of conditions that aprotic solvent and carbon structure are used as electrolyte and cathode in battery cell.[17] In addition, because the electrochemical reaction is irreversible in $Li-CO_2$ battery, the electrochemical reaction in the charge process is still veiled. Therefore, it is necessary to closely investigate the mechanistic domain of electrochemical reaction covering both charge and discharge processes, and a theoretical approach can be an effective solution.

Herein, we revealed the reaction mechanism in the charge process and discharge process of high-power-density $Li-CO_2$ cell based on a quinary molten salt electrolyte containing Ru nanoparticles on the carbon cathode *via* DFT calculation. For the charge process, we could derive three reaction pathways of Li_2CO_3 decomposition, which were differentiated by operating temperature (*e.g.* 100 and 150 °C). These reaction pathways were validated with differential electrochemical mass spectrometry (DEMS) and X-ray photoelectron spectroscopy (XPS) data in experimentally synthesized quinary molten salt Li-CO_2 battery. In addition, we explored the reaction pathway of Li_2CO_3 formation on the discharge process depending on the existence of Ru surface to examine the catalytic effect of Ru nanoparticle. As the result, we could find that thermodynamic barrier energy was strikingly reduced when the reaction progress on Ru surface, which was supported by the electron transfer between CO_2 and Ru surface. Our theoretical method plays a key role in explaining the reason why the power density of $Li-CO_2$ battery is improved with the introduction of Ru surface.

4.2 Simulation Details

4.2.1 Calculation Details

The decomposition mechanism of Li_2CO_3 compound (charge process), and the formation mechanism of Li_2CO_3 with and without Ru surface (discharge process) were by DFT calculation. DFT calculations were performed with the $DMol^3$ program[24,25]. GGA and PBEsol were used for exchange-correlation functional[26]. The effective core potentials were used for core treatment with the basis set of DNP 4.4 level. The convergence tolerances of energy, force and displacement were set to 1×10^{-5} Ha, 0.002 Ha $Å^{-1}$, and 0.005 Å, respectively. To include van der Waals interaction effect, TS scheme was used[27]. The Brillouin-zone was sampled by a Monkhorst–Pack and k-point meshes for the bulk and slab models were set to ($2\times3\times3$) and ($2\times1\times1$), respectively. The COSMO solvation model was applied and the dielectric constant of quinary molten salt ($\varepsilon = 5.0$) was used. [28,29] Single LST and QST methodologies were applied to calculate transition states in reaction pathways of Li_2CO_3 decomposition, and the convergence criteria value of the rms force was set to 0.003 Ha $Å^{-1}$.[30,31]

4.2.2 Model Systems

The unit cell structure of Li_2CO_3, which was reported from previously experimental X-ray diffraction study, was optimized by DFT calculations (**Figure 4.1(a)**)[32]. The optimized lattice parameters for the monoclinic Li_2CO_3 (*i.e.* $a = 8.25$ Å, $b = 4.90$ Å, and $c = 5.89$ Å) were well matched with those of experimental crystal. To construct the surface slab models, we considered (001)-oriented three layers of the Li_2CO_3 slab model because of the most stable surface energy (**Figure 4.1(b)**)[33,34]. In all calculations for slab model, one layer on the top was allowed to relax, while two layers at the bottom were fixed to their position to represent the bulk phase during geometry optimization calculation. The vacuum space with a height of at least 12 Å was applied to slab model. To estimate the synergistic effect of quinary molten nitrate salts and Ru nanoparticles in discharge process, we constructed a Ru surface slab model, which consisted of (101) surface observed in the experiment. The slab models for our calculations consisted of 4 atomic layers. Among four layers, two layers on the top were relaxed while two layers on the bottom were fixed to represent the bulk phase. The vacuum space was applied at least 20 Å for all slab models. For the charge balance of system, K^+, which has the largest molar ratio in molten salt, was added explicitly to vacuum space of each slab model (**Figure 4.2**). Note that the vacuum space was treated to be implicitly the molten salt environment by the COSMO method.

(a)

(b)
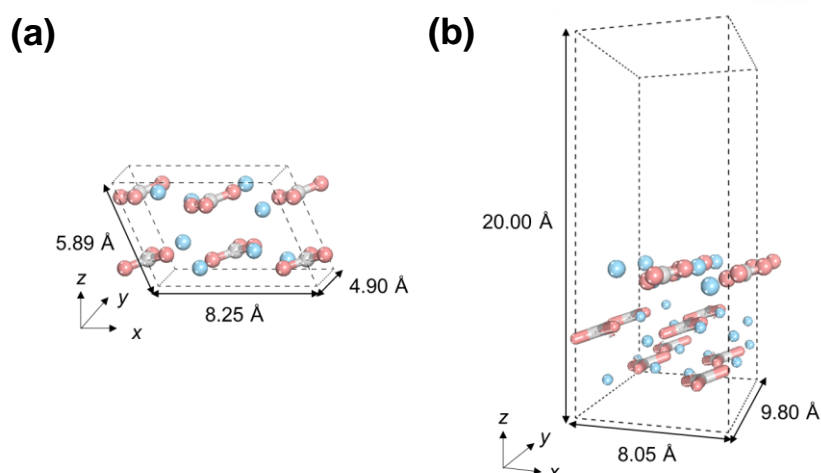
Figure 4.1 Li_2CO_3 model systems employed for reaction step calculation. (a)-(b) Unit cell structure (a) for monoclinic Li_2CO_3 (space group - $C2/c$), and slab model (b) of three layered Li_2CO_3 on (001) direction. Carbon, oxygen, and lithium atoms are colored in light gray, pink, and sky blue, respectively. For clear view in (b), top layer is presented by ball-and-stick style, and bottom two layers, which are fixed in position, are displayed in stick style. Copyright © 2020, Springer Nature.
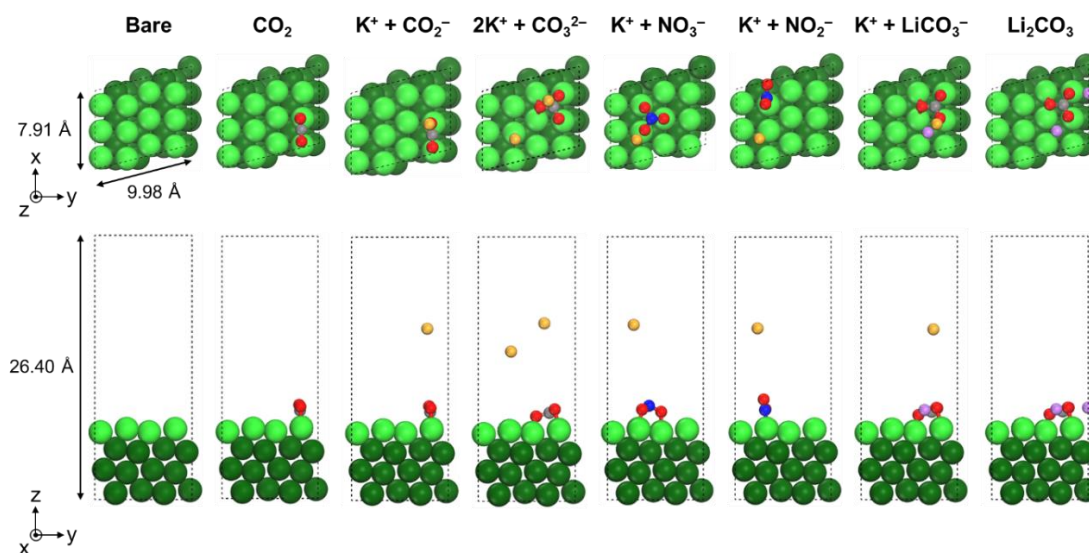
Figure 4.2 Optimized configurations of each molecule adsorbed on Ru (101) surface for discharge process. The empty region was treated by the COSMO method to impose the explicit molten salt phase. To balance an atomic charge, K^+ ion was added in explicit solvent phase of each model wherever necessary. Nitrogen, carbon, oxygen, ruthenium, lithium, and potassium atoms are colored in blue, light gray, red, dark cyan, purple, and yellow, respectively. For the clear view, Ru atoms in the top layer were colored in mint green. Copyright © 2020, Springer Nature.

4.2.3 Free Energy Calculation

The Li$^+$ extraction free energy, reaction free energy, activation free energy for decomposition reactions were calculated as follows,

$$\Delta G_X = \Delta E_X + \Delta ZPE - T\Delta S \ (X = \text{TRV, R, a}) \tag{4.1}$$

where ΔE_X represents the Li$^+$ extraction energy (ΔE_{TRV}) in electrochemical reaction, and the heat of reaction (ΔE_R), and activation energy (ΔE_a) for each reaction, ΔZPE is the change of zero-point vibrational enthalpy, and $-T\Delta S$ is the entropic contribution at 100 °C and 150 °C, where T is the temperature of system and ΔS is the change of entropy. Notably, the electrochemical reaction energy, which is calculated directly from the differences between total energies of before and after the extraction of lithium, is represented as the theoretical lithiation–delithiation reaction voltage (ΔE_{TRV})[35]. This energy was calculated as follows,

$$\Delta E_{TRV} = E_{Li_xCO_3} + (2-x)E_{Li} - E_{Li_2CO_3} \ (x = 0, 1, 2) \tag{4.2}$$

where $E_{Li_xCO_3}$ and $E_{Li_2CO_3}$ are the total energies of a formula unit for Li$_x$CO$_3$ and Li$_2$CO$_3$ structure, respectively, and E_{Li} is the energy of one atom in the lithium metal.

For the discharge process after charge process in **Figure 4.7** and **4.8**, Gibbs free energies were calculated based on equation (4.1) substituting ΔZPE with the vibrational enthalpy in each temperature.

4.3 Results and Discussion

4.3.1 Reaction Mechanism in Charged Process

Although the exact electrochemical reaction remains unclear, we examined the Li_2CO_3 decomposition mechanism by the DFT calculation to explain the variation of generating amount of CO_2 depending on the operating temperature (*i.e.* 100 °C and 150 °C) of Li−CO_2 cells (**Figure 4.1**). The Li_2CO_3 decomposition mechanism under implicit quinary molten salt condition was divided into the electrochemical reaction step, where Li ion is extracted by the charge potential, and the thermodynamic reaction step, where the carbonate on the surface participates in the reaction. We compared the Li extraction energy and activation energy of CO_2 formation reaction by NO_2^- to determine the reaction priority (**Figure 4.3**). Since the Li extraction energy (*i.e.* 2.79 and 3.24 eV for the first and second Li extraction, respectively) was lower than the activation energy of CO_2 formation reaction (*i.e.* 4.01 eV), it was predicted that the CO_2 formation reaction could occur after the Li extraction reaction. Thus, we suggest path a ($Li_2CO_3 + NO_2^- \rightarrow 2Li^+ + CO_2 + NO_3^- + 2e^-$) for the decomposition mechanism of Li_2CO_3 at 100 °C (**Figure 4.4(a)-(c)**). In path a, after the two Li atoms were extracted, carbonate ion reacted with NO_2^- to produce $[CO_3NO_2]^-$ at the first intermediate state (IM1). From IM1 to IM2, a bridge O atom bonded to C and N atoms was moved to form NO_3^- and produce CO_2. Then, CO_2 was desorbed from the surface in final state (FS). The full-charge N1s XPS analysis showed no peak of NO_2^- because of the generation of NO_3^- as we conjectured (**Figure 4.5(c)**). At 150 °C, as shown in **Figure 4.4(b)-(c)**, the Li_2CO_3 decomposition mechanism initially followed the same reaction process of path a. However, after CO_2 and NO_3^- are formed on the surface (IM2') in path b ($2Li_2CO_3 + NO_2^- \rightarrow 4Li^+ + C_2O_5^{2-} + NO_3^- + 2e^-$), CO_2 could react further with the adjacent carbonate to form $C_2O_5^{2-}$ (FS'). Separately, the unstable carbonate could react with the adjacent carbonate to form $C_2O_6^{2-}$ (FS'') in path c ($2Li_2CO_3 \rightarrow 4Li^+ + C_2O_6^{2-} + 2e^-$), where NO_2^- was not used as the reactant in the Li_2CO_3 decomposition mechanism. The three paths in the reaction mechanisms predicted to be occurred at 150 °C were consistent with experimental results, where NO_2^- and NO_3^- presented on the surface and small amount of CO_2 was released (**Figure 4.5(a)-(c)**). We speculated that the thermal energy at the higher temperature could promote the reactions of paths b and c; the activation energies of the two mechanisms (*i.e.* 1.39 eV for path b and 1.54 eV for path c at 150 °C) were higher than the activation energy for the mechanism to produce CO_2 gas (*i.e.* 0.99 eV for path a at 100 °C). Interestingly, CO_2 was favored in the adsorbed state considering the endothermic heat of reaction from IM2 to FS in path a without a transition state. This also could be a reason for CO_2 to undergo the reaction step from IM2 to FS' at 150 °C. All of the optimized configurations in each reaction mechanism were depicted in **Figure 4.6**. It should be noted that because the proposed pre-equilibrium electrochemical reactions are not the complete reaction mechanism of the charge process, the generation of the short-lived

intermediate $C_2O_6^{2-}$ produces new adducts, resulting in irreversible CO_2 evolution at 150 °C in the DEMS measurements in **Figure 4.5**.

(a)

(b)
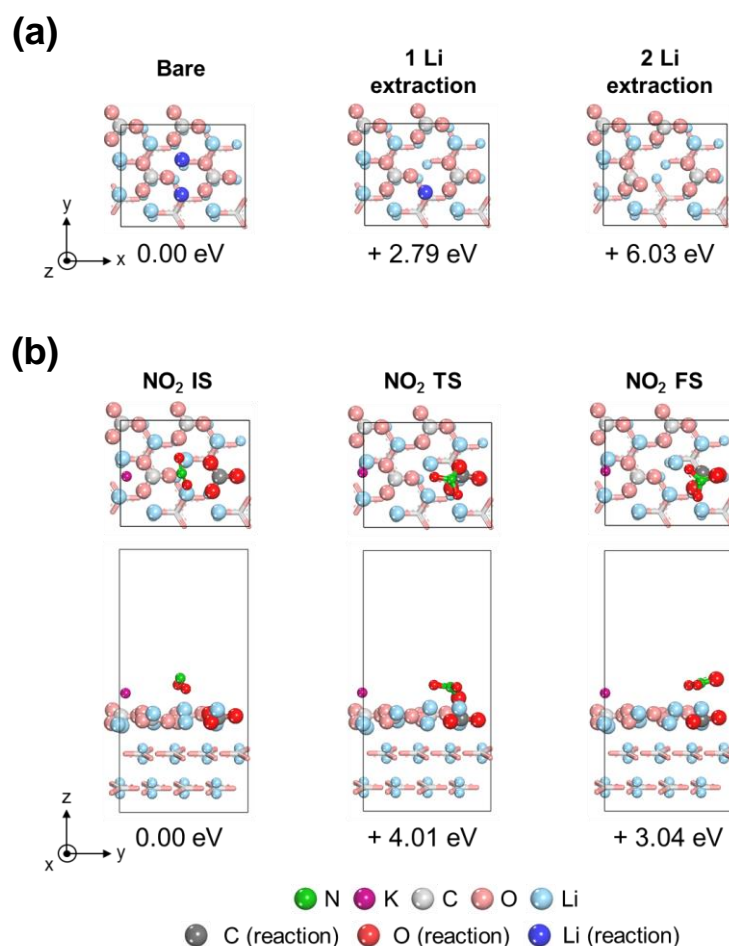
Figure 4.3 Comparison of the electrochemical reaction step and reaction step of Li_2CO_3 decomposition on the surface at 100 °C. (a) Optimized configurations of the extraction of Li reactions. (b) Optimized configurations of the reaction mechanism between CO_3^{2-} and NO_2^{-} to produce CO_2 and NO_3^{-}. The states and relative energies are written in the top and bottom of each figure. NO_2 IS, NO_2 TS, and NO_2 FS represent initial state, transition state, and final state, respectively. Nitrogen, potassium, carbon, oxygen, and lithium atoms are colored in green, purple, light gray, pink, and sky blue. And, for the clear view, the carbon, oxygen, and lithium atoms which participate in the reaction are colored in dark gray, red, and blue. Copyright © 2020, Springer Nature.
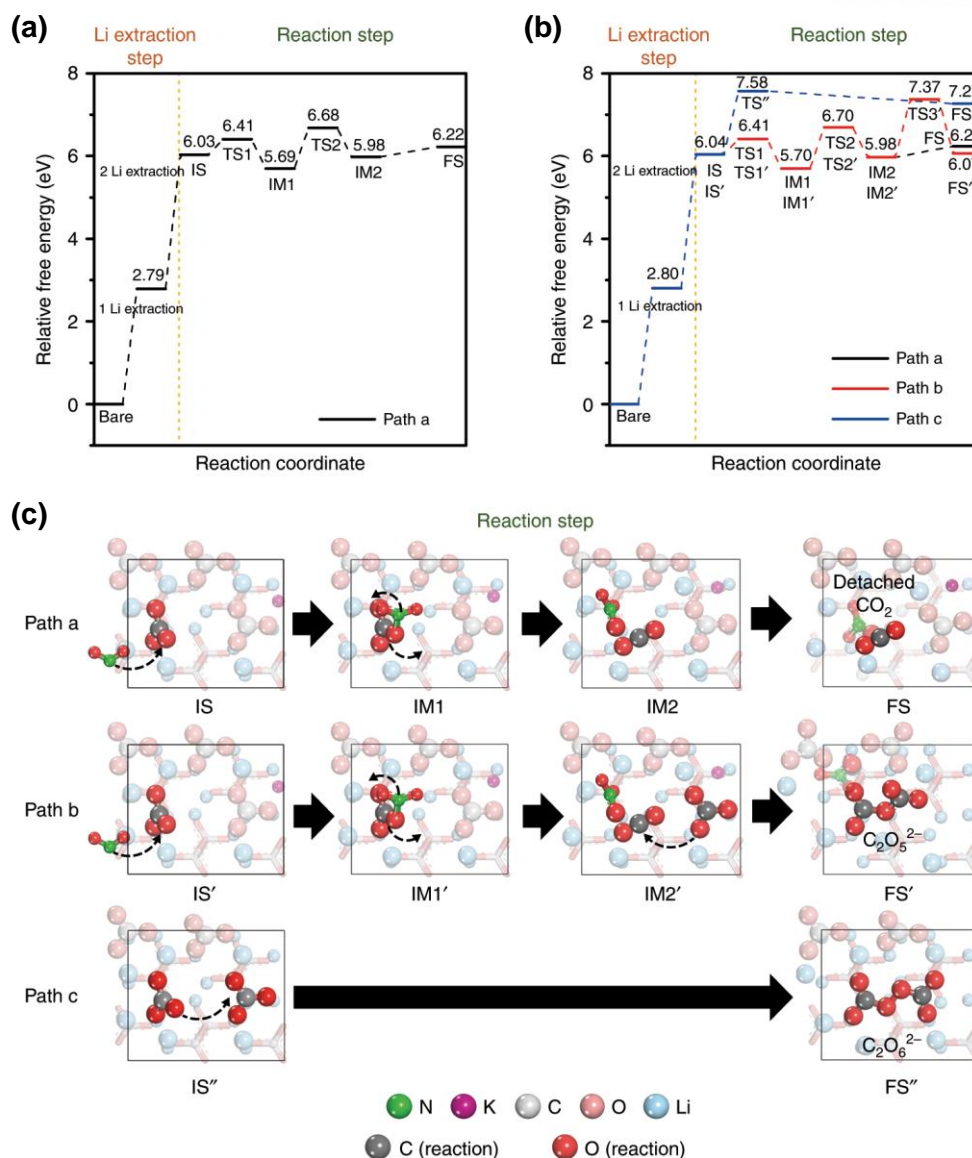
Figure 4.4 Reaction mechanism of Li_2CO_3 decomposition. (a) Reaction coordinate of one possible path a to produce CO_2 and NO_3^- (black line) at 100 °C. (b) Reaction coordinate of three plausible pathways (*i.e.* path a, path b to produce $C_2O_5^{2-}$ and NO_3^- (red line), and path c to produce $C_2O_6^{2-}$ (blue line)) at 150 °C. (c) Optimized configurations on three plausible pathways for reaction step corresponding to (a) and (b). IS, IM, and FS in each reaction mechanism represent the initial state, intermediate state, and final state, respectively. The yellow dotted line is the boundary between the Li extraction step and the reaction step, and the numbers represent the relative free energies based on that of bare surface in (a) and (b). Nitrogen, potassium, carbon, oxygen, and lithium atoms are colored in green, purple, light gray, pink, and sky blue. And, for the clear view, the carbon, oxygen, and lithium atoms which participate in the reaction are colored in dark gray, red, and blue. Arrow dotted lines represent the movement of molecules from state to state. For the clear view, the molecules except reacting molecules were made to be translucent in (c). Copyright © 2020, Springer Nature.
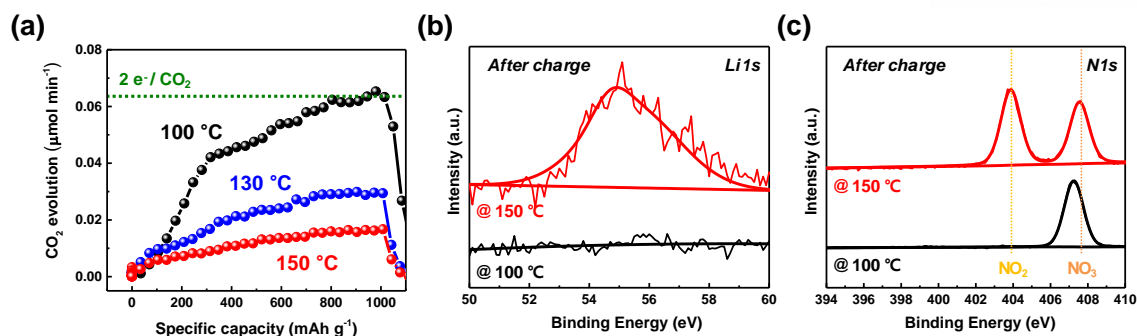
Figure 4.5 Experimental characterizations of Li−CO_2 battery using quinary molten salt electrolyte. (a) DEMS result of the Li−CO_2 cell containing quinary molten salt electrolyte at different operating temperatures during charge process. The green dots correspond to the theoretical amount of CO_2 evolution. (b)-(c) High-resolution XPS Li1s (b) and N1s (c) spectra of the carbon cathodes after 1000 mAh g^{-1} discharge and charge processes. The black and red lines indicate the results at operating temperatures of 100 and 150 °C, respectively. Copyright © 2020, Springer Nature.
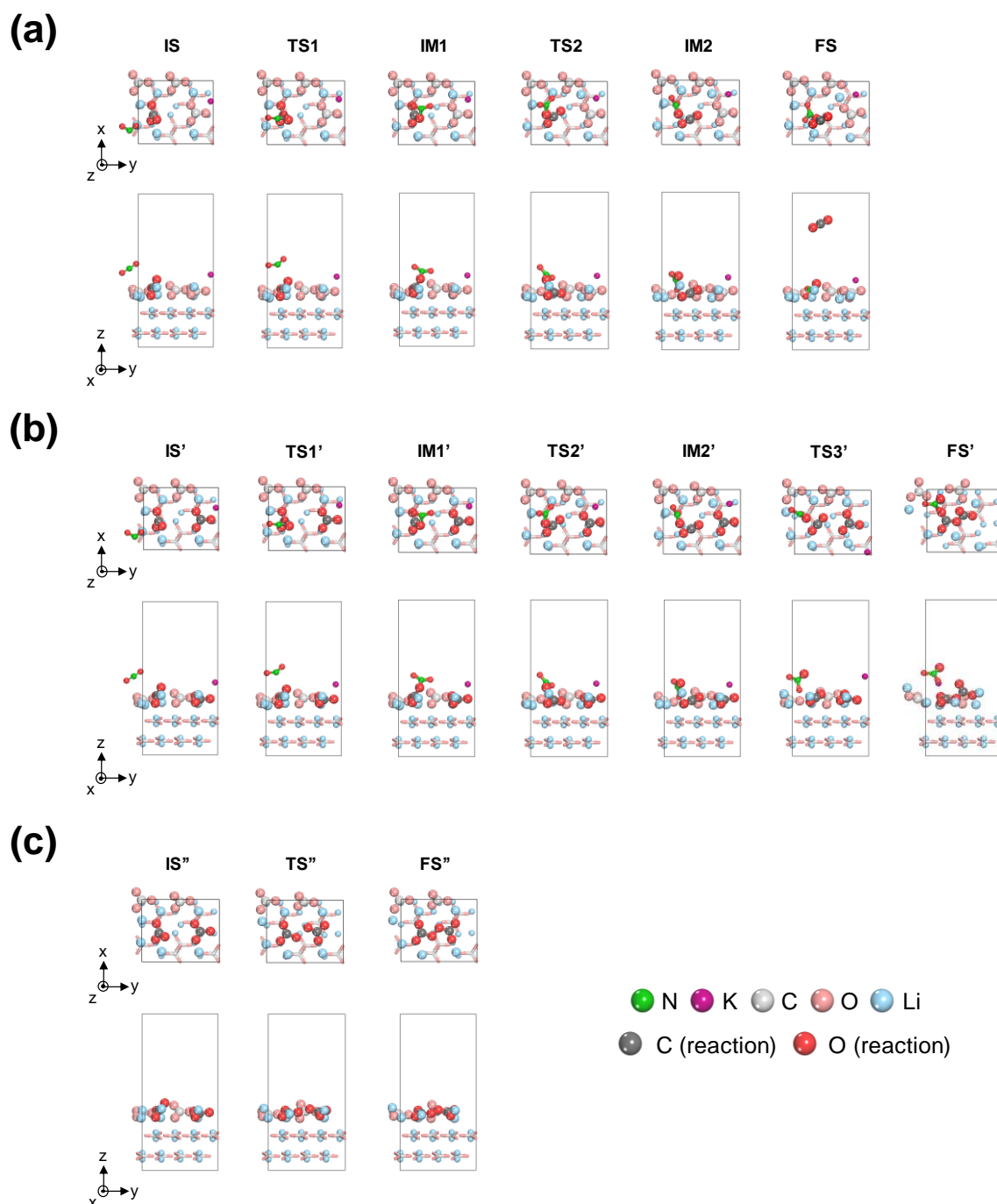
Figure 4.6 Optimized configurations of three plausible pathways for reaction step of Li_2CO_3 decomposition. (a)-(c) Reaction path a (a), reaction path b (b), and reaction path c (c) which produce NO_3^- and CO_2, NO_3^- and $C_2O_5^{2-}$, and $C_2O_6^{2-}$, respectively. The names of states are written on the top of each figure. IS, IM, TS, and FS in each reaction mechanism represent the initial state, intermediate state, transition state, and final state, respectively. Color scheme is same with **Figure 4.3**. Copyright © 2020, Springer Nature.

4.3.2 Reaction Mechanism in Discharged Process

To estimate the energy change along reaction coordinate in CO_2RR mechanism, energy states of reaction intermediates in the discharge process were estimated on free energy diagram depending on temperature of battery operation (**Figure 4.7**). As the result, the thermodynamic barrier for Li_2CO_3 formation was the step from CO_2 to CO_2^-. The barrier was slightly reduced at 150 °C but overall reaction went through same pathway. In addition, Gibbs free energy of reaction was estimated, and the value was substituted into the Nernst equation to derive the discharge potential at different temperatures as follows,

$$\Delta G = -nFV \tag{4.3}$$

where ΔG is the free energy of the reaction, n is the number of electrons in the electrochemical reaction, F is the Faraday constant, and V is the discharge potential. The resulting discharge potentials are 2.42 and 2.39 V at 100 and 150 °C (**Table 4.1** and **Figure 4.7**), respectively, and these values are in the range of experimental data. Additionally, the trend in the plot of the temperature versus discharge potential matches the trend reported in a previous Li–CO_2 study[22].
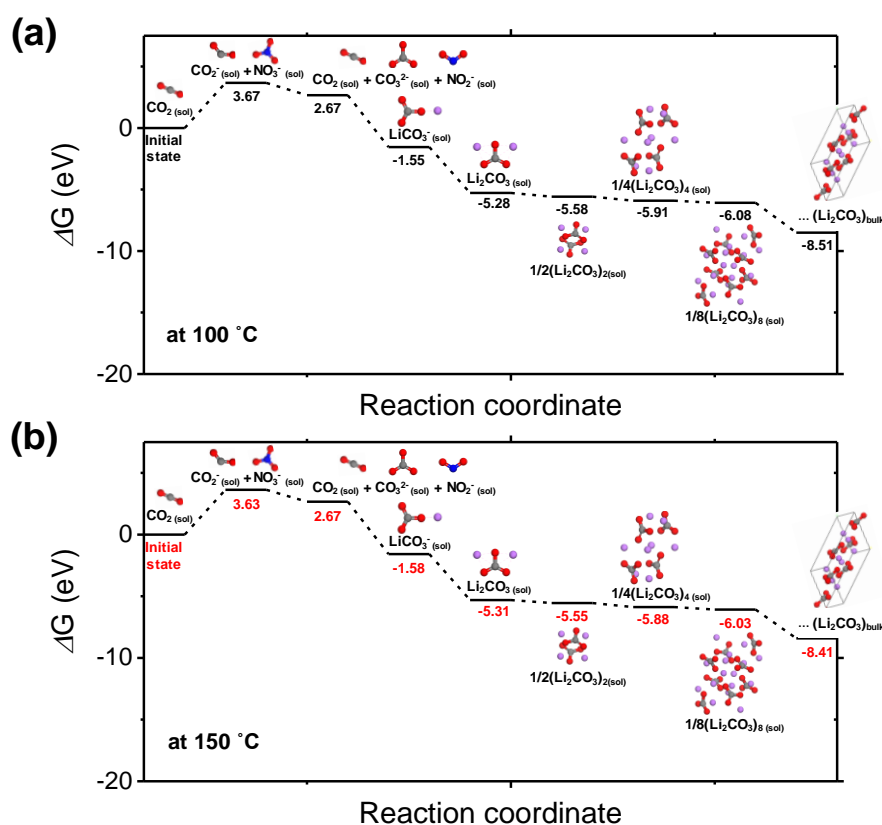
Figure 4.7 Free energy diagrams of the discharge process at 100 and 150 °C. (a)–(b) The electrochemical reaction starts from CO_2. The black numbers in (a) and the red numbers in (b) below each energy state represent the relative free energies compared to each initial state at 100 and 150 °C. Oxygen, carbon, nitrogen, and lithium atoms are colored in red, gray, blue, and purple, respectively. Copyright © 2020, Springer Nature.

Table 4.1 Thermodynamic energy terms in the Gibbs free energy of reaction. Copyright © 2020, Springer Nature.

Electrochemical reaction	Temp. (°C)	ΔH (eV)	$-T\Delta S$ (eV)	ΔG (eV)	Discharge potential versus Li/Li$^+$ (V)
$2Li^+ + CO_2 + 2e^- + NO_3^-$ $\rightarrow Li_2CO_3 + NO_2^-$	100	5.23	0.40	-4.83	2.42
	150	5.21	0.43	-4.78	2.39

Furthermore, the role of Ru nanoparticles on the improvement of battery performance was investigated by comparing the free energy diagrams. Gibbs free energies (ΔG) on each state in discharge process from initial state to the formation of Li_2CO_3 were calculated with and without Ru particles (**Figure 4.8**). Overall, ΔG, which is the free energy of reaction till the formation of Li_2CO_3, decreased by 0.87 eV at 100 °C and 0.66 eV at 150 °C, respectively, when the reaction occurs on the Ru surface. Interestingly, at the potential determining step that requires the largest endothermic energy change (*i.e.* thermodynamic barrier) in the discharge process: $Li^+ + e^- + CO_2 \rightarrow Li^+ + CO_2^-$, ($\Delta G$ decreased by 2.07 eV at 100 °C and 2.04 eV at 150 °C, respectively. In the operation of battery cell, thermodynamic barrier is directly proportional to the overpotential. Therefore, the overpotential was reduced by the addition of Ru. This result corresponds to the operating voltage and power density *versus* current density of the Li-CO$_2$ battery measured in the experiment that the power density was dramatically increased with the Ru catalyst (**Figure 4.9(a)-(b)**). Therefore, the addition of Ru nanoparticles induced a lower decrease in operating voltage at high current densities, indicating the decrease of overpotential.

To gain further insight into the origin of reduction of thermodynamic barrier, we looked at atomic charge states. It was found that charges of adsorbed CO_2 and CO_2^- were similar value to each other (*i.e.* −0.451 and −0.429) (**Figure 4.10(a)**). However, charges of Ru with adsorbed CO_2 and CO_2^- were +0.451 and −0.562, respectively (**Figure 4.10(b)**). The integrated DOS also showed that Ru with adsorbed CO_2^- showed more numbers of electrons than that of Ru with adsorbed CO_2 (**Figure 4.10(c)**). Thus, electron transfer occurred from CO_2^- to Ru, indicating that CO_2^- was easily stabilized on Ru surface. Consequently, these results can explain the synergistic effect of the quinary molten salts and Ru nanoparticle contributing to the swift improvement of power density of Li−CO$_2$ battery.
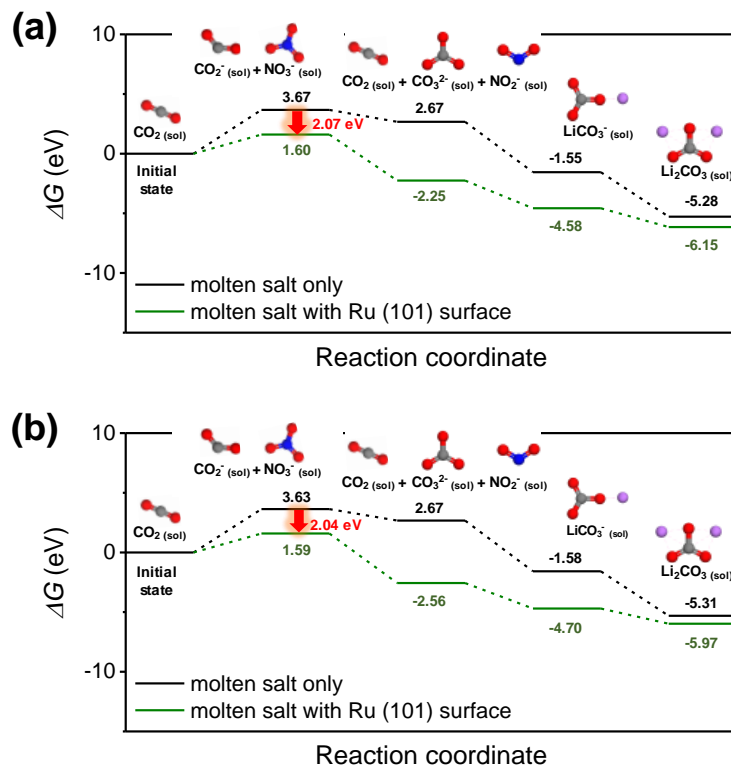
Figure 4.8 Free energy diagrams of discharge process from CO_2 reduction to one Li_2CO_3 formation at 100 °C and 150 °C. Electrochemical reaction starts from CO_2 at 100 °C (a) and 150 °C (b), respectively. The black and green numbers in each (a) and (b) represent the relative free energies compared to each initial state of molten salt only and Ru (101) surface. Oxygen, carbon, nitrogen, lithium atoms are colored in red, gray, blue, and purple, respectively. Red arrow and number represent the change of ΔG in potential determining step. Copyright © 2020, Springer Nature.

(a) **(b)**
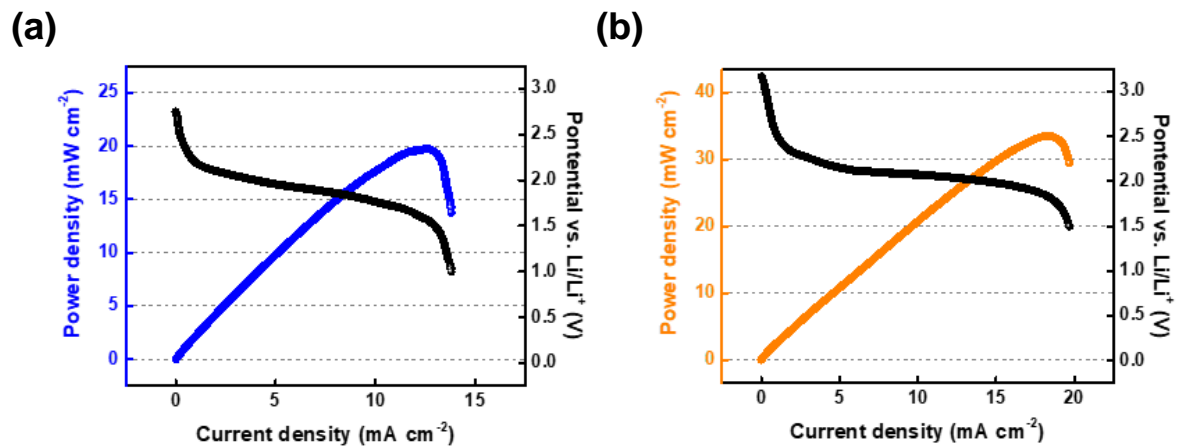
Figure 4.9 Electrochemical performance of Li−CO₂ battery cell with quinary-molten salt electrolyte. Profile of operating voltage and power density *versus* current density of the Li-CO2 battery at 150 °C with scan rate of 0.01 mA s⁻¹ without Ru nanoparticle (a) and with Ru nanoparticle (b). Copyright © 2020, Springer Nature.

(a) **(b)** **(c)**

total charge of CO₂ : −0.451   total charge of CO₂ : −0.429

total charge of Ru : + 0.451   total charge of Ru : −0.562
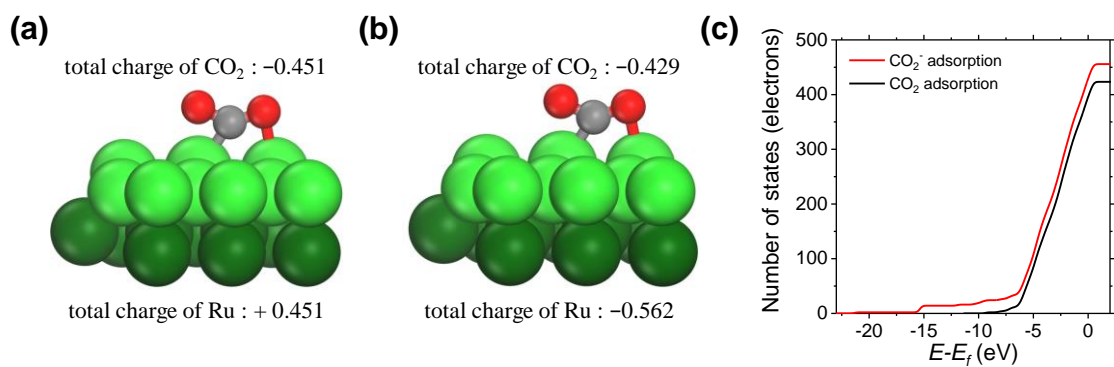
Figure 4.10 Atomic charges and configurations of CO₂−Ru surface (a) and CO₂⁻ −Ru surface (b). Integrated DOS of all Ru atoms in CO₂−Ru surface and CO₂⁻−Ru surface (c). Copyright © 2020, Springer Nature.

4.4 Conclusion

Electrochemical reaction pathways in charge and discharge process on a high-performance Li$-$CO$_2$ cell based on the quinary molten salt electrolyte with Ru nanoparticles on the carbon cathode were theoretically investigated. For the calculation of energy state in each reaction intermediate on charge process, it was found that reaction pathways were varied with temperature and especially three plausible pathways coexisted in 150 °C. In addition, free energy diagrams in discharge process were compared to examine the catalytic effect of Ru nanoparticle. As the result, it is found that Ru surface effectively reduced thermodynamic barrier on discharge process, which was identified with electron transfer. Through our finding, we could effectively explain the synergistic effect on the improvement of Li$-$CO$_2$ battery performance through a combination of molten salt electrolyte and Ru catalyst.

4.5 References

1. Girishkumar, G.; McCloskey, B.; Luntz, A. C.; Swanson, S.; Wilcke, W. Lithium−air battery: promise and challenges. *J. Phys. Chem, Lett.* **2010,** 1, 2193–2203.

2. Bruce, P. G.; Freunberger, S. A.; Hardwick, L. J.; Tarascon, J.–M. Li–O_2 and Li–S batteries with high energy storage. *Nat. Mater.* **2012,** 11, 19–29.

3. Lu, J.; Li, L.; Park, J.–B.; Sun, Y.–K.; Wu, F.; Amine, K. Aprotic and aqueous Li–O_2 batteries. *Chem. Rev.* **2014,** 11, 5611–5640.

4. Kang, S. J.; Mori, T.; Narizuka, S.; Wilcke, W.; Kim, H.–C. Deactivation of carbon electrode for elimination of carbon dioxide evolution from rechargeable lithium–oxygen cells. *Nat. Commun.* **2014,** 5, 3937.

5. Qiao, Y.; Yi, J.; Wu, S.; Liu, Y.; Yang, S.; He, P.; Zhou, H. Li–CO_2 electrochemistry: a new strategy for CO_2 fixation and energy storage. *Joule* **2017,** 1, 359–370.

6. Zhou, J.; Li, X.; Yang, C.; Li, Y.; Guo, K.; Cheng, J.; Yuan, D.; Song, C.; Lu, J.; Wang, B. A quasi-solid-state flexible fiber-shaped Li–CO_2 battery with low overpotential and high energy efficiency. *Adv. Mater.* **2018,** 31, 1804439.

7. Zhang, Z.; Wang, X.–G.; Zhang, X.; Xie, Z.; Chen, Y.–N.; Ma, L.; Peng, Z.; Zhou. Z. Verifying the rechargeability of Li-CO_2 batteries on working cathodes of Ni nanoparticles highly dispersed on N-doped graphene. *Adv. Sci.* **2018,** 5, 1700567.

8. Xing, Y.; Yang, Y.; Li, D.; Luo, M.; Chen, N.; Ye, Y.; Quan, J.; Li, L.; Yang, D.; Wu, F. Crumpled Ir nanosheets fully covered on porous carbon nanofibers for long-life rechargeable Lithium–CO_2 batteries. *Adv. Mater.* **2018,** 30, 1803124.

9. McCloskey, B. D.; Speidel, A.; Scheffler, R.; Miller, D.; Viswanathan, V.; Hummelshøj, J.; Nørskov, J; Luntz, A. Twin problems of interfacial carbonate formation in nonaqueous Li–O_2 batteries. *J. Phys. Chem. Lett.* **2012,** 3, 997–1001.

10. Ottakam Thotiyl, M. M.; Freunberger, S. A.; Peng, Z.; Bruce, P. G. The carbon electrode in nonaqueous Li–O_2 cells. *J. Am. Chem. Soc.* **2013,** 135, 494–500.

11. McCloskey, B. D.; Methune, D. S.; Shelby, R. M.; Mori, T.; Scheffler, R.; Speidel, A.; Sherwood, M.; Luntz, A. C. Limitations in rechargeability of Li-O_2 batteries and possible origins. *J. Phys. Chem. Lett.* **2012,** 3, 3043–3047.

12. Zhao, Z.; Huang, J.; Peng, Z. Achilles' Heel of lithium–air batteries: Lithium carbonate. *Angew. Chem. Int. Ed.* **2018,** 57, 3874–3886.

13. Zhang, X.; Zhang, Q.; Zhang, Z.; Chen, Y.; Xie, Z.; Wei, J.; Zhou, Z. Rechargeable Li–CO_2 batteries with carbon nanotubes as air cathode. *Chem. Commun.* **2015,** 51, 14636–14639.

14. Li, C.; Guo, Z.; Yang, B.; Liu, Y.; Wnag, Y.; Xia, Y. A rechargeable Li-CO_2 battery with a gel polymer electrolyte. *Angew. Chem. Int. Ed.* **2017,** 56, 9126–9130.

15. Hu, X.; Li, Z.; Chen, J. Flexible Li-CO$_2$ batteries with liquid-free electrolyte. *Angew. Chem. Int. Ed.* **2017,** 129, 5879–5883.

16. Yang, S.; Qiao, Y.; He, P.; Liu, Y.; Cheng, Z.; Zhu, J.–j.; Zhou, H. A reversible lithium–CO$_2$ battery with Ru nanoparticles as a cathode catalyst. *Energy Environ. Sci.* **2017, 10**, 972–978.

17. Liu, B.; Sun, Y.; Liu, L.; Chen, J.; Yang, B.; Xu, S.; Yan, X. Recent advances in understanding Li–CO$_2$ electrochemistry. *Energy Environ. Sci.* **2019,** 12, 887-922.

18. Wang, Q.; Luo, J.; Zhong, Z.; Borgna, A. CO$_2$ capture by solid adsorbents and their applications: current status and new trends. *Energy Environ. Sci.* **2011,** 4, 42–55.

19. Liu, Y.; Wang, R.; Lyu, Y.; Li, H.; Chen, L. Rechargeable Li/CO$_2$-O$_2$ (2:1) battery and Li/CO$_2$ battery. *Energy Environ. Sci.* **2014,** 7, 677–681.

20. Zhang, Z.; Zhang, Q.; Chen, Y.; Bao, J.; Zhou, X.; Xie, Z.; Wei, J.; Zhou, Z. The first introduction of graphene to rechargeable Li-CO$_2$ batteries. *Angew. Chem. Int. Ed.* **2015,** 57, 6550–6553.

21. Qie, L.; Lin, Y.; Connell, J. W.; Xu, J.; Dai, L. Highly Rechargeable Lithium-CO$_2$ Batteries with a Boron- and Nitrogen-Codoped Holey-Graphene Cathode. *Angew. Chem. Int. Ed.* **2017,** 56, 6970–6974.

22. Xu, S.; Das, S. K.; Archer, L. A. The Li–CO$_2$ battery: a novel method for CO$_2$ capture and utilization. *RSC Adv.* **2013,** 3, 6656–6660.

23. Ahmadiparidari, A.; Warburton, R. E.; Majidi, L.; Asadi, M.; Chamaani, A.; Jokisaari, J. R.; Rastegar, S.; Hemmat, Z.; Sayahpour, B.; Assary, R. S.; Narayanan, B.; Abbasi, P.; Redfern, P. C.; Ngo, A.; Vörös, M.; Greeley, J.; Klie, R.; Curtiss, L. A.; Salehi-Khojin, A. A Long-Cycle-Life Lithium–CO$_2$ Battery with Carbon Neutrality. *Adv. Mater.* **2019,** 1902518.

24. Delley, B. An all-electron numerical method for solving the local density functional for polyatomic molecules. *J. Chem. Phys.* **1990, 92**, 508–517.

25. Delley, B. From molecules to solids with the Dmol^3 approach. *J. Chem. Phys.* **2000,** 113, 7756–7764.

26. Perdew, J. P.; Ruzsinszky, A.; Csonka, G. I.; Vydrov, O. A.; Scuseria, G. E.; Constantin, L. A.; Zhou, X.; Burke, K. Restoring the density-gradient expansion for exchange in solids and surfaces. *Phys. Rev. Lett.* **2008,** 100, 136406.

27. Tkatchenko, A.; Xcheffler, M. Accurate molecular van der Waals interactions from ground-state electron density and free-atom reference data. *Phys. Rev. Lett.* **2009,** 102, 073005.

28. Klamt, A.; Schüürmann, G. COSMO: a new approach to dielectric screening in solvents with explicit expressions for the screening energy and its gradient. *J. Chem. Soc. Perkin Trans. 2* **1993,** 5, 799–805.

29. Looyenga, H. Dielectric constants of homogeneous mixture. *Mol. Phys.* **1965,** 9, 501–511.

30. Bell, S.; Crighton, J. S. Locating transition states. *J. Chem. Phys.* **1984,** 80, 2464–2475.

31. Halgren, T. A.; Lipscomb, W. N. The synchronous-transit method for determining reaction

pathways and locating molecular transition states. *Chem. Phys. Lett.* **1977,** 49, 225–232.

32. Dffenberger, H.; Zemann, J. ζristallographie. Z. Kristallogr, *Cryst. Mater.* **1979,** 150, 133–138.

33. Liu, Z.; Qi, Y.; Lin, Y. X.; Chen, L.; Lu, P.; Chen, L. Q. Interfacial study on solid electrolyte interphase at Li metal anode: implication for Li dendrite growth. *J. Electrochem. Soc.* **2016,** 163, A592–A598.

34. Ling, C.; Zhang, R.; Takechi, K.; Mizuno, F. Intrinsic Barrier to Electrochemically Decompose Li_2CO_3 and LiOH. *J. Phys. Chem. C* **2014,** 118, 26591−26598.

35. Kalantarian, M. M.; Asgari, S.; Mustarelli, P. Theoretical investigation of Li_2MnSiO_4 as a cathode material for Li-ion batteries: a DFT study. *J. Mater. Chem. A* **2013,** 1, 2847–2855.

Chapter 5. Summary and Future Perspectives

5.1 Summary

Estimation of the reaction characteristics is essential for advanced nanomaterials in energy application because it can grasp and predict physicochemical properties of nanomaterials and provide guidelines for development. This doctoral dissertation includes theoretical studies on reaction characteristics of energetic nanomaterials and $Li-CO_2$ battery *via* multi-scale molecular simulation approach.

In **Chapter 2**, we theoretically investigated and quantified reaction characteristics of Ni-Al nanolayer by MD simulations. The overall procedure of reaction process between Ni and Al nanolayer showed marginal difference by varying different ignition temperature, bilayer thickness, and stoichiometry of Ni-Al nanolayer. However, the rate and range of atomic diffusion in the reaction of Ni-Al nanolayer varied with each condition. In particular, the reaction time decreased with an increase in the ignition temperature and decrease in bilayer thickness of Ni-Al nanolayer. The stoichiometry which exhibited maximized thermodynamic and kinetic properties in reaction was $Ni_{0.5}Al_{0.5}$.

In **Chapter 3**, we studied explosion dynamics of a nanobomb depending on various modifications of nanobomb components and external shocks *via* multi-scale molecular simulation approach. It was found that higher packing density of NM and initial heating temperature reduced the time for bursting but the overall bursting sequence of nanobomb was consistent to every packing density and heating temperature.

Subsequently, the effects of every physicochemical modifications (*e.g.* chirality, nitrogen-doping, and monovacancy defect) of CNT were examined in reaction characteristics of nanobomb. Among physicochemical modifications, monovacancy defect distinctly accelerated the explosion of nanobomb due to its lowest energy for SW defect formation and strong binding with reaction intermediates from NM decomposition. In addition, we observed the different explosion trends by each heating method (*e.g.* electric spark and electromagnetic induction) and their continuity on time for shocking on nanobomb.

Thirdly, we investigated the bursting dynamics of nanobomb where NM and detonating molecule were co-encapsulated into nanocontainer. HMX and RDX were selected as target detonating molecules by screening thermodynamic and detonating properties using K−J equation and NERMD simulations of their bulk models. After co-encapsulation with NM, both HMX and RDX shortened the bursting time of nanobomb. This was because detonating molecules were decomposed prior to NM and their reaction

intermediates help to decompose NM.

In **Chapter 4**, we theoretically investigated mechanistic domains in electrochemical reactions of molten-salt based Li$-$CO$_2$ battery cell. In charge process, there was one reaction pathway at 100 °C and three reaction pathways at 150 °C simultaneously, which were possible to go over the activation energy barrier by thermal energy at high temperature. Further, we sketched free energy diagram of Li$_2$CO$_3$ formation in discharge process. Thermodynamic barrier was located on the reduction of CO$_2$ (CO$_2$ + e$^-$ $\rightarrow$ CO$_2{}^-$) and Ru surface could lower down the barrier energy by energetic stabilization of CO$_2{}^-$.

In summary, we theoretically investigated reaction pathways and estimated thermodynamic and kinetic properties of nanomaterials, which can be utilized for energy applications. We expect our fundamental studies to lay the groundwork for the development of optimized nanomaterials for energy applications to meet the commercial needs.

5.2 Future Perspectives

It is necessary to discuss the direction of the future theoretical studies for suggesting smart and efficient design of nanomaterial in energy applications. In other words, we would like to address the perspectives on current technological trends and propose alternatives to solve existing problems in energetic applications of nanomaterials.

First, in the case of reactive multilayers such as Ni-Al system, recent studies have been focused on the investigation of reaction characteristics in the interface of multilayers, including the contents in **Chapter 2** of this doctoral thesis. However, thermodynamic and kinetic properties associated with the reaction pathway on the surface of each layer have not been fully established. In particular, if reactive multilayers are used in the form of nanoparticles with a size of few nanometers, the reaction process at the atomic level becomes very complicated as the proportion of surface where uncoordinated sites exist gets much higher than that in bulk foils, and sintering and merging between nanoparticles should be considered in reaction progress. Therefore, it is necessary to conduct screening and quantification of reaction characteristics of exothermic multilayers for various conditions such as heating temperature, system size, stoichiometry of constituent elements, and crystal morphologies through multi-scale molecular simulation approaches.

In addition, researches have been actively conducted to manipulate high-energy nanomachinery such as nanobomb in recent years. These encapsulated HEMs are expected to be applicable for biomedical purposes (*e.g.* killing harmful bacteria) and military purposes (*e.g.* destroying electronic device) through combination with functional polymers. However, there are still limitations in the actual production and application due to lack of physicochemical data on these nanomaterials. To overcome these shortcomings, synthetic methods need to be systematically and repeatedly examined to ensure the physicochemical stability and reproducibility in encapsulation of HEM into the nanocontainer with high density. Furthermore, theoretical studies on polymer candidates are needed to determine which polymer can form nanomaterial complex much stable when it binds to encapsulated HEMs by responding only to specific stimuli and strengthen physical and chemical stabilities.

Since Li−CO_2 battery cells have only been studied with limited combinations of cathodes and electrolytes, more researches are needed to establish a battery system that enables an ideal electrochemical reaction.[1,2] Screening appropriate electrolytes is needed to increase chemical stability by avoiding unwanted side reactions and to maximize the efficiency of battery performance. The catalyst should therefore be investigated further. Additionally, it is essential to present an optimized pathway in the electrochemical reaction by investigating every possible reaction intermediate on energy surfaces that can be generated on the operation of Li−CO_2 battery depending on possible conditions. In

this series of research processes, it can be expected that a mechanistic study through a multi-scale molecular simulation approach can incessantly provide important information in the future.

5.3 References

1. Qiao, Y.; Yi, J.; Wu, S.; Liu, Y.; Yang, S.; He, P.; Zhou, H. Li-CO_2 electrochemistry: a new strategy for CO_2 fixation and energy storage. *Joule* **2017,** 1, 359–370.

2. Liu, B.; Sun, Y.; Liu, L.; Chen, J.; Yang, B.; Xu, S.; Yan, X. Recent advances in understanding Li–CO_2 electrochemistry. *Energy Environ. Sci.* **2019,** 12, 887-922.

List of Publications

SCI publications (first or co-first author) [†: equal contribution]

1. **<u>Woo Cheol Jeon</u>†**, Jeong Hyeon Lee†, Jin Chul Kim†, Seok Ju Kang, Sang-Hyun Jung, Soo Gyeong Cho, and Sang Kyu Kwak*, "Reaction kinetics of mixtures of nitromethane and detonator confined in carbon nanotube"
Journal of Industrial and Engineering Chemistry, **2020**, *83*, 64-71.

2. **<u>Woo Cheol Jeon</u>†**, Jeong Hyeon Lee†, Jin Chul Kim†, Sang-Hyun Jung, Soo Gyeong Cho, and Sang Kyu Kwak*, "Controllable Explosion of Nanobomb by Modifying Nanocontainer and External Shocks"
Journal of Physical Chemistry C, **2020**, 124, 3341-3351.

3. Kyungeun Baek†, **<u>Woo Cheol Jeon</u>†**, Seongho Woo, Jin Chul Kim, Jun Gyeong Lee, Kwangjin An*, Sang Kyu Kwak*, and Sang Hoon Joo*, "Synergistic effect of quinary molten salts and ruthenium catalyst for high-power-density lithium-carbon dioxide cell"
Nature Communications, **2020**, *11:456*. [News Broadcasting]

4. Gwan Yeong Jung†, **<u>Woo Cheol Jeon</u>†**, Sukbin Lee, Sang-Hyun Jung, Soo Gyeong Cho, and Sang Kyu Kwak*, "Reaction characteristics of Ni-Al nanolayers by molecular dynamics simulation"
Journal of Industrial and Engineering Chemistry, **2018**, *57*, 290-296.

5. Jeong Hyeon Lee†, Jin Chul Kim†, **<u>Woo Cheol Jeon</u>†**, Soo Gyeong Cho*, and Sang Kyu Kwak*, "Explosion Study of Nitromethane Confined in CNT Nanocontainer via Reactive Molecular Dynamics"
Journal of Physical Chemistry C, **2017**, 121, 6415-6423.

SCI publications (co-author)

6. Gyutae Nam†, Yeonguk Son†, Sung O Park†, **<u>Woo Cheol Jeon</u>**, Haeseong Jang, Joohyuk Park, Sujong Chae, Youngshin Yoo, Jaechan Ryu, Min Gyu Kim*, Sang Kyu Kwak*, and Jaephil Cho*, "A Ternary $Ni_{46}Co_{40}Fe_{14}$ Nanoalloy-Based Oxygen Electrocatalyst for Highly Efficient Rechargeable Zinc–Air Batteries"
Advanced Materials, **2018**, *30*, 1803372.

7. Woong Gi Lee†, Do Hyeong Kim†, **<u>Woo Cheol Jeon</u>**, Sang Kyu Kwak*, Seok Ju Kang*, and Sang Wook Kang*, "Facile control of nanoporosity in Cellulose Acetate using Nickel(II) nitrate additive and water pressure treatment for highly efficient battery gel separators"
Scientific Reports, **2017**, 7:1287.

8. Eun Min Go†, Tae Kyung Lee†, Sa Hoon Min†, **<u>Woo Cheol Jeon</u>**, Byeong-Su Kim*, Min Sun Yeom*, and Sang Kyu Kwak*, "Theoretical Study on Enhancement of Sensing Capability of Plasmonic Dimer Au Nanoparticles with Amphiphilic Polymer Brushes"
Journal of Physical Chemistry C, **2016**, 120, 11068-11077.

Non-SCI publications

9. Gwan Yeong Jung, **<u>Woo Cheol Jeon</u>**, Eun Hye Shin, and Sang Kyu Kwak*, "Application of Multiscale Molecular Modeling and Simulation Methods"
    News & Information for Chemical Engineers, **2014,** *32*, 775-779. (Magazine)

Acknowledgements